Materials Issues for
Tunable RF and Microwave
Devices III

Materials Issues for Tunable RF and Microwave Devices III

Symposium held April 2–3, 2002, San Francisco, California, U.S.A.

EDITORS:

Steven C. Tidrow
U.S. Army Research Laboratory
Adelphi, Maryland, U.S.A.

James S. Horwitz
Naval Research Laboratory
Washington, D.C., U.S.A.

Xiaoxing Xi
The Pennsylvania State University
University Park, Pennsylvania, U.S.A.

Jeremy Levy
University of Pittsburgh
Pittsburgh, Pennsylvania, U.S.A.

M|R|S

CONTENTS

BST FILMS AND APPLICATIONS

POSTER SESSION

*Invited Paper

*Invited Paper

vii

PREFACE

This volume contains 29 of some 45 papers presented at Symposium H, "Materials Issues for Tunable RF and Microwave Devices III," held April 2–3 at the 2002 MRS Spring Meeting in San Francisco, California. Generous financial support by DARPA, ONR, ARL and seed money from MRS allowed us to invite and provide partial financial support to leading academic, industry and government scientists throughout the international community as well as partial financial assistance to graduate students presenting their research results at the Meeting.

The purpose of this symposium was to bring together researchers from a broad range of disciplines to discuss the challenges facing the implementation of an affordable tunable RF and microwave device technology. Low cost, tunable, microwave devices will have a tremendous impact on a variety of commercial and military systems, including, but not limited to, tunable band-select filters for wireless communications, phase shifters and true time delay devices for electronic scanning antennas, tunable radiating structures for frequency hopping, and tunable transformers to reduce RF impedance mismatch.

The papers of this proceedings discuss a wide range of topics from materials issues through devices and even a system level demonstration of electronic beam steering. Specific materials issues discussed are: new tunable materials; issues of tunability, preparation and optimization of bulk and thin film properties; materials, surface, and interface characterization; evaluation of material loss and loss mechanisms; effects of microstructure; and temperature stability. At the device level, phase shifters are discussed and a new device concept for variable true time delay versus phase shift is introduced. At the system level, a paraelectric lens is used to demonstrate electronic beam steering of an antenna at 10 GHz with about 2 dB of loss.

It is hoped that the reader of this volume will come away with some appreciation for the fine work presented by the participants of this symposium, and the contribution that these papers make to the area of materials issues for tunable RF and microwave devices.

Steven C. Tidrow
James S. Horwitz
Xiaoxing Xi
Jeremy Levy

June 2002

MATERIALS RESEARCH SOCIETY SYMPOSIUM PROCEEDINGS

MATERIALS RESEARCH SOCIETY SYMPOSIUM PROCEEDINGS

BST Films and Applications

Investigations on Sol-Gel Derived $Ba_{0.5}Sr_{0.5}Ti_{1-\delta}Mn_\delta O_3$ (δ = 0.0 to 5.0 at%) Thin Films for Phase Shifter Applications

R.S. Katiyar[1], M. Jain[1], S.B. Majumder[1],
R.R. Romanofsky, F.W. van Keuls, and F.A. Miranda
[1]PO Box 23343, Department of Physics, University of Puerto Rico, San Juan, PR 00931,U.S.A.
NASA, Glenn Research Center, Cleveland, OH 44135, U.S.A.

ABSTRACT

Highly (100) oriented $Ba_{0.5}Sr_{0.5}Ti_{1-\delta}Mn_\delta O_3$ thin films were deposited on (100) $LaAlO_3$ (LAO) substrate by sol-gel technique. We have studied systematically the effect of Mn doping on the degree of texturing, surface morphology, dielectric properties and phase transition behavior of barium strontium titanate (BST) thin films. Up to 3 at % Mn doping the degree of (100) texturing and grain size of BST (50/50) thin films were markedly improved, which led to an increased tunability from 29% (undoped) to 39% (3 at % Mn doped); measured at 1 MHz and $2.34V/\mu m$ bias field. The transition and Curie-Weiss temperatures of BST (50/50) thin films were found to be about 266 K and 185 K respectively, which confirmed the first order phase transition in the films. The variation of transition temperatures as a function of Mn doping contents in BST (50/50) thin films were influenced by the variation of stress state and surface morphology modifications induced by Mn doping. The bias field dependence of the dielectric constant and loss tangents of undoped and Mn doped films were analyzed in terms of a model based on Devonshire theory. Phase shift measurements showed that the degree of phase shift increases from 239° to 337° with 0 to 3 at% Mn doping. The insertion loss also increases from 5.4 dB (undoped) to 9.9 dB (3 at % Mn doped) with doping content so that there is no effective improvement in the κ factor, which remains in the range of 33 - 44°/dB. Modification in surface morphology and film stoichiometry induced by Mn doping is thought to play significant role in observed phase shifter characteristics.

INTRODUCTION

Modern electronic scan phase array antennas can steer transmitted and received signals without mechanically rotating the antenna. Ferroelectric phase shifters have low power requirement as compared to the ferrite based phase shifters and also, they exhibit low loss at microwave frequencies as compared to semiconductor based phase shifters. $Ba_xSr_{1-x}TiO_3$ (BST) thin films, paraelectric at room temperature (x < 0.7), are attractive candidates for tunable dielectric devices such as voltage-controlled oscillators (VCO), tunable filters, phase-shifters,

Contact author: R. S. Katiyar
email : rkatiyar@rrpac.upr.clu.edu
Tel: (787)-751-4210, Fax: (787)-764 -2571

tunable matching networks and frequency multipliers. High dielectric tunability and low dielectric loss at GHz frequencies are required for microwave applications. Moreover, for impedance matching purposes the dielectric constants of the films should be low with low leakage current densities. Fabrication of phase shifter utilizing bulk BST remains unsuccessful due to higher voltage requirement as well as higher dielectric constant. In thin film form the dielectric constant of BST is low as compared to its bulk counterpart due to finer grain size as well as presence of interfacial layers and also the dielectric can be tuned at moderate voltage compatible with modern electronic circuitry. To achieve low dielectric loss BST thin films should be grown with low defect densities and it has been reported that epitaxially grown film on lattice matched substrates has better tunability as compared to polycrystalline thin films [1]. However, epitaxially or textured thin films usually have higher leakage current densities as compared to polycrystalline thin films [2]. Efforts have been made to modify the electrical characteristics of BST thin films by adding impurity elements. Up to 1 at % Mn doping was found to increase the dielectric constant of undoped BST from 1736 to 2093, the loss tangent was reduced from 0.0153 to 0.0033 whereas the tunabilty was reduced from 66 to 63 % [3]. Mg^{2+} doping up to 5 at% in BST (60/40) thin films was found to yield single-phase perovskite thin films, however, excess Mg^{2+} addition up to 20 at% was found to yield multi-phase material [4]. The reduction of dielectric constant, loss tangent and leakage current densities with Mg doping were attractive for phase shifter application, however, the tunability of undoped BST was also found to be decreased from 28 % to 7.9 % with 20 at % Mg doping. Al^{3+} doping was found to modify the microstructure of BST (40/60) ceramics and up to 1 at % Al doping the grain size is increased and then decreased with further Al addition [5]. The dielectric constant was found to decrease with Al addition. B^{3+} doping was found useful to initiate liquid phase sintering and impart better sinterability and lower surface roughness of BST thin films. Boron was found to form highly insulating B_2O_3 layer at the grain boundary, which was claimed to be responsible for the lower leakage current densities of Boron doped BST thin films [6].

From the literature review, it appears the addition of impurity element has significant impact on the phase formation behavior, and microstructure evolution of BST thin films. In the present work we have made a systematic attempt to synthesize highly oriented Mn doped $Ba_{0.5}Sr_{0.5}Ti_{1-x}Mn_xO_3$ (x = 0.0 to 5.0 at %) thin films by an economic sol-gel process. The effect of Mn doping on the phase formation behavior, growth characteristics, surface morphology, and electrical characteristics were studied. We have fabricated eight elements coupled micro-strip phase shifters using Mn doped BST films and the quality of these films were evaluated in terms of their degree of phase shift and insertion loss characteristics.

EXPERIMENTAL METHODS

To prepare the BST precursor sol, barium and strontium acetates were co-dissolved in acetic acid and ethylene glycol. The solution was heated for complete dissolution of the precursor materials. Ti iso-propoxide was dissolved in acetic acid and the solution was added to Ba-Sr complex solution at 50°C. The sol, thus prepared was stirred for 30 minutes for complex formation and termed as parent sol. For thin film deposition, the parent sol was diluted to a concentration of $0.35ML^{-1}$ by adding acetic acid. Films were deposited by spinning the coating

sol onto clean LAO substrates at a 2500 rpm for 5s. The heating schedule of the film was decided on the basis of the thermal analysis of BaTiO$_3$ gel [7]. All films were annealed at 1050 ^{0}C for two hours. The phase formation behavior, the degree of orientation and the quality of in-plane epitaxy of the deposited films were studied using the X-ray diffraction technique. The surface morphology of the films was studied using an atomic force microscope (AFM). The low frequency (1kHz-1MHz) dielectric properties of BST thin films as a function of temperature were measured in planar electrode configuration using an impedance analyzer (HP 4294). The capacitor consists of 50 fingers that are 7 mm long, 20 ìm wide, and spaced 15ìm apart. A computer controlled thermal stage (MMR Inc.) and a thin film probe station was used to measure the temperature dependent dielectric and ferroelectric properties. The reported dielectric constant (K) was extracted from the capacitance using the conformal mapping technique originally developed by Gevorgian *et. al* [8]. Standard lift-off chemical etching technique was used to fabricate eight- element coupled micro strip phase shifters at NASA Glenn Research Center. The performance of these coupled micro-strip phase shifters at microwave frequencies were evaluated using a network analyzer (HP 8510 C, Agilent Technology).

RESULTS AND DISCUSSION

Textured growth and surface morphology of Mn-BST Films

Figure 1 shows the X-ray diffractograms of (a) undoped, (b) 1.0, (c) 3.0 and (d) 5.0 at% Mn doped BST (50/50) thin films on LAO (100) substrates. The appearance of intense (100) type diffraction peaks clearly indicates the highly (100) textured nature in all these films. The degree of (100) texture improves with Mn doping upto 3 at% as envisaged by the increased intensities of (100) type diffraction peaks and disappearance of misaligned planes (marked by small arrows in
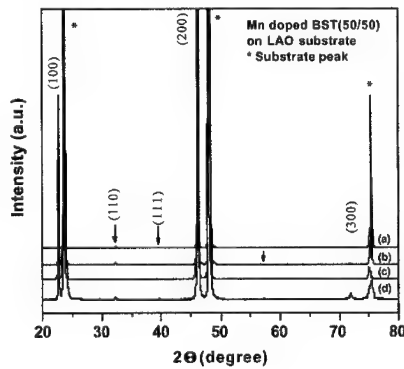
Figure 1 X-ray diffractograms of (a) undoped, (b) 1.0, (c) 3.0, and (d) 5.0 at% Mn doped BST (50/50) thin films.

Fig. 1(a) and (b)). With further addition of Mn, the degree of (100) texture deteriorates (Fig. 1(d)). The in-plane epitaxial quality of the Mn-doped BST thin films was analyzed by X-ray pole-figure analysis. The details of the pole-figure analysis can be found else where [9]. The pole-figure results indicate that all these films are textured in (100) direction and the degree of texturing as well as in-plane orientation improve upto 3 at% Mn doping and deteriorates with further Mn addition. Mn doping has significant influence on the surface morphology of BST (50/50) thin films. Figure 2 shows the AFM micrographs of (a) undoped, (b) 1.0 at%, (c) 3 at%, and (d) 5 at% Mn-doped BST thin films. The average grain size of these films was measured by linear intercept technique. Table I shows the variation of grain size and surface roughness of BST (50/50) with Mn doping.

Table I Variation of average grain size and surface roughness with Mn doping.

Mn content (at%)	Average grain size (nm)	RMS roughness (nm)
0	141	14.3
1	152	12.1
3	252	27.5
5	213	24.2

Upto 3 at% doping content, Mn^{3+} acts as acceptor replacing Ti^{4+} at B site; and to maintain the charge neutrality oxygen vacancies are created in the lattice. The vacant lattice sites in turn increase the grain boundary mobility and therefore upto 3 at% Mn doping the grain size is increased. Beyond 3 at% Mn content, the solubility of Mn is limited in the BST lattice and probably it gets precipitated at grain boundary and thereby reduces the grain boundary mobility. This explains the smaller grain size of 5 at% film as compared to 3 at% Mn doped BST films.
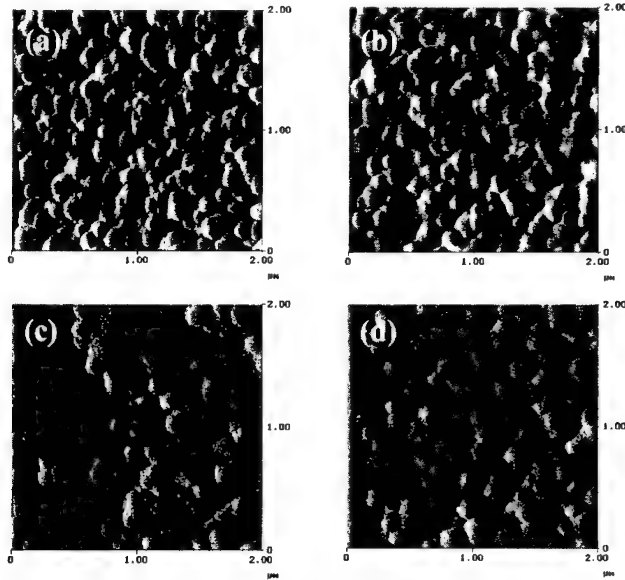
Figure 2 AFM micrographs of (a) undoped, (b) 1.0 at%, (c) 3 at%, and (d) 5.0 at% Mn doped BST thin films.

Dielectric and Leakage Current Behavior

Figure 3 shows the frequency dispersion of (a) the capacitance and (b) the loss tangent of Mn doped BST (50/50) films. The capacitance increases up to 3 at% Mn doping and then decreases with further Mn addition. The increase in capacitance could be due to the increased grain size of the BST films up to 3 at% Mn doping. Tsu *et. al.* [10] reported that since the volume of dielectric polarization is proportional to the size of the grain, the dielectric constant is

increased with the increase in grain size. As mentioned earlier, up to 3 at % Mn doping, the grain size was found to be increased in BST (50/50) thin films, which may also result in the observed increase in capacitance and thereby in dielectric constant. For the undoped and Mn doped BST (50/50) thin films, the relatively higher capacitance with low frequency dispersion indicate the absence of any low capacitance interfacial layers. The loss tangents of undoped and Mn doped films also had minimal frequency dispersion and tanδ reduces with increase in Mn
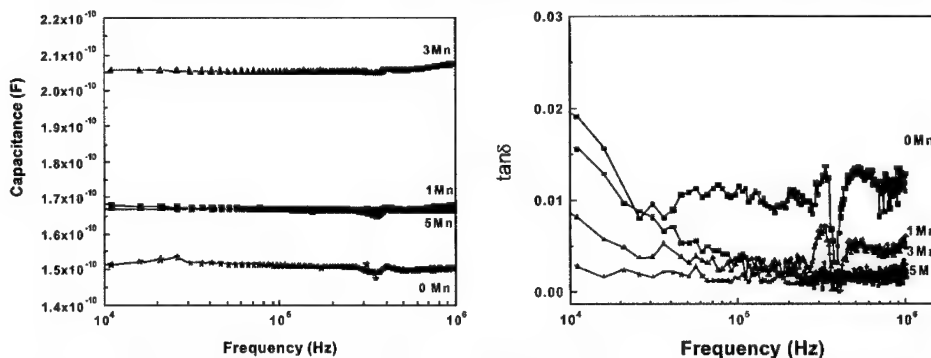
Figure 3 Frequency dispersion (a) Capacitance and (b) loss tangent of undoped and Mn doped BST thin films.

content. Mn^{+3} replaces Ti^{+4} and acts as an acceptor and thereby prevents the reduction of Ti^{+4} to Ti^{+3} by neutralizing the donor action of oxygen vacancies. Probably this reduces the loss tangent [4].

The leakage current behavior of Mn doped BST thin films were measured by measuring the current at a constant dc bias of 7 V as a function of time. The leakage current systematically increases with the increase of Mn content in BST thin films. The current (I)-voltage (V) characteristics also show similar trends (not shown). The increase of leakage current with Mn doping could be due to the fact that Mn^{3+} acts as an acceptor in BST lattice replacing Ti^{4+} and thereby creates oxygen vacancies to maintain the charge neutrality. The creation of charged vacancies in turn introduces mobile charge carriers (in this case electrons), which increase the leakage current densities.

Phase transition behavior

Figure 4 shows the temperature dependence of the measured capacitance and loss tangent of 50 fingers ID capacitor at 1MHz. The capacitance- temperature plot shows a broad maxima centered around 266K. For bulk BST (50/50) an empirical equation (T_c (°C) = 371x − 241; where x is the Ba fraction) estimates the m3m-4mm (cubic to tetragonal) transition temperature to be 217.5 K [11]. The observed transition temperature of BST (50/50) thin film is thus 48 K higher than the bulk ceramics. The calculated dielectric constant is low and a broad capacitance maxima is distinguished in thin films as compared to bulk. The discrepancy between the bulk and the thin films could be due to various possible factors, which include grain size effect, non-stoichiometry, and stress. Tahan *et. al* [12] observed no maxima in the dielectric constant vs temperature curves for $Ba_xSr_{1-x}TiO_3$ (x= 0.6 to 1.0) thin films and this phenomenon was attributed to the nanoscale
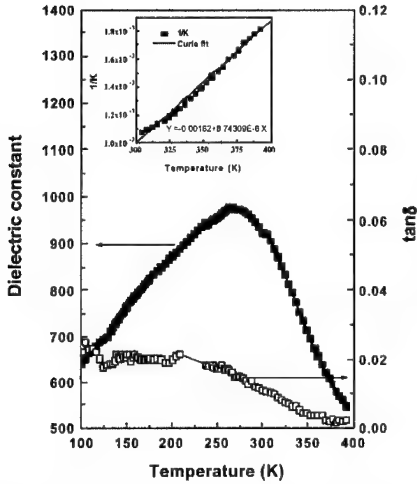
Figure 4 Temperature dependence of the capacitance and loss tangent of BST (50/50) thin film measured at 1 MHz. Inset shows the film follows a typical Curie-Weiss behavior in paraelectric state.

grain size of these films. As compared to bulk ceramics relatively finer grain size (R 252 nm) of undoped and Mn doped BST (50/50) thin films could be responsible for the diffuse nature of dielectric anomaly. Table II summarizes the phase transition data of undoped and Mn doped BST films. The role of Mn , in changing the transition temperature is not clearly understood. Probably Mn doping modifies the film stress state. Moreover the change in grain size with Mn doping could also be responsible for the observed variation of transition temperature. Studies are in progress to understand the reported results more clearly.

In the paraelectric state the capacitance was fitted according to the Curie-Weiss equation:

$$K = C_{Curie} / (T - \theta_c) \quad \dots\dots\dots\dots\dots \quad (1)$$

Where, K is the dielectric constant, C_{Curie} is the Curie constant in Kelvin, T is the temperature and θ_c is the Curie temperature. Fig. 4 (inset) shows that a plot of 1/K vs T yields a straight line as predicted by equation (1) and from the linear fit the Curie constant and the Curie temperature was estimated to be 1.45×10^5 K and 185 K respectively. The fact that $\theta_c < T_m$ (where T_m is the temperature corresponding to the capacitance maxima of the K vs T plot) confirms the first order phase transition of BST films [13]. We have carried out the analysis of the observed broad dielectric behavior and the results indicate that there are more than one transitions in the films in the investigated temperature region.

Table II Summary of phase transition data of Mn-BST thin film.

Film	Dielectric constant at T_c	T_m (K)	θ_c (K)	C_{Curie} (x 10^5) (K)
Undoped BST	926	266	185	1.45
1 at % Mn-BST	846	220	108	1.6
3 at % Mn-BST	2161	255	213	2.1
5 at % Mn-BST	1149	268	150	1.7

It is known that the ionic positions and vibrations in a ferroelectric are modified by the stress, and since these changes are coupled to the polarization mechanisms in the ferroelectric, effectively the dielectric and ferroelectric properties of thin films are also affected. [14]. The effect of strain on the dielectric constant of BST thin films has recently been reported by Chang *et al* [15] based on phenomenological thermodynamic theory of bulk ferroelectrics originally developed by Devonshire [16]. Both theoretical calculation and experimental observations have verified that for tensile strain parallel to the direction of electric field vector the dielectric constant and tunability increase whereas for compressive strain they are decreased. In the present work X-ray line broadening analysis is performed to investigate the nature of strain in

annealed BST (50/50) thin film. Assuming the line broadening (β) is due to strain (e) and crystallite size (t), the following equation is used to determine the nature and magnitude of strain and crystallite size of annealed BST (50/50) film on lanthanum aluminate substrate [17].

$$\beta \cos\theta_B/\lambda = 1/t + 4e \sin\theta_B/\lambda \dots\dots\dots\dots (2)$$

Where, β is the line width at half maximum, θ_B is the Bragg angle and λ is the X-ray wavelength. We have used (100) type of the diffraction peaks and to obtain accurate peak width at half maxima (β) and Bragg angle (θ_B), the X ray lines were fitted using two Pearson VII peaks using a commercial program (PeakFit-4, Jandel Scientific), to separate out $K_{\alpha1}$ and $K_{\alpha2}$ contributions and obtain the values of β and θ_B. Fig.5 shows a plot of $\beta cos\theta_B/\lambda$ vs $sin\theta_B/\lambda$. The crystallite size (t) and strain (e) estimated from the linear fit is 31 Å and +0.86% respectively. The tensile nature of the strain of the film could be due to thermal expansion mismatch or lattice mismatch between BST (50/50) film and LAO (100) substrates. The lattice parameter and thermal expansion coefficient of BST (50/50) (3.947 Å, $10.5 \times 10^6/°C$ respectively) are larger than the lattice
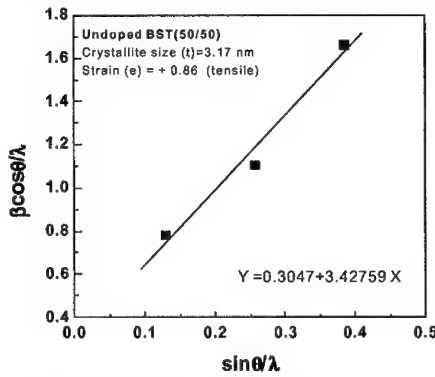
parameter and thermal expansion coefficient of LAO (3.787 Å and $10 \times 10^6/°C$ respectively), hence it is expected that after annealing films are under tension [15]. The shift of capacitance maxima (corresponding to the transition temperature) towards higher temperature is believed to be related to the tensile strain in the annealed BST film. As mentioned, the induced film stress arises from several contributions, eg. lattice mismatch, thermal expansion mismatch between the film and substrate. Additionally the stress field is also influenced significantly by the presence of oxygen vacancies, which alter the lattice parameter and may therefore increase, decrease or screen the overall film stress [15].

Figure 5 A plot of $\beta cos\theta/\lambda$ vs $sin\theta/\lambda$ of BST (50/50) thin film.

Bias field effect on dielectric properties

Fig.6 shows the room temperature frequency dispersion of capacitance and loss tangent of BST thin films measured at various sub-switching oscillation voltage levels. The increase in dielectric constant (capacitance) with the increase in oscillation voltage could be due to de-pinning of ferroelectric domain walls from the defects [18]. The increase in loss tangent with oscillation voltage also indicates that the film is not fully paraelectric at room temperature.

According to Devonshire's theory in the perovskite cubic structure, Ti ion oscillates in an anharmonic potential of the form $ar^2 + br^4$ where r is the position of the Ti ion. The Helmholtz free energy F (P,T) of the Ti ion can be expanded in even powers of the polarization P with coefficients that are a function of the temperature only; that is

$$F(P,T) = F(0,T) + A(T-\theta)P^2 + BP^4 + CP^6 \dots\dots (3)$$

Where, θ is the Curie-Weiss temperature, and A, B, C are the expansion coefficients. In the paraelectric state the free energy increases as polarization, and there is only one minimum at $P = 0$. If a small field 'E' is applied on the materials then the P^6 term can be neglected. Moreover, in the paraelectric state, where the polarization is much smaller than that in the ferroelectric state,

neglecting the P^6 term in the expansion of free energy is appropriate. The dielectric constant (ε_r) can be obtained by taking the second derivative of the free energy with respect to polarization. The lattice anharmonic interaction of Ti ions is responsible for the field dependence of the dielectric constant of the BST system. According to a model proposed by Johnson one can obtain a phenomenological equation that is valid in the paraelectric state [19]

$$K'/K'_o = 1 / (1 + a K'^3_o E^2)^{1/3} \qquad \ldots\ldots\ldots\ldots(4)$$

Where $a = 12\ B/(4\pi)^3$ is the anharmonic coefficient. Johnson also derived that the imaginary part of the relative permittivity follows another phenomenological equation

$$K''/K_o'' = 1 / (1 + a K'^3_o E^2)^{2/3} \qquad \ldots\ldots\ldots\ldots(5)$$

Where (K', K'_o) and (K'', K_o'') are the real and imaginary parts of the dielectric constant K respectively, under a field E and zero bias field respectively. Based on Eqns 4 and 5, the field variation of loss tangent ($tan\delta_c$) can be expressed as

$$tan\delta_c = K''/K' = tan\delta_{co} / (1 + aK'^3_o E^2)^{1/3} \qquad \ldots\ldots\ldots\ldots(6)$$

The above equations are valid only in the paraelectric state where the polarization value is negligible to that in the ferroelectric state and the applied electric field (E) is small.
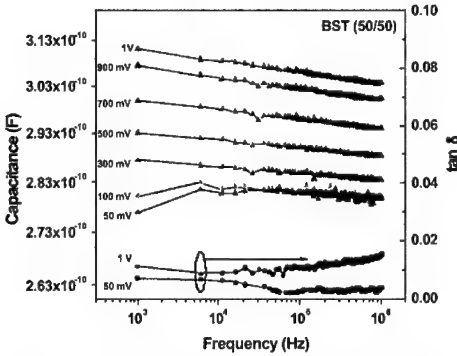
Figure 6 Room temperature frequency dispersion of capacitance and loss tangent values of BST thin film measured at different oscillation voltages.
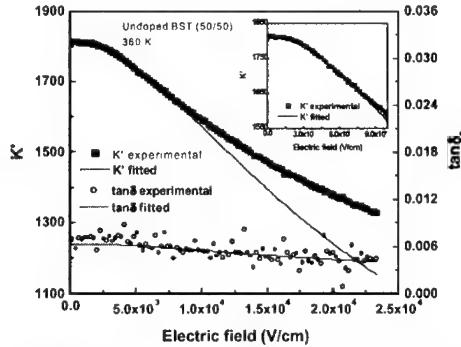
Figure 7 Bias field dependence of dielectric constant (K') and loss tangent of undoped BST film measured at 360 K applying oscillation voltage 500 mV a t 1 MHz.

Fig.7 shows the field (E) dependence of the real part of dielectric constant (K') and loss tangent ($tan\delta_c$) measured at 360K. The solid lines shown in the plot are obtained by curve fitting with equation (4) and (6) for K' and $tan\delta_c$ respectively. As shown in the Figure, the theoretical plot matches well with the experimental data when the applied electric field is low (≤ 7.5kV/cm) and deviates at higher electric field. This is expected since at higher field the polarization contribution cannot be neglected and in other words eqn. 4 and 6 are not strictly valid in describing the field dependence of dielectric constant and loss tangent [20]. Similar fitting was performed to the experimental field dependence of K' and $tan\delta_c$ at different temperatures ranging from 300 to 400 K (i.e in the paraelectric state of the film). Fig. 8 shows the temperature dependence of the anharmonic coefficient (a) and the tunability of undoped and Mn-BST (50/50) thin films. The figure shows that for undoped and Mn-doped BST (50/50) films 'a' parameter and tunability (measured at 1 MHz) and 2.33 V/μm) decrease with the increase in temperature. Note that equation (4) also indicates that tunability decreases with the decrease in 'a', K_o' or E
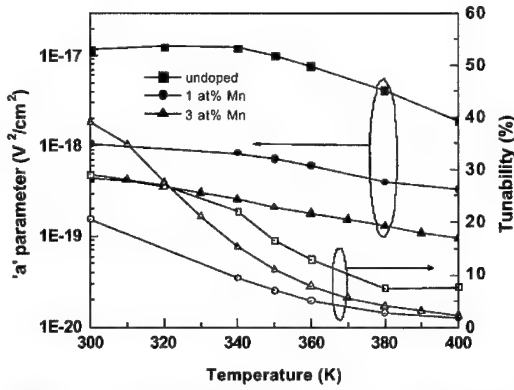
Figure 8 Temperature variation of 'a' parameter and tunability of undoped and Mn doped BST thin films.

values. The maximum tunability is obtained for 3 at% Mn-BST thin films in the vicinity of its transition temperature (~255 K) and decreases with increase in temperature. Hysteresis loop measurement of these films as a function of temperature indicates the presence of remnant polarization even at corresponding transition temperatures. The domain movement and capacitance hysteresis under dc field due to the ferroelectric nature of the film could yield unpredictable dielectric characteristics. Therefore for all practical purposes it is recommended that the working temperature for practical device slightly above the transition temperature where the hysteresis is minimized at the same time the tunability remains appreciable. It should be worthwhile to mention at this stage that Devonshire theory assumes a stress free condition. However, as mentioned earlier our film contains residual tensile stress, which could be responsible for the broadening of ferroelectric to paraelectric transition and also dilute the contribution of the anharmonic coefficient towards the tunability [20].

As shown in Fig.7 the experimental field variation of $tan\delta$ of BST film matches well with the theoretical prediction (eqn. 6) up to field strength of about 22 kV/cm. At a particular measurement frequency $tan\delta$ can be expressed as [21]

$$tan\delta = tan\delta_c + tan\delta_R \qquad \ldots\ldots\ldots\ldots (7),$$

Where $tan\delta_c$ is the intrinsic dielectric loss expressed by eqn 6 and $tan\delta_R$ is the conduction loss expressed as

$$K''/K' = 1/ K' \omega RC_o \qquad \ldots\ldots\ldots.. (8)$$

Where ω is the angular frequency, R is the resistance and C_o is the capacitance at zero field. Figure 9 shows the current (I) –voltage (V) characteristics of BST (50/50) thin film. In this voltage range leakage current exhibits perfect linear variation confirming the ohmic nature of conduction behavior. At room temperature and also at higher temperature the calculated $tan\delta_R$ is negligible as compared to $tan\delta_c$ indicating the voltage variable capacitor loss
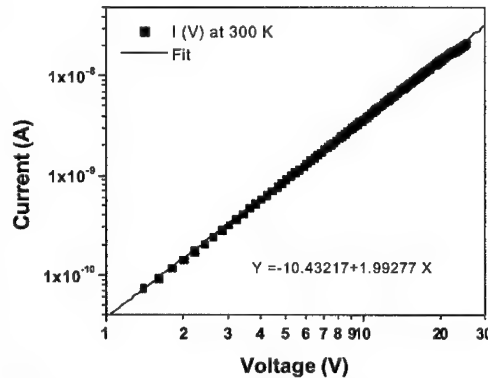
Figure 9 At low applied voltage the I-V characteristics of BST (50/50) thin film exhibits ohmic conduction behavior.

component ($tan\delta_e$) dominates the overall loss tangent characteristics under the applied field regime.

Phase Shifter Characteristics

A ferroelectric phase-shifter is an electric delay line, in which the amount of electrical delay, i.e. phase shift, is controlled by the dielectric constant, and hence the scan angle of a radar beam can be controlled by changing the dielectric constant of the material. We have used the highly textured undoped and Mn doped BST (50/50) films to fabricate eight element coupled micro-strip phase shifters to be used in low cost steerable antennas for communication applications.To fabricate phase shifters, the BST films were metallized with a 15 nm chromium (Cr) adhesion layer followed by a 2 im to 2.5 im thick gold (Au) film using the electron beam evaporation at NASA Glenn Research Center. Standard lift-off chemical etching techniques were used to fabricate the Au/BST/LAO phase shifters. Finally, a Cr/Au ground plate with the same thickness were e -beam evaporated on the back of the substrate. The performance of these coupled micro-strip phase shifters at microwave frequencies was evaluated by measuring the transmission (S_{21}) scattering parameters between 14 to 17 GHz using an HP 8510C network analyzer. All loss measurements quoted here include the losses due to the SMA launchers, which are estimated to be 0.25 to 0.5 dB. The measurements were taken in vacuum to avoid the dielectric breakdown in the air under high dc fields between coupled micro-strip sections.

The degree of phase shift and insertion loss (in the frequency range of 13.5 to 15 GHz) of undoped and Mn doped BST (50/50) thin films as a function of bias voltage are shown in Fig. 10. The phase shift increases systematically from 239° (undoped) to 337° (3 at% Mn doping) and decrease with further Mn addition The degree of phase shifts, insertion losses and the figure of merits (κ, defined by the ratio of phase shift /insertion loss) for undoped and Mn doped BST (50/50) films are tabulated in Table III. As shown in the table, although there is a significant improvement of the degree of phase shift up to 3 at % Mn doping, the insertion loss also increases (5.4 - 9.9 dB) with the increase in dopant concentration and as a result the effective κ factor does not improve significantly and remains in the range of 33 – 44 °/dB. The improvement of the degree of phase shift could be due to either the increased grain size or the improvement of
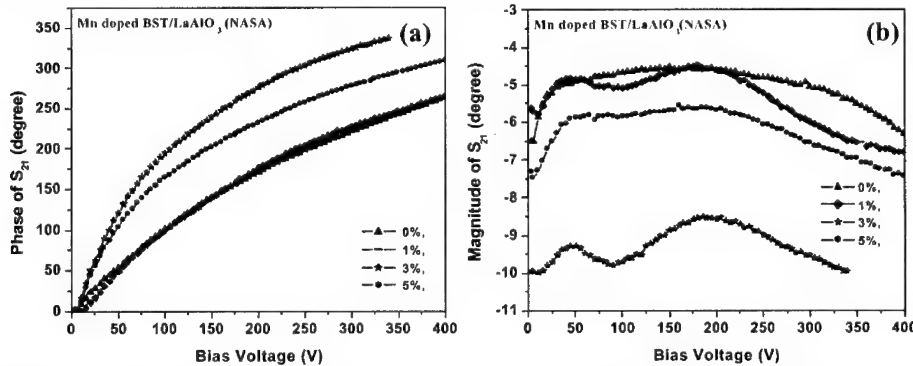
Figure 10 Variation of (a) Phase shift, and (b) insertion loss, for undoped and Mn doped BST films as a function of bias voltage.

(100) texturing up to 3 at % Mn doping. As mentioned earlier the surface roughness also increases with the increase in Mn content up to 3 at %. The higher insertion loss with the increase in Mn content could be either due to higher surface roughness or creation of oxygen vacancies due to the acceptor nature of Mn doping in BST lattice.

Table III Phase shifter characteristics of Mn doped BST (50/50) thin films measured at 16 GHz and at 339 Volts.

Film composition	Phase shift (^{o})	Insertion loss (dB)	κ factor (^{o}/dB)
Undoped BST (50/50)	239	5.4	44
1Mn-BST	242	6.5	37
3Mn-BST	337	9.9	34
5Mn-BST	291	6.9	42

CONCLUSIONS

Highly (100) oriented undoped and Mn doped BST (50/50) thin films were successfully grown on LAO (100) substrates by sol-gel technique. Our results demonstrated that Mn doping has a strong influence on the growth characteristics; microstructure and electrical properties of BST (50/50) thin films. Up to 5 at % Mn doping BST (50/50) thin films crystallize into single-phase perovskite structure. The degree of (100) texturing improves up to 3 at % Mn doping. Pole-figure analysis shows the improvement of in-plane epitaxy upto 3 at % Mn doping. The grain size increases up to 3 at % Mn doping, however the surface roughness also increases with the grain growth. From the dielectric measurements we found that the dielectric constant of the BST (50/50) film increases up to 3 at % Mn doping, maintaining low dielectric loss values (tanδ ~10^{-2}). We have fabricated eight element coupled micro-strip phase-shifters (CMPS) and tested them in terms of their degree of phase shift and insertion loss characteristics. Phase shift measurements showed the maximum tunability increases from 239° to 337° with 0 to 3 at% Mn doping however, the insertion loss also increases (~5.4 dB (undoped) to 9.9 dB (3at % Mn doped)) with the increase with doping content so that there is no effective improvement in the κ factor which remains in the range of 33 – 44°/dB. The improvement in degree of phase shift in case of 3 at % Mn doped BST (50/50) film is attractive for phase shifter application. However the insertion loss should be minimized for practical device applications. The relatively higher insertion loss in 3 at% Mn doped films could be due to its rougher surface morphology. Further research is in progress to further optimize the process parameters to grow dense and smoother Mn doped BST (50/50) films with reduced insertion loss and higher κ factor.

REFERENCES

1. D. Dimos and C.H. Muller, *Ann. Rev. Mater. Sci.,* **28**, 397 (1998).
2. K. Abe and S. Komatsu, *Jpn. J. Appl. Phys.,* **32**, 4186 (1993).
3. H. D. Wu and F. S. Barnes, *Integrated Ferroelectrics,* **22**, 291 (1998).
4. M. W. Cole, P. C. Joshi, M. H. Ervin, M. C. Wood, and R. L. Pfeffer, *Thin Solid Films,* **374**, 34 (2000).
5. L. Wu, Y. C. Chen, Y. P. Chou, Y. T. Tsai, and S. Y. Chu, *Jpn J. Appl. Phys.,* **38**, 5154 (1999).
6. S.I. Jang, H.M. Jang, *Thin Solid Films,* **330**, 89 (1998).
7. S.B. Majumder, M. Jain, A. Martinez, R.S. Katiyar, F.W. van Kuels, and F.A. Miranda, *J. Appl. Phys.,* **90**, 896 (2001).
8. S. Gevorgian, E. Carlsson, S. Rudner, L. D. Wernlund, X. Wang, and U. Helwersson, *IEEE Proc. Microm. Antennas Propag.,* **143**, 397 (1996).
9. M. Jain, S.B. Majumder, A. Martinez, R.S. Katiyar, F.W. van Kuels, R.R. Ramanofsky, and F.A. Miranda, *Integrated Ferroelectrics,* **42**, 207 (2002).
10. R. Tsu, H.Y. Liu, W. Y. Hsu, S. Summerfelt, K. Aoki, and B. Gnade, *Mat. Res. Soc. Symp. Pro.,* **361**, 275 (1995).
11. B. Jaffe, W.R. Cook Jr, and H. Jaffe, *Piezoelectric Ceramics,* (R.A.N Publishers, Marietta, OH, 1991).
12. D.M. Tahan, A. Safari, L.C. Klein, *J. Am. Ceram. Soc.,* **79**, 1593 (1996).
13. Y. Xu., *Ferroelectric Materials and Their Applications,* (Elsevier Science Publishers B.V., NY 1991).
14. W. Chang, C.M. Gilmore, W.J. Kim, J.F. Pond, S.W. Kirchoefer, S.B. Qadri, D.B. Chrisey, and J.S. Horwitz, *J. Appl. Phys.* **87**, 3044, (2000).
15. W. Chang, J.S. Horwitz, A.C. Carter, J.M. Pond, S.W. Kirchoefer, C.M. Gilmore, and D.B. Chrisey, *Appl. Phys. Lett.,* **74**, 1033 (1999).
16. A.F. Devonshire, *Philos Mag.* **42**, 1065 (1951).
17. W.H. Hall, *Proc. Phys. Soc.* **62**, 741, (1949).
18. Dragan Damjanovi,*Rep. Prog. Phys.* **61** (9), 1267 (1998).
19. K.M. Johnson, *J. Appl. Phys,* **33**, 2826 (1962).
20. J.W. Liou and B.S. Chiou, *J. Am. Ceram. Soc.,* **80**, 3093 (1997); J.F. Scott, *Ferroelectric Review,* 1, 1 (1998).
21. L. Wu, Y.C. Chen, Y.P. Chou, Y. Tsai, and S.Y. Chu, *Jpn. J. Appl. Phys.,* **38**, 5154 (1999).

Reliability and Stability of Novel Tunable Thin Film

G. H. Lin, R. Fu, S. He, J. Sun, X. Zhang & L. Sengupta
Paratek Microwave, Inc.
6935 Oakland Mills Road, Columbia, MD 21045, U.S.A.

ABSTRACT

A new process has been developed in Paratek Microwave Inc. to formulate stable tunable (Ba, Sr)TiO$_3$ (BST) based thin film material. Varactors, with a co-planar structure, were fabricated by using the new material. The varactor Q of 105 tested at 2 GHz was observed with average tunability of 58 % at 150V (37.5 V/μm). The lifetime tests indicated that this material is very stable under continuous 100 to 150 V dc bias both at the room temperature and in 70 °C environment. Thus, this novel tunable thin film material opens a new avenue to develop high quality tunable microwave devices. Tunable IF filters have been built by using this novel material for microwave backhaul radios and handset applications. Initial results of a RF phase shifter are also included and demonstrate another application of these films.

INTRODUCTION

Voltage-tunable devices, such as phase shifters, tunable filters and voltage-controlled oscillators, are highly desirable in RF and microwave applications. Currently, most these tunable devices are based on ferrite materials and semiconductor diode varactors. Ferrite tunable devices have problems of low tuning speed and high cost. On the other hand, diode varactors show low Q (especially at frequency > 2 GHz), low power handling and high intermodulation distortion.

Recently, voltage tunable (Ba, Sr) TiO3 (BST) materials have been extensively investigated, due to their high power handling, low loss, rapid tuning, and high tolerance to burnout over a wide frequency range [1-5]. Thin films of BST type materials are desirable, because they can be easily integrated with standard IC processing and can therefore be scaled for mass production [6-9]. However, there are some problems that need to be solved before these materials can be used for the above-mentioned applications. These problems include leakage current development and capacitance drift during the dc bias. It was reported that various kinds of defects, such as oxygen vacancies, in the films might cause leakage current as well as the degradation of loss tangent. The development of leakage current directly results in short lifetime of the films. The capacitance drift can cause device or system error and stability problems. Paratek has developed a group of Parascan^{TM} tunable microwave materials. New processes and new-doped BST thin films have been developed, to solve the above-mentioned problems of BST thin film materials. In this paper, we present the experimental results of extensive testing of the microwave properties, lifetime and stability of fabricated varactors. The performance of RF devices, such as tunable filters and phase shifters, implementing this material are also shown. The results show promising properties of thin film Parascan^{TM} materials in the application of commercial microwave tunable devices.

EXPERIMENT RESULTS AND DISCUSSION

Thin film varactors were fabricated by means of pulsed laser (KrF excimer laser) deposition using doped BST targets. The targets were fabricated at Paratek by using traditional ceramic process. The doping elements include tungsten, MgO and others. The films were deposited onto a variety of substrates such as MgO, sapphire and polycrystalline Al_2O_3. The doped BST thin films were deposited at a temperature range from 25 °C to 800 °C, and under oxygen pressures between 100 to 400 mtorr. A thin buffer layer may be inserted between the substrate and the main part of the thin film. Post annealing was accomplished in an environment of oxygen or air. Typical film thickness was 3000 Å to 5000 Å, measured by a step profilometer. Co-planar structures, both single gap and interdigitated electrode (IDE) patterns, were fabricated to build the varactors. The thickness of top gold electrodes was between 2 to 3 microns. The typical gap sizes ranged from 2 to 6 microns. The finger numbers were varied to reach required capacitance. The data presented here is mostly from IDE type varactors with a 4 microns gap deposited on MgO substrate. Varactors were tested at a frequency of 2 GHz by using an HP 8722ES Network Analyzer with a calibrated fixture. The bias voltage was applied and the leakage currents were measured by means of a Keithley 487 Picoammeter/voltage source.

Testing results for three typical batches of BST films, fabricated in different processes and using different Parascan^{TM} materials are shown in Figs. 1-3. Fig. 1 shows the tuning, defined as (Cp (0 Volt) – Cp (Bias Volt))/Cp (0 Volt), for these three BST batches at two bias voltages. Each data point in the figure represents an average value of all varactors in the testing batch. The tuning at 150V is generally 10 to 15% higher comparing to that at 100V. The average tuning at 100 V reaches 51%, and reaches 58% at 150 V. Fig. 2 shows the average Q value for the same batches of samples at 0 bias voltage. The average Q reaches 110 for one batch of BST films. Normally, Q slightly increases with increasing bias voltage for good quality varactors. Fig. 3 shows an average figure of merit (FOM) for these three batches of samples. In this figure, FOM is calculated by tunability (150V) × Q (0). The average FOM is more than 6000 for one-batch of BST varactors.
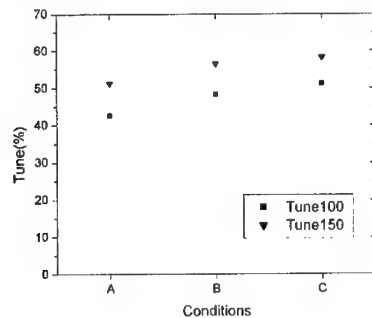
Fig. 1. Average tuning at two bias voltages, 100V (25 V/μm) and 150 V (37.5 V/μm), measured at 2 GHz, for three different batches of samples.
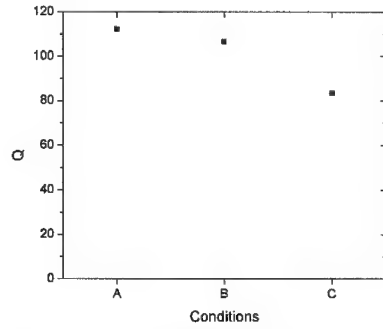
Fig. 2. Average Q value, measured at 2 GHz and 0 volt bias, for three different batches of samples.

The varactors were also tested over a wide temperature range from –30 ºC to 85 ºC. The selection of this temperature range is based on common RF device requirements. Figure 4 shows tunability, measured at 150V of biasing, as a function of test temperature. Tuning generally drops as the temperature increases. As high as 40% of tuning is observed at the temperature of 80 ºC. At low temperature (-20 °C), the tuning reaches more than 70%. The Q is also temperature related. The Q value increases as the temperature rises.

Stability is an important topic for the RF application of thin film BST based material. Increase in leakage current and decrease in Cp and tuning are two related phenomena. It is our understanding that the stability of thin film varactors is related to both the bulk part of thin film and the two interfaces. These interfaces are the interface between film and substrate and the interface between the film and the metal electrodes. The properties of both the bulk part of
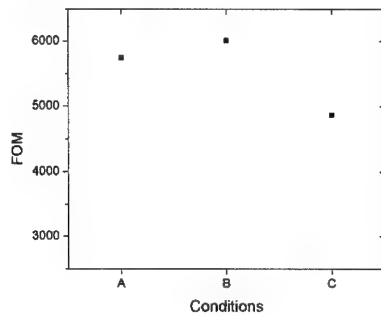
Fig. 3. Figure of Merit (FOM), calculated by tunability (150V) × Q (0) and measured at 2 GHz, for different batches of samples. The average FOM reaches more than 6000 for batch B samples.
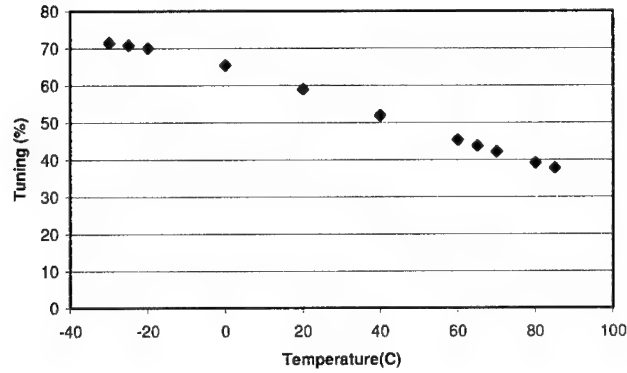
Fig. 4. Tuning at 150 V (37.5 V/µm), measured at 2 GHz, as a function of temperature.

material and the two interfaces relate to thin film material itself as well as the device fabrication processes. So we need to optimize both the composition and the associated processing to improve the stability of varactors. Generally, a decrease in tuning from 8 – 20 %, has been observed for BST thin film devices. The method of initial burn out has been previously suggested to compensate this tuning degradation.

Our process has improved the tuning stability. As a typical example, a varactor was biased at 100V continuously for 170 hours. Fig. 5 shows the normalized tuning at 100V, i.e., Tuning (t)/Tuning (0), as a function of bias time. The data indicated that this varactor is stable
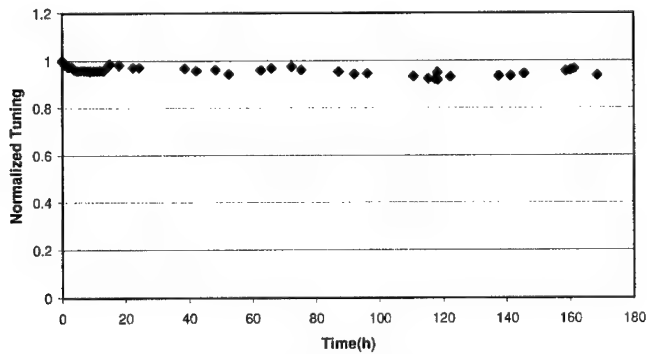
Fig. 5. Normalized tuning as a function of bias time. The test varactor was biased at 100 V (25 V/µm) constantly.

18
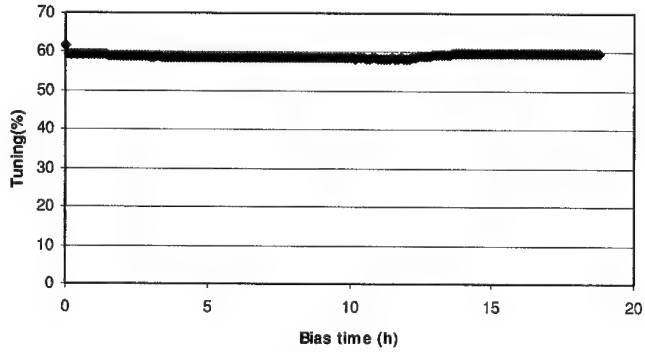
Fig. 6. Tuning as a function of bias time. The test varactor is biased at 150 V (37.5 V/μm) constantly.

under long -term biasing conditions. The tuning decreased about 5 to 7 % during the 170 hour time period. No leakage current was developed during this experiment.

The stability was improved when specific dopants were incorporated into the thin film devices. Fig. 6 and Fig. 7 show the results. The varactor was biased at 150V continuously for 18 hours, and the tuning at 150 V and Q were tested. Fig. 6 shows tuning as a function of bias time. Tuning decreased less than 4%in the first 6 minutes. Then, it became stable for the remaining experimental time period. Fig. 7 shows the normalized FOM, defined as tunability (150V,t) × Q (0V,t) / tune (150V, 0) × Q (0V, 0), as a function of dc bias time. Considering the experimental variation of Q value, the FOM is stable the entire 18 hours with constant 150 V of applied dc bias.
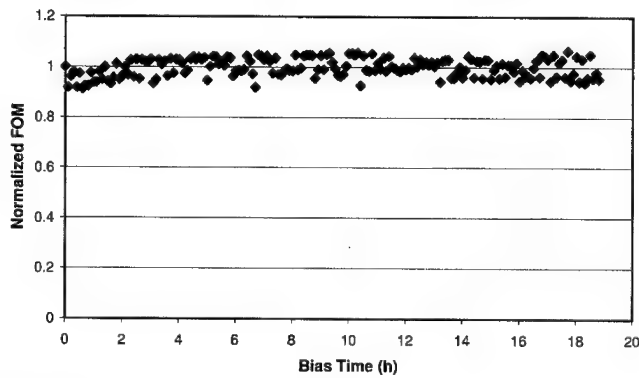
Fig. 7. FOM variation as a function of bias time.
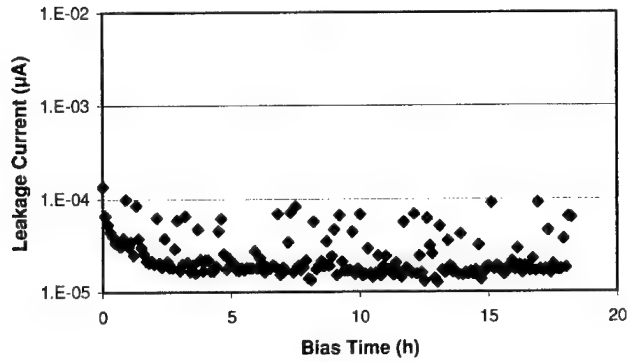
Fig. 8. Leakage current measured at 150 V (37.5 V/μm) as a function of bias time. The varactor was constantly dc biased at 150 V.

The leakage current was also measured while the varactor was continuously biased. For a good quality varactor, the leakage current is stable, with a value well below 10^{-4} μA, under 150 V of applied bias. Fig. 8 shows a typical leakage current behavior at 150 V bias for 18 hours. The leakage current was measured each 6 minutes under 150V of applied dc bias. The leakage currents I (150) dropped from 10^{-4} μA to 2×10^{-5} μA in the first three hours. Then, it became stable during the remaining experimental time period.

The lifetime behavior at 70 °C was also measured. The sample varactor and its testing fixture were kept in a temperature chamber at 70 °C. The varactor was continuously dc biased at 100 V. The Cp measurements at 50 V and 100 V were taken automatically every 15 minutes.
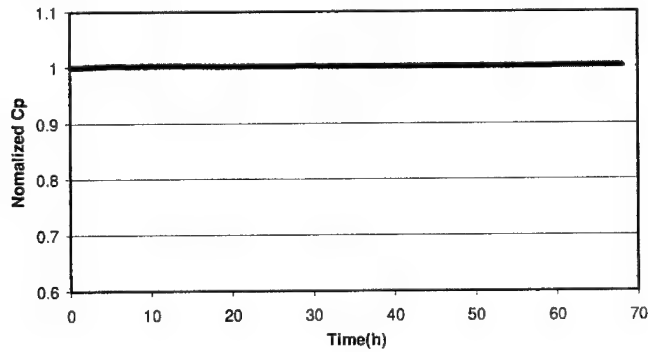
Fig. 9. Normalized Cp, measured at 50 V bias, as a function of time. The varactor and its fixture were kept in a temperature chamber of 70 °C.
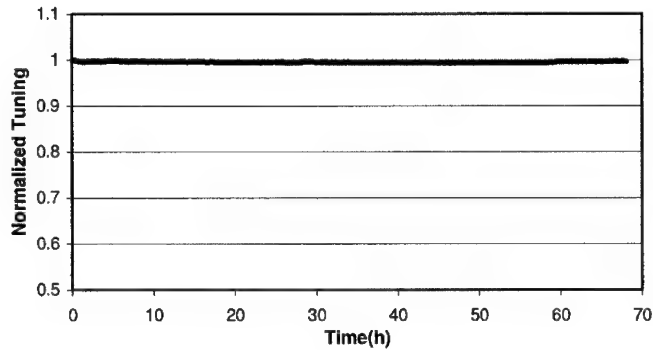
Fig. 10. Normalized tuning, from 100 V to 50 V, as a function of bias time. The varactor and its fixture were kept in a temperature chamber of 70 °C.

The experimental results are shown in Fig. 9 and 10. Fig. 9 shows the normalized Cp variation, measured at 50 V, as a function of biasing time. The Cp variation in the 68-hour experiment is less than 0.3 %. The Cp variation at 100 V is less than 0.4 %. Both the Cp variations (at 50V and 100V) fall within the experimental error range of the measurement equipment. Thus, the Cp, measured from 50 V to 100 V, is extremely stable in the temperature of 70 °C, as the varactor is constantly biased at 100 V. Fig. 10 shows the normalized tuning as a function of bias time. The observed maximum tuning drop, in the whole experimental period, is 0.6 %, which is also within the experimental error range of the measurement equipment. Figs. 9-10 indicate stable characteristics of varactors fabricated by our new processes and new materials at 70 °C.

Tunable IF filters that incorporating this novel material have been fabricated and tested. The IF tunable filter is constructed using a 4-pole microstrip structure, and operates at 2 GHz with bandwidth of 50 MHz. The filter can cover a tuning range of 300 MHz frequency at a temperature range of 0 °C to 65 °C. The insertion loss of the filter is 4.2 dB to 5.2 dB with return loss of better than 20 dB in the tuning range.

A phase shifter, with a 90 degree phase change was fabricated at Paratek by using the varactors made from our new thin film processes. The initial results indicated that the insertion loss of the phase shift, induced by thin film varactors, was 0.25 dB at all bias conditions at 2.4 GHz. Thus, our new process also opens a potential avenue for microwave antenna applications.

CONCLUSIONS

Our new-doped Parascan[TM] BST based thin film has high tunability and high Q. The varactor Q of 105 tested at 2 GHz, was observed with an average tunability of greater than 40% at 70 °C. The lifetime test results indicate that this material is very stable at both the room temperature and 70 °C environment. Leakage current less than 2×10^{-5} μA was achieved under constant dc biasing of 37.5 V/μm. Tunable filters and phase shifters have been fabricated using these thin film varactors. These devices demonstrated the advantage of a simple structure, small

size, low cost, low bias voltage and low loss. Thus, this novel tunable thin film material opens a new avenue to develop high quality tunable microwave devices.

REFERENCES

1. A. Kozyrev, V. Keis, O. Buslov, A. Ivanov, T. Samoilova, O. Soldatenkov, V. Loginov, A. Tumarkin and L. C. Sengupta, Integrated Ferroelectrics, **39**, 427(2001).
2. P. K. Park, S. H. Kim, J. Gandolfi, R. T. Tadaki, T. K. Dougherty, D. Patel, J. Rao, L. Sengupta, S. Wolf, and D. Treger, Digest 2000 IEEE Antennas and Propagat, Soc. Int. Symp. **2**, 974 (2000).
3. L. Sengupta and S. Sengupta, Mat. Res. Innovat., **2**, 278(1999).
4. J. Rao, D. Patel, V. Krichevsky, L. Sengupta, L. Chiu, X. Zhang, Y. Zhu, S. Stowell, S. Sengupta and A. Moffat, Integrated Ferroelectrics, **24**, 309(1999).
5. S. Sengupta, L. Sengupta, J. Synowczynski and D. Rees, IEEE Trans. Ultrason., Ferroele ct., Freq. Contr., **45**, 1444(1998).
6. A. Kozyrev, A. Ivanov, T. Samoilova, O. Soldatenkov, K. Astafiev and L. C. Sengupta, J. Appl. Phys. **88**, 5334 (2000).
7. W. J. Kim, W. Chang, S. B. Qadri, J. M. Pond, S. W. Kirchoefer, D. B. Chrisey and J. S. Horwitz, Appl. Phys. Lett., **76**, 1185 (2000).
8. Q. X. Jia, A. T. Findkoglu, D. Reagor and P. Lu, Appl. Phys. Lett., **74**, 1033 (1999).
9. S.Stowell, Y. Zhu, X. Zhang, S. Sengupta, L. Sengupta and A. Hsieh, Integrated Ferroelectrics, **21**, 441(1998).

A New Ferroelectric Varactor From Water Based Inorganic Precursors

T. Kirk Dougherty[1], John Drab, Mike Brand[1] and Kathleen Kehle
Raytheon Infrared Operations, Goleta, CA, U.S.A
[1]Raytheon Company, El Segundo, CA, U.S.A

ABSTRACT

Solution deposition processes for the production of thin multi-element metal oxide films continue with great interest and varied success. Solution deposition via either sol-gel or MOD (Metal Organic Decomposition) methods are of interest due to the ability to produce a wide variety of compositional products at low capital investment cost. The sol-gel method generally uses hydrolytically sensitive metal alkoxides as the starting materials. Manipulation of the reagents and different hydrolysis rates for multi-element mixtures are issues. The MOD method utilizes large organic acid metal salts as the starting materials. In general, MOD solutions are more hydrolytically stable than the sol-gel solutions. MOD process challenges include large quantities of carbon to be decomposed during the firing, shrinkage and stress of the thin films, variable chemistry in synthesis of the starting materials (especially when the starting materials for the MOD precursors are metal alkoxides), and long reaction times for the synthesis. For both the sol-gel and MOD precursors, toxic and volatile organic chemical (VOC's) solvents are employed as the vehicle.

This paper will review the chemistry-related issues to production of consistent high-quality metal oxide films via the MOD process. The fabrication of thin $Ba_xSr_{(1-x)}TiO_3$ (BST) films is described. A new class of MOD precursor has been implemented using polyether acids as the organic vehicle. These new materials are both water stable and water soluble. High quality BST thin films made from these precursors are described and capacitors made from these films are compared to the aliphatic acid MOD materials. Improved capacitors using lower resistance electrodes and interconnects are described, as well as devices designed specifically for our specific application.

INTRODUCTION

The use of sol-gel and MOD ceramic precursor solutions for production of thin-film and other ceramic materials is well known and documented.[1] MOD spin-on precursor materials for ferroelectrics are described in US Patent 5,423,285[2] and elsewhere. The MOD precursor solutions are usually made from large aliphatic acid (for example 2-ethylhexanoic acid) salts of the desired metal and a compatible solvent (for example xylenes) is used to adjust the concentration. As compared to sol-gel precursors, the MOD precursors have excellent shelf life and long term stability. Although the MOD solution precursors are commercially available for some elements (for example bismuth-2-ethylhexanoate, Strem 83-2400), they are not readily available for the less common and higher valent elements.

For the group I and II metals the MOD precursors can be easily prepared by an oxidation reaction of the reactive metal with the organic acid (see Equation 1).
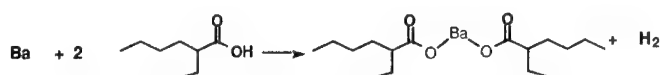
Equation 1. Reaction of alkaline earth metal Barium with 2-ethylhexanoic acid

For the higher valent elements, MOD precursors may be synthesized by interchange of the corresponding metal alkoxide with the free acid (See Equation 2).
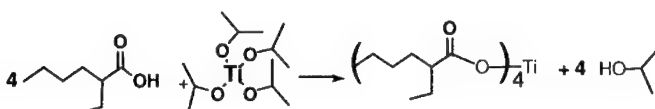
Equation 2. Idealized Reaction of Titanium Isopropoxide with 2-ethylhexanoic acid.

Inconsistent results with the precursors made by the acid alkoxide interchange reaction have been previously discussed.[3] The reaction as shown in Eq. 2 has several issues. In particular, the reactions may take several days to complete. Hydrolysis and condensation reactions also compete with idealized process. Our group has previously reported [4] an improved method to quickly synthesize the MOD precursors using the anhydride of the organic acid and the metal alkoxides. (Equation 3).
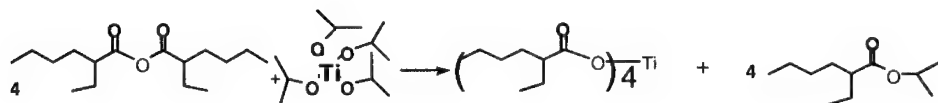
Equation 3. Reaction of 2-ethylhexanoic anhydride with Titanium Isopropoxide

We have made over one hundred batches of both BST and SBTN MOD precursors solutions using 2-ethylhexanoic acid anhydride. These reactions take several hours to complete and the products obtained when processed into devices give consistent results. In this paper we describe results for new environmentally-friendly MOD precursors which give improved quality thin films.

New Water Soluble Ferroelectric MOD Precursors

The need for environmentally benign precursors for production of thin film, thick film and bulk ceramics has been reviewed.[5] A class of water soluble, water stable MOD ceramic precursors have been described for lower valent metals including aluminum[5], yttria[6], iron[7], nickel[7], and the alkaline earth metals[8]. The metal ions are complexed with polyether acid molecules as compared to the aliphatic acids used in the more common MOD precursors. Equation 4 shows a comparison of the decomposition products of Titanium MOD precursors made from 2-ethylhexanoic acid and the etheracid methoxyacetic acid.

$$\text{32 } CO_2 + TiO_2 + \text{30 } H_2O$$

$$\text{12 } CO_2 + TiO_2 + \text{10 } H_2O$$
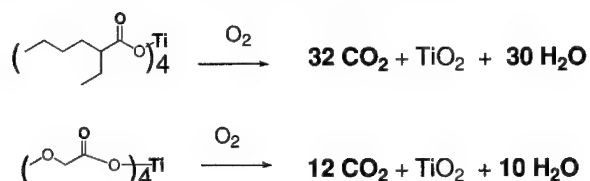
Equation 4. Thermooxidative Decomposition of new PolyetherAcid MOD Precursors Forms Significantly Less Byproducts as Compared to the Aliphatic Acid Analogues

The thermooxidative reaction of the new water soluble MOD precursor shows that almost 60% less material (by volume) is evolved during decomposition as compared to the aliphatic MOD analogues. This may lead to less shrinkage and stress during the decomposition process, especially after removal of the solvent. Fired ceramics with improved properties may result.

BST Capacitors from Water Soluble MOD Precursors

We have synthesized new polyether acid precursors of titanium, barium and strontium and processed these new materials into high quality BST thin films[9]. For the Group II metals, the polyether acid precursors are easily synthesized from the acid and metal. For the higher valent metals, the water soluble MOD precursors were made from the reaction of commercially available metal alkoxides and the anhydride of the corresponding polyether acid. The water soluble BST MOD precursor was spun on to metalized (evaporated Pt) silicon wafers. Single coat films using spin speeds from 1000 –3000 rpm gave crack-free, smooth 800-2500A thick BST films af r evaporation and firing[10] Top electrode and passivation layers were added and patterned capacitors were fabricated using standard thin film processes. A typical capacitance vs. Bi: curve is shown in Figure 1 on the next page.

B S T tu n In g
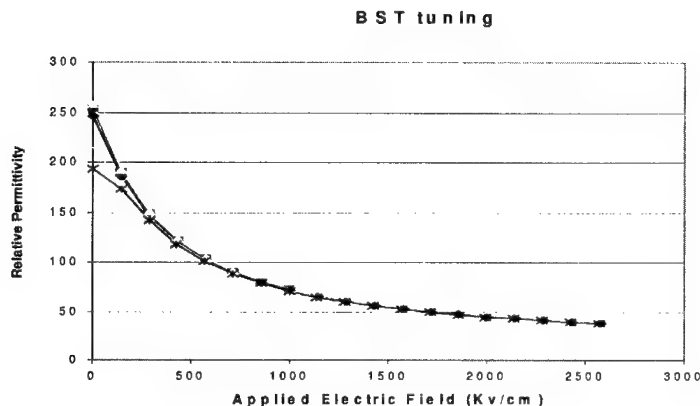
Figure 1. C-V Curve of thin film BST capacitors made with water based spin-on MOD
Precursors to Bias Field of 2.5MV/cm

This measurement shows the large tuning range (>5:1) and breakdown strength of these
devices. These devices have been tested at field strengths of 2.5 MV/cm for over 125 hours
without breakdown or significant degradation. The capacitors produced from these films have
leakage currents on the order of 10^{-8} a/cm^2. The results highlight the excellent material properties
of the BST films. However, at higher frequencies (>1MHz) the Q of the initial devices we
fabricated was disappointing. Q's measured at the bond pad for these capacitors at 30MHz were
only in the range of 10-30, which was not sufficient for our intended application.

High Q Devices – Improvement of ESR (equivalent series resistance)

These particular capacitors are being developed for to replace semiconductor varactor
diodes in a high-power voltage regulator circuit.[11] This application requires high Q devices that
can survive very high field strengths and large AC signals. The application frequency is in the
range of 10-100Mhz. The initial devices we fabricated utilized a stack and design that was
developed for another application. This initial stack consisted of BE, TE and interconnect metal
of Ti/Pt materials with thickness of 1850, 1100, and 1850 A respectively. Tests of the devices at
frequencies above 1MHz demonstrated that the major losses were due to series resistance of the
metal layers and not losses in the BST.
Since the top electrode would ultimately be covered by the interconnect layer, experiments
to improve the sheet resistance of the bottom and interconnect metals were performed. By
depositing a thicker layer of Pt (3500A) as the bottom electrode (BE) on a heated substrate a
lower resistance BE was produced that had less stress and smoother surfaces than the baseline
electrode. Resistance of the new BE improved from 0.87 to 0.36 ohm/sq while actually
improving yield and breakdown characteristics of the capacitors. For the interconnect metal a
more complicated two step process was developed. The first interconnect layer is an evaporated
Ti/Pt material that is etched and annealed to remove stress. This initial interconnect is unchanged
from our original process which allows us to objectively compare low frequency performance data

with earlier devices. A Titanium barrier and a thick Aluminum layer are then added to reduce resistivity. This two layer interconnect improves the sheet resistance from 0.82 ohms/sq for the baseline to just 0.02 ohm/sq for the improved conductor.

Although the reduction in series resistance of the metal layers was significant, it was clear that further reduction in series resistance was easily achievable through changes in the device geometry. By using high aspect ratio structures it is possible to minimize the path length of the higher resistance BE in the devices or trade path length in BE for path in the lower resistivity M3 layer. Several high aspect ratio 600pF capacitors were designed and built. Examples of these structures are shown in Figure 2.
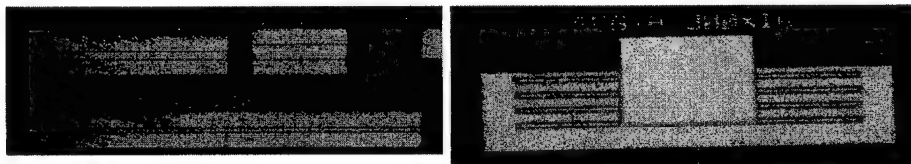
Figure 2. Image of high aspect ratio capacitors.

When these structures were combined with the new water-based ferroelectric precursors and the improved lower resistivity metal layers, the result was a great improvement in performance over the baseline devices. The measured Q at 30MHz with zero bias was increased from about 20 to over 100 at zero field and higher Q's were observed with bias.

CONCLUSION

An improved method is described for the production of MOD precursors for ferroelectric materials. New water soluble and stable MOD ceramic precursors were synthesized for barium, strontium and titanium elements. For the Group II metals, the polyether acid precursors are easily synthesized from the acid and metal. For the higher valent metals, the MOD precursors were made from the reaction of commercially available metal alkoxides and the anhydride of the corresponding polyether acid. BST thin films were made by spin-on processing of the water based materials. These new precursor materials provide a no VOC and lower toxic route to a wide range of thin film, thick film and bulk ceramic materials. In order to realize performance goals, improved BE and interconnect conductors were also developed as well as application specific geometries. Electrical properties of these devices give a tunabiltiy of over 5 to1, leakage on the order of 10^{-8} a/cm^2, and Q values of over 100 at 0 field, and Q's approaching 400 at higher fields. Breakdown strength of the devices was excellent with representative devices surviving over 125 hours at 2.5MV/cm.

REFERENCES

1. G.M. Vest et. Al. Synthesis of Metallo-Organic Compounds For MOD Powders and Films, Mat. Res. Soc. Symp. Proc., vol. 60, pp 35-42 (1986); J.Y. Mantese, et al. Characterization of potassium tantalum niobate films formed by metalorganic decomposition, Journal of Applied Physics, vol. 72, pp. 615-619 (15 Jul. 1992).
2. C.A Paz de Araujo, J.D. Cuchiaro, M. T. Scott, L.D. McMillan. US Patent 5,423,285. Process for fabricating materials for ferroelectric, high dielectric constant, and integrated circuit applications. 13 June 1995.
3. R. W. Schwartz et. al. Solution Chemistry Effects in Pb(Zr,Ti)O3 Thin Film Processing , Integrated Ferroelectrics, vol 2, pp. 243-254, 1992.
4. T. K. Dougherty and O.G. Ramer. US Patent 5,721,009, Controlled carbon content MOD precursor materials using organic acid anhydride; 24 Feburary, 1998.
5. R. Barron et. al. Aqueous Synthesis of Water-Soluble Alumoxanes: Environmentally Benign Precursors to Alumina and Aluminum-Based Ceramics. Chem Mater., vol. 9, pp. 2418-2433, 1997 and references therin.
6. A.W. Appblett et. al. Metal Organic Precursors For Yttria, Phosphorous, Sulfur, Silicon and relat. elem., vol. 93-94, pp 481-2, 1994.
7. A.W. Appblett et. al. Preparation of Nickel Ferrite Using Liquid Metal Carboxylates. Chem Mater., vol. 10, pp. 1265-1269, 1998
8. T.P. Hanussa et. al., Heavy Alkaline Earth Polyether Carboxylates. The Crystal Structure of (Ca)OOC(CH2)O(CH2)2)O(H2O)2)2. Inorg. Chem., vol. 36, pp. 5413-5415, 1997.
9. T. K. Dougherty J.J Drab and O.G. Ramer. US Patent 6,054,600; Non-Toxic solvent soluble group IV and V metal acid salt complexes using polyether acid anhydrides. 25 April 2000.
10. T. K. Dougherty and J.J Drab US Patent 6,316,651. Environmentally benign group II and group IV or V spin-on precursor materials. 12 Nov, 2000.
11. M. Brand, T. K. Dougherty J.J Drab and B.P Pierce. US Patent 6,101,102, Fixed frequency regulation circuit employing a voltage variable dielectric capacitor. 8 August, 2000.

Microstructural and Electrical Characterization of Barium Strontium Titanate-based Solid Solution Thin Films Deposited on Ceramic Substrates by Pulsed Laser Deposition

Costas G. Fountzoulas[1], Daniel M. Potrepka[2] and Steven C. Tidrow[2]

[1] Weapons Materials Research Directorate, Army Research Laboratory, Aberdeen Proving Ground, MD 21005-5069, U.S.A.
[2] Sensors and Electron devices Directorate, Army Research Laboratory, Adelphi, MD 20783-1197, U.S.A.

ABSTRACT

Ferroelectrics are multicomponent materials with a wealth of interesting and useful properties, such as piezoelectricity. The dielectric constant of the BSTO ferroelectrics can be changed by applying an electric field. Variable dielectric constant results in a change in phase velocity in the device allowing it to be tuned in real time for a particular application. The microstructure of the film influences the electronic properties which in turn influences the performance of the film. $Ba_{0.6}Sr_{0.4}Ti_{1-y}(A^{3+}, B^{5+})_y O_3$ thin films, of nominal thickness of 0.65 μm, were synthesized initially at substrate temperatures of 400°C, and subsequently annealed to 750°C, on $LaAlO_3$ (100) substrates, previously coated with LaSrCoO conductive buffer layer, using the pulsed laser deposition technique. The microstructural and physical characteristics of the post-annealed thin films have been studied using x-ray diffraction, scanning electron microscopy, and nano indentation and are reported. Results of capacitance measurements are used to obtain dielectric constant and tunability in the paraelectric ($T>T_c$) regime.

INTRODUCTION

Ferroelectrics are multicomponent materials with a wealth of interesting and useful properties, such as piezoelectricity and paraelectricity. These properties derive from their non-centrosymmetric crystal-lattice structure in which spontaneous polarization is observed. The most widespread and potentially important use for ferroelectrics exists in the area of nonvolatile random access memories (NVRAM). Ferroelectrics are also of interest in the paraelectric regime for voltage-tunable, radio frequency, and microwave phase shifters, filters, and true-time delay devices for electronic scanning antenna technology [1]. The critical materials parameters for many microwave device designs are: low dielectric constant, high tunability, low-temperature Curie peak (T_c), low dielectric loss tangent, low leakage current and small temperature coefficient of permittivity.

For electrically tunable microwave devices with a coplanar waveguide structure, BST is used as an active dielectric layer in thin-film form [2]. To achieve a high dielectric constant and a low dielectric loss tangent (tan δ), the BST film is usually grown epitaxially on single-crystal substrates such as $LaAlO_3$ (LAO) [a=0.3793 nm, α=1ppm/°C], which has a comparatively small dielectric constant ($\approx$25) and a low dielectric loss (loss tangent <10^{-4}), both necessary for microwave applications [3]. For phase shifting ceramics, it is desirable to operate the device in the paraelectric region,

hence the desire for low T_c [4]. However, in general, the higher the dielectric constant, the more tunable the ceramic will be [4]. By adding 40 mol% $SrTiO_3$ to $BaTiO_3$, the Curie peak can be shifted from 120 to –5°C but a relatively high dielectric constant can be maintained above T_c. For capacitor ceramics of perovskite structure, doping in small amounts with acceptor ions on Ti sites can greatly affect dielectric properties [4, 5]. Acceptor dopants are defined as ions with a lower valency than the ions they replace, while donor dopants are ions with higher valency. Chan et al. [5] postulated that acceptor impurities are mostly compensated for by oxygen vacancies.

We have investigated and report the microstructural and electrical characterization of selected barium strontium titanate-based solid solution thin films deposited on $LaAlO_3$ ceramic substrates by pulsed laser deposition.

EXPERIMENTAL

Selected charge-balanced binary substitutions, using $A^{3+} = Y^{3+}$ and Sc^{3+} and $A^{5+} = Ta^{5+}$ were made for Ti^{+4} to obtain $Ba_{0.60}.Sr_{0.40}Sc_{0.05}Ta_{0.05}Ti0.90O_3$ and $Ba_{0.60}.Sr_{0.40}Y_{0.05}Ta_{0.05}Ti0.90O_3$ targets. Starting materials of 99.9%$ purity or better precursors were mixed until homogeneous, then compacted with steel die and calcined in air at 1100°C for 8h. The calcined materials were then reground to powders with 75 μm or smaller grain size, pressed at 350 MPa (50 kpsi) in an isostatic press, and sintered at 1450-1550°C for 40 h in air. Details can be found in reference [1].

The experimental apparatus consists of a pulsed laser deposition chamber equipped for optical diagnostics. The 248-nm output of an excimer laser (Lambda Physik, EMG 300 MSC) was directed through a 50-cm focal length lens and focused at 45° near the target, which was mounted inside a stainless-steel chamber on a high-vacuum, rotating holder. The details of this deposition technique are given elsewhere [6]. In this work thin films of $Ba_{0.60}.Sr_{0.40}Sc_{0.05}Ta_{0.05}Ti_{0.90}O_3$ (DP1) and $Ba_{0.60}.Sr_{0.40}Y_{0.05}Ta_{0.05}Ti_{0.90}O_3$ (DP2), were deposited by the PLD technique on 1 to 2 cm^2 LAO (100) substrates, previously coated with LaSrCoO (LSC) conductive buffer layer, deposited also by the PLD technique. Both, the BST film and the LSC buffer layers, were deposited at about 400°C, using 550 mJ laser energy, at 10 Hz repetition rate, and 26.6 x 10^{-4} Pa partial oxygen pressure [1 mTorr = 1.33 x 10^{-4} Pa], for 45 minutes. Prior to film synthesis the substrates were cleaned for 5 minutes in warm (70-75 °C) methanol and ethanol baths and rinsed in warm (70-75 °C) distilled water for another 5 minutes. All films were subsequently annealed at 750°C for 45 minutes in a tube furnace in a continuous oxygen flow.

The microstructure of the films was observed by optical and scanning electron microscopy (SEM); the crystallinity of the films was determined by Glancing Angle X-ray Diffraction (GAXRD); the thickness of the films was determined with the aid of a Tencor profilometer; and the modulus of elasticity (Young's Modulus) and the hardness of the films were determined with the aid of a nanoindenter, using a Berkovich pyramid diamond indenter.

Cylindrical electrodes of various sizes were placed on the DP1(DP2)/LSC/LAO structure. Unfortunately, each electrical pad was shorted to the LSC ground plane such that electrical measurements could not be made using these contact pads as intended. Instead an HP 16034E test fixture was used for electrically characterize of the samples.

The capacitance of the test fixture was measured before sample insertion. Each sample was loaded into the test fixture using the spring loading of the test fixture; with the electrical pin on the low bias side contacting the back of the 20 mil thick substrate and the electrical pin on the high bias side contacting the surface of the film. An alligator clip attached from the low bias side was clipped to one of the contact pads thus making electrical contact to the ground plane of the capacitor structure. A universal LCR meter (120 Hz and 1kHz) was used in conjunction with the test fixture to measure the capacitance and resistance of the sample. If sufficient contact pressure was made using the bias pins, consistent results were obtained. If too much pressure is applied the pin breaks through the thin film and makes electrical contact to the LSC ground plane. If not enough pressure is applied inconsistent results are obtained.

RESULTS AND DISCUSSION

Thickness and Adhesion

The average thickness of the composite structure, DP1 (DP2) and LSC films, was 1.3 μm. Since the synthesis of the DP1 (DP2) film and LSC film took place under identical deposition parameters, we assumed that the average thickness of each film was 0.65 μm. These thicknesses are smaller than those predicted using the laser ablation energy.

The adhesion of the BST and the LSC film and the LSC on the LAO substrate was excellent. All films passed the standard "scotch-tape pull test". Furthermore, neither of the films delaminated during the measurement of the hardness by the nano indenter and during the setup of the electrical measurements.

We also observed that the adhesion of the structure, DP1 (DP2) film and LSC film, deposited at ambient temperature, followed by subsequent annealing at 750°C was poor, resulting in film delamination even with slight finger pressure. However, the adhesion was improved dramatically when the synthesis of the films took place at higher substrate temperatures. This may be attributed to the increased thermal diffusion and consequent alloying of the films on the underlying substrate due to the increased deposition temperature.

Microstructure

The microstructure and morphology of the BST films was determined using optical microscopy and SEM. All films observed by naked eye and metallographic microscopy exhibited red and green elliptical striations, indicative of the thickness variation throughout the substrate, an inherent disadvantage of the PLD technique. After annealing, the color of the DP1 films became white opaque, which is indicative of the existence of the perovskite phase [7]. The surface of the films, before and after annealing, was relatively very smooth on a macroscopic and microscopic scale, as observed in the metallographic and scanning electron microscopes. Due to that surface smoothness, it was very difficult to obtain better quality SEM photomicrographs. However, particulates, expelled parts of the PLD target, were evident on the surface of

the films (Fig. 1a and 1b). Initial depositions of films at higher oxygen partial pressure of 39.9 x 10^{-4} Pa (30 mT) showed higher particulate density.

<table>
<tr><td>(a)</td><td>(b)</td></tr>
</table>
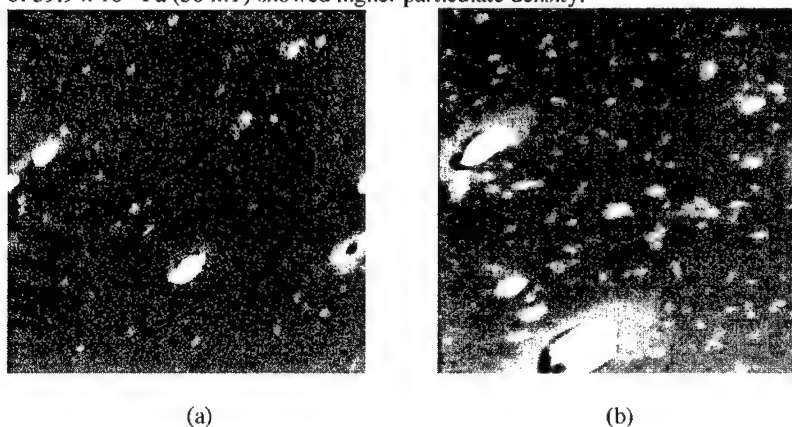
Fig. 1 Scanning Electron Photomicrographs: (a) DP1 (2,000 X), (b) DP 2 (2,000 X)

Glancing Angle X-ray Diffraction

The GAXRD analysis showed that, while all pre-annealed films were amorphous, all post-annealed films were crystalline. The unit cell of all annealed films belonged to the cubic system. The average lattice constant "a" is about 0.398 nm, in very good agreement with other published values [8]. The diffraction pattern of all post-annealed films exhibited all the peaks from the diffraction pattern of the target. Some extra peaks observed in the film pattern were identified and are attributed to the underlying LAO substrate.
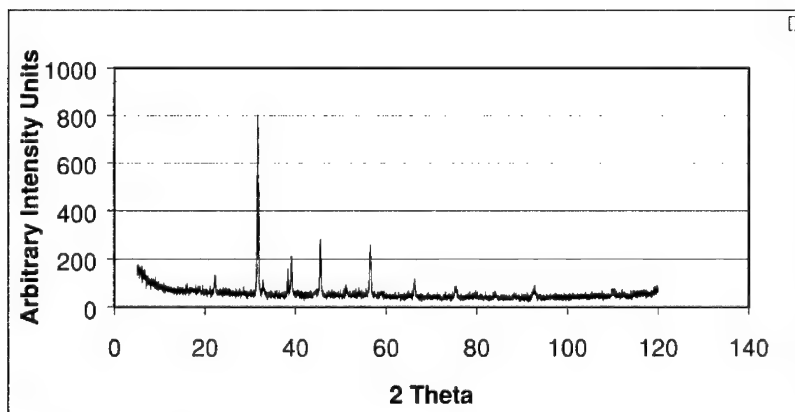
Fig. 2. Typical XRD pattern of post-annealed DP1 film.

Nanohardness and Modulus of Elasticity

The nanohardness and modulus of elasticity profile of all films determined up to 2000 nm indentation depth, at 200 nm intervals, is shown in Table 1. In order to minimize the substrate effect on the film measurements, it is recommended that, the depth of indentation must be between 10% and 25% of the total film thickness [9]. To minimize the statistical error and the effect of the indentation plastic zone on the values of the measured film properties, all measurements were averaged over nine indentations for every indentation depth, each indentation being 50 μm apart from each other. Therefore, the modulus of elasticity and the hardness of the DP1 and DP2 films, defined at 200 nm (Table 1) were 118 $\pm$ 5.30 and 103 $\pm$ 0.40 GPa, and 4.22 $\pm$ 0.44 and 3.58 $\pm$ 0.95 GPa, respectively. As it can be seen in Table 1, the barium strontium titanate films containing Scandium are slightly harder than the BST films containing Yttrium. The hardness and modulus of elasticity of the LSC film can be deduced from the corresponding values at 800 nm (Table 1).

Depth (nm)	Modulus of Elasticity (GPa)		Hardness (GPa)	
	DP1	DP2	DP1	DP2
200	118 $\pm$ 5.30	103 $\pm$ 0.40	4.22 $\pm$ 0.44	3.58 $\pm$ 0.95
400	146 $\pm$ 21.4	130 $\pm$ 19.30	5.03 $\pm$ 1.09	5.00 $\pm$ 1.13
600	153 $\pm$ 10.91	165 $\pm$ 9.61	5.39 $\pm$ 0.55	5.83 $\pm$ 0.22
800	187 $\pm$ 4.33	181 $\pm$ 7.64	5.67 $\pm$ 0.19	5.23 $\pm$ 0.32
1200	177 $\pm$ 8.65	186 $\pm$ 44.90	6.04 $\pm$ 0.29	5.24 $\pm$ 1.71
2000	190 $\pm$ 31.4	215 $\pm$ 7.30	4.31 $\pm$ 1.48	6.46 $\pm$ 0.610

Table 1. Modulus of elasticity and hardness of post-annealed films

Dielectric Properties

The measured resistance of the film was greater than 10 MΩ. The area of the pin is estimated to be 1x 10^{-7} m^2 thus yielding a resistivity, at room temperature, of about 10^9 Ω-cm for films estimated to be 6500 Å thick. The $Ba_{0.60}.Sr_{0.40}Sc_{0.05}Ta_{0.05}Ti_{0.90}O_3$ sample was measured at room temperature to have a capacitance between 6.0-6.6 pF and dissipation factor between 0.006-0.019, and 7.4-7.7 pF and 0.011-0.025 over the surface of the sample at 120Hz and 1 kHz, respectively, and capacitance of 5.8-6.8 at 1 MHz. The capacitance of the $Ba_{0.60}.Sr_{0.40}Y_{0.05}Ta_{0.05}Ti_{0.90}O_3$ sample was measured at room temperature to have a capacitance between 7.1-8.0 pF and dissipation factor between 0.014-0.017, 6.6-7.6 pF and 0.017-0.094 over the surface of the sample at 120Hz and 1 kHz, respectively, and capacitance of 7.6-8.0 at 1 MHz . At 1 MHz, the capacitance of each sample was measured as a function of temperature and applied voltage. The capacitance for the $Ba_{0.60}.Sr_{0.40}Sc_{0.05}Ta_{0.05}Ti_{0.90}O_3$ sample changed by less than 15% over the temperature range from –70 to 20°C and the tunability was less than 10% at 60 V/μm. At 1 MHz, the capacitance of the sample was measured as a function of temperature and applied voltage. The capacitance for the $Ba_{0.60}.Sr_{0.40}Y_{0.05}Ta_{0.05}Ti_{0.90}O_3$ sample changed

about 60% over the temperature range from –70 to 20°C with peak in capacitance at about –20°C and the tunability was less than 15% at 60 V/μm. Breakdown field strengths were about 80 kV/cm for these samples.

CONCLUSIONS

The crystallinity, surface morphology, adhesion, modulus of elasticity, hardness and dielectric constants of selected $Ba_{0.6}Sr_{0.4}Ti_{1-y}(A^{3+}, B^{5+})_yO_3$ thin films synthesized on LAO (100) substrates, previously coated with LSC conductive buffer layer, using the pulsed laser deposition technique. As shown by GAXRD analysis, all post-annealed films were crystalline. The capacitance for the $Ba_{0.60}Sr_{0.40}Sc_{0.05}Ta_{0.05}Ti_{0.90}O_3$ sample changed by less than 15% over the temperature range from –70 to 20°C and the tunability was less than 10% at 60 V/μm. The capacitance for the $Ba_{0.60}Sr_{0.40}Y_{0.05}Ta_{0.05}Ti_{0.90}O_3$ sample changed about 60% over the temperature range from –70 to 20°C with peak in capacitance at about –20°C and the tunability was less than 15% at 60 V/μm. Breakdown field strengths were about 80 kV/cm for these samples.

REFERENCES

1. D. M. Potrepka, S. C. Tidrow, and A. Tauber, *Mat. Res. Soc. Symp. Proc.*, **656E**, (2001).
2. A. T. Findikoglu, Q. X. Jia, D. W. Reagor, and X. D. Wu, *Microwave Opt. Technol. Lett.*, **9**, 306 (1995).
3. Y. Gim, T. Hudson, Y. Fan, C. Kwon, A. T. Fidikoglu, B. J. Gibbons, B. H. Park, and Q. X. Jia, *Appl. Phys. Lett.*, **77** (8), pp. 1200-1202 (2000).
4. S. B. Herner, F. A. Selmi, V. V. Varadan and V. K. Varadan, Mat. Lett., **15**, pp. 317-324 (1993).
5. N. H. Chan, R. K. Sharma and D. M. Smyth, *J. Am. Ceram. Soc.*, **65**, 165 (1982).
6. J. Lee, R. Ramesh and V. G. Keramidas, *Mat. Res. Soc. Proc*, **361**, 67 (1995).
7. K. D. Preston and G. H. Harting, *Appl. Phys. Lett.* **60** (23), 2831 (1992).
8. B. A. Baumert, L. H. Chang, A. T. Matsuda, T. L. Tsai, C. J. Tracy, D. J. Taylor, T. Otsuki, E Fujii, a. Hayashi and K. Suu, *J. Appl. Phys.*, **82**, (5), pp. 3558-3565 (1997).
9. G. M. Pharr, and W. C. Oliver, *MRS Bulletin* **17**, 28 (1992).

Off Axis Growth of Strontium Titanate Films with High Dielectric Constant Tuning and Low Loss

Satreerat Kampangkeaw and Charles T. Rogers
Department of Physics, University of Colorado at Boulder,
Boulder, Colorado 80309, U.S.A.

ABSTRACT

We have measured the nonlinear dielectric properties of strontium titanate (STO) thin films grown on neodymium gallate (NGO) and lanthanum aluminate (LAO) substrates. The films prepared by off-axis pulsed laser deposition were characterized by their dielectric constant and loss tangent at 1 MHz and 2 GHz, and from room temperature down to 4 K. The resulting films show significant variations of dielectric properties with position of the substrates with respect to the plume axis. STO films on LAO substrates show low loss and high dielectric constant in regions near the plume axis. On the other hand, STO on NGO shows this effect only on the films grown far from the plume axis. We also obtained a figure of merit from the relative variation of the dielectric constant divided by the loss tangent in the presence of a DC electric field up to +/- 4 V/μm. Careful mapping of the plume crossection allowed us to improve the quality and reproducibility of the dielectric films, obtaining a best figure of merit at 2 GHz and 4 K close to 100 for NGO substrate but only well off axis.

INTRODUCTION

The dielectric constant of strontium titanate (STO) is a strong function of the applied electric field [1]. Thus, it is a promising material for fabricating RF and microwave devices such as phase shifters, tunable filters and dielectric varactors [2]. Also, the lattice mismatch between STO and the high temperature superconductors such as $YBa_2Cu_3O_{7-x}$ is on the order of 2% or better. This property as well as its good chemical compatibility make STO a good candidate for superconducting microwave electronics. The dielectric response of thin films shows a significantly different behavior than is seen for bulk STO. Unstressed bulk strontium titanate is an incipient ferroelectric material and it remains paraelectric down to the lowest temperature due to quantum fluctuations [3]. The dielectric constant of bulk STO increases nonlinearly from 300 at room temperature to 30000 at 4 K. On the other hand, thin films of STO, while showing a dielectric constant close to 300 at room temperature, typically reach a maximum between 1000 and 10000 in the 30 K to 100 K range depending on the film. Thin STO films also show a loss tangent which is an order of magnitude higher than the 10^{-3}-10^{-4} of bulk STO. The microwave applications are hindered by the high dielectric loss in the material. Defects arising from lattice mismatch between the substrate and the film are believed to cause some of the loss, but other film defects could be involved [4]. Recently, approaches to produce films with reduced loss involved epitaxial lift off to relieve the strain in the films [5,6,8,9]. This method requires the growth of a sacrificial intermediate layer that needs to be etched away in order to release the film, hence involving a number of steps.

In this paper, we show that the pulsed laser deposition (PLD) growth conditions in different locations with respect to the plume axis can be chosen to produce good quality films in a single

growth step, thus avoiding a lift off technique. We report dielectric properties measurements performed on the films prepared with the off axis growth.

EXPERIMENTAL

Pulsed laser deposition (PLD) was used to deposit STO films on lanthanum aluminate and neodymium gallate substrates. This method has been used by a number of groups to prepare high quality STO films. The choice of the substrates was based on the lattice parameters in order to minimize the mismatch with STO (lattice parameters 0.3905 nm for STO (100), and roughly 0.379 nm and 0.385 nm for LAO (100) and NGO (110) respectively). A KrF excimer laser (1.8-2.3 J/cm^2, 246nm, 4Hz) was directed onto a rotating STO target (single crystal, purity 99.9%). The substrates were cut from commercial single crystal wafers, ultrasound cleaned in acetone and methanol and washed with distilled water. Cleaned substrates were mounted on a heating stage and placed in a vacuum chamber with an oxygen background pressure of 600 mtorr. The temperature of the stage was ramped from room temperature to 820 C, and maintained thereafter, until the desired film thickness was obtained. We obtained these optimized growth conditions from previous studies in our laboratory [7]. After the growth, the films were cooled down under 600 torr of oxygen pressure to avoid oxygen vacancies in the films. Ellipsometry was used to measure the film thickness, which was varied from 300-900 nm.

In order to perform dielectric constant measurements, Au coplanar capacitor electrodes were fabricated with the 25 micron gap separation, 1.5 mm total gap width and with overall 1×2 mm size. The capacitors were patterned on the surface of the films using a standard photolithographic technique, and were diced individually to 1×2 mm size. Capacitance measurement were taken with a network analyzer (HP 8510) for microwave frequencies, and with a LCR meter (HP 4275A) in the low frequency range, using a previously described ring resonator technique [6]. The capacitors were mounted in a temperature controlled ring resonator.

RESULTS AND DISCUSSION

In figure 1, (left panel) we compare the dielectric function at 1 MHz for STO films grown on LAO for different locations on the heating stage. Our heater stage is located 8.7 cm from the ablation target. The figure is labeled with the radial distance from where the plume center hits the heater stage. The thickness obtained from ellipsometry measurements is also shown in the figure 1. Notice that the films grown near the center of the plume show the highest values up to 8000 for the dielectric function. However, the exact position of the maximum is not at the plume axis. We also obtained data for the loss tangent shown on the right panel on figure 1. The loss tangent for all these films is lower than 0.015, which is significantly lower than the losses reported to date for STO films.
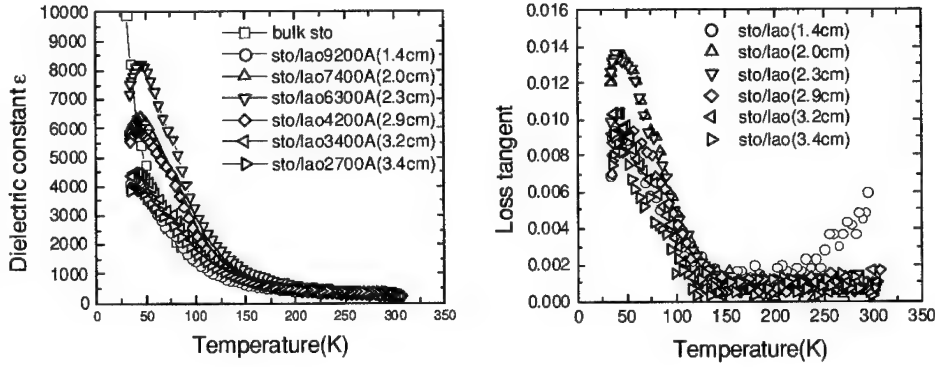
Figure 1. Dielectric constant and loss tangent at 1 MHz as a function of temperature of films STO grown on LAO at different locations with respect to the plume axis.

Similarly, figure 2 shows the dielectric function (left panel) and the loss tangent (right panel) at 1 MHz for STO films on NGO. The loss is also very small and, comparable to those of the STO films on LAO substrates. Films grown on NGO at the plume center have very poor dielectric response ($\varepsilon < 1000$) and are not shown. Also from these observations, some of the films show an increase in their loss tangent at higher temperatures probably due to conductive loss.
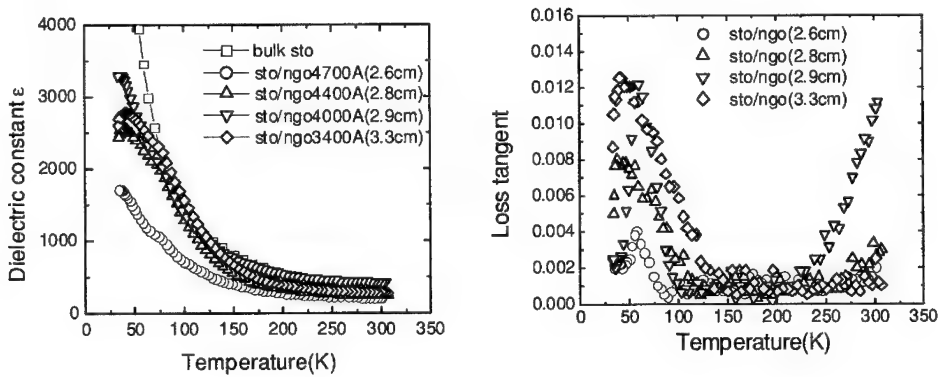
Figure 2. Dielectric constant and loss tangent at 1 MHz as a function of temperature of films STO grown on NGO at different locations with respect to the plume axis.

Figure 3 (left panel) shows the effect of substrate locations with respect to the plume axis on the maximum dielectric constant and loss tangent. The maximum of dielectric constant and loss tangent for films grown on different substrates mounted different location is plotted on the same graph. Notice that the films on LAO that sampled regions near the plume axis appear to have the higher maxima for the dielectric constant and the loss is low comparable to other films grown on edge of plume axis. On the other hand, the films on NGO mounted toward the edge of the plume have the higher maxima for the dielectric constant compared to the films on NGO mounted closed to the plume axis. The maximum for dielectric constant of films on LAO is higher than that of films on NGO.

To take the competing effects of tunability and loss into account, the figure of merit (K_E) is defined as the derivative of dielectric constant with respect to electric field divided by the product of dielectric constant and loss tangent. Figure 3 (right panel) shows the obtained figure of merit for different STO films. We observed that the figure of merit STO films grown on LAO and NGO have the maxima around 1000 at 1 MHz and 35 K, but only when the films are grown far from the plume axis. Thus, although the highest dielectric constant on LAO occurs near the plume center, the best tuning figure actually occurs about 3 cm off axis and at the same location as for optimal NGO based films. Based on the resulting figure of merit at 1 MHz and 35 K, the best films can be obtained by off axis growth.
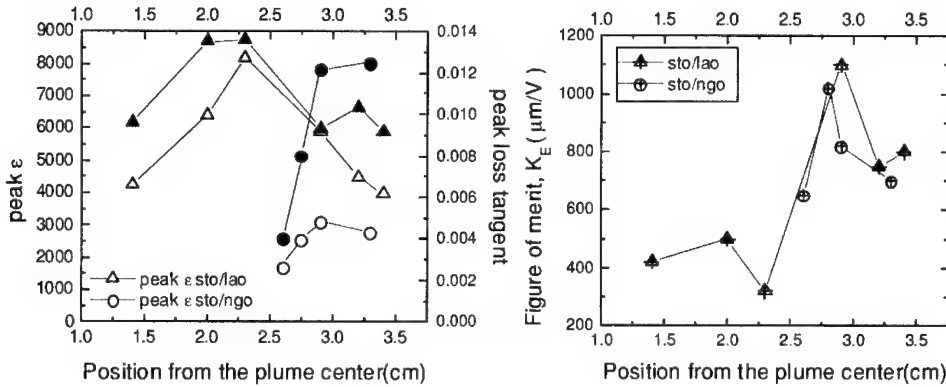
Figure 3. Effect of LAO and NGO substrate locations with respect to the plume axis 0 cm on the maximum of dielectric constant and loss tangent at 1 MHz ; open triangle- dielectric constant of STO on LAO, solid triangle- loss tangent of STO on LAO, open circle- dielectric constant of STO on NGO, solid circle- loss tangent of STO on NGO.

Finally, we have chosen one of the best films grown on NGO at 2.9 cm from the plume axis to study the microwave response. Figure 4 shows the dielectric constant and loss tangent as a function of temperature down to 4 K of this film measured at 2 GHz. The obtained peak dielectric is about 3000, and the loss tangent is less than 0.03.
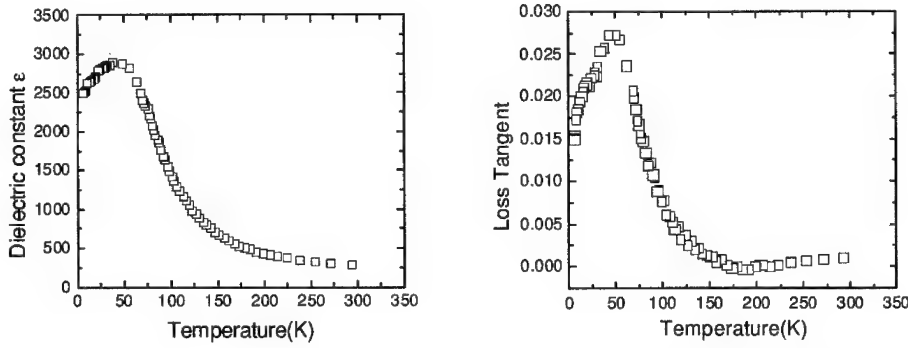
Figure 4. Dielectric constant and loss tangent at 2 GHz as a function of temperature of the best films STO grown on NGO at 2.9 cm from the plume axis.

With a DC electric field up to +/- 4 V/um, the film dielectric constant at 2 GHz and 4 K can be tuned by a factor of 4 and the loss is less than 0.015 as shown in figure 5 (right panel). Figure 5 (left panel) shows that the best obtained figure of merit at 2 GHz and 4 K is about 100. In the reference [6], the obtained figure of merit for films released from the growth substrate was 50. Thus, we have obtained twice the figure of merit while avoiding the epiaxial lift off method by using off axis PLD growth.
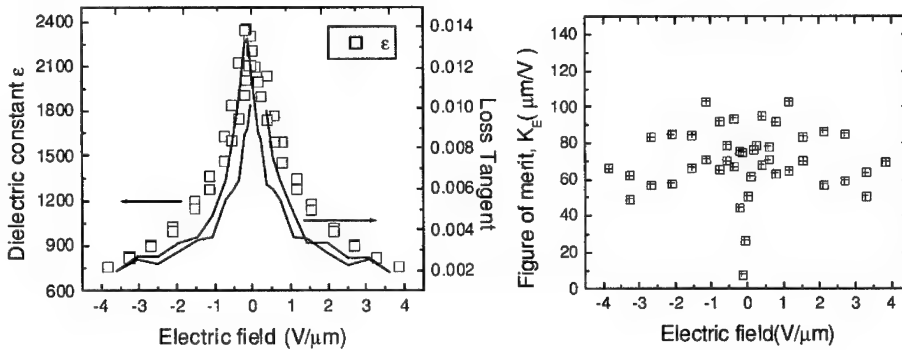
Figure 5. Tunability and figure of merit at 2GHz and 4 K of one of the best films on NGO.

CONCLUSIONS

STO films grown by PLD on different substrates at different locations with respect to the plume axis show significant variations of dielectric response. We observed that the STO films grown on LAO close to the plume axis has the maximum dielectric constant, while the same effect occurred on the films grown on NGO only far from the plume axis. The best figure of merit at 1 MHz and 35 K close to 1000 can be obtained when the films were grown on both substrates mounted roughly 3 cm from the plume axis. Also, we obtained a best figure of merit at 2 GHz and 4 K close to 100 for NGO substrate, but only for growth well off axis.

REFERENCES

1. O. G. Vendik, L. T. Ter-Mertirosyan, A. I. Dedyk, S. F. Karmanenko, and R. A. Chakalov, *Ferroelectrics* **144**, 33 (1993).
2. H. C. Li, W. Si, A. D. West, and X. X. Xi, *Appl. Phys. Lett*, **73**, 190 (1998).
3. K. A. Muller and H. Burkard, *Phys. Rev. B*, **19**, 3593 (1979).
4. O. G. Vendik, L. T. Ter-Mertirosyan and S. P. Zubko, *J. Appl. Phys.* **84**, 995 (1998).
5. M. M. Eddy, R. Hanson, M. R. Rao, B. Zuck, J. S. Speck, and E. J. Tarso, *Mater. Res. Soc. Symp. Proc.* **474**, 365-371 (1997).
6. M. J. Dalberth, PhD. Thesis, University of Colorado at Boulder, 1999.
7. M. J. Dalberth, R. E. Stauber, J. C. Price, and C. T. Rogers, *Appl. Phys. Lett.* **72**(4), 507-509 (1998).
8. K. Bouzehouane, P. Woodall, B. Marchilhac, A. N. Khodan, D. Crete, E. Jacquet, J. C. Mage and J.P. Contour, *Appl. Phys. Lett.* **80**(1), 109-111 (2002).
9. C.T. Rogers, M.J. Dalberth and J.C. Price, *Materials Issues for Tunable RF and Microwave Device. Symposium* **603**, 265 (2000).

Structure-Property Relationships in W Doped (Ba,Sr)TiO$_3$ Thin Films Deposited by Pulsed Laser Deposition on (001) MgO

N. Navi[1,*], J.S. Horwitz, H.-D. Wu[2] and S.B. Qadri,
Naval Research Laboratory, Washington DC, 20375
[1]G.W. University, Washington, DC
[2]SFA, Largo, MD

ABSTRACT

Ba$_x$Sr$_{(1-x)}$TiO$_3$ films (BST) with x=0.5, 0.6, 0.7, containing 1% W, were grown by pulsed laser deposition on MgO (001) substrates in an oxygen pressure from 3 to 500 mTorr, at a substrate temperature of 720 C. The crystal structure of the film, as determined from x-ray diffraction, was fit to a tetragonal distortion of a cubic lattice having two in-plane lattice parameters. The in and out-of-plane lattice parameters **c**, **a**, **a$'$**, and lattice distortion (**a/c** and **a$'$/c**) were calculated from the positions of the measured BST reflections ((004), (024) and (224)). The dielectric properties of the film at 2 GHz were measured using gap capacitors deposited on top of the dielectric film, at room temperature. For all compositions, as a function of the oxygen deposition pressure, a peak in the change in the dielectric constant, as a function of an applied electric field (0 – 80 kV/cm), was observed for films deposited in 50 mTorr of oxygen. Unlike the pure BST, the dielectric Q was insensitive to the oxygen deposition pressure. The largest K-factor (K=(ε(0)-ε(V)/ε(0) x Q(0)) for films deposited from Ba$_{0.6}$Sr$_{0.4}$TiO$_3$ target were observed in a film that had a minimum in-plane strain, where **a~a$'$**.

INTRODUCTION

The large electric field induced change in dielectric constant of (Ba$_x$Sr$_{1-x}$)TiO$_3$ (0 ≤ x ≤ 1), is currently being used to develop a new class low of loss, tunable microwave devices, such as tunable oscillators, delay lines and phase shifters [1]. These devices will reduce the size and the operating power of the current semiconducting and ferrite based devices, and will soon have a significant impact on both radar and wireless communication systems [2]. An issue in the fabrication of these devices is optimizing the processing of the material such that it exhibits a large change in the dielectric constant with an applied bias while minimizing the dielectric loss at microwave frequencies.

The dielectric properties of thin films are affected by many factors, such as Ba/Sr ratio, grain size, defect chemistry, oxygen vacancies, strain, and dopants. A strong relationship between structural and dielectric properties of the film has been reported in (Ba$_x$Sr$_{1-x}$)TiO$_3$ x=0.4 and x=0.5 films grown by pulsed laser deposition (PLD) with different oxygen deposition pressures [3,4]. As-deposited (Ba, Sr)TiO$_3$ films with minimal stress, grown in a relatively low pressure of O$_2$, exhibited the highest microwave figure of merit (% change ε with DC bias x Q$_{0v}$) [5-7].

Normally, oxygen deposition pressures around 300 mTorr are used during the PLD of oxide thin films to minimize the formation of oxygen vacancies. The lattice of an oxygen

---

* Permanent address - Nuclear Research Center-Negev (NRCN), Beer Sheva 9001, Israel.

deficient perovskite film expands beyond the size reported for the corresponding bulk ceramic. During heteroepitaxial thin film growth, strain due to the lattice mismatch between the film and the substrate changes the structure of the film. In addition, strain due to the thermal expansion difference between the film and the substrate also alters the structure of the deposited film during cooling from the deposition temperature to room temperature. The resulting strain in the film at room temperature has been correlated with the microwave dielectric properties of the films [3,4].

In previous studies [5,6], it was observed that a minimum in the film strain was realized for BST films deposited in a relatively low partial pressure of oxygen ($\sim$ 50 mTorr). The reduction in film strain resulted in a high overall microwave FOM for the deposited film. However, the improvement in the microwave loss due to minimizing film strain is at the cost of additional free carriers introduced into the film as a consequence of oxygen vacancies. Acceptor and donor dopants such as Mn and W have been used to minimize microwave losses due to the presence of free carriers [3,8-10]. In this paper, we report a systematic study of the influence of the oxygen deposition pressures on the structure and microwave dielectric properties of W doped, BST thin films grown on (001) MgO by PLD. Here we use oxygen vacancies, to control BST film strain and W, as a dopant, to reduce the number of free carriers generated by the additional oxygen vacancies.

EXPERIMENTAL

Thin ($\sim$0.5 μm) (Ba, Sr)TiO$_3$ (BST) films were deposited onto (001) oriented MgO single crystals by pulsed laser deposition. A KrF excimer laser pulse (248 nm, 30 ns FWHM) was focused on a rotating target, at a fluence of 1.5-2.0 J/cm^2. Three commercial BST targets from Target Materials Inc., that were 2 in. diameter by 0.125 in. thick, were used. The target compositions were Ba$_{0.7}$Sr$_{0.3}$TiO$_3$, Ba$_{0.6}$Sr$_{0.4}$TiO$_3$ and Ba$_{0.5}$Sr$_{0.5}$TiO$_3$. All the targets contained 1 mole % W as a dopant. The (001) MgO substrate temperature was maintained at 720 C while the oxygen pressure was varied from 3 to 500 mtorr. A deposition rate calibration at 50 mTorr was made prior to every deposition series. The film thickness was measured using a Tencor P-10 surface profilometer to determine the number of shots required for 0.5 μm thick BST film. An array of straight gap capacitors were fabricated on the BST films by photolithography and metal lift-off patterning using a multi-level resist process. A thin Cr adhesion layer ($\sim$100 Å) was used for the gold capped silver electrode. The silver was deposited in an e-beam evaporator over the patterned multi-level resist, to a thickness of 4 μm. Lift-off was then used to delineate the gap capacitor pattern. Thick silver is used to reduce the conductor loss of the capacitor caused by the skin effect at the microwave frequency. The gap length of the capacitor varied from 20 to 50 mil, and gap width was fixed a 5 μm.

The structural properties of the film were determined by analysis of x-ray diffraction pattern using Cu K$_\alpha$ radiation from a Rigaku rotating anode source and a powder diffractometer using standard θ-2θ geometry. The lattice parameter **c**, along the film normal direction, was calculated from the positions of the measured BST symmetric (004) peak. Using the calculated value for **c**, the in-plane lattice parameters, **a** and **a'**, were calculated from the positions of the measured BST asymmetric reflections ((024) and (224)) assuming a tetragonal structure. Differences between **a** and **a'** values indicated an additional in-plane distortion. The lattice parameter a, is defined as the larger value between **a** and **a'** since the **a** and **a'** directions could not be distinguished from the XRD data. Each BST peak was fitted with either a Gaussian/Lorentzian (or a combination of them) function to obtain the maximum intensity peak

position. The diffraction peaks of the MgO substrate were used as an internal reference for each BST peak. The lattice parameters were used to calculate the degree of distortion, $a'c$ and a'/c. Rutherford Backscattering Spectrometry (RBS) analysis was used to determine composition of films that deposited from $Ba_{0.6}Sr_{0.4}TiO_3$ target. The microwave dielectric properties of the deposited films were measured at 2 GHz with HP8510C network analyzer and 250-μm pitch GS probe. The capacitance and Q of the gap caps were calculated from the measured S11-parameters of the caps using a parallel resistor-capacitor circuit model. The conformal mapping technique for the analysis of gap capacitors on layered substrates is used to extract the dielectric constant of the BST films from the calculated capacitance values.

RESULTS AND DISCUSSION

Recently, we have shown a strong correlation between the structure and microwave dielectric properties of BST thin films deposited onto MgO substrates. As deposited BST films have lattice parameters that are different from the corresponding bulk materials. In addition, oriented films, deposited onto (001) MgO, show deviations from the expected cubic structure. These deviations occur as a consequence of the strain generated by the difference between the lattice parameter of the film and the substrate as well as differences between the thermal expansion coefficients between the film and the substrate. A correlation has been observed between the magnitude of the deviation from expected cubic and the microwave dielectric properties. For $(Ba_{0.5}Sr_{0.5})TiO_3$ films that are nearly cubic (i.e., with minimal stress) we observe the highest microwave figure of merit (%tuning x Q_{0V}, where Q_{0V} is Q at 0 kV/cm) [5-7]. These films were deposited in a relatively low partial pressure of oxygen (50 mTorr). Normally a higher oxygen deposition pressure is used during film growth in PLD to prevent the formation of oxygen vacancies. The lattice of an oxygen deficient perovskite film expands beyond the size reported for the corresponding bulk ceramic. The strain induced modification of the dielectric properties has been reported for BST x=0.5 [6] as well as x=0.4 [7].

The use of donor/ acceptor dopants such as W and Mn is well documented as a means to correct for oxygen vacancies in BST thin films. Presumably, the high oxidation state of these ions reduces the number of free carriers. There have been no reports of the effect of lattice distortion on the structure and microwave dielectric properties of doped BST materials. Here we report the lattice induced distortion in $Ba_xSr_{(1-x)}TiO_3$ thin films (x=0.5, 0.6,and 0.7) for 1% W doped thin films deposited on MgO.

The composition, structure, and microwave dielectric properties of W doped BST were measured as a function of the oxygen deposition pressure. The deposition rate typically increased up to ~60% as the oxygen deposition pressure was increased from 200 to 500 mTorr. For all composition investigated, as deposited BST films on (001) MgO are single phase, and well oriented with respect to the substrate, both in-plane and normal to the surface. A typical specular θ/2θ XRD pattern taken with Cu K_α for BST film on MgO is shown in Figure 1.
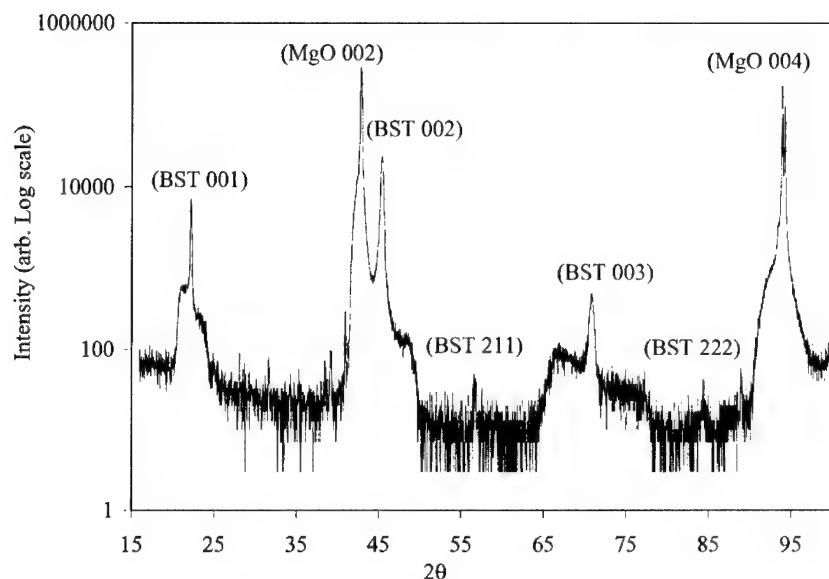
Figure 1: XRD patterns for BST film (x=0.6) deposited on MgO in 50 mTorr of oxygen at 720 C.

Film Structure

An analysis of the x-ray diffraction data for x=0.5, 0.6 and 0.7 film (1% W) shows a strong dependence of the film structure on the oxygen pressure with. For x=0.5 and 0.6, the deposited film is expected to be cubic at room temperature. All deposited films exhibit tetragonal distortion. The largest distortion is typically observed for films deposited at low partial pressures of oxygen ($\leq$ 50 mTorr). Typical in-plane lattice compression ($c > a$, a') is observed up to 200 mTorr. An in-plane tension ($c < a$, a') is observed at higher oxygen deposition pressures (figure 2).

Films deposited from $Ba_{0.6}Sr_{0.4}TiO_3$ and $Ba_{0.5}Sr_{0.5}TiO_3$ targets show larger differences between the in-plane lattice parameters, a and a', than the $Ba_{0.7}Sr_{0.3}TiO_3$ composition, suggesting an anisotropic in-plane strain for those compositions (figure 2). This could be due to a large lattice mismatch between the film and the substrate. Figure 2 also shows lattice distortion and (Ba+Sr)/Ti as a function of oxygen pressure for films deposited from $Ba_{0.6}Sr_{0.4}TiO_3$ target. The in-plane lattice compression is associated with a Ti deficiency whereas an in-plane tension is associated with a Ti excess. An analysis of the FWHM from ω scan of (002) film planes shows a minimum at high oxygen deposition pressures. That suggests a minimum number of film defects at high oxygen deposition pressures.
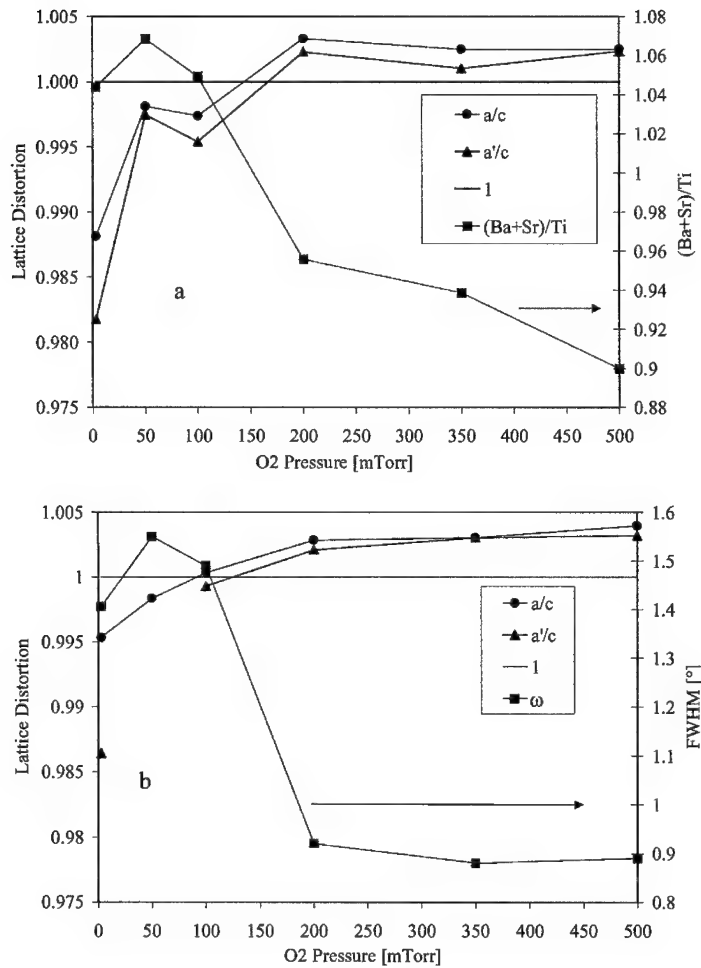
Figure 2: (a) Lattice distortion and cations ratios as a function of oxygen deposition pressure for films deposited from $Ba_{0.6}Sr_{0.4}TiO_3+1\%$mole W target. (b) Lattice distortion and ω scan of (002) for films deposited from $Ba_{0.7}Sr_{0.3}TiO_3+1\%$mole W target.

Dielectric properties

The capacitance, electric field dependence and capacitor Q for W doped BST films was measured for gap capacitors as a function of the oxygen deposition pressure for x=0.5, 0.6 and 0.7. The dielectric Q for the paraelectric phase composition ($Ba_{0.6}Sr_{0.4}TiO_3$ 1%W doped) and the ferroelectric phase composition ($Ba_{0.7}Sr_{0.3}TiO_3$ 1%W doped) are similar and do not show any

significant dependence on the oxygen pressure or film composition (figure 3).   The Q is relatively independent of the oxygen deposition pressure, therefore, the K factor observed in these films follows the oxygen pressure dependence of the tunability, which is observed to have a peak at 50 mTorr for all compositions.
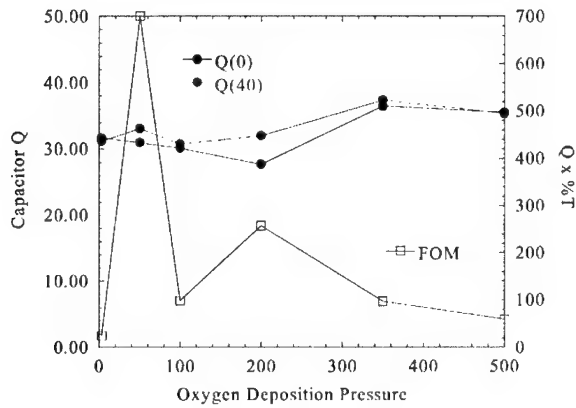
Figure 3: Q and K measured at 2 GHz as a function of oxygen deposition pressure for films deposited from $Ba_{0.6}Sr_{0.4}TiO_3$+1%mole W target.

Figure 4 show a summary of the K-factor as a function of oxygen deposition pressure for all W doped compositions. All films show peak in the oxygen deposition pressure dependence at 50 mTorr where the film is observed to be in compressional distortion ($c>a$, a'). From figure 2, we can see that for the $Ba_{0.6}Sr_{0.4}TiO_3$ composition this maximum occurred where an isotropic in-plane lattice parameter exist ($a \sim a'$). The $Ba_{0.5}Sr_{0.5}TiO_3$ composition shows only a local maximum K at 50mTorr. It is possible that a lack of significant maximum is a consequences of the highly anisotropic strain observed for the in-plane lattice parameters ($a \neq a'$) at 50mTorr.
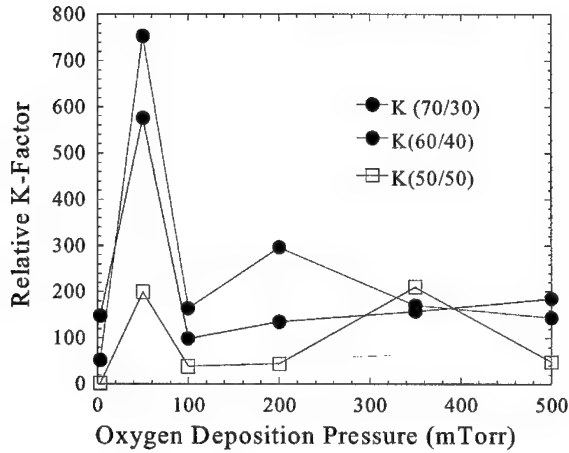
Figure 4: K-factor (2 GHz) as a function of oxygen pressure for all W doped films compositions.

SUMMARY

BST thin films, x=0.5, 0.6, 0.7 containing 1% mole W, were grown by PLD on MgO (001) substrates with oxygen deposition pressures from 3 to 500 mTorr, at a substrate temperature of 720 C. The crystal structure of the films was determined by x-ray diffraction using the (004), (024) and (224) reflections. The dielectric properties (ϵ(V) and Q(V)) were measured at 2 GHz. Q was relatively insensitive to the oxygen deposition pressure for all compositions (unlike pure BST [6]). Presumably, W^{+6} substitutes for Ti^{+4} and reduces the number of free carriers generated by the oxygen vacancies. As a consequence, a peak in oxygen deposition pressure dependence of the K-factor corresponds to a deposition condition that yields the largest tunability. In all materials investigated here, this was observed at an oxygen deposition pressure of 50 mTorr. An analysis of the diffraction data, assuming a tetragonal structure, indicates that $Ba_{0.6}Sr_{0.4}TiO_3$ and $Ba_{0.5}Sr_{0.5}TiO_3$ films could have an anisotropic in-plane distortion ($\mathbf{a} \neq \mathbf{a}'$). The anisotropy is larger if an orthorhombic distortion is assumed. The largest K-factor was observed in $Ba_{0.6}Sr_{0.4}TiO_3$ film corresponded to a deposition condition which resulted in a minimum of the in-plane strain, where $\mathbf{a} \sim \mathbf{a}'$, suggesting that in-plane anisotropic strain might also play a significant role in the dielectric properties of the film. It has been reported previously that anisotropic dielectric behavior occurs due to differences between in-plane and out-plane lattice parameters [11]. The effect of the in-plane anisotropy could have an influence on capacitors geometry and is currently being investigated.

REFERENCES

1. J.S. Horwitz, D.B. Chrisey, J.M. Pond, R.C. Auyeung, C.M. Cotell, K.S. Grabowski, P.C. Dorsey and M.S. Kluskens, Integrated Ferroelectrics, **8**, 5150 (1995).
2. D.J. Taylor in *Ferroelectric Film Devices*, Handbook of thin film devices, Vol 5, Academic Press (2000).
3. J.S. Horwitz, W. Chang, A.C. Carter, J.M. Pond, S.W. Kirchoefer, D.B. Chrisey and C. Hubert, Integrated Ferroelectrics, **22**, 279 (1998).
4. J.S. Horwitz, W. Chang, W.J. Kim, S. B. Qadri, J.M. Pond, S.W. Kirchoefer and D.B. Chrisey, J. Electroceramics, **4:2/3**, 357 (2000).
5. W.J. Kim, H. D. Wu, W. Chang, S. B. Qadri, J.M. Pond, S.W. Kirchoefer and J.S. Horwitz, J. Appl. Phys. **88**, 5448 (2000).
6. W.J. Kim, W. Chang, S. B. Qadri, J.M. Pond, S.W. Kirchoefer, D.B. Chrisey, and J.S. Horwitz, Appl. Phys. Lett. **76**, 1185 (2000).
7. W. Chang, C.M. Gilmore, W.J. Kim, J.M. Pond, S.W. Kirchoefer, S. B. Qadri, D.B. Chrisey, and J.S. Horwitz, J. Appl. Phys. **87**, 5448 (3044).
8. I. Takeuchi, H. Chang, C. Gao, P.G. Schultz, X-D. Xiang, R.P. Sharma, M.J. Downes, and T. Venkatesan, Appl. Phys. Lett. **73**, 894 (1998).
9. H. D. Wu, and F.S. Barnes, Integrated Ferroelectrics, **22**, 291 (1998).
10. H. Chang, C. Gao, Y. Yoo, I. Takeuchi, P.G. Schultz, X-D. Xiang, R.P. Sharma, M.J. Downes, and T. Venkatesan, Appl. Phys. Lett. **72**, 2185 (1998).
11. Y.G. Wang, M. E. Reeves, W. J. Kim, J.S. Horwitz and F. J. Rachford, Appl. Phys. Lett. **78**, 3872 (2001)

Poster Session

Characteristics Analysis of Saw Filter Using $Al_{0.36}Ga_{0.64}N$ Thin Film

Sun-Ki Kim, Min-Jung Park, Cheol-Yeong Jang, Hyun-Chul Choi, Jung-Hee Lee, and Yong-Hyun Lee
School of Electronic Engineering & Computer Science, Kyungpook National University,
1370 Sankyuk-Dong, Buk-Gu, Daegu, Korea, e-mail : yhlee@ee.knu.ac.kr

ABSTRACT

$Al_xGa_{1-x}N$ sample with x=0.36 was epitaxially grown on sapphire by MOCVD. SAW velocity of 5420 m/s and TCF (temperature coefficient of frequency) of -51.20 ppm/℃ were measured from the SAW devices fabricated on the $Al_xGa_{1-x}N$ sample, when kh value was 0.078, at temperatures between −30 ℃ and 60 ℃. Electro-mechanical coupling coefficient was ranged from 1.26 % to 2.22 %. The fabricated SAW filter have shown a good device performance with insertion loss of -33.853 dB and side lobe attenuation of 20 dB.

INTRODUCTION

AlN, GaN, and their alloys are important piezoelectric III-Ⅴ semiconductors suitable for optoelectric devices as well as blue/green light emitters and surface acoustic wave (SAW) applications [1,2]. Especially AlN is a promising materials for SAW devices because its high SAW velocity which qualifies it for GHz-band applications. Devices working at 2 GHz have already been built [3]. The respective SAW velocities of GaN and AlN are 4800 m/s and 5700 m/s [4]. Theoretical SAW velocity of $Al_xGa_{1-x}N$ is therefore expected to be between these values by varying from x = 0 to x = 1, which indicates that the operating frequency of the SAW can be controllable by simply changing Al-mole fraction.

EXPERIMENTS

The $Al_xGa_{1-x}N$ with x=0.36 piezoelectric thin film was grown on sapphire substrate using MOCVD at 1035 ℃ with TMAl flow rate of 40 μmol/min, H_2/ NH_3 flow of 4/4 slpm, and growth pressure of 50 torr. Prior to the epitaxial $Al_xGa_{1-x}N$ growth, 180 Å thick GaN initial buffer layer was grown at 550 ℃ with TMGa flow rate of 30 μmol/min. The surface morphology and crystallinity of the $Al_xGa_{1-x}N$ thin films were characterized using SEM (scanning electron microscopy) and X-ray rocking curve. To estimate the characteristic parameters, SAW filters with unapodized interdigital transduscer/$Al_xGa_{1-x}N$/sapphire structure were used.
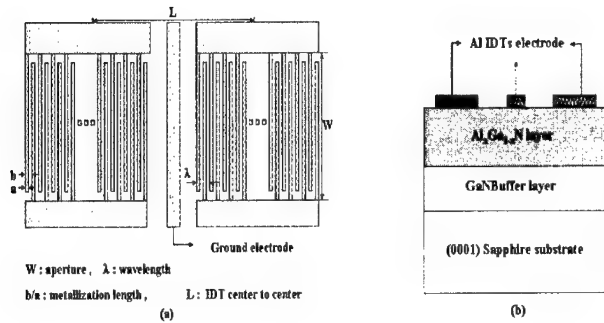
Figure 1. *(a) IDT pattern (b) schematic diagram of the cross-section of fabricated $Al_xGa_{1-x}N$ SAW filter.*

The electrode wavelength of the SAW filter was 20, 40, 60 μm. Al electrodes with thickness of 200 nm were evaporated. The patterning of the electrodes for the SAW IDT was performed by a conventional lift-off process. The respective schematic IDT pattern and the cross-section of the devices are shown in Figure 1 (a) and (b), respectively. The detailed specification is summarized Table I. The frequency response of the SAW filters was measured using a HP 8753C network analyzer. SAW velocities were calculated by estimating center frequency from the measured S_{21}. Electromechanical coupling coefficient k^2 were also calculated from conductance from the measured S_{11} and the crossed-field equivalent model [5] as in equation (1) and (2).

$$k^2 = (1/8N^2f_c)(G_0/C_s) \tag{1}$$

$$k^2 = (\pi/4N)(G_0/B_0) \tag{2}$$

Here, N is IDT electrode finger pair number, and f_c is the center frequency. G_0, C_s and B_0 are the radiation conductance, capacitance and susceptance of center frequency response [3,6].

Table I. SAW IDT pattern specifications.

Wavelength(λ)	20,40,60 μm
Aperture(W)	1800 μm
IDT finger pairs	160,82,54 pairs
IDT center to center spaces(L)	3650,4100,5000,6800 μm
Metallization ratio(a/b)	0.5

RESULTS AND DISCUSSIONS

Analysis of Al$_x$Ga$_{1-x}$N thin film

Smooth surface was of the Al$_{0.36}$Ga$_{0.64}$N is evident in SEM image in Figure 2. A smooth morphology is important to reduce propagation loss of the SAW filter at high frequency. Figure 3 shows X-ray rocking curve of the film with full width at half maximum of 536.76 arcsec, which is reasonable value for Al$_x$Ga$_{1-x}$N with such a with Al mole fraction[7].

Characteristics of surface acoustic wave

Fabricated SAW filter has the input and output IDTs with 82 split-electrode finger-pairs with wavelength ranger of 20 ~ 60 μm. Figure 4 show frequency response of Al$_x$Ga$_{1-x}$N SAW filter with wavelength 60 μm. The center frequency is 90.336 MHz, bandwidth is 1.12MHz, and Q factor is 81.236. Insertion loss is –33.853 dB and side lobe attenuation is 22 dB. Figure 5 shows SAW velocity as a function of kh (k = 2π/λ, h is the thickness of Al$_x$Ga$_{1-x}$N thin film) value, which was calculated from center frequency. That was decreased from 5510 to 5100 m/s as kh was increased from 0.0628 to 0.167. This is because, as kh value increase, the wave, which travels along the surface of the Al$_x$Ga$_{1-x}$N thin film with slower velocity than that of the sapphire substrate, becomes dominant [3,4,8].

And Electro-mechanical coupling coefficient was ranged from 1.26 % to 2.22 %.

The temperature coefficient of frequency (TCF) of Al$_x$Ga$_{1-x}$N SAW filter was measured in the temperature range between –30 ℃ and 60 ℃. The measured TCF was –51.20 ppm/℃.
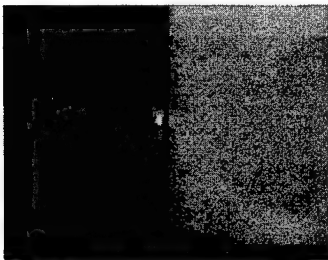
Figure 2. *Al$_x$Ga$_{1-x}$N thin film SEM image.*
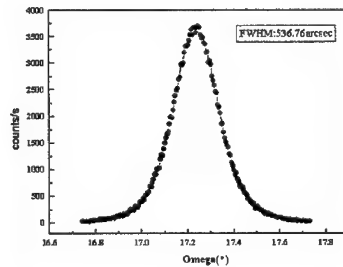
Figure 3. *X-ray rocking curve pattern of Al$_x$Ga$_{1-x}$N thin film.*

(a)   (b)
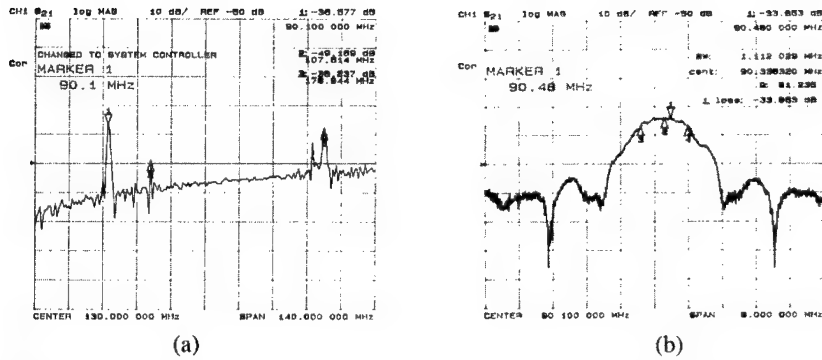
Figure 4. *Frequency response characteristics of fabricated Al$_x$Ga$_{1-x}$N SAW filter with wavelength of 60 μm. (a)Wide frequency scan including fundamental and harmonic mode and (b) narrow frequency scan mode.*

Figure 6 shows insertion loss as function of input-to-output IDT space width.

The value of propagation velocity, k^2, and TCF for Al$_x$Ga$_{1-x}$N SAW filter were summarized in Table II and they compared to those obtained from other SAW materials [9,10,11]. The propagation velocity and TCF of Al$_x$Ga$_{1-x}$N SAW filter have lower value than AlN SAW filter and higher value than undoped GaN SAW filter. It seems that the propagation velocity and TCF in Al$_x$Ga$_{1-x}$N SAW filter was able to be controlled by Al mole fraction [12].

CONCLUSION

MOCVD grown Al$_x$Ga$_{1-x}$N thin film were grow and investigated for the possible use in high frequency SAW application. Electro-mechanical coupling coefficient k^2 are
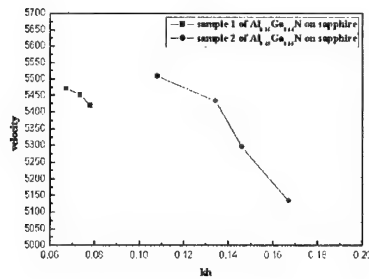
Figure 5. *SAW velocity as function of kh value.*
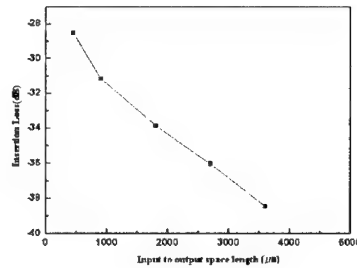
Figure 6. *Insertion loss as function of IDT space length.*

Table Ⅱ. Properties of piezoelectric substrates for SAW filter. All values were cited from [1,10,11,12].(* : measured value in this work)

subrate	Propagation Velocity (m/s)	K^2 (%)	TCF (ppm/°C)
Quartz (ST-X)	3158	0.14	0
LiNbO3 (128° Y-X)	3992	5.3	-75
LiNbO3 (Y-Z)	3488	4.5	-94
LiTaO3 (X-112°Y)	3288	0.6	-18
AlN film	5750-5765	0.15 - 0.8	-55-63
ZnO film(c-axis)	2600	0.6 - 1.9	-25
Undoped GaN film	4900-5500*	0.2 - 4.7*	-60.8*
Al$_{0.36}$Ga$_{0.64}$N film	5510-5100*	1.26 - 2.22*	-51.20*
Mg-doped GaN film	5806*	4.3*	-18.3*

from 1.26 % to 2.22 % with changing kh values. Due to its high SAW velocity (larger than 5000 m/s) and the low temperature coefficient of frequency (less than –60 ppm/°C), the SAW filters fabricated on the epitaxial Al$_x$Ga$_{1-x}$N thin film would have a strong potential for GHz band applications.

ACKNOWLEDGMENTS

REFERENCES

1. H. Okano, N. Tanaka, Y. Takahashi, T. Tamaka, K. Shibata, and S. Nakano, Appl. Phys. Lett. 64, 166-168 (1994).
2. M. AsifKhan, X. Hu, G. Sumin, J. Yang, R. Gaska, and M. S. Shur, IEEE Electron Device Letters, Vol. 21, No. 2, 63-65 (2000).
3. G. D. O'Clock and M. T. Morkoc, Appl. Phys. Lett., vol. 23, No. 2, 55-56 (1973).
4. C. Deger, E. Born, H. Angerer, O. Ambacher, M. Stutzmann, J. Hornsteiner, E. Riha, and G. Fischerauer, Appl. Phys. Lett., Vol. 72, No. 19, 2400-2402 (1998).
5. C. K. Campell, Surface Acoustic Wave Devices for Mobile and Wireless Communications. New York : Academic, (1998).
6. K. H. Choi, Jin Yong Kim, Hyeong Joon Kim, Hyung Kook Yang, and Jong Chul Park, IEEE Ultrasonics Symp., 353-356 (2000).
7. D. Brunner, H. Angerer, E. Bustarret, f. Freudenberg, R. Hopler, R. Dimitrov, O. Ambacher, and M. Stutzmann, J. Appl. Phys. 82(10), 15, November (1997).

8. I. S. Didenko, F. S. Hickernell, and N. F. Naumenko, IEEE Trans. Ultrason. Ferroelectr. Freq. Control 47, 179 (2000).

9. S. Tonami, A. Nishikata, and Y. Shimizu, Jpn. J. Appl., pt. 1, vol. 34, 2664-2667, May (1995).

10. T. Sato and H. Abe, IEEE Trans. Ultrason. Ferroelectr. Freq. Contr., vol. 45, Jan (1998).

11. J. G. Gualtieri, J. A. Kosinski, IEEE Trans. Ultrason. Ferroelectr. Freq. Contr., vol. 41, Jan (1994).

12. Suk-Hun Lee, Hwan-Hee Jeong, Sung-Bum Bae, Hyun-Chul Choi, Jung-Hee Lee, and Yong-Hyun Lee, IEEE Trans. Electron Devices, Vol. 48, 524-529 (2001).

Microwave Dielectric Spectroscopy of Ferroelectric Thin Films

Beomjin Kim, Victor Kazmirenko[*], Minki Jeong, Yuri Poplavko[*], and Sunggi Baik
Department of Materials Science and Engineering, Pohang University of Science and Technology, Pohang, 790-784, Korea
[*]Department of Microelectronics, National Technical University of Ukraine, Kiev, 252054, Ukraine

ABSTRACT

We devised a measurement method of microwave dielectric constants of dielectric thin films without applying electrodes. The method uses a rectangular waveguide in which the dielectric thin films prepared on a substrate are filled vertically at the center. The frequency dependence of S-parameter measured by network analyzer enables us to calculate the dielectric constant and loss factor of the films at the microwave region through simulation. We prepared $Ba_{0.6}Sr_{0.4}TiO_3$ thin films on (001) MgO single crystal substrate by pulsed laser deposition (PLD), and determined their dielectric constant and loss factor at ~10GHz using this method.

INTRODUCTION

Nonlinearity of ferroelectric thin films has been studied for applications to tunable microwave devices such as tunable filters, tunable phase shifters, and steerable antennas [1-3]. We need ferroelectric thin films with high tunability and low loss at microwave frequencies to develop tunable devices of good properties. The tunability of ferroelectric thin films generally increases in proportion to their dielectric constant. Therefore, it is indispensable to measure accurately dielectric properties of ferroelectric thin films at the frequencies that tunable devices are operated. The investigation has been usually made through measuring the capacitance of an interdigital capacitor on ferroelectric thin films. The precise analysis of this method needs an appropriate model that can extract the capacitance of ferroelectric thin films from the total one [4]. In addition, we cannot utilize the ferroelectric thin films for the device fabrication after the measurement.

In this study, we devised a simple method that can measure microwave dielectric properties of ferroelectric thin films without applying electrodes. Because the method does not damage ferroelectric thin films, it is possible to fabricate tunable devices directly on them after the measurement of their dielectric properties. Using this method, we investigated the dielectric constant and loss factor of $Ba_{0.6}Sr_{0.4}TiO_3$ (BST) thin films on (001) MgO single crystal substrate prepared by pulsed laser deposition (PLD).

MODEL: PARTIALLY FILLED WAVEGUIDE

When we investigate dielectric properties of a sample in a waveguide, we usually use the sample with which the cross section of the waveguide is fully filled. However, we cannot use such a structure for ferroelectric thin films that are very thin and their dielectric constant are very high. Instead, it is desirable to use the partially filled waveguide that can provide increased propagation of microwaves. In this case, as shown in figure 1, the sample is filled at the center of the waveguide to maximize the interaction with the electric field of propagated waves and to enhance the resolution of the measurement.
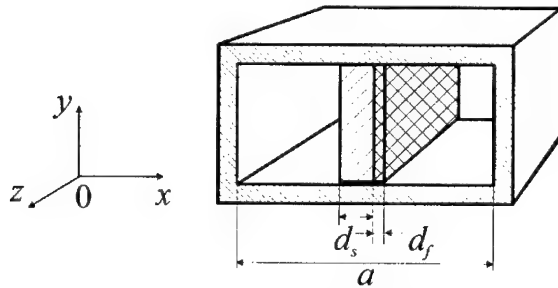
Figure 1. The scheme of partially filled waveguide.

The comparison between measured and calculated S-parameters at the situation shown as figure 1 enables us to find the dielectric constant and loss factor of the ferroelectric thin film. To find calculated S-parameters, we need to solve the electromagnetic field problem of the partially filled waveguide. From the calculated equations on the electromagnetic field problem of the structure, we can find the dielectric constant and loss factor of ferroelectric thin films at a certain frequency. However, the accuracy of the one-point technique is strongly affected by the

accidental errors [6]. We can enhance the accuracy by using calculated S-parameters provided the dielectric constant and loss factor of ferroelectric thin films are constant at the frequency region concerned. If a dielectric constant and loss factor of the ferroelectric thin film are given, we can calculate S-parameters of the partially filled waveguide. We can finally find the dielectric constant and loss factor of ferroelectric thin films by minimize errors between measured and calculated S-parameters through several iterations.

Electromagnetic field calculation of the partially filled waveguide

When the substrate with a ferroelectric thin film is situated at the center of the waveguide as shown in figure 1, TE^z or TM^z mode alone cannot satisfy the boundary conditions of the partially filled waveguide, but combinations of TE^z and TM^z modes can satisfy them.

If we use these hybrid modes for the calculation of partially filled waveguide, the electromagnetic field problem can be solved as follows: [5]

$$\beta_s \tan\left(\beta_s \frac{a}{2} - \varphi_s\right) = \beta_f \tan\left(\beta_f \frac{a}{2} - \varphi_f\right)$$

$$\varphi_s = \beta_s\left(\frac{a}{2} - d_s\right) + \tan^{-1}\left[\frac{\beta}{\beta_s}\cot\left\{\beta\left(\frac{a}{2} - d_s\right)\right\}\right]$$

$$\varphi_f = \beta_f\left(\frac{a}{2} + d_f\right) + \tan^{-1}\left[\frac{\beta}{\beta_f}\cot\left\{\beta\left(\frac{a}{2} + d_f\right)\right\}\right]$$

$$\beta = \sqrt{k_0^2 - \gamma^2}, \quad \beta_s = \sqrt{\varepsilon_s k_0^2 - \gamma^2}, \quad \beta_f = \sqrt{\varepsilon_f k_0^2 - \gamma^2}$$

where a is the width of waveguide, d_s is the thickness of substrate, d_f is the thickness of ferroelectric thin films. Also, β, β_s, β_f are transverse wave numbers in the media of air, substrate, and ferroelectric thin films, respectively, and γ is the propagation constant.

EXPERIMENT

$Ba_{0.6}Sr_{0.4}TiO_3$ thin films were deposited on $22\times10\times0.5$ mm^3 (001) MgO single crystal substrate at 730°C under 50mTorr oxygen using KrF excimer laser. Thickness of the films is 840nm. We filled the center of a rectangular waveguide (width a =22.86mm, height b =10.16mm) partially with the MgO substrate deposited with a BST thin film (see figure 1.) and

measured S-parameters by a network analyzer (HP-8510C) at the frequencies of 8.2-12.4GHz. Because we need to know the microwave dielectric properties of MgO substrate for the analysis of ferroelectric thin films, we also measured S-parameters of MgO substrate without a BST thin film in the same way. Before measuring the S-parameters, we calibrated the network analyzer with a calibration kit for a rectangular waveguide (WR-90) to remove attenuations at the adaptor for coaxial to rectangular waveguide.

RESULTS AND DISCUSSION

We found the dielectric constant ε and loss factor $\tan\delta$ of ferroelectric thin films using a nonlinear least square curve fitting technique between measured and calculated S-parameters as follows:

$$\min \sum_k \sigma_k \left[S_k^{meas} - S(f_k, \varepsilon, \tan\delta) \right]^2$$

where σ_k is a weight function, S_k^{meas} is the measured S-parameter at frequency f_k, and $S(f_k, \varepsilon, \tan\delta)$ is the calculated value of S-parameter at the same frequency.
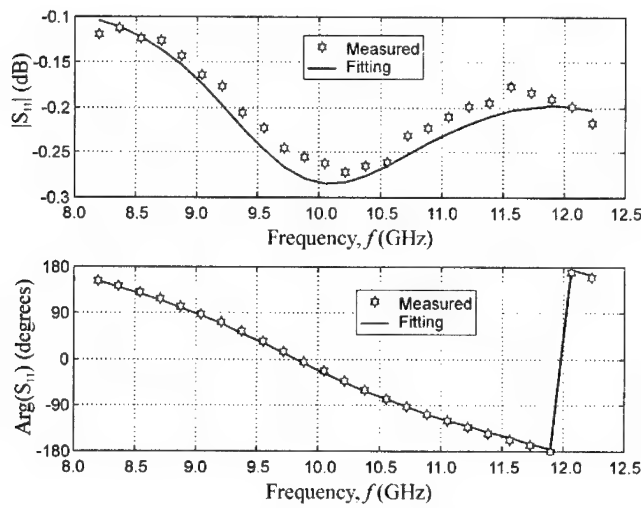
Figure 2. Comparison between measured and calculated S-parameters of ferroelectric thin films deposited on MgO substrate in the partially filled waveguide.

Figure 2 shows measured S-parameters and calculated ones that minimize errors between them, which are well matched each other. We found that the dielectric constant (ε) and loss factor ($\tan\delta$) of ferroelectric thin films were 450 and 0.05 at frequencies of 8.2-12.4GHz, respectively. In this measurement, we used microwave properties of MgO substrate measured with the same method, ant its dielectric constant and tangent loss were 9.91 and 0.0004, respectively, at the same frequency region. If we compare these values of the MgO substrate with those reported previously [7], there exists small difference for the dielectric constant. However, the loss factor measured with our method was slightly larger than the reported value. The loss may include the contributions from the waveguide and/or the non-ideal substrate. However, the loss factors of thin films determined by our method do not include such factors because they could be removed by using the loss factor of the MgO substrate that includes them.

CONCLUSIONS

We investigated microwave dielectric properties of $Ba_{0.6}Sr_{0.4}TiO_3$ thin films on (001) MgO single crystal substrate deposited by pulsed laser deposition (PLD) with no electrodes. The analysis was made using a partially filled waveguide through comparing between measured S-parameter with network analyzer and calculated ones at the same situation. From the method, we found that their dielectric constant was 450 and tangent loss was 0.05 at the frequencies of 8.2-12.4GHz.

ACKNOWLEDGMENTS

REFERENCES

1. K. Bouzehouane, P. Woodall, B. Marcilhac, A. N. Khodan, D. Crete, E. Jacquet, J. C. Mage, and J. P. Contour, *Journal de Physique IV* **11**, 41 (2001).
2. B. J. Kim, S. Baik, Y. Poplavko, Y. Prokopenko, J. Y. Lim, and B.M. Kim, *Integrated Ferroelectrics* **34**, 207 (2001).

3. C. M. Carlson *et al.*, in *Materials Issues for Tunable RF and Microwave Devices*, edited by Q. Jia, F. A. Miranda, D. E. Oates, X. Xi, (Mater. Res. Soc. Proc. **603**, Boston, MA, 2000) pp. 15-25.4. S. S. Gevorgian, P. L. J. Linner, and E. L. Kollberg, *IEEE Trans. Microwave Theor. Tech.* **44**, 896 (1996).

5. C. A. Balanis, *Advanced Engineering Electromagnetics*, 1st ed. (John Wiley & Sons, New York, 1989) p. 394.

6. J. Baker-Jarvis, R. G. Geyer, and P. D. Domich, *IEEE Trans. Instrum. Meas.* 41, 646 (1992).

7. J. C. Mage, B. Marcilhac, X. Gerbaux, and A. Hadni, *International Journal of Infrared and Millimeter Waves* **15**, 1189 (1994).

Synthesis of Nanostructured Magnetic Mixed-Oxide Ferrite Powders by Using A Novel Chemical Method

N N Ghosh
Chemistry Group, Birla Institute of Technology and Science- Pilani, Rajasthan- 333031, India.
E-mail: naren70@yahoo.com

ABSTRACT

In the present investigation, an attempt has been made to establish a new chemical route for synthesis of the nanostructured mixed oxide ferrite powders. By using this chemical method a variety of ferrite powders having spinel structure and doped with Co, Ni, Mn, Zn etc has been prepared. In this method nitrate salts of the different metals were used as starting materials. The aqueous solutions of the metal nitrates were mixed according to the molar ration of the compositions. Then the mixtures were mixed with an aqueous solution of water soluble polymer (polyvinyl alcohol). This mixture after drying yield fluffy brown powders. These powders were then calcined at different temperatures ranging from $400\,^{0}C$ to $700\,^{0}C$. Nanostructured powders were obtained from the thermal decomposition of the brown powders. The powders, prepared by calcinations at different temperatures, were characterized by using X-Ray diffraction analysis, IR spectroscopy, TGA/ DTA, and TEM. It was observed that the average particle size of the powders are in nanometer scale with a narrow size distribution. The average particle size of the powders was increased with the increase of calcinations temperature.
This chemical method has proved to provide a convenient process for the preparation of nanostructured ceramic powders at comparatively low temperatures and offers the potential of being a simple and cost-effective route.

INTRODUCTION

Research in the field of nanostructured ceramic powders have gained immense importance because of their potential application in many areas of technology. Technologically, fine-particle ferrites have been of interest due to their wide spectrum of applications as inductor cores in RF systems, circulators, permanent magnets, advanced memories, sintered electrodes, microwave devices, anti-detection (stealth) technology applications, catalysts etc. The surface properties and the microstructures of such powders, which control most of the parameters required for any particular application, often depend on the method of their preparation. Conventional solid state reactions described as ceramic techniques do not provide nanostructured ferrite materials having homogeneous composition. In the conventional ceramic method for the preparation of ferrites long heating schedules and high temperatures, sinter the final product and result in the loss of the fine particle nature of the powders. This method is thus affected by a poor control of the particle size, morphology and microscopic homogeneity (1).

The chemical synthesis routes for the production of fine ferrite powders have overcome many of the limitations of the ceramic method. The important chemical synthesis routes, which have gained substantial popularity over the years, include the precursor compound method, the co precipitation method, the sol-gel method, the solvent evaporation method, the hydrothermal method and the combustion method (2-12).

Although several chemical routes exist for the preparation of fine ferrite powders, the consideration of affordability and versatility of a route still remain a major challenge for the materials scientists, involved in the development of new synthetic routes.
In the present investigation, a novel chemical route which is both affordable and versatile for the synthesis of a series of ferrite powders has been developed. By using this chemical method ferrites having general formula MFe_2O_4 [where M= Ni(II), Co(II), Zn(II)] has been prepared.
.

EXPERIMENTAL METHOD

Preparation of the precursor materials for MFe_2O_4

To prepare precursors of the mentioned oxide systems appropriate amounts of the desired metal nitrates were taken into aqueous solution.10%(w/v) aqueous solution of a water-soluble polymer (Polyvinyl alcohol) is then added to each of the mixed metal nitrate solutions.

An aqueous solution containing equal weight percentage of sucrose and tartaric acid (20 wt%) was prepared. 50ml of this mixture was added to the of water soluble polymer and metal nitrates. This resulting viscous liquid mixture was evaporated to dryness to obtain a voluminous organic based fluffy precursor powder.
Ultrafine ferrite powders were obtained by calcining the precursor powders at varying temperature (400 ^{0}C to 700 ^{0}C) for varying periods of time.

Thermal gravimetric and differential calorimetric (TG/DSC) studies of the precursor material, were performed on the STA-625 thermal DSC. All experiments were performed in air atmosphere with a heating rate of 10^0C/min. the infrared spectra for the precursor and the heat treated powders were recorded on the Perkin Elmer 883 infrared spectrophotometer from 400to 4000 cm^{-1} by the KBr pellet method. The X-ray powder diffraction (XRD) patterns for the precursor and the heat treated powders were recorded using Phillips P.W. 1710 X-ray diffractometer with CuK$_\alpha$ radiation and Nickel filter. Transmission electron microscopy (TEM) studies of the prepared powders were done on CM-12 Phillips electron microscope. A vibrating sample magnetometer was used for the room temperature magnetic studies of the prepared powders.

RESULTS AND DISCUSSION

The simultaneously recorded TG and DSC data for the $NiFe_2O_4$, $CoFe_2O_4$ and $ZnFe_2O_4$ precursor powders produced ,by this chemical method, follow a similar trend. The themograms reveal that the precursor powders involve a single step decomposition between 200 ^{0}C to 400 ^{0}C. The precursor powders are found to decompose between 210^0C to 360 ^{0}C   with an exothermic peak at 302^0C. The process involves an exothermic heat liberation of 300 mcal/mg with 35% weight loss. The exothermic heat liberation is due to the combustion of the carbonaceous remains of the polymer and decarboxylation of the precursor material, which is accompanied by the evolution of gases such as CO, CO_2 and H_2O (water vapor). The thermal effects are thus accompanied by weight loss in TG curve.

The XRD of the ferrite powders, produced by this chemical route, reveals that the precursor powders are X-ray amorphous. From XRD spectra it was found the $NiFe_2O_4$ first formed when its precursor powder was calcined at 400 ^{0}C for 5hrs. A broad XRD peak corresponding this ferrite phase was observed. Similarly $CoFe_2O_4$ and $ZnFe_2O_4$ were formed when their precursor powders were calcnied at 500 ^{0}C for 4 hrs and 550 ^{0}C for 6hrs. The XRD peaks, corresponding to the ferrite phase, increase in intensity with subsequent heat treatments. This indicates the growth of crystallity in the powders with increase in heat treatment temperature and time.

IR spectra of all the precursor powders and powders prepared by calcinations of precursors was taken. In the precursor powders IR bands at 3387 cm^{-1} and 1619 cm^{-1} are due to the presence of moisture in the materials. The intensity of these bands diminishes and vanishes with the increase in heat treatment. The absorption bands at 1394 cm^{-1}, 1087 cm^{-1}, and 822 cm^{-1} in the precursor materials, can be assigned to the various vibrational modes of carboxylate ions. These absorption bands disappear after heat treatment at 450 ^{0}C. The absorption bands at 578 cm^{-1} and 420 cm^{-1} were observed for calcined powders are due to the lattice absorption of metal ferrites. These band intensity increases with increase in heat treatment temperature.

The crystallite size of the prepared powders are determined from XRD line broadening using the Scherrers' equation. These studies reveal that with the increase in the calcinations temperature the crystallite size gradually increases for all the powders.
The average particle size of the powders prepared by calcining at different temperature with varying calcinations time was measured by TEM. The average particle size of the powders of $NiFe_2O_4$, $CoFe_2O_4$ and $ZnFe_2O_4$ are shown in table1. From TEM it was observed that the average particle size of the powders are in nanometer scale ($\pm$ 10 nm) with a narrow size distribution.

Table 1 Average particle size (nm) of the powders calcined as different temperatures.

Sample	Calcination Temperature								
	500 ^{0}C			600 ^{0}C			700 ^{0}C		
	4 hrs	6 hrs	10hrs	4 hrs	6 hrs	10 hrs	4 hrs	6 hrs	10 hrs
$NiFe_2O_4$	40nm	45nm	54nm	53nm	65nm	74nm	65nm	78nm	80nm
$CoFe_2O_4$	35nm	42nm	49nm	57nm	68nm	74nm	63nm	74nm	82nm
$ZnFe_2O_4$	37nm	45nm	56nm	61nm	70nm	75nm	70nm	80nm	85nm

CONCLUSION

A number of nanosized ferrite has been prepared by using a novel chemical method. This method is technically simpler, cost effective, and more time and energy- efficient than the other reported methods for preparation of single phase mixed-oxide powders. This chemical route has the potential to apply for synthesis of a variety of mixed oxide systems at relatively low temperature.

REFERENCES

1. B. K. Das, "Preparation and characterization of materials" ed. J. M Honig and   C. N. R. Rao (New York Academy Press 1981).
2. J. M. D. Coey, *Phys. Rev. Lett.*17,1140 (1991).
3. B. Martinez, X. Obradors, L. balcells, A. Rouanet and C. Monty, *Phys.Rev.Lett.* **8**,181 (1998).
4. M. V. Cabarias, J. M . G. Z. Calbet, J. R. Cavajal and M. V. Ragi, *J. Sol. State Chem.***111**, 229 (1994).
5. K. Melzer and A. Martin, *Phys. State. Sol.* **107**,247 (1987).
6. L. Patron, E. Segal, F. G.llie and M. Brezeanu, *J. Mater. Sci.* **6**, 932 (1987).
7. W.Schuele, *J.Phys.Chem.* **63**, 83 (1959).
8. H. Dishlich, *Angew.Chem. Int. Ed.* **12**, 367 (1971).
9. D. J. Anderson and F. R. Sale, *Powder. Metal* **1**,1 (1979).
10. P. Pramanik, *Bull. Mater. Sci.* 19, 957 (1996).
11. K. Suresh, T. S. Panchapakesan and K. C. Patil, *Solid State Ionics* **126**, 299, (1999)
12. Y. S. Cho, D. Scheffer, V. L. Burdick and V. R. W.Amarakoon, *Mater. Res. Bill* **14**, 2361 (1999).

The Effects of Plasma Induced Damage on The Channel Layers of Ion Implanted GaAs MESFETs during Reactive Ion Etching(RIE) and Plasma Ashing Processes

Hokyun Ahn, Honggu Ji, Jaekyoung Mun, Min Park and Haecheon Kim
Wireless Communication Devices Department, Basic Research Laboratory
Electronics and Telecommunications Research Institute (ETRI)
161, Kajong-Dong, Yusong-Gu, Taejon, Korea 305-600

ABSTRACT

The gate length of GaAs MESFETs is required to be shorter for higher microwave frequency applications. The side-wall process using silicon nitride is one of the effective processes to fabricate short gate length GaAs MESFETs. The side-wall process consists of deposition and anisotropic etching of silicon nitride and delivers plasma induced damages on the channel layers of the devices. In this study, the effects of plasma induced damage on the channel layers of ion implanted GaAs MESFETs during reactive ion etching and plasma ashing processes have been investigated. The plasma induced damage was characterized by sheet resistance measurement, X-ray photoelectron spectroscopy(XPS) and auger electron spectroscopy(AES) of different etched surfaces, compared with a chemically wet-etched reference surface. Also the effect of the plasma induced damage on the device performance was investigated. As a result, plasma ashing can deteriorate the plasma-induced damage by RIE.

INTRODUCTION

GaAs MESFETs have been widely used in the microwave frequency application. Recently, as a higher frequency application is demanded, shorter gate length GaAs MESFETs should be fabricated through appropriate processes such as the side wall process using silicon nitride. The side wall process includes plasma-related processes such as reactive ion etching (RIE) and plasma ashing which are generally used due to the advantages of anisotropic etching profile and clean surface. However, these processes are usually accompanied with the plasma induced damage and contamination on the channel layers, which cause the degradation of the device performance. In this paper, the damaged layer has been characterized by X-ray photoelectron spectroscopy (XPS) and auger electron spectroscopy (AES). The effects of the plasma induced damage on the performance of GaAs based devices were also discussed.

EXPERIMENTAL DETAILS

For the experiment, liquid-encapsulated-czochralski (LEC) grown semi-insulating GaAs (100) wafers were used. To get the abrupt and shallow channel layers, Be implantation was performed at 40KeV and $2\times10^{-2}cm^{-2}$ before Si implantation at 60KeV and 7×10^{-2} cm^{-2}. Doped Si and Be were electrically activated by rapid thermal annealing at 900°C with the wafer capped by silicon nitride. All samples were dipped in HF solution to remove the silicon nitride after the activation and a new silicon nitride was deposited on the front side of the samples. AuGe/Ni/Au source/drain ohmic contacts were formed by thermal evaporation and rapid thermal annealing at 380°C for only GaAs MESFET samples. In this study, two kinds of gate region processes were performed. Generally, after the 0.35um gate length was defined by using I-line optical stepper, the silicon nitride capping layer was etched by reactive ion etching (CF_4/O_2 plasma) at 30mTorr until it was completely removed. Photo resist was removed by plasma ashing (N_2/O_2 plasma) for 10 minutes at 500mTorr. The gate recess etching was performed in $H_3PO_4 + H_2O_2 + H_2O$ (4:1:180) solution and a first-level metal (Ti/Pt/Au) on the recessed region was patterned by lift-off. However, we modified the gate region process because the microwave ashing may cause the plasma induced damage on the channel layers. When the silicon nitride was etched by RIE, the capping layer was remained as much as 250Å in the thickness so that microwave ashing should be performed with the channel layer capped. After the remained silicon nitride was removed by RIE, the same recess etching and metalization processes were followed. Three kinds of analysis samples were prepared without patterning. One sample was treated by RIE and microwave ashing, another by RIE and the other by wet etching(BOE 6:1). Surfaces of the analysis samples were analyzed by X-ray photoelectron spectroscopy (XPS), auger electron spectroscopy (AES) and contactless sheet resistance measurement. XPS and AES analysis were performed by using each the VG scientific ESCALAB 200R and the VG scientific MICROLAB 310D(X-ray source : Al-Kα). XPS data were calibrated to 284.8eV carbon 1s peak.

RESULT AND DISCUSSION
Surface analysis

GaAs surfaces were analyzed by auger electron spectroscopy (AES) and X-ray photoelectron spectroscopy (XPS) to characterize the surface contamination, the stoichiometry and the chemical bonding. Surface of a chemically wet etched sample (HF solution) was used as a reference. Fig 1 shows AES depth profile of the channel layers for different etching conditions of silicon nitride on
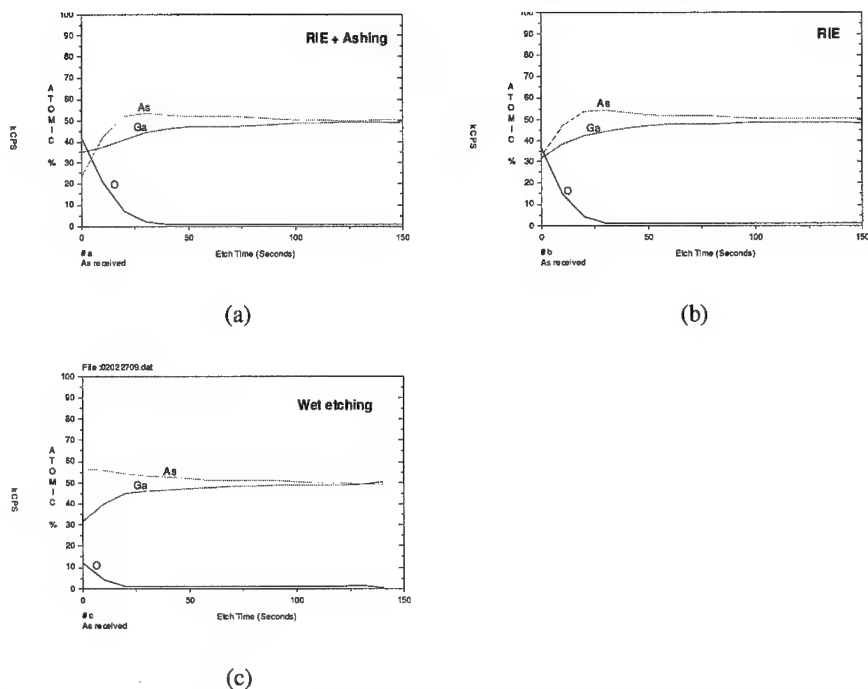
Fig. 1 AES depth profile of GaAs samples for (a) RIE + ashing, (b) RIE and (c) wet etching of silicon nitride on GaAs substrate.

GaAs substrate. Oxygen content of the surface in the RIE treated sample was larger than that in the wet etched sample and oxygen existed more deeply in the RIE-treated sample than that in the wet-etched sample. Arsine content of the surface in the RIE treated sample was smaller than that in the wet etched sample. (Fig. 1 (b), (c)) Microwave ashing increased these effects. (Fig.1(a)) Fig. 2 shows Ga-3d and As-3d XPS signal of GaAs surface. After RIE, the Ga 3d peak broadened on the high binding energy of Ga-oxide (Ga_2O_3) and the maximum peak position of the Ga 3d peak also shifted to the high binding energy. (Fig 2. (c), (e)) The As 3d peak of low binding energy of GaAs also broadened and the peak intensity of high binding energy (As_2O_3, As_2O_5) relative to the intensity of low binding energy (GaAs) increased. (Fig 2. (d), (f)) [1]. This difference in the degree of oxidation between the RIE treated sample and the wet etched sample may be attributed to the formation of highly reactive porous surface by RIE.[2] This means that GaAs was oxidized in the upper side of the channel and some portion of the channel layer was changed to the GaAs-oxide. Fig 2(a), (b) shows that the damage layer induced by RIE is more

reactive in the microwave ashing plasma than in the air. The degradations of the RIE treated samples leaded to the increase of the sheet resistance in GaAs MESFET channel layer from 930ohm/sq to 1070 ohm/sq. Microwave ashing of the RIE treated sample delivered an additional increase as much as about 260ohm/sq.
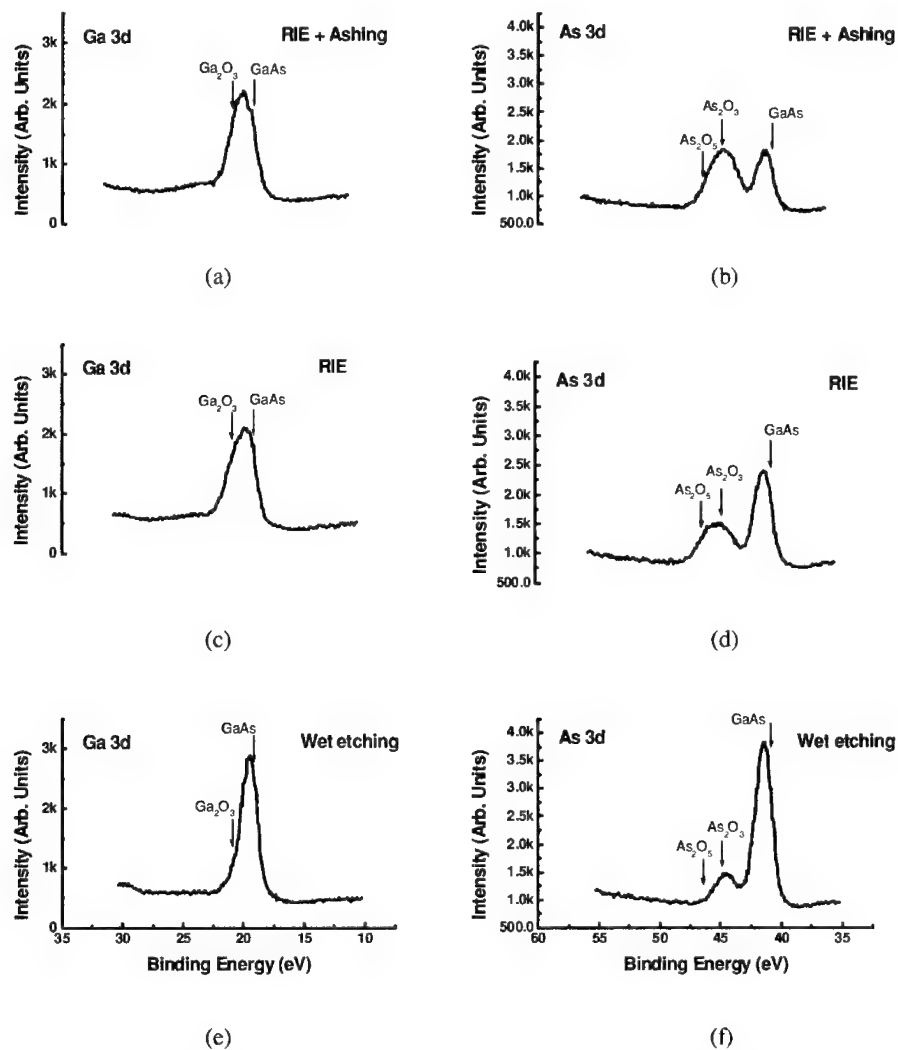
Fig 2. Ga 3d and As 3d XPS signal of GaAs samples for RIE + ashing, RIE and wet etching of silicon nitride on GaAs substrate.

MESFET performance

RIE process was performed to open the gate region, followed by microwave ashing in order to remove photo resist. RIE process decreased the slope of I-V and the saturated channel current from 90mA to 80.6mA, corresponding to the increase of the sheet resistance in the channel layer after RIE. These damages are attributed to the formation of the oxide layer in the upper side of the channel layer during RIE . Microwave ashing caused the additional decrease as much as 20.2mA in the saturated current. Fig 3 shows I-V characteristics after the gate metalization without recess etching. After microwave ashing, the slope of I-V curve and the saturated current level decreased, corresponding to the additional increase of sheet resistance in the channel layer due to the increased degradation, such as the GaAs oxidation, induced by microwave ashing. [3]

| (a) | (b) |
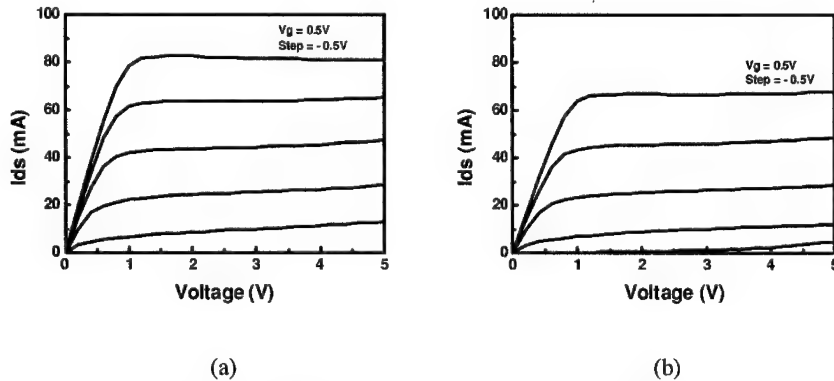
Fig 3. I-V characteristics for different etching conditions of silicon nitride, (a) RIE and (b) RIE + Ashing.

Depletion-mode MESFETs were fabricated in order to show the effect of microwave ashing on the performance of GaAs MESFETs. The ashing-exposed channel layer was recessed for 40sec and the capped channel layer was recessed for 70sec. After the gate recess etching, two channels had the same current level. The ashing-exposed MESFET showed the shift of threshold voltage from –0.66V to –0.59V and the longer tail of transconductance line in Fig 4. The reverse saturation current of the gate/n-GaAs schottky contact in the capped MESFET ($J_o = 0.702pA$) was smaller than that in the ashing-exposed MESFET ($J_o = 4.53pA$), indicating that the barrier height of the gate/n-GaAs schottky contact in the capped MESFET was higher than that in the ashing-exposed MESFET. The increased oxidation of GaAs in some portion of the channel layer by microwave ashing leaded to the reduction of the barrier height, evident from the reduction of the drain source current at Vgs (gate-source voltage) = 0V. When the capped channel layer was

recessed for 60sec, the MESFET with 60sec channel recess etching had the same threshold voltage (Vth = -0.66V) as the ashing-exposed MESFET. However, the drain-source current in the former MESFET was larger than that in the latter MESFET. Therefore, Fig 4 shows that the channel of the capped MESFET pinches off more easily if both the ashing-exposed MESFET and the capped MESFET have the same drain-source current at Vgs (gate-source voltage) = 0V.

(a)   (b)
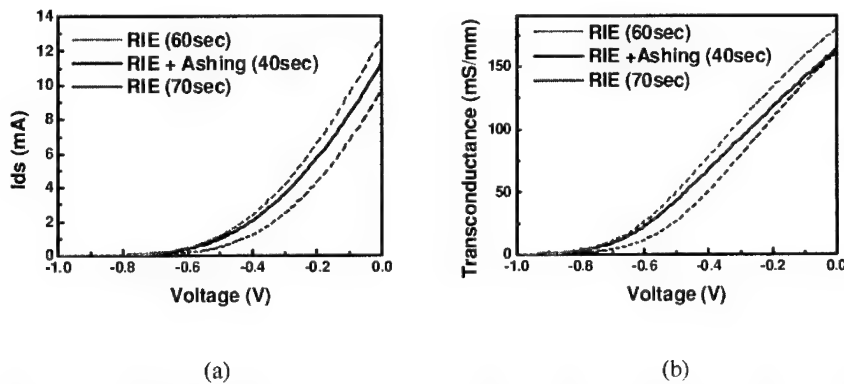
Fig 4. Transconductance and the drain-source current as a function of the gate-source voltage for different process conditions.

CONCLUSION

After the RIE treatment, the oxidation of GaAs surface increased and some portion of the channel layer was changed into GaAs-oxide such as Ga_2O_3, As_2O_3 and As_2O_5. The Arsine was depleted in GaAs surface during RIE process. These effects increased by the additional microwave ashing of the RIE treated GaAs surface. The RIE damage leaded to the reduction of the channel current. The additional microwave ashing delivered the reduction of the barrier height in the gate / n-GaAs schottky contact and deteriorated the pinch-off characteristics of GaAs MESFET.

REFERENCES
1. J. F. Moulder, William F. Stickle, Peter E. Sobol and Kenneth D. Bomben, "Handbook of X-ray Photoelectron Spectroscopy"
2. N. Vodjdani and P. Parrens, J. Vac. Sci. Technol. B5(6), Nov/Dec 1591 (1987)
3. F. Ren, J. W. Lee, C. R. Abernathy, S. J. Pearton, C. Constantine, C. Barratt and R. J. Shul, J. Vac. Sci. Technol. B 15(4), Jul/Aug ,1956 (1997)

RF Sputtered BZN Pyrochlore Thin Films for Voltage Tunable Dielectric Device Applications

Young Pyo Hong[†], Seok Ha, Ha Yong Lee, Young Cheol Lee and Kyung Hyun Ko
Department of Materials Science and Engineering, Ajou University, Suwon, Korea
[†]yphong91@hanmail.net
Dong Wan Kim[*], Hee Bum Hong[*] and Kug Sun Hong[*]
[*]School of Materials Science and Engineering, College of Engineering, Seoul National University, Seoul, Korea

ABSTRACT

The BZN pyrochlore thin films were prepared on platinized Si substrates using a reactive RF magnetron sputtering. The structures, surface morphologies, dielectric properties and voltage tunable properties of films with deposition parameters were investigated. The BZN thin films have a cubic pyrochlore phase and secondary phases of zinc niobate, bismuth niobate when crystallized at 600°C ~ 800°C. The dielectric constant and tunability of thin films are O_2/Ar ratio and post-annealing temperature dependent. The BZN thin films sputtered in 15% O_2 and annealed at 700°C had a dielectric constant of 153, tan δ of ~0.003 and maximum tunability of 14% at 1,000kV/cm.

INTRODUCTION

Ferroelectric thin film such as $SrTiO_3$, $Ba_{1-x}Sr_xTiO_3$ has been exploited as voltage tunable dielectric materials [1-6]. Suggested applications of these thin films are planar capacitors, coplanar waveguides, tunable phase shifters and tunable filters, etc. But, ferroelectric thin films have an inherently capacitive hysteresis in the microwave region resulting in large dielectric losses. Therefore, it is necessary to develop new paraelectric tunable materials without hysteresis.

Bi_2O_3-ZnO-Nb_2O_5 (BZN) pyrochlore systems are paraelectric with medium dielectric constant and low dielectric loss [7]. There are two main phases in the BZN system depending on composition; a cubic pyrochlore structure(base composition of $(Bi_{1.5}Zn_{0.5})(Zn_{0.5}Nb_{1.5})O_7$)and pseudo-orthorhombic pyrochlore structure(base composition of $Bi_2(Zn_{1/3}Nb_{2/3})_2O_7$). These two compositions are members of the general family of $(Bi_{3x}Zn_{2-3x})(Zn_xNb_{2-x})O_7$, with x=1/2 and x=2/3, respectively [8]. Previous studies on the BZN pyrochlore ceramics have been focused mostly on the applicability to low firing temperature multilayer capacitors as a bulk form [9]. Recently, several studies on the dielectric tunability and dielectric property of BZN thin film prepared by metalorganic deposition (MOD) [10] and pulsed laser deposition (PLD) [11] process has been reported. It was found that the composition of $(Bi_{1.5}Zn_{0.5})(Zn_{0.5}Nb_{1.5})O_7$ thin films prepared by MOD process have voltage tunable dielectric properties, while the composition of $Bi_2(Zn_{1/3}Nb_{2/3})_2O_7$ thin films were nearly field independent. From a current industrial point of view, it might be necessary to investigate another process technique other than PLD or MOD process. In that case, the sputtering deposition technique would be another highly attractive process for commercial production.

In this work, we report on the fabrication and dielectric properties of BZN thin films by conventional reactive RF magnetron sputtering and the correlation between deposition parameters and the tunability of BZN thin films is also discussed.

EXPERIMENTAL PROCEDURE

The composition of $(Bi_{1.5}Zn_{0.5})(Zn_{0.5}Nb_{1.5})O_7$ cubic pyrochlore target materials were prepared by a conventional mixed-oxide process and shaped into 2 inch disk. The BZN thin films were deposited by reactive RF magnetron sputtering with system geometry of target to substrate was off-axis type. The base pressure in the process chamber evacuated 3.0×10^{-6} Torr and high purity Ar and O_2 were used as sputtering and reactive gases respectively. The discharge was generated at a constant RF power of 150W and the flow rate of Ar were kept at a constant value and O_2/Ar ratios were variable in 5%, 10%, 15% and 20%, receptively, working pressure was maintained at 10mTorr using throttle valve. As a bottom electrode and substrate, (111) oriented platinum coated p-type Si wafers (Pt/TiO$_2$/SiO$_2$/Si) were used. The as-deposited films were amorphous and annealed at 600~800℃ for 3hr in air to have crystallized films with a pyrochlore structure. The thickness of the films prepared was 4,000~4,500Å. The standard capacitor type Metal-Insulator-Metal (MIM) heterostructure devices were then fabricated for dielectric properties measurements. The silver dots of 250μm diameter as the top electrode were deposited by the thermal evaporation for electric contact probing.

The crystal structure of films was characterized by x-ray diffraction (XRD, Mac Science M18XHF) using Cu$K\alpha$ radiation and an Alpha-Step surface profiler was used for measuring the thickness of all the samples. The microstructure and surface morphology of the film was investigated by scanning electron microscopy (SEM, JEOL JSM-6330F) equipped with a field emission. The dielectric properties of the BZN films(capacitance(Cp) and dissipation factor(tan δ)) were measured with an Agilent 4294A precision impedance analyzer in the 40Hz-10MHz range with a 500mV root-mean-square(rms) oscillation voltage. Using the measured capacitances, the dielectric constants were calculated with the measured film thickness and top electrode area. The bias electric field dependence of the dielectric properties were measured in 1MHz with a maximum dc bias field was ±40V.

RESULTS AND DISCUSSION

Crystal structure

The XRD patterns of BZN films deposited with various O_2/Ar ratios and post-annealed at different temperatures are shown in Fig. 1. The films were amorphous at 500℃ and below. Films annealed at 600℃ were crystalline and showed a cubic pyrochlore structure and secondary phases. These secondary phases were indexed by orthorhombic zinc niobate phases: $Zn_3Nb_2O_8$ and $ZnNb_2O_6$. The films annealed at 700℃ have a pyrochlore structure while those annealed at 600℃ exhibit the zinc niobate structure with the $ZnNb_2O_6$ phase increasing significantly for 20% O_2. With increasing the annealing temperature up to 800℃, the BZN films started to contain small amounts of orthorhombic bismuth niobate phase ($BiNbO_4$) as well as even larger amounts of zinc niobate. These secondary phases are different from those found in MOD or PLD-BZN films [10-11].

Surface morphology

Fig. 2 shows surface micrographs of the BZN thin films deposited with O_2/Ar of 15% and annealed at different temperatures. It can be seen that grain size became about 30nm in average
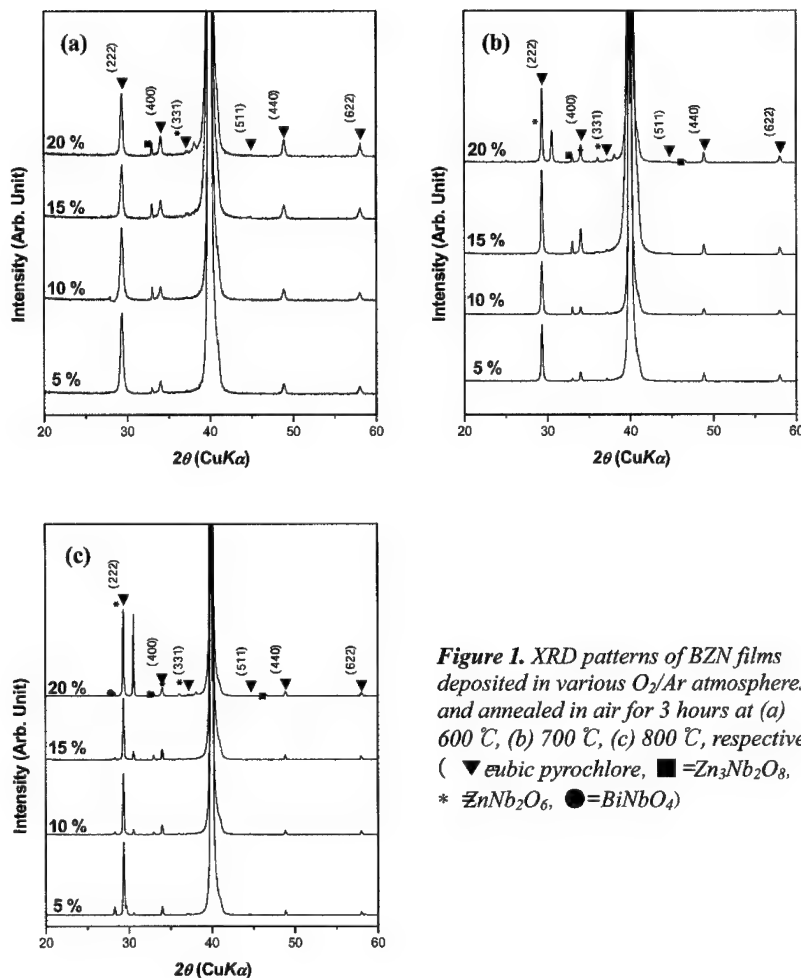
Figure 1. XRD patterns of BZN films deposited in various O_2/Ar atmospheres and annealed in air for 3 hours at (a) 600 ℃, (b) 700 ℃, (c) 800 ℃, respectively. (▼ cubic pyrochlore, ■ =$Zn_3Nb_2O_8$, * =$ZnNb_2O_6$, ●=$BiNbO_4$)

diameter after annealing at 600 ℃. The average grain sizes increased with annealing temperature. At temperature of 800 ℃, the grain size reached around 400nm. The surface grain size was not changed at the same annealing temperature even though oxygen content increased from 5% to 20%. These results show that oxygen contents, unlike annealing temperature, during sputter deposition had not so great effects on the microstructures of BZN thin film.
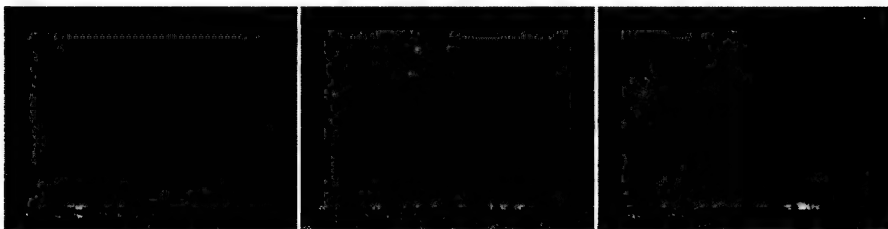
Figure 2. *FE-SEM surface morphology of BZN films deposited in 15% O_2 and annealed in air for 3 hours.*

Dielectric properties

The dielectric properties of sputtered BZN films as a function of O_2/Ar ratios and annealing temperature are shown in Fig. 3. The dielectric constants of films that were annealed at same temperature increased up to O_2/Ar of 15% and decreased again at that of 20%. Also, films annealed at 700℃ had high dielectric constants as compared with 600℃ and 800℃. The dielectric constant of the BZN films had a maximum value of 153 at O_2 of 15%, 700℃ annealing. All films exhibited very low dielectric losses (0.0015 < tan δ < 0.0054, measurement frequency = 1MHz). With increasing O_2 % and decreasing annealing temperature, the loss tangents continuously decreased.

The dc bias electric field dependence of the dielectric properties of the BZN films was investigated. Fig. 4 gives the voltage tunability of films with O_2/Ar ratios and annealing temperature. The tunability (%) is defined as $(C_0-C_v)/C_0$ where C_0 and C_v are the capacitance
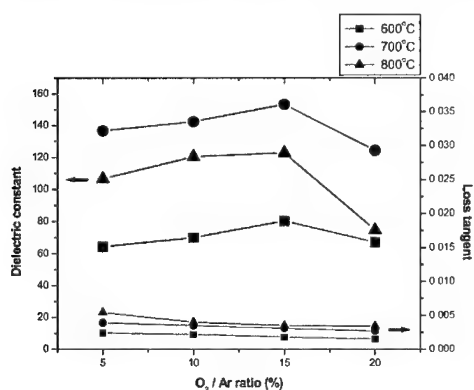
Figure 3. *Dielectric constant and loss tangent of BZN films annealed at different temperature as a function of O_2/Ar ratio (measurement frequency=1MHz).*
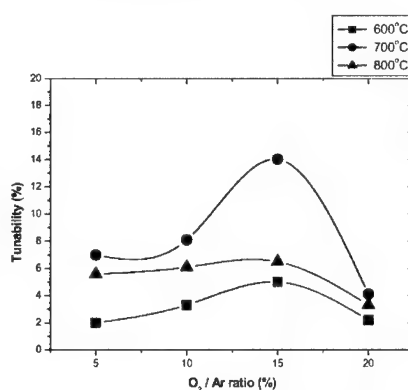
Figure 4. *Tunability of BZN films annealed at different temperature as a function of O_2/Ar ratio (measurement frequency=1MHz, maximum dc bias field=±40V).*
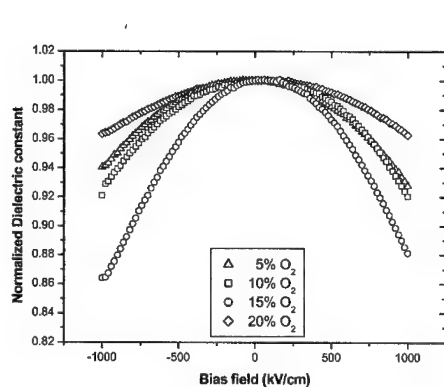
Figure 5. *Normalized dielectric constant versus dc bias field plots for BZN films deposited in various O₂/Ar atmospheres and annealed in air for 3 hours at 700 ℃.*
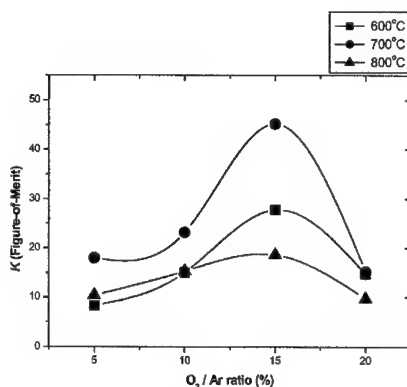
Figure 6. *The Figure-of-Merit, K factors of BZN films annealed at different temperature as a function of O₂/Ar ratio.*

values at zero and maximum dc voltage levels. For the BZN films deposited with 15% of oxygen and annealed at 700℃, the maximum tunability of 14% achieved under a bias 1,000kV/cm.

Fig. 5 shows normalized dielectric constant versus bias field plots for BZN films deposited with various O_2/Ar ratios and annealed at 700℃. The dielectric constant decreased with the bias field, while the loss tangent was constant (not shown in the figure). The curve was symmetric with respect to zero bias and had no hysteresis. There is no evidence of saturation in the tunability up to the maximum measurement field. For tuning applications, both tunability and tan δ must be considered when comparing the relative merits of different film compositions, process techniques and device configurations. So the figure of merit, the K-factor, defined as $K = (C_0-C_v) / (C_0 \tan \delta)$ where tan δ is measured without dc bias was measured. The K factors of BZN films are shown in Fig. 6. The films annealed at 700℃ possess high K values, but the films annealed at 800℃ possess lower K values than 600℃ due to the high loss.

Conclusively, it could be seen that the composition of reactive gas mixture and post-annealing treatment were very effective to control basic dielectric properties and tunability.

CONCLUSIONS

The BZN thin films were successfully prepared by the reactive RF magnetron sputtering. The BZN films showed the cubic pyrochlore structure. The sputtered cubic BZN thin films have the voltage tunability in spite of the containing secondary phases. It was found that O_2/Ar ratio during sputtering and annealing temperature was the primary critical factors on the dielectric constant and tunability. The maximum tunability of 14% at 1,000kV/cm was achieved from films post-annealed at 700℃ after deposition in a 15% O_2/Ar ratio mixture at pressure of 10mTorr and RF power of 150W.

ACKNOWLEDGEMENT

REFERENCE

1. X. X. Xi, H.-C. Li, W. Si, A. A. Sirenko, I. A. Akimov, J. R. Fox, A. M. Clark and J. Hao, *J. Electroceram.,* **4[2/3]**, 393 (2000)
2. P. Padmini, T. R. Taylor, M. J. Lefevre, A. S. Nagra, R. A. York and J. S. Speck, *Appl. Phys. Lett.,* **75[20]**, 3186 (1999)
3. H.-M. Christen, L. A. Knauss and K. S. Harshavardhan, *Materials Science and Engineering,* **B56**, 200-203 (1998)
4. A. Outzourhit, J. U. Trefny, T. Kito, B. Yarar, A. Naziripour and A. M. Hermann, *Thin Solid Films,* **259**, 218-224 (1995)
5. D. Fuchs, C. W. Schneider, R. Schneider and H. Rietschel, *J. Appl. Phys.,* **85[10]**, 7362 (1999)
6. A. B. Kozyrev, T. B. Samoilova, A. A. Golovkov, E. K. Hollmann, D. A. Kalinikos, V. E. Loginov, A. M. Prudan and O. I. Solddatenkov, *J. Appl. Phys.,* **84[6]**, 3326 (1998)
7. M. Valant and P. K. Davies, *J. Am. Ceram. Soc.,* **83[1]**, 147 (2000)
8. X. Wang, H. Wang and X. Yao, *J. Am. Ceram. Soc.,* **80[10]**, 2745 (1997)
9. D. P. Cann, C. A. Randall and T. R. Shrout, *Solid State Commu.,* **100[7]**, 529 (1996)
10. W. Ren, S. Trolier-McKinstry, C. A. Randall and T. R. Shrout, *J. Appl. Phys.,* **89[1]**,767 (2001)
11. H.-F. Cheng, Y.-C. Chen and I.-N. Lin, *J. Appl. Phys.,* **87[1]**, 479 (2000)

Comparison of Microwave Dielectric Properties of between (001) and (011) Ferroelectric Ba$_{1-x}$Sr$_x$TiO$_3$ Thin Films grown by Pulsed Laser Deposition

Seung Eon Moon, Eun-Kyoung Kim, Su-Jae Lee, Seok-Kil Han[1], Kwang-Yong Kang, and Won-Jeong Kim
Wireless Communication Devices Department, Electronics and Telecommunications Research Institute, Taejon, 305-350, Korea.
[1]Rftron Co., Ltd, Seoul, 151-050, Korea.

ABSTRACT

The effects of anisotropic dielectric properties of ferroelectric Ba$_{1-x}$Sr$_x$TiO$_3$ (BST) films on the characteristics of phase shifter have been studied in microwave regions at room temperature. Ferroelectric BST films with (001) and (011) orientation were epitaxially grown on (001) and (011) MgO substrates, respectively, by pulsed laser deposition method. The structures of BST films were investigated using x-ray diffraction measurement. The microwave properties of orientation engineered BST films were investigated using coplanar waveguide transmission lines that were fabricated on BST films using a thick metal layer by photolithography and etching process. The measured differential phase shift and insertion loss (S$_{21}$) for (011) BST films are larger than those for (001) BST films. Dielectric constants of the ferroelectric BST films are calculated from the measured S$_{21}$ using a modified conformal-mapping model.

INTRODUCTION

Tunable microwave devices using ferroelectric thin films has been proposed for long time to take advantage of the electric field dependent dielectric constant of the ferrolectricity, which may have advantages over other materials, such as semiconductors and ferrites[1]. Ferroelectric thin films, especially (Ba$_{1-x}$Sr$_x$)TiO$_3$ (BST), have been extensively investigated to explore the possibility of the microwave tunable devices. Nevertheless such a great effort, realization of the device is not achieved yet. To realize this feature, we need that ferroelectrics exhibit with a large dielectric constant change with a relatively low external bias field, and a low microwave loss.

The dielectric properties measured at microwave frequencies for BST films deposited by various deposition method have been reported to be affected by many factors, such as oxygen vacancies, strain and stress between films and substrates (due to lattice mismatch and the thermal expansion difference between the films and the substrates), film thickness, grain size, dopant type, Ba/Sr ratio. To attain these goals, several topics have been studying by many groups such as multi-layers, doping, making composite, high temperature annealing, compensating Ba/Sr deficiencies etc[2-12].

Thin film cubic perovskites have been known to be under stressed status because of lattice mismatch between film and substrate[13]. Furthermore, dielectric properties of distorted film are expected to be anisotropic, since polarizations in the cubic and non-cubic is different. To understand more for ferroelectricity, orientation dependent dielectric properties of the ferroelectric thin film is very important[14].

In this paper, we present studies of the effect of the film orientation on the microwave dielectric properties of epitaxially grown BST films on MgO (001) and (011) single crystals by pulsed laser deposition (PLD), respectively.

EXPERIMENTAL DETAILS

Epitaxial (001) and (011) BST films were deposited onto (001) and (011) MgO single crystals by PLD, respectively. A focused pulse laser from a Kr:F eximer gas laser (~2J/mm^2) transfer the materials of stoichiometric $(Ba_{0.6}Sr_{0.4})TiO_3$ to the heated substrate attached on heater. The oxygen pressure in the deposition chamber was fixed at 200 mTorr, while the substrate temperature was maintained at 825 °C. The structural properties of BST films were characterized by x-ray diffraction (XRD) measurement using a Rigaku x-ray diffractometer equipped with Cu K_α radiator source and a 4-circle X-ray diffractometer. The thickness of the deposited BST films was about 420 nm, which was confirmed by a cross sectional scanning electron microscope (SEM). Microwave dielectric properties of the BST films were measured by a HP 8510C network analyzer at frequency range of 0.05-20 GHz using coplanar waveguide (CPW) type phase shifters fabricated from a thick Au electrode (about 2 μm) with a thin Cr adhesion layer. The gap width between center and ground electrodes is 7 μm, while the center conductor width is fixed at 20 μm. The physical length of the BST CPW device is 3 mm. A DC bias field between center and ground electrodes to control the dielectric constant of BST film is applied through bias tees to protect the HP 8510C network analyzer. Coaxial cables and equipment were calibrated up to the microwave picoprobes to minimize measurement uncertainty using a commercial standard kit. Dielectric constants were extracted using a modified conformal-mapping model from the measured S_{21} and dimension of the CPW[15,16].

DISCUSSION

Though the structural properties of the BST thin films are strongly dependent on the direction of the substrate, growth condition of the films are critical to get epitaxial film without secondary orientations. Epitaxial BST film growth on (001) MgO were achieved in broad deposition conditions; heater temperature higher than 650 °C, and oxygen pressure between 50 to 500 mTorr. The higher heater temperature leads the better thin film quality and epitaxiality.
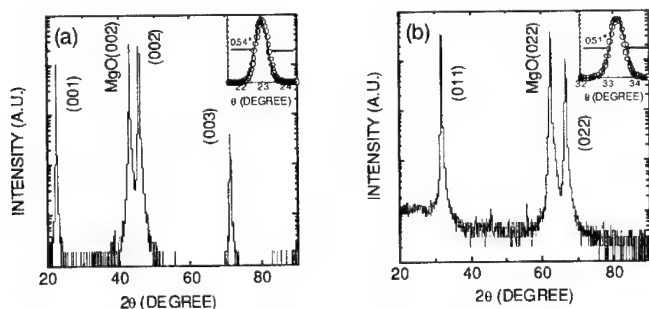
Figure 1. X-ray θ-2θ diffraction scan patterns of (a) (001) and (b) (011) BST/MgO, respectively. The insets show the XRD ω-rocking curve from the BST (002) and BST (022) of (001) and (011) BST films, respectively.
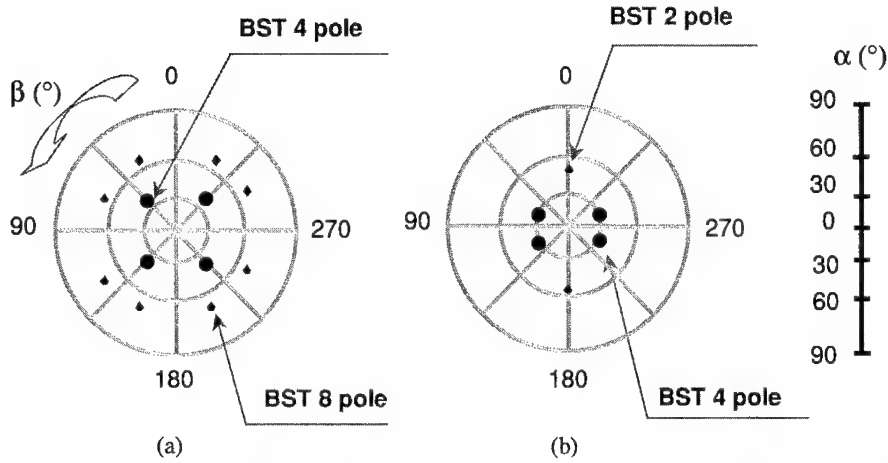
Figure 2. X-ray diffraction pole figure plots of the {112} reflections for (a) (001) and (b) (011) BST film deposited on (001) and (011) MgO substrate, respectively.

Furthermore oxygen pressure higher than 500 mTorr lead nucleation of the secondary orientations, such as (011), and (111). BST films grown on (011) MgO exhibit a narrower deposition conditions than those on (001) MgO. Deposition temperature higher than 800 °C shows a negligible intensity of (001) orientation. At 825 °C, epitaxial (011) BST film with 200 mTorr of oxygen pressure was grown successfully without other intensities. Epitaxial growth of each BST films on (001) and (011) MgO single crystals were confirmed by 4-circle diffractometer before fabricating devices. The XRD patterns of (001) and (011) oriented BST films on (001) and (011) MgO substrates, respectively, are shown in fig. 1. Secondary orientations are not shown in both XRD patterns, which suggest that each BST film is oriented along one direction and single phase. The insets in fig. 1 show the XRD ω-rocking curves from the BST (002) and BST (022) of (001) and (011) BST films, respectively. The full width half maximum (FWHM) values for (001) and (011) BST films are 0.54 and 0.51°, respectively, suggesting that the structures of films are reasonably good.

X-ray pole figure analysis was used to determine the orientation relationship between the films and the MgO substrates. The XRD pole figure plots of the {112} reflections for both the BST films and MgO substrates are shown in fig. 2. For (001) BST films, two sets of peaks are expected to be seen in XRD pole figure by interplanar angles calculation. One set is 4 poles, $\alpha = 35.3°$, $\beta = 90°$ ((112), ($\bar{1}$12), (1$\bar{1}$2), ($\bar{1}\,\bar{1}$2)), another set is 8 poles, $\alpha = 65.9°$, $\beta = 36.9°$ and 53.1° ((121), ($\bar{1}$21), (1$\bar{2}$1), ($\bar{1}\bar{2}$1), (211), ($\bar{2}$11), (2$\bar{1}$1), ($\bar{2}\bar{1}$1)), coinciding with the experimental results and indicating alignment of the BST <001> and <100> parallel with the <001> and <100> of the substrate, respectively. For (011) BST films, two sets of peaks are expected to be seen in XRD pole figure by interplanar angles calculation. One set is 4 poles, $\alpha = 30°$, $\beta = 70.5°$ and 109.5° ((121), ($\bar{1}\bar{2}$1), (211), ($\bar{2}\bar{1}$1)), Another set is 2 poles, $\alpha = 54.7°$, $\beta = 180°$ ((112), ($\bar{1}\,\bar{1}$2)), coinciding with the experimental results and indicating alignment of the BST
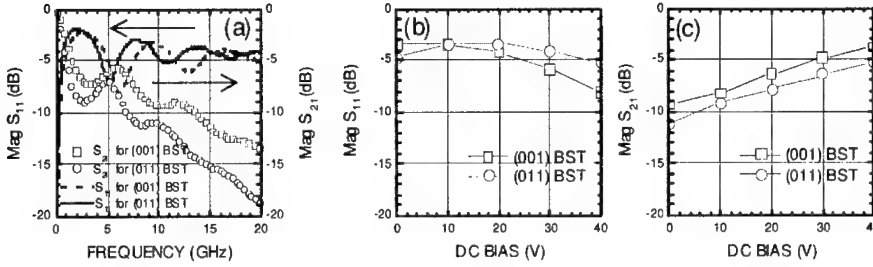
Figure 3. The measured microwave properties of the CPW device based on (001) and (011) BST films. (a) The losses as a function of frequency, (b) reflection loss (S_{11}), and (c) insertion loss (S_{21}) as a function of DC bias at 10 GHz for (001) and (011) BST films, respectively.

<011> parallel with the <011> of the substrate, which is equivalent with $<100>_{BST}//<100>_{MgO}$ and $<001>_{BST}//<001>_{MgO}$.

Figure 3 shows the measured microwave properties of the CPW device based on (001) and (011) BST films. Frequency dependant return loss (S_{11}) and insertion loss (S_{21}) of the CPW for (001) and (011) BST films at 0 V, respectively, are plotted in fig. 3 (a). The losses decrease with increasing applied DC bias field. The characteristic impedance of the CPW is not matched to that of the probes (50 Ω) resulting high return losses (S_{11}). Furthermore insertion loss (S_{21}) ranges -9.4 ~ -3.8 dB and -11.2 ~ -5.2 dB for (001) and (011) BST films, respectively, at 10 GHz with DC bias of 0 ~ 40 V, shown in fig. 3 (b) and (c). The values can be improved further by using a matched design.

The differential phase shift from 0V bias is shown in fig. 4 (a). As applied bias voltage and frequency increase, the differential phase shift also increase continuously. At the proposed operating frequency ranges (10 – 20 GHz), 63 ~ 122° and 94 ~ 183° of differential phase shift of S_{21} are observed with 40 V of a maximum applied DC bias voltage for (001) and (011) BST films, respectively. The applied DC bias voltage was limited by the commercial DC bias tees. However, the differential phase shift observed in the device is not saturated yet, which suggests that the differential phase shift will be increased further with a higher DC bias field.

Dielectric constants of the ferroelectric BST films are calculated from the phase value of S_{21}. First, phase length (ϕ) of the CPW can be expressed as following,

$$\phi_{21} = 2f_o\sqrt{\varepsilon_{eff}\mu_{eff}} \times l \times 180/c, \text{---------- (1)}$$

where f_0 is the operating frequency, ε_{eff} and μ_{eff} are the effective dielectric constant and magnetic permeability of CPW, respectively, l is the physical length of the CPW, and c is the light velocity in the air. Figure 4 (b) and (c) show total phase of S_{21} for the CPW and fitted results using eq. (1) when $\mu_{eff} = 1$ for (001) and (011) BST films on MgO substrates, respectively. To extract the dielectric constant of ferroelectric film, a modified conformal mapping technique has been used. Dielectric constant of substrate, film, and air has the following relation,
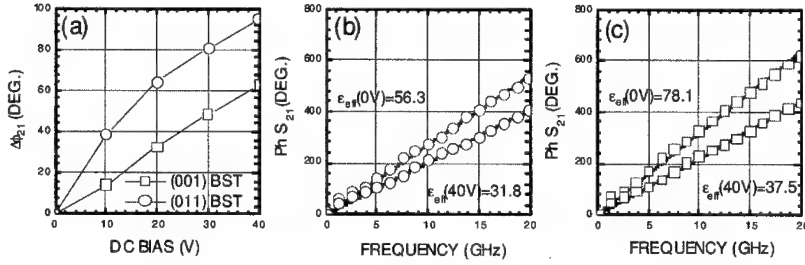
Figure 4. (a) Differential phase shift for (001) and (011) BST films at 10 GHz as a function of DC bias voltage, respectively. Total phase of S_{21} for (b) (001) BST films and (c) (011) BST films as a function of frequency with DC bias 0 and 40 V and linear fitting to extract effective dielectric constant of CPW. The open symbols indicate the measured data, the lines indicate the fitting results.

$$\varepsilon_{eff} = k_{sub}\varepsilon_{sub} + k_{film}\varepsilon_{film} + k_{air}\varepsilon_{air}, \text{---------}(2)$$

where k_i corresponds to the filling factors for the substrate, film and air, respectively. The calculated film dielectric constant decreases from 1400 and 2000 at 0 V to 750 and 900 at 40 V for (001) and (011) BST, respectively. This is corresponding to 46 % and 55 % of dielectric constant tunability with less than 70 kV/cm for (001) and (011) BST, respectively, which is comparable with those of the reported BST films. This suggest that the dielectric constant tunability of (011) BST films is larger than that of (001) BST films. Furthermore, to achieve larger differential phase angle, CPW on (011) BST might have advantage over that on (001), since BST on (011) has larger dielectric constant and larger tunability at the same time than that on (001). More test results with matched CPW will be studied in a future.

CONCLUSIONS

In summary, coplanar waveguide-type phase shifters were fabricated on (001) and (011) BST films. Under DC bias field, the measured differential phase shift and insertion loss (S_{21}) in the device on (011) BST films are larger than those in the device on (001) BST films. The calculated film dielectric constants and dielectric constant tunability for (011) BST films are also larger than those for (001) BST films.

ACKNOWLEDGMENTS

REFERENCES

1. M. J. Lancaster, J. Powell, and A. Porch, *Supercond. Sci. Technol.* **11**, 1323 (1998).
2. J. V. Mantese, N. W. Schubring, A. L. Micheli, A. B. Catalan, M. S. Mohammed, R. Naik, and G. W. Auner, *Appl. Phys. Lett.* **71**, 2047 (1997).
3. W. Chang, C. M. Gilmore, W. J. Kim, J. M. Pond,, S. W. Kirchoefer, S. B. Qadri, D. B. Chirsey, and J. S. Horwitz, *J. of. Appl. Phys.* **87**, 3044 (2000).
4. F. W. Van Keuls, C. H. Mueller, F. A. Miranda, R. R. Romanofsky, C. L. Canedy, S. Aggarwal, T. Venkatesan, R. Ramesh, J. S. Horwitz, W. Chang, and W. J. Kim, *IEEE MTT-S* **2**, 737 (1999).
5. S. Jun, Y. S. Kim, Y. W. Kim, and J. Lee, *Appl. Phys. Lett.* **78**, 2542 (2001).
6. C. M. Carlson, T. V. Rivkin, P. A. Parilla, J. D. Perkins, D. S. Ginley A. B. Kozyrev, V. N. Oshadchy, and A. S. Pavlov, *Appl. Phys. Lett.* **76**, 1920 (2000).
7. C. L. Canedy, S. Aggarwal, H. Li, T. Venkatesan, R. Ramesh F. W. Van Keuls, R. R. Romanofsky, and F. A. Miranda, *Appl. Phys. Lett.* **77**, 1523 (2000).
8. E. G. Erker, A. S. Nagra, Y. Liu, P. Periaswamy, T. R. Taylor, J. Speck, and R. A. York, *IEEE Micro. And Guided Wave Lett.* **10**, 10 (2000).
9. B. H. Park, E .J. Peterson, Q. X. Jia, J. Lee, X. Zeng, W. Si, and X. X. Xi, *Appl. Phys. Lett.* **78**, 533 (2001).
10. W. Chang, J. S. Horwitz, W. J. Kim, J. M. Pond , S. W. Krichoefer, C. M. Gilmore, S. B. Qadri, and D. B. Chrisey, *Mat. Res. Soc. Symp. Proc.* **541**, 699 (1999).
11. L. C. Sengupta, E. Ngo, M. E. O'Day, S. Stowell, and R. Lancto, *ISAF '94. Proceedings of the Ninth IEEE International Symposium on Applications of Ferroelectrics* 622 (1995).
12. W. J. Kim, W. Chang, S. B. Qadri, J. M. Pond, S. W. Krichoefer, D. B. Chrisey, and J. S. Horwitz, *Appl. Phys. Lett.* **76**, 1185 (2000).
13. W. Chang, J. S. Horwitz, W. J. Kim, J. M. Pond , S. W. Krichoefer, C. M. Gilmore, S. B. Qadri, and D. B. Chrisey, *Mat. Res. Soc. Symp. Proc.* **541**, 693 (1999).
14. W. J. Kim, W. Chang, S. B. Qadri, J. M. Pond, S. W. Kirchoefer, J. S. Horwitz, and D.B. Chrisey, *Appl. Phys. A* **70**, 313 (2000).
15. S. S. Gevorgian, T. Martinsson, P. I. J. Linner, and E.L. Kollberg, *IEEE Trans. Microwave Theory Tech.* **44**, 896 (1996).
16. E. Carlsson, and S. Geovorgian, *IEEE Trans. Microwave Theory Tech.* **47**, 1544 (1999).

Sub 0.1 μm Asymmetric Γ-gate PHEMT Process Using Electron Beam Lithography

W. S. Sul, D. H. Shin and J. K. Rhee

Millimeter-wave INnovation Technology Research Center (MINT)

Dongguk University, Seoul, Korea

Tel : +82-2-2260-3335,   Fax : +82-2-2277-4796,   E-mail : jkrhee@dongguk.edu

ABSTRACT

In this paper, we have studied on the fabrication of GaAs-based pseudomorphic high electron mobility transistors (PHEMT's) for the purpose of millimeter-wave applications.

To fabricate the high performance GaAs-based PHEMT's, we have developed unit processes, such as 0.1 μm Γ-gate lithography, silicon nitride passivation, and air-bridge process to achieve high performance of device characteristics. The DC characteristics of the fabricated PHEMT was measured at a unit gate width of 70 μm and 2 gate fingers, and showed a good pinch-off property (V_P = -1 V) and a drain-source saturation current density (I_{dss}) of 373.53 mA/mm. Maximum extrinsic transconductance (g_m) was 522.4 mS/mm at V_{gs} = -0.3 V, V_{ds} = 1.5 V, and I_{ds} = 0.5 I_{dss}.

The RF measurements were performed in the frequency range of 1.0 ∼ 50 GHz. For this measurement, the drain and gate voltage were 1.5 V and -0.3 V, respectively. At 50 GHz, 9.2 dB of maximum stable gain (MSG) and 4.2 dB of S_{21} gain were obtained, respectively. A current gain cut-off frequency (f_T) of 113 GHz and a maximum frequency of oscillation (f_{max}) of 180 GHz were achieved from the fabricated PHEMT with a 0.1 μm gate length.

INTRODUCTION

Millimeter-wave resources, of which frequency is greater than 30 GHz, have been used for the military applications, such as radars, electronic warfares, guided missiles and measurements of the nuclear radioactivity. However, the role of millimeter-wave resource in commercial business is recently emphasized because a great demand emerges in commercial applications in the high-speed broadband wireless communications [1]. The rapid improvement in device performance for millimeter-wave applications can be attributed to progress in both the epitaxy of heterostructures and processing technology. Therefore, much effort is being made aggressively on the technology development for the millimeter-wave modules and systems. Recently, new material-based HEMT's, such as InAlAs/InGaAs/InP HEMT's, show the highest cut-off frequency and the lowest microwave noise of all three terminal semiconductor devices [2-4].

For this reason, it is widely believed that they are one of the promising devices for millimeter-wave low-noise applications, and however, are still under research stage because of the high production cost, the technology immaturity and low breakdown voltage. Therefore, conventional GaAs-based PHEMT's are still one of the key active devices for millimeter-wave circuits, and modules [5]. In this paper, we report the DC and RF characteristics of the fabricated PHEMT using the asymmetric Γ-shaped gate structures with a 0.1 μm gate-length.

FABRICATION TECHNOLOGY

The PHEMT epitaxial structure was grown by molecular beam epitaxy (MBE) on a semi-insulating GaAs substrate and consists of the following layers: a 1 μm undoped GaAs buffer, a 120 Å undoped $In_{0.2}Ga_{0.8}As$ channel, a 40 Å undoped $Al_{0.25}Ga_{0.75}As$ spacer layer, delta doping plane (5×10^{12} cm^{-2}), a 250 Å undoped $Al_{0.25}Ga_{0.75}As$ Schottky contact layer, a 300 Å n-type doped GaAs cap (5×10^{18} cm^{-3}). A schematic cross-section view of the PHEMT's structure is given in Fig. 1.
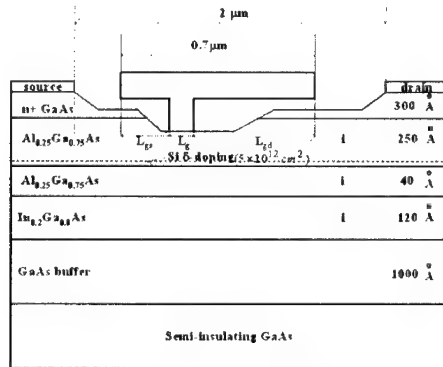
Fig.1 Schematic cross-sectional view of the PHEMT's.

The epitaxial layers showed a 2 dimensional electron carrier density of 2.1×10^{12} cm^2 and Hall mobility of 6670 cm^2/V-s at the room temperature. The PHEMT's were designed to have the off-set gate structures, which normally exhibit the high transconductance and the low gate-source resistance. The relation between the intrinsic transconductance(g_m) and the measurable transconductance(g_m') of the PHEMT's is given by equation 1. Therefore, it is expected that an enhanced g_m' can be achieved at a low gate-source resistance of the Γ-shaped gate.

The gate-source resistance can reduce by minimizing the source-gate spacing [6].

$$g_m' = \frac{g_m}{1+R_{gs}g_m} \tag{1}$$

As shown in Fig. 1, the Γ-shaped gate structures were employed to obtain a sufficient space-margin between the source and the gate-heads. For this purpose, the design parameters of 0.1 μm gate length, 2.0 μm source-drain spacing, 0.7 μm gate-head length, and 0.75 μm source-gate spacing were adopted, respectively, for the transistor structure. The PHEMT's were fabricated 3500 Å mesa for electric isolation using the etchants of $H_2SO_4/H_2O_2/H_2O$ (1 : 8 : 160) and AuGe/Ni/Au (1150/280/1600 Å) ohmic metallization with a specific contact resistance of around $1\sim 2 \times 10^{-7}$ $\Omega\cdot$cm. Ohmic alloy was performed by the two-step rapid thermal annealing at 300 and 350 $^\circ$C for 10 and 20 seconds, respectively. 0.1 μm offset Γ-gate patterning was done by electron beam lithography using a Leica Microsystems Ltd Electron Beam Pattern Generator (EBPG-4HR system) operating at an acceleration voltage of 50kV, a beam size of 50 nm and a beam current of 1 nA. Resist profiles with an overhang structure for metal liftoff and 0.1 μm offset Γ-gate with electron beam resists of a tri-layer structure consisting of PMMA 4%+MCB/ P(MMA-MAA) / PMMA 4% (1000/6000/2000 Å). Selective etching is an important step in processing GaAs/AlGaAs structures because the etched depth is limited within a few hundred angstroms and critically affects the threshold voltage of devices. The gate recess profiles were controlled by a two-step wet-etching method using the 50 % citric acid solution /H_2O_2/H_2O (1 : 3 : 1). Fig. 2 shows the surface quality on the etched samples by using an AFM and SEM.

In our AFM results, the surface etched by the selective etchant of 50 % citric acid solution /H_2O_2/H_2O (1 : 3 : 1) solution is smoother than that by another volume ratio etchants.
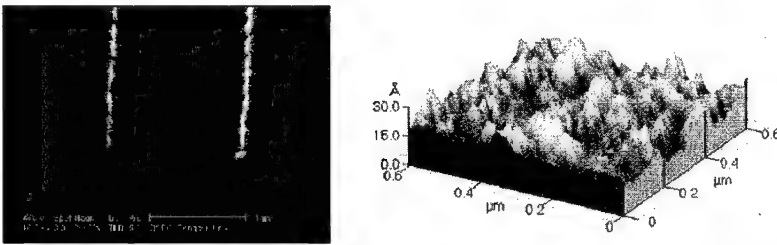
Fig. 2 SEM and AFM images taken from the surfaces etched by a solution of 50 % citric acid solution/H_2O_2/H_2O (1 : 3 : 1).

After Ti/Au (500/4500 Å) gate metallization , the devices were fully passivated by 800 Å Si_3N_4 deposited at the RF plasma enhanced CVD (PECVD) system. A SEM micrograph of 0.1 μm offset Γ-gate after lift-off and passivating with a Si_3N_4 film is shown in Fig. 3.
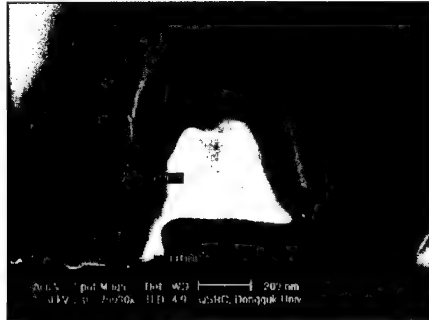
Fig.3 SEM micrograph showing 0.1 μm offset Γ-gate after lift off and passivating with a Si_3N_4. film.

As shown in Fig. 4, air-bridge metals of the Ti/Au (200/15000 Å) were then formed after patterning the dielectric and photo-resist to interconnect the isolated electrodes [7]. Fig. 5 shows the micrograph of the fabricated PHEMT's of 70 μm unit gate width and 2 fingers.
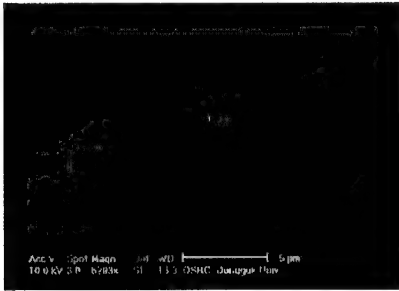
Fig.4 SEM micrograph of the air-bridge interconnections.
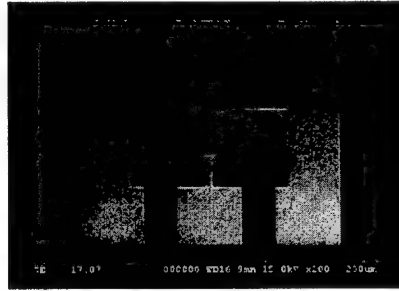
Fig.5 Plan view SEM micrograph the fabricated 70 μm × 2 PHEMT's.

RESULTS AND DISCUSSION

The DC and RF characteristics of the fabricated PHEMT's were measured by a HP 4156A DC parameter analyzer and a HP 8510C network analyzer. The DC characteristics of the offset PHEMT's with L_{gd} = 1.15 μm and L_{gs} = 0.75 μm are shown in Fig. 6, 7. The current-voltage characteristics of the 70 μm unit gate width with 2 gate fingers are given in Fig. 6. From this measurement results, we obtained a pinch-off property (V_P = -1 V) and a drain-source saturation

current (I_{dss}) of 52.3 mA. The maximum drain current density that is defined as the saturation current density measured at a gate-to-source voltage (V_{gs}) of 0V is 373.53 mA/mm.

The maximum extrinsic transconductance (g_m') is 522.4 mS/mm at $V_{ds} = 1.5$ V and $V_{gs} = -0.3$V, as shown in Fig. 7.
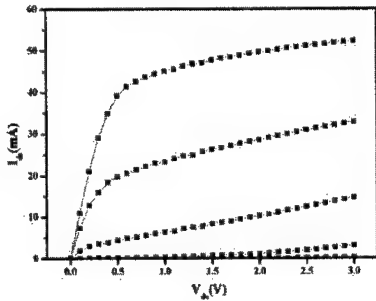
Fig. 6 I_{ds} Vs. V_{ds} characteristics of PHEMT's.
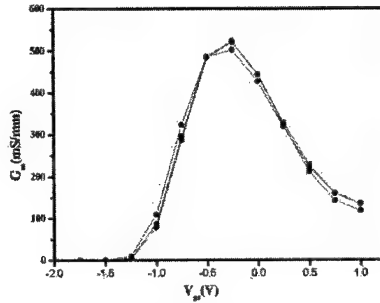
Fig. 7 Transconductance characteristics of PHEMT's.

The RF measurements were performed in a frequency range of 1.0 ~ 50 GHz. For this RF measurement, the drain and gate voltages of 1.5 V and –0.3 V were used, respectively.

At 50 GHz, a maximum stable gain (MSG) of 9.2 dB and a S_{21} gain 4.2 dB were obtained.

A current gain cut-off frequency (f_T) of 113 GHz and a maximum frequency (f_{max}) 180 GHz were achieved from the fabricated PHEMT's of 0.1 μm gate length. Fig. 8 shows a plot of S_{21} gain, the current gain H_{21}, G_{ms}(maximum stable gain), U(Unilateral power gain) versus the frequency. The f_T and f_{max} were calculated using the H_{21} and the G_{ms} values at 50 GHz by an extrapolation of -6 dB/octave.
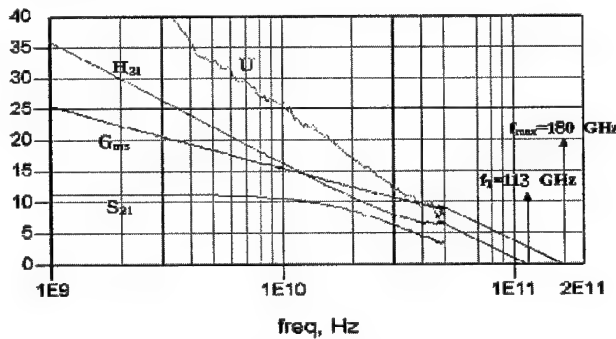
Fig. 8 RF characteristics of the fabricated PHEMT's.

CONCLUSIONS

We have fabricated the GaAs-based 0.1 μm Γ-gate PHEMT's for millimeter-waves. To fabricate the PHEMT's we carried out development of unit processes such as 0.1 μm Γ-gate lithography, gate recess, silicon nitride passivation and air-bridge process. f_{max} of 180 GHz, f_T of 113 GHz and good DC characteristics such as the pinch-off property ($V_p = -1V$) were achieved by applying an offset Γ-gate and recess technology using an electron beam lithography and the mixed etchant of 50 % citric acid solution/H_2O_2/H_2O (1 : 3 : 1) for PHEMT's grown by MBE.

ACKNOWLEDGEMENT

REFERENCE

1. J. Mikkonen, C. Corrado, C. Evci and M. Progler, *IEEE Communication Magazine*, Vol. 36, Issue 2, 112, (1998).
2. A. Chin, C. C. Liao and C. Tsai, IEEE *Electron Device Letters*, Vol. 18, No. 4, 157 (1997).
3. Y. C. Chen, R. Lai, E. Lin, H. Wang, T. Block, H. C. Yen, D. Streit, W. Jones, P. H. Liu, R. M. Dia, T. W. Huang, P. P. Huang and Kn. Stamper, *IEEE Microwave and Guided wave Letters*, Vol. 7, No. 5, 133 (1997).
4. Y. L. Kok, H. Wang, T.W. Huang, R. Lai, M. Barsky, Y.C Chen, M. Sholley, T. Block, D.C. Streit, B.R. Allen, L. Samoska and T. Gaier, *IEEE Microwave and Guided wave Letters*, Vol. 9, No. 8, 311 (1999).
5. T. Hongsmatip, F. Carrez and J. Fenton, *2000 IEEE MTT-S Digest*, Vol. 1, 357, (2000).
6. J. L. B. Walker, in *High-Power GaAs FET Amplifier*, (Artech House, 1993).
7. I. H. Lee, S. D. Lee and J. K. Rhee, *Journal of the Korean Physical Society*, Vol. 35, No. 12, S1043 (1999).

Electrically Tunable Phase Shifters With Air-Dielectric Sandwich Structure

Minki Jeong, Victor Kazmirenko[*], Yuriy Poplavko[*], Beomjin Kim, and Sunggi Baik
Department of Materials Science and Engineering, Pohang University of Science and Technology, Pohang, 790-784, South Korea
[*]Department of Microelectronics, National Technical University of Ukraine, Kiev, 03056, Ukraine

ABSTRACT

Electrically tunable microwave phase shifter was developed by inserting dielectric slab and piezoelectric actuator inside a waveguide. Air-dielectric sandwich structure of dielectric material and thin air gap was placed inside a waveguide, where the thickness of air gap is controlled by the actuator. Small changes in the ratio between the thickness of dielectric material and air gap induce significant changes in the effective dielectric constant of the air-dielectric sandwich structure. Phase shifts of 20~200 degrees were realized with the dielectric materials such as (Mg, Ca)TiO$_3$ while the thickness of air gap is changed between 0 to 30 μm by piezoelectric control. Since the dielectric ceramics has very small loss (tan$\delta \sim 10^{-4}$) and the air gap has practically no loss, the total structure shows low insertion loss.

INTRODUCTION

Microwave phase shifter is one of the essential components for modern microwave communication systems. One interesting application of the phase shifter is devoted to the phased array antenna, where the phase shifters located in one or two dimensional array with differential phase change provide fast steering of microwave signals. Commercial applications include global positioning system (GPS), car collision avoidance radar, aircraft surveillance radar and so on [1]. Development of electrically tunable phase shifters with low loss and low cost have been the key issue for determining the performance and cost of those microwave systems. Electrically tunable phase shifters using either ferrite or PIN diode have supported these microwave systems so far despite of severe disadvantages such as high cost and high insertion loss [2]. Moreover, they have fundamental frequency limitation of increasing loss in the millimeter-wave range where future communication systems may take place. Recently, ferroelectric phase shifters [3], micro-electro-mechanical systems (MEMS) phase shifters [4], and microstrip line phase shifters with piezoelectric control [5] have been studied, yet they are still far from practical applications.

We have developed a simple idea of realizing low loss phase shifter by combining well known conventional microwave dielectric ceramics and piezoelectric actuator [6]. As a high dielectric constant material is introduced inside a waveguide leaving a small air gap facing upper wall of the waveguide, the effective dielectric constant of the sandwich structure of dielectric material and air gap can be changed by controlling the thickness of air gap. Since the propagation constant of transmitting microwave changes as the effective dielectric constant of the sandwich structure changes, the structure can serve as a phase shifting element. We attached an electromechanical actuator in contact with dielectric material to control the air gap electrically in fast and accurate way.

THEORY AND EXPERIMENT

Let us consider a waveguide partially loaded with dielectric material as shown in figure 1. With this configuration, TE or TM modes cannot satisfy the boundary conditions any more. Rather the hybrid modes of them appear [7]. The propagation constant for the present configuration can be derived according to the equations,

$$\frac{\beta_{ya}}{\varepsilon_0} \tan(\beta_{ya}\Delta) + \frac{\beta_{yd}}{\varepsilon_d \varepsilon_0}(\beta_{yd}(b-\Delta)) = 0,$$

$$\beta_{ya} = \sqrt{\omega^2 \varepsilon_0 \mu_0 - \gamma^2 - \beta_x^2},$$

$$\beta_{yd} = \sqrt{\omega^2 \varepsilon_d \varepsilon_0 \mu_0 - \gamma^2 - \beta_x^2},$$

where β_{ya} is the transverse wave number in the air region, β_{yd} is the transverse wave number in the dielectric region, γ is the propagation constant, ε_d is the dielectric constant of dielectric material, Δ is the thickness of air gap, and b is the height of waveguide where dielectric material is placed. The solution can be obtained numerically. The effective dielectric constants of the air-dielectric sandwich structure for several different dielectric materials are shown in figure 2. The
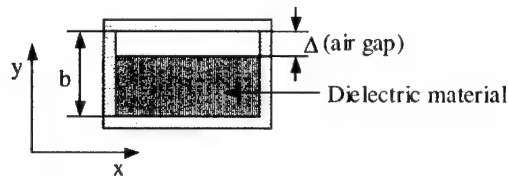
Figure 1. Cross section of the waveguide partially loaded with dielectric material.
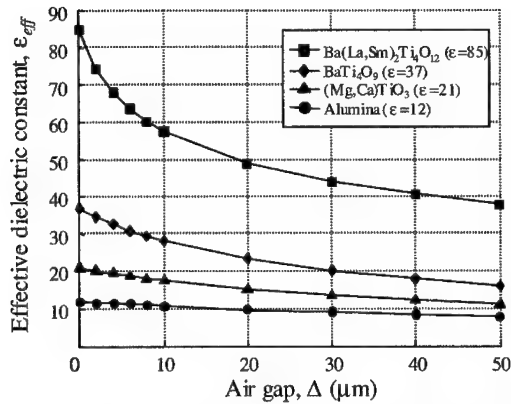
Figure 2. Effective dielectric constants of the air-dielectric sandwich structure for several different dielectric materials of 2 mm in the thickness.

effective dielectric constants decrease as the air gap is widened and such an effect is more significant for the materials with higher dielectric constants.

We devised a waveguide phase shifter in which the air-dielectric sandwich structure is constructed with a piezoelectric actuator to control the thickness of air gap electrically. As shown in figure 3, the air gap is controlled from 0 to 30 μm by applying voltage from 150 V down to –30V to the actuator. Scattering parameters were measured by HP 8510C Vector Network Analyzer. Simple matching sections with Teflon were provided before and after the dielectric materials to reduce reflection. The back side of the ceramic plate is covered by silver electrode, so the cavity where phase shift occurs is constructed.
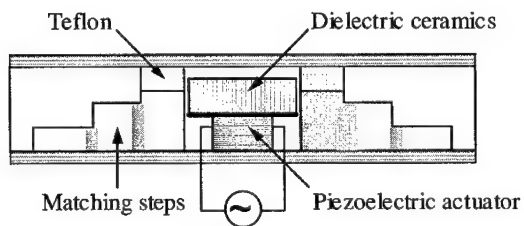
Figure 3. Side view of the waveguide loaded with an air-dielectric sandwich structure.

RESULTS

Experimental results of relative phase shift for the air-dielectric sandwich structure for different materials are shown in figure 4 and table I compares the results with the estimated values based on the results in figure 2. As the thickness of air gap is increased, noticeable phase change occurred depending on the dielectric materials. The effect of small air gap was more significant when the material with higher dielectric constant was used. Relative phase shift of 200 degrees was realized for $Ba(La,Sm)_2Ti_4O_{12}$ while 25 degrees for alumina. With a small variation in the thickness of air gap, materials with higher dielectric constant are preferred to induce large phase shift. However, it becomes difficult to match impedances for materials with very high dielectric constant, which results in severe reflection loss. Thus, there should be a compromise between high dielectric constant and ease of impedance matching.
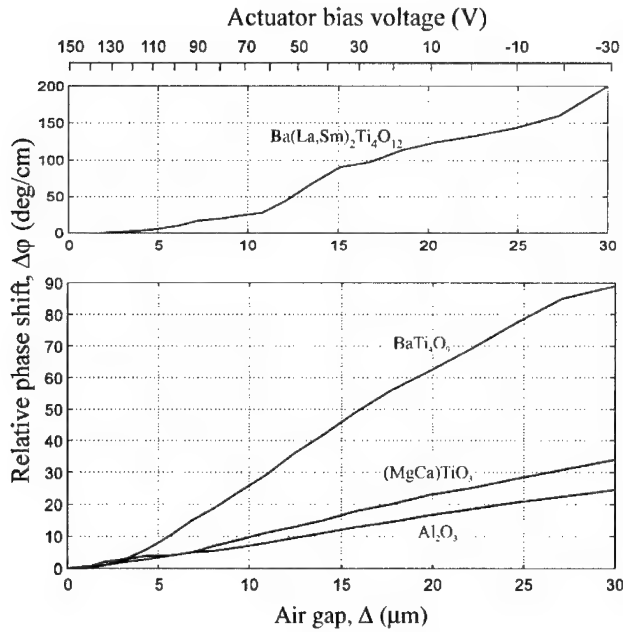
Figure 4. Relative phase shift for the air-dielectric sandwich structure with different dielectric materials measured at 10.5 GHz.

Table I. Comparison between the estimated phase shifts and the observed values with 10 mm dielectric slabs and 30 μm air gap.

Dielectrics	$\Delta\varphi$ expected (degree)	$\Delta\varphi$ observed (degree)
$Ba(La,Sm)_2Ti_4O_{12}$ ($\varepsilon = 85$)	311	200
$BaTi_4O_9$ ($\varepsilon = 37$)	83	89
$(Mg, Ca)TiO_3$ ($\varepsilon = 21$)	54	34
Alumina ($\varepsilon = 12$)	50	25

CONCLUSIONS

Electrically tunable microwave phase shifter was developed with the air-dielectric sandwich structure. We induced the phase shift by adjusting the thickness of air gap between waveguide wall and dielectric slab electrically by an electromechanical actuator inside a waveguide. It was possible to obtain 20~200 degrees of relative phase change depending on dielectric materials for the sample length of 10 mm. The present phase shifter seems to replace the conventional waveguide phase shifter with ferrite that is massive and expensive especially for phased array antennas. As we select the microwave ceramics with relatively low loss, it becomes possible to build low loss-phase shifters at the millimeter wave range, where commercial low loss phase shifters are non-existent.

ACKNOWLEDGEMENTS

REFERENCES

1. R. C. Hansen, in *Encyclopedia of Electrical and Electronics Engineering*, edited by J. G. Webster (John Wiley & Sons, New York, 1999) p. 685.
2. V. K. Varadan, K. A. Jose, V. V. Varadan, R. Hughes, and J. F. Kelly, *Microwave Journal*, **35** 116 (1992).
3. J. B. L. Rao, D. P. Patel, and V. Krichevsky, *IEEE Transactions on Antennas and Propagation*, **47** (3), 458 (1999).
4. N. Scott Barker and Gabriel M. Rebeiz, *IEEE Transactions on Microwave Theory and Techniques*, **46** (11), 1881 (1998).

5. T. –Y. Yun and K. Chang, *IEEE Microwave and Guided Wave Letters*, **10** (3), 96 (2000).

6. S. Baik, M. Jeong, B. Kim, Y. Poplavko, and Y. Prokopenko, Korea Patent pending No. 2001-0050515 (22 August 2001).

7. C. A. Balanis, *Advanced Engineering Electromagnetics*, (John Wiley & Sons, 1989), p. 394-409.

H3.13

Deposition of Polycrystalline ZnO Films by Two-Step Method and Characterization of Thermal Annealing Effects

Jin-Bock LEE, Myung-Ho LEE, Hye-Jung LEE, and Jin-Seok PARK
Department of Electrical Engineering, Hanyang University
1271 Sa 1-dong, Ansan, Kyonggi-do 425-791, South Korea

ABSTRACT

Polycrystalline ZnO thin films were deposited on $SiO_2/Si(100)$ substrate using RF magnetron sputtering. The film deposition performed in this work was composed of following two procedures; the 1st-deposition for 30 min without oxygen at 100 W and the 2nd-deposition with oxygen in the range $O_2/(Ar+O_2) = 10\sim50$ %. Deposited ZnO films revealed a strongly c-axis preferred-orientation (the corresponding texture coefficient ~ 100 %) as well as a high resistivity ($> 10^7$ Ωcm). It was also observed that the crystallite size of ZnO was noticeably increased by thermal-annealing.

INTRODUCTION

With the rapid progress of communication technology, there has been an increasing interest in developing thin-film band-pass filters, including surface acoustic wave (SAW) filters and film bulk acoustic resonators (FBARs) [1,2]. These devices require the thin films to have c-axis preferred orientation, excellent crystallinity, and high electrical resistivity. Polycrystalline ZnO has been considered as one of promising materials for such device applications. The sputtering method has widely been used to obtain the c-axis oriented ZnO film. Very often the impurities (Li, Cu, etc.) and/or the oxygen have been injected during deposition to increase the resistivity of ZnO [2-4]. However, it seems that there is a trade off between the c-axis preferred orientation and the electrical resistivity of ZnO.

In the present study a new deposition technique for improving both the c-axis preferred orientation and the resistivity of ZnO film is proposed. In addition, the effect of thermal-annealing on the ZnO film is also discussed.

EXPERIMENTAL DETAILS

ZnO films were deposited on SiO_2/Si substrate using RF magnetron sputtering. During deposition the substrate was rotated at a low speed of 5 rpm to enhance the thickness uniformity of deposited films. The deposition method proposed in this work consisted of the 1st-step deposition without addition of oxygen and the 2nd-step deposition with addition of oxygen in the range $O_2/(Ar+O_2) = 10\sim50$ %. In addition, thermal treatment on deposited ZnO films was performed with varying the temperature from RT to 800 °C. Details of deposition and thermal-annealing conditions are summarized in Table 1.

Texture coefficient (TC) values for c-axis (002)-orientation and crystallite sizes of ZnO films were evaluated from the XRD (X-ray diffractometer, Bede D3 system) spectra. I-V characteristics were measured to calculate the resistivity of ZnO, in the voltage range $0 \sim 1$ V

with 0.01 V-step by using a pico-ampere meter/DC voltage source (HP 4140B). Raman spectra (Jobin Yvon T64000) were also monitored for all ZnO films to identify the oxygen-deficiency in the film.

Table 1 Conditions for two-step deposition and thermal-annealing

	One-step method	Two-step method 1st-step	2nd-step	Thermal annealing	
$O_2/(Ar+O_2)$ [%]	10~50	0	10~50	Ann-temp [°C]	200, 400, 600, 800
RF power [W]	100	100	100		
Pressure [mTorr]	5	5	5	Ann-time [min]	120
Sub-temp [°C]	200	200	200		
Depo-time [min]	120	30	90	Ambient	Air

RESULTS AND DISCUSSION

Figure 1 (a) and (b) shows the XRD peak patterns measured from the ZnO films deposited by using the conventional one-step method and the proposed two-step method, respectively. In case of using the one-step deposition the (002)-orientation peak was relatively the most intense when the ZnO film was deposited without oxygen. However, as the amount of added oxygen was increased, the (002)-peak intensity was lessened and finally disappeared at $O_2/(Ar+O_2) = 50$ %. It seemed that oxygen neutrals were embedded in lattice sites or interstitials during the growth of films, which caused a strain and change in the lattice constant and orientation of film [5].
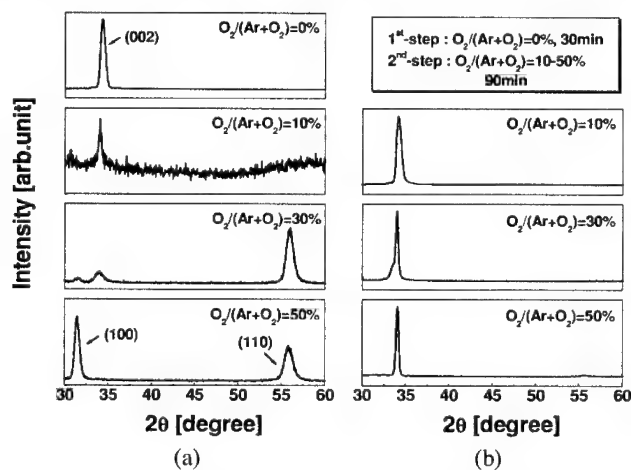
Figure 1. XRD peak patterns of deposited ZnO films; (a) films prepared by one-step deposition and (b) films prepared by two-step deposition, respectively

On the other hand, as shown in Figure 1 (b), the ZnO films deposited using the proposed method revealed a highly (002)-oriented growth nature, irrespective of $O_2/(Ar+O_2)$ ratio used in the 2nd-deposition step. It has generally been considered that the matching in the lattice parameter and crystal structure between the film and the substrate, on which the film is grown, may significantly affect the growth habit of the film [6]. It should be noted that in the 1st-deposition step of the proposed method the oxygen was not added. The 1st-deposited thin ZnO layer was expected to exhibit a highly (002)-oriented behavior and consequently act as a good substrate for the subsequently-grown 2nd-step ZnO film. This was believed to be one of important reasons why the ZnO films deposited using the two-step method revealed a (002)-preferred orientation with little affected by the oxygen.

The crystallite size estimated from the XRD results was depicted in Figure 2, as a function of $O_2/(Ar+O_2)$ ratio. When the same $O_2/(Ar+O_2)$ ratio was used, the crystallite size of ZnO films deposited by the two-step method was almost twice higher than that of films deposited by the one-step method. This was also attributed due to the reduction of mismatching between the film and the substrate, as already discussed in two-step deposition case. In addition, the crystallite size was observed to decrease with increasing $O_2/(Ar+O_2)$ ratio.
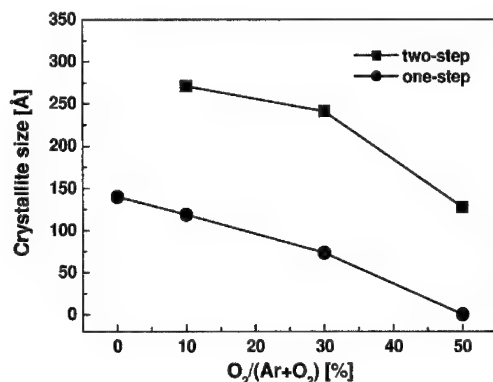
Figure 2. The crystallite size of ZnO films prepared by one-step (●) and two-step (■) method, respectively, as a function of $O_2/(Ar+O_2)$ ratio

Figure 3 shows the electrical resistivity measured for the ZnO films deposited by one-step and two-step method, along with the TC values for (002)-orientation estimated from the corresponding XRD peak patterns as shown in Figure 1. The film deposited using the one-step method without oxygen exhibited a low resistivity ($< 10^6$ Ωcm), while the TC value was almost 100 %. As the $O_2/(Ar+O_2)$ ratio increased, the resistivity rapidly increased, but the TC value significantly decreased. The similar trend regarding the effect of oxygen on the change of resistivity was also observed for the films deposited using the two-step method. However, it should be noted that the (002) TC value was not decreased and kept high, regardless of $O_2/(Ar+O_2)$ ratio. At a typical ratio of $O_2/(Ar+O_2) = 50$ %, the ZnO film deposited using the two-step method showed the resistivity as high as about 2.5×10^9 Ωcm and at the same time revealed a high TC value of about 100 %.
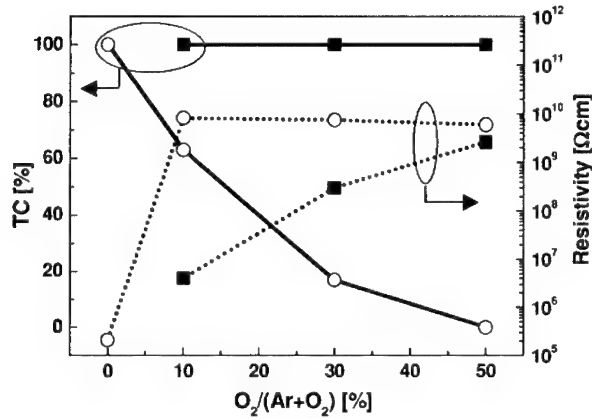
Figure 3. The changes of (002) TC value and resistivity of ZnO films, as a function of $O_2/(Ar+O_2)$ ratio (O: one-step deposition, ■: two-step deposition)

Figure 4 shows the Raman spectra of ZnO films deposited by one-step and two-step methods. It has been known that the peak at 430 cm^{-1} originates from E_2 mode of ZnO associated with wurtzite structure and the peak at 570 cm^{-1} is a contribution of $E_1(LO)$ mode of ZnO associated with oxygen deficiency [7,8]. At the $O_2/(Ar+O_2)$ ratio of 10 % (see Figure 4 (a)), the peak at 430 cm^{-1} was observed to be dominant for all the films. On the other hand, at the $O_2/(Ar+O_2)$ ratio of 50 % (see Figure 4 (b)) the peak at 430 cm^{-1} weaken for both films, but the peak at 570 cm^{-1} emerged very intense, especially for the film deposited by two-step. This indicated that a considerable amount of oxygen-vacancies were present in the ZnO film deposited by two-step.
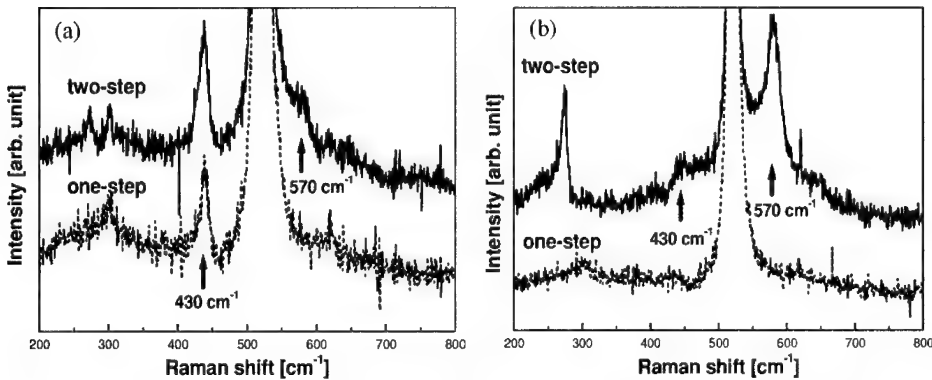
Figure 4. Raman spectra of ZnO films deposited using the one-step and two-step method : (a) $O_2/(Ar+O_2)$ = 10 % and (b) $O_2/(Ar+O_2)$ = 50 %, respectively

Thermal annealing on the deposited ZnO films was performed in air at 200 °C ~ 800 °C for 120 min. The changes of crystallite size and resistivity were measured as a function of annealing temperature. As shown in Figure 5 (a) and (b), with increasing the annealing temperature the crystallite size monotonically increased and the resistivity significantly decreased. This was ascribed due to the enhanced carrier mobility which was resulted from the reduction of grain boundary defects [9,10]. It may also be noted that the change in the crystallite size and resistivity was larger for the film deposited at $O_2/(Ar+O_2) = 10$ % by using the two-step method, compared with the other films. This was explained by analyzing the Raman spectra obtained from those films. Figure 6 indicated that for the two-step deposited films the peak related to the oxygen-vacancy (at 570 cm^{-1}) noticeably decreased as the annealing temperature increased, while it rarely changed for the one-step deposited films. It was previously reported that the oxygen deficiency could be reduced by thermal annealing because some of oxygen atoms in air were combined with atomic Zinc in the ZnO film [11]. In addition, the (002) TC values of ZnO films were observed to be scarcely changed after thermal annealing.
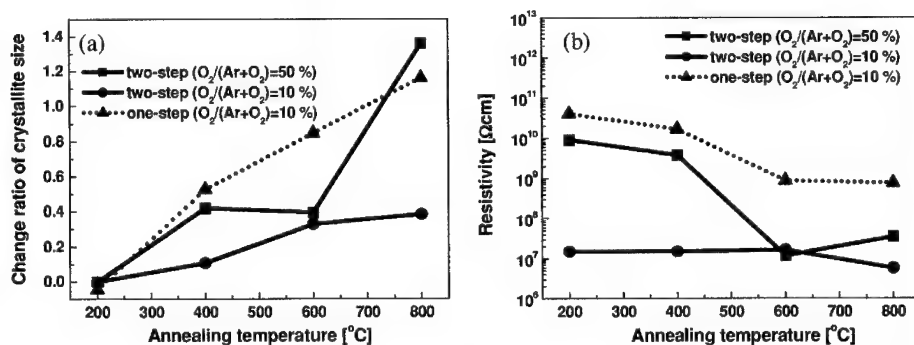
Figure 5. Effects of thermal annealing on the change of (a) crystallite size and (b) resistivity of ZnO films deposited by one-step and two-step methods
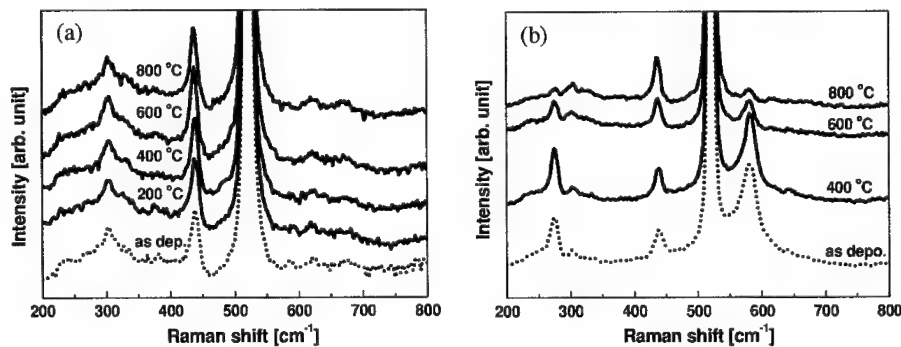
Figure 6. Effects of thermal annealing on the Raman spectra of ZnO films deposited by (a) one-step method and (b) two-step method

CONCLUSIONS

It was shown from this work that a highly resistive (> 10^9 Ωcm) and (002)-oriented (TC ~ 100 %) polycrystalline ZnO film could be achieved by using the proposed two-step deposition method. XRD peak patterns showed that, in contrast to the films deposited through the conventional one-step process, the films prepared using the two-step deposition method were grown along the (002) preferred-orientation even at a high $O_2/(Ar+O_2)$ ratio. It was also found from Raman spectra that the variations of crystallite size and electrical resistivity due to thermal annealing were closely related to the enhancement of crystallinity of ZnO films.

ACKNOWLEDGMENTS

REFERENCES

1. S.H.Park, B.C.Seo, and G.W.Yoon, *J. Vac. Sci. Technol.A* **18(5)**, 2432 (2000).

2. Y.Yoshino, T.Makino, Y.Katayama, and T.Hata, *Vacuum* **59**, 538 (2000).

3. M.Wu, W.Shih, and W.Tsai, *J. Phys. D:Appl. Phys.* **31**, 943, (1998).

4. J.B.Lee, H.J.Lee, S.H.Seo, and J.S.Park, *Thin Solid Films* **398-399**, 641 (2001)

5. S.Srivastav, CVR.V.Kumar, and A.Mansingh, *J. Phys. D:Appl. Phys.* **22**, 1768 (1989).

6. W.T.Lim, B.K.Son, D.H.Kang, and C.H.Lee, *Thin Solid Films* **382**, 56 (2001).

7. X.L.Xu, S.P.Lau, J.S.Chen, and B.K.Tay, *J. Crystal Growth* **223**, 201 (2001).

8. G.J.Exarhos and S.K.Sharma, *Thin Solid Films* **270**, 27 (1995).

9. N. Fujimura, T.Nishihara, S.Goto, J.Xu, and T.Ito, *J. Crystal Growth* **130**, 269 (1993).

10. H.Nanto, T.Minami, S.Shooji, and S.Takata, *J. Appl. Phys.* **55(4)**, 1029 (1983)

11. J.Yin, Z.G.Liu, H.Liu, X.S.Wang, T.Zhu, and J.M.Liu, *J. Crystal Growth* **220**, 281 (2000).

On the GHz Frequency Response in Nanocrystalline FeXN Ultra-Soft Magnetic Films

N.G. Chechenin, C.B. Craus, A.R. Chezan, T. Vystavel, D.O. Boerma, J.Th. M. De Hosson and L. Niesen
Materials Science Centre, University of Groningen, Nijenborgh 4, NL-9747 AG Groningen, The Netherlands

ABSTRACT

The periodicity and angular spread of the in-plane magnetization for ultrasoft nanocrystalline FeZrN films were estimated from an analysis of the ripple structure, observed in Lorentz transmission electron microscopy (LTEM) images. The influence of the micromagnetic ripple on the ferromagnetic resonance (FMR) width is analyzed using an approach based on the Landau-Lifshitz equation. A strong dependence of the resonance width on the magnetic moment dispersion is predicted. To a large extent this particular aspect explains the high frequency response in some of our films.

INTRODUCTION

Nanocrystalline FeXN films proved to exibit excellent ultrasoft magnetic properties with a saturation magnetization up to or above $4\pi M \approx 15$ kG and a high magnetic susceptibility in the frequency range around and above 1 GHz [1-4]. The influence of the grain size, D, on the dc-magnetism has been analyzed in Hoffman's and Herzer's papers ([5,6] and ref. therein). A grain size much smaller than the size of the coupling volume is necessary to average out the magnetocrystalline anisotropy. The residual magnetocrystalline anisotropy, proportional to $D^{3/2}$, causes a stray field predominantly oriented along the easy axis and an angular spread of the magnetization, which is observed as a ripple structure in LTEM [7,8]. The amplitude of the angular spread β_0, which is a measure of the stray field, was obtained from an analysis of the LTEM ripples for the films deposited and post-treated under various conditions. The range of operating frequencies for these films is limited by the frequency and by the width of the FMR. Besides contributions to the FMR width due to dissipation sources, which are characteristic for crystalline and polycrystalline ferromagnetic films, an additional contribution exists in nanocrystalline films due tothe local variation of the magnetization. Despite of its importance, so far only few publications have addressed this problem.

Here we discuss the effect of the micromagnetic ripples on the FMR response, using an approach based on the Landau-Lifshitz equation where the effective field includes the internal stray field. We predict a strong dependence of the resonance width on the magnetic moment dispersion and show that the internal stray field can be a major cause of broadening of the FMR.

SAMPLE PREPARATION

Fe-Zr-N films were prepared by dc magnetron reactive sputtering. Films with a thickness between 50 and 1000 nm were deposited at several temperatures between room temperature and 200 ºC. The films were grown in a nanocrystalline structural state on glass or silicon substrates. Polymer or Cu underlayers were used to be able to float the film on a grid for TEM investigation. The deposition conditions were chosen to obtain a composition $(Fe_{99}Zr_1)_{1-x}N_x$, where the concentration of nitrogen was in the range $x \leq 25$ at%. An 800 Oe magnetic field was applied in the plane of the samples during deposition. More details on the film deposition can be found in [9]. X-ray diffraction (XRD), as well as conventional TEM and selected area diffraction (SAD), reveal a 2-30 nm size of crystallites for most of the investigated sputter-deposited films, see, for example, Fig.1a.

LTEM ANALYSIS

The LTEM image in Figs. 1b, shows a ripple pattern, strongly dependent on the microstructure. For grain sizes of 10-50 nm and smooth, flat surfaces, the ripples are almost parallel (Fig.1a,b), while for films with a large roughness, grain size, porosity or other type of large size (>1µm) defects, the LTEM ripples start branching (Fig.1c,d) or form a disordered structure.
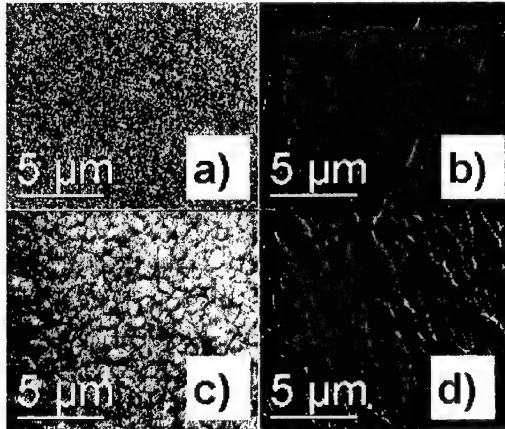
Figure 1. The ripples for two films with different microstructure.

It was noted [7] that, due to exchange interactions, longitudinal oscillations of the transversal component of the magnetization $\Delta M_y(x)$ are energetically more favorable than the transversal oscillations $\Delta M_y(y)$. Here the xy-plane is assumed to be parallel to the film surface and the x-axis parallel to the easy axis (EA). Approximating the oscillation by a single period harmonic function:

$$\Delta M_y(x) = M\beta_0 sin(2\pi x/\lambda), \tag{1}$$

one can relate, using the theory of electron diffraction, the contrast of the LTEM picture, C_x, with the periodicity, λ_x (in nm), of the ripples, with the deviation angle, β_0 (in degrees), of the local magnetization from the mean direction [10]

$$C_x = [Ix(0) - Ix(\lambda_x/2)]/Ix(\lambda_x/4) = = (4\pi M \beta_0 t \lambda_x/2\Phi_0) sin[\Delta z \lambda_0/(2\pi\lambda_x^2)], \qquad (2)$$

where $Ix(0)$, $Ix(\lambda_x/2)$ and $Ix(\lambda_x/4)$ are the image intensities in the maximum, in the minimum and in the middle point of the ripples, respectively, t is the thickness of the film (in nm), $\Phi_0 = h/2e$ is the flux quantum, Δz is the defocus distance in the microscope and λ_0 is the electron wavelength ($\lambda_0 = 2.5$ pm for the 200 keV- electrons). For maximum contrast one can obtain the relation, which has been used before [11]:

$$\beta_0 \approx 0.59\times10^5 C/(4\pi M t \lambda). \qquad (3)$$

The periodicity in our films varies in a wide range from 200 nm to 2 μm, depending on the micro(magnetic) structure of the film. The uncertainty in the experimental values of λ and C was about ±20% and was due to a large variation in the distance between ripples, meaning that the ripples are not strictly periodic. Applying this analysis to different films, we obtained for β_0 values between 0.3^0 and 2.0^0. The β_0 values are $0.8^0 \pm 0.2^0$ and $1.5^0 \pm 0.3^0$ for the films shown in Fig.1a and 1c, respectively.

RF AND DC FIELD MEASUREMENTS
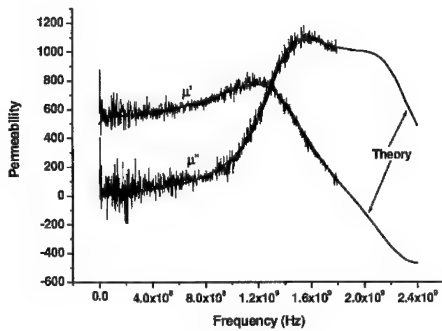
Figure 2. Frequency dependences $\mu'(f)$ and $\mu''(f)$. Experimental curves are fitted using (14) and (15) averaged over the period of the stray-field oscillations.

The technique for high frequency measurements was similar to that in [12]. The frequency dependences of the real, μ', and imaginary, μ'', parts of the permeability, plotted in Fig.2, correspond to the same sample as in Figs. 1a,b, i.e. for the sample with a polymer underlayer. The spectra were obtained in the absence of a dc-field and with the rf-field perpendicular to the easy direction (EA). The sample does not show the best RF properties we obtained, but allows a fair comparison between LTEM and RF data. The observation limit of the frequency response was $f = \omega/2\pi \approx 1.8$ GHz, which is lower than the resonance frequency $f_{00} = 1.9$ GHz, determined by zero-crossing of μ'. The $\mu''(f)$ dependence shows a bump at 1.6 GHz, i.e. at a significantly lower value than f_{00}.

THEORY

Let the local EA be at an angle β with the x-axis. The magnetization M is at an angle ϕ with the x-axis, at θ with the surface normal (z-axis) or at $\psi = 90^0 - \theta$ with the film surface. H_{dc} is the magnitude of the dc-magnetic field applied along the x-axis, H_{rf} is the high frequency the field applied along the hard axis direction. The Landau-Lifshiz equation reads:

$$dM/dt = \gamma M \times (-\nabla E) - (\alpha \gamma/M) M \times [M \times (-\nabla E)], \tag{4}$$

where α is a damping coefficient, γ is the gyromagnetic ratio, $-\nabla E$ is the generalized force. For the free energy we have

$$E = K \sin^2(\phi - \beta) - M [H_{dc} \cos\psi\cos\phi + H_{str}\cos\psi\cos(\phi - \phi_0) + H_{rf} M \cos\psi\sin\phi - (1/2)N_z M \sin^2\psi], \tag{5}$$

where K is the anisotropy constant, $N_z = 4\pi$ is the demagnetizing factor and ϕ_0 defines the local direction of M, when only dc-field is applied. For a single-harmonic longitudinal oscillation of magnetization vector, Eq. (1), one can obtain for the stray field

$$H_{str,x} = - \pi M_0 \beta_{10}^2 \cos(4\pi x/\lambda), \tag{6}$$

Assuming $\alpha, \phi, \phi_0, \beta, \psi \ll 1$, $H_{str}, H_{dc}, H_k = 2K/M \ll M$, and $H_{rf} \ll H_{str}, H_{dc}, H_k$ one can obtain a linear differential equation:

$$d^2\phi/dt^2 + \alpha\gamma 2N_z M(d\phi/dt) + \omega_0^2\phi + \gamma^2\beta H_k = = (\gamma^2 N_z M + i\alpha\gamma\omega)H_{rf}, \tag{7}$$

where $\omega_0^2 = \gamma^2 N_z M(H_{eff} + H_{str})$ with $H_{eff} = H_{dc} + H_k$ $\quad$ (8)

If $H_{rf} = h_{rf} \exp(i\omega t)$, then a solution can be found in the form of

$$\phi = \phi_0 + \phi_1 \exp(i\omega t + i\delta), \tag{9}$$

Substituting $\phi(t)$ into the differential equation (7) gives

$$\phi_0 = \beta H_k/H_{eff},$$
$$\phi_1 = \gamma^2 h_{rf} N_z M /[(\omega_0^2 - \omega^2)^2 + (\alpha\gamma\omega N_z M)^2]^{1/2}, \tag{10}$$
$$tg\delta = \alpha\gamma\omega N_z M /(\omega_0^2 - \omega^2).$$

When the dc-field is perpendicular and the rf field parallel to the EA similar expressions can be obtained. This case can be easily treated when $H_{dc} >> Hk$ and the angle ϕ is close to $\pi/2$, so $\eta = \pi/2 - \phi \ll 1$, for which the differential equation (7) is valid with $H_{eff} = H_{dc} - H_k$ in Eq. (8).

Note, that the local variation of the resonance frequency ω_0 in (8) can be large if the magnitude of the stray field is comparable with the anisotropy and dc fields. Within the approximations made, we can write

$$\omega_0^2 = \gamma^2 N_z M (H_{dc} + H_{str} \pm H_k),$$ (11)

where + and − correspond to dc-field parallel and perpendicular to the EA, respectively. When the amplitude of the local variation of the stray field does not exceed the effective field $H_{eff} = H_{dc} \pm H_k$ then the broadening of the FMR width due to the stray field can be estimated roughly as

$$<\Delta\omega_0^2> = \gamma^2 N_z M <H_{str}^2>^{1/2} = \pi\gamma^2 N_z M^2 \beta_0^2 /(2)^{1/2}$$ (12)

Eq. (12) can only be used for a rough evaluation and the average HF-response from the whole sample must be taken into account for a more quantitative analysis. For the magnetic permeability we can write

$$\mu = 4\pi M (\phi - \phi_0)/H_{rf} + 1 = 4\pi M \phi_1 exp(i\delta)/h_{rf} + 1$$ (13)

So, for the real and imaginary parts of the local permeability one obtains:

$$\mu' = \frac{4\pi\dfrac{M}{H_{eff}}[1+\dfrac{H_{str}}{H_{eff}}-(\dfrac{\omega}{\omega_{00}})^2]}{[1+\dfrac{H_{str}}{H_{eff}}-(\dfrac{\omega}{\omega_{00}})^2]^2 +\alpha^2(\dfrac{\omega}{\omega_{00}})^2\dfrac{N_z M}{H_{eff}}}$$ (14)

$$\mu'' = \frac{4\pi\alpha(\dfrac{\omega}{\omega_{00}})(N_z)^{1/2}(\dfrac{M}{H_{eff}})^{3/2}}{[1+\dfrac{H_{str}}{H_{eff}}-(\dfrac{\omega}{\omega_{00}})^2]^2 +\alpha^2(\dfrac{\omega}{\omega_{00}})^2\dfrac{N_z M}{H_{eff}}}$$ (15)

where $\omega_{00} = \gamma[N_z M H_{eff}]^{1/2}$ is the resonance frequency when the stray field is absent and H_{str} varies from place to place , according to (6). The average of the permeability over the film volume is obtained by numerical integration.

The averaged theoretical dependencies $\mu'(f/f_{00})$ and $\mu''(f/f_{00})$ with $f_{00}= 1.9$ GHz are fitted to the experimental data in Fig.2, with $H_{dc}=0$ and $H_k = 18$ Oe as obtained from dc-measurements. An almost perfect fit was obtained with only slightly different parameters for the μ' ($\alpha=0.016$, $\beta_0=2.4^0$, $4\pi M = 14$ kG) and for μ'' ($\alpha=0.011$, $\beta_0=2.4^0$, $4\pi M= 14$ kG). An increase of the α in the fitted expression depresses the bump in $\mu'(f)$, while a decrease of the β_0-value leads to a too sharp $\mu''(f)$ and to a shift of both, μ' and μ'' to a higher frequency region. It is important to note that the model perfectly reproduces the asymmetric shape of the $\mu''(f)$ with a maximum below the f_{00}-value.

However, in order to reproduce the f_{00}-value, the anisotropy field has to be assumed somewhat higher than it follows from dc-measurements. In the example discussed above this difference is about $H_i\approx 10$ Oe, assuming $H_{eff} = H_k + H_i$. In other cases the difference is small. A similar extra field was necessary to postulate to describe observations in [13]. The value $\beta_0=2.4^0$, obtained above is about 3 times higher than the value, obtained from LTEM patterns. The origin of the

increase of the anisotropy field and the large angle of the oscillation of the magnetization is not clear at this moment. We suppose that both items point to a more complex magnetic response of the spin system in the GHz-region, than was assumed in the theory. The dynamical response is more complicated for films, which have a stronger static ripple structure. In spite of this, the shape of $\mu'(f)$ and $\mu''(f)$ are well described because the theory operates with the reduced frequencies (f/f_{00}), reduced magnetization, M/H_{eff}, and reduced stray field H_{str}/H_{eff}, as follows from (14) and (15).

CONCLUSIONS

From the LTEM data, we obtained a large variation of the periodicity and dispersion angle of the micromagnetic ripple for films deposited on different substrates and under different conditions. A large dispersion angle correlates with a large FMR width in high frequency scans. These observations are in a good correspondence with the theoretical analysis, which shows a large effect of the internal stray field in nanocrystalline soft magnetic films on the FMR response.

ACKNOWLEDGMENTS

REFERENCES

1. B. Viala, M.K. Minor, J.A. Barnard, *J. Appl. Phys,* **80** (1996) 3941
2. H.Y. Wang, E.Y. Yang, H.L. Bai, P. Wu, Y.Wang, F.F. Gong, *J. Phys.: Condens. Matter.* **9** (1997) 8443
3. S. Jin, W. Zhu, T.H. Tiefel, V. Korenivski, R.B. van Dover, and L.H. Chen, *J. Appl. Phys.,* **81** (1997) 4042
4. O. Shimizu, K. Nakanishi, S. Yoshida, *J. Appl. Phys.* **70** (1991) 6244
5. H. Hoffmann, *Thin Solid Films,* **58** (1979) 223
6. G. Herzer, *Scripta Metallurg. Materialia,* **33** (1995) 1741
7. H.W. Fuller and M. E. Hale, *J. Appl. Phys.,* **31**, (1960) 238, *ibid,* 31 (1960) 1699
8. D. Wohlleben, *J. Appl. Phys.* **38** (1967) 3341
9. A.R. Chezan , C.B. Craus, N.G. Chechenin, L. Niesen, and D. O. Boerma, *Physica Status Solidi (a),* **189** (2002) 833
10. N.G. Chechenin et al, to be published
11. N.G. Chechenin, A.R. Chezan, C.B. Craus, T. Vystavel, D. O. Boerma, J.Th.M.De Hosson and L. Niesen, *J. Magn. Magn. Mater.,* **239** (2002) p. 180
12. V. Korenivski, R.B. van Dover, P.M. Mankiewich, Z.-X Ma, A.J. Becker, P.A. Polakos, and V.J. Fratello, *IEEE Trans. Magn.* **32** (1996) 4905
13. D. Spenato, A. Fessant, J. Gieraltowski, H. Le Gall, and C. Tannous, *J. Appl. Phys.,* **85** (1999) 6010

BST Film Characterization

A Statistical Analysis of Laser Ablated $Ba_{0.50}Sr_{0.50}TiO_3$ /$LaAlO_3$ Films for Microwave Applications

R.R. Romanofsky*, N.C. Varaljay*, S.A. Alterovitz*, F.A. Miranda*, C.M. Mueller**,F.W. VanKeuls***, J. Kim****, and K.S. Harshavardhan****
*NASA Glenn Research Center, Cleveland, OH 44135
**Hadron, Inc. Cleveland, OH 44135
***Ohio Aerospace Institute, Brookpark, OH 44142
****Neocera, Inc., Beltsville, MD 20705

ABSTRACT

The NASA Glenn Research Center is constructing a 616 element scanning phased array antenna using thin film $Ba_xSr_{1-x}TiO_3$ based phase shifters. A critical milestone is the production of 616 identical phase shifters at 19 GHz with $\approx$4 dB insertion loss and at least $337.5°$ phase shift with 3 percent bandwidth. It is well known that there is a direct relationship between dielectric tuning and loss due to the Kramers-Kronig relationship and that film crystallinity and strain, affected by the substrate template, play an important role. $Ba_{0.50}Sr_{0.50}TiO_3$ films, nominally 400 nm thick, were deposited on 48 0.25 mm thick, 5 cm diameter $LaAlO_3$ wafers. Although previous results suggested that Mn-doped films on MgO were intrinsically superior in terms of phase shift per unit loss, for this application phase shift per unit length was more important. The composition was selected as a compromise between tuning and loss for room temperature operation (e.g. crystallinity progressively degrades for Ba concentrations in excess of 30 percent). As a prelude to fabricating the array, it was necessary to process, screen, and inventory a large number of samples. Variable angle ellipsometry was used to characterize refractive index and film thickness across each wafer. Microstructural properties of the thin films were characterized using high resolution X-ray diffractometry. Finally, prototype phase shifters and resonators were patterned on each wafer and RF probed to measure tuning as a function of dc bias voltage as well as peak (0 field) permittivity and unloaded Q. The relationship among film quality and uniformity and performance is analyzed. This work presents the first statistically relevant study of film quality and microwave performance and represents a milestone towards commercialization of thin ferroelectric films for microwave applications.

INTRODUCTION

Scanning phased array antennas could offer a highly desirable solution for futuristic near Earth and deep space science mission scenarios. For example the Laser Interferometer Space Antenna will consist of three spacecraft flying 5 million km apart in the shape of an equilateral triangle. The formation flying spacecraft will form a giant Michelson interferometer, measuring the distortion of space caused by passing gravitational waves. The antenna needs to measure the distance between proof masses separated by 5 million km with an accuracy of 20 picometers. Hence mechanically induced vibrations from gimbaled parabolic communications system antennas are unacceptable. While other solutions exist an affordable and efficient phased array would be preferred. Numerous applications for phased arrays exist for low Earth orbiting (LEO) scientific and commercial spacecraft. And a suitable scanning phased array technology is also being sought for

high data rate LEO-to-ground communications, automotive radar, and other remotes sensing and industrial applications.

The current state-of-practice in scanning phased arrays is represented by GaAs monolithic microwave integrated circuit (MMIC) technology or ferrite phase shifters[1,2]. Cost and weight are still significant problems. Moreover, conventional manifold fed arrays suffer from beam-forming loss that places considerable burden on MMIC amplifiers. The inefficiency can result in severe thermal management problems. A ferroelectric reflectarray antenna that overcomes these limitations is being assembled at the NASA Glenn Research Center [3]. The enabling component of the array is a low loss thin film $Ba_{0.50}Sr_{0.50}TiO_3$ coupled microstrip phase shifter. While we have demonstrated good performance from these devices ($\approx 60°/dB$) it was not known if a sufficient quantity of high quality and uniform films could be produced economically. And, the correlation among film thickness, crystallinity and microwave performance was still under investigation.

In this work we examine a batch of 48 $Ba_{0.50}Sr_{0.50}TiO_3$ on $LaAlO_3$ wafers in terms of film uniformity, microstructure and microwave performance. Variable angle ellipsometry was used to characterize refractive index and film thickness across each wafer. Microstructural properties of the thin films were characterized using high resolution X-ray diffractometry. Finally, prototype phase shifters and resonators were patterned on each wafer and RF probed to measure tuning as a function of dc bias voltage as well as peak (0 field) permittivity and unloaded Q

FILM PREPARATION

A set of film specifications was targeted based on our prior experience with various devices and material from different vendors. All $(Ba_{0.60}Sr_{0.40})TiO_3$ films were to be deposited on 5 cm diameter, 0.25 mm thick single-crystal $LaAlO_3$ substrates. The nominal film uniformity sought was a film thickness of 400 nm ± 40 nm at any point on the wafer except the 2 mm diameter ring at the edge of the wafer. The desired crystalline quality was a full-width, half-maximum value of the (002) peak < 0.12° (432 arc seconds) and the full-width, half-maximum values of the (103) peak <0.20° (720 arc seconds) with a concomitant peak intensity (002) > 4500 counts per second. The expected lattice parameters were a cubic unit cell, where the difference between $a_{<100>}$ and $a_{<001>}$ was less than 0.01 Å. Ideally, both $a_{<100>}$ and $a_{<001>}$ would not deviate by more than 0.03 Å from the bulk lattice parameters for $Ba_{0.5}Sr_{0.5}TiO_3$. Admittedly, these were ambitious goals

The films were deposited at Neocera, Inc. by Pulsed Laser Deposition (PLD). A Lambda-Physik Kr-F excimer laser operating at 248 nm was used. The laser energy density at the target during film deposition was $3J/cm^2$. The deposition temperature was 800 C. The oxygen partial pressure during film deposition was 300 mTorr. After film deposition the chamber was back filled with 500 Torr of oxygen and the substrates were cooled to room temperature. To obtain uniform film thickness the substrates were mounted on a rotating substrate stage. This special substrate holder facilitates the substrate rotation about their axes as well as about the axis of the stage, executing a planetary rotation. To maximize the thickness uniformity the laser beam is also raster scanned over the target surface using a laser beam scanner. The beam scanner is computer controlled to facilitate a uniform deposition rate over the substrate area. The films were delivered in two batches of 24 each.

ELLIPSOMETRIC ANALYSIS

Experimental Procedure

Ellipsometric measurements were taken on a "J. A. Woollam Co., Inc." spectroscopic ellipsometer model M-2000L at an angle of incidence of 65º at 800 wavelengths in the range 2450-9000Å. Each wafer was measured in the center, 0.5" and 0.75" off center. In some cases, several measurements were done at almost the same spot, to obtain a lower "depolarization" factor. In this study an unusual problem was encountered and it was due to the twins in the LaAlO$_3$ substrates. These twins were scattering part of the incoming light in a non-specular way, thus breaking a main ellipsometry assumption. The fraction of the light which was lost is a measurable quantity and is called the "depolarization" factor. In the present study, non-zero "depolarization" factors were measured for all samples which affected Ψ and Δ experimental results. This could cause increased values for mean square error (MSE) and errors in the value of the sample parameters. A detailed explanation follows.

An example of a large "depolarization" factor experiment is shown in Fig. 1. Adjacent spots on wafer #37, 0.5" off center were measured at an angle of incidence of 65º and gave the "depolarization" factors shown in the figure. The large "depolarization" measurement probably was done with the light being reflected from a spot that included a large twin boundary. Fig. 2 depicts the experimental ψ vs. λ graph showing a large effect of the "depolarization" on the ψ (and Δ) results. As a result of this, the final values obtained in the least squares fit for the sample parameters were also affected, especially keeping in mind the parameters correlations problem (see below). For example, a layer thickness difference of 200Å (out of 3600Å) between the two spots was obtained in the fits, even though such a difference is essentially impossible.
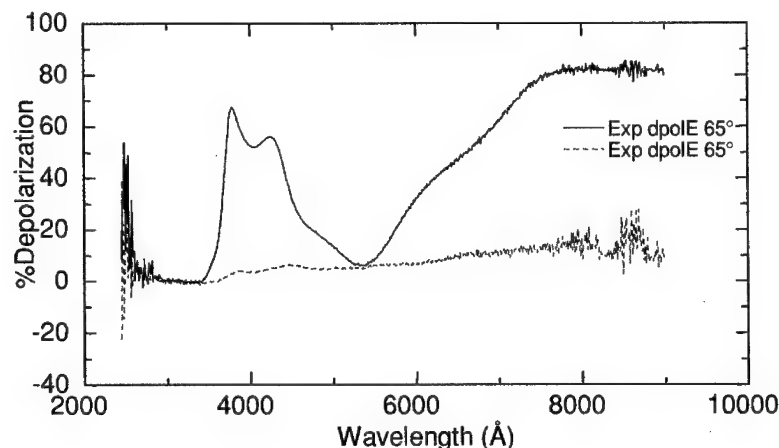
Fig. 1. Experimental "depolarization" factor vs. the wavelength λ for two adjacent spots on wafer #37, 0.5" off center. An ideal sample has a vanishing "depolarization" factor.
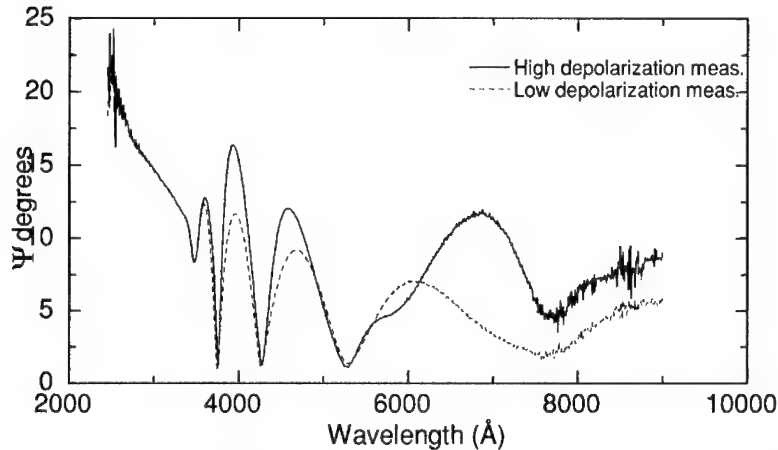
Fig. 2. Experimental ψ vs. the wavelength λ for two adjacent spots showing the "depolarization" effects on other ellipsometric parameters. (Wafer #37, 0.5" off center)

An empirical rule was found which states that least squares fits with 4 variables having MSE below 25 were considered to have good confidence, while fits with MSE above 40 were considered unreliable. However, no exact estimate of the errors was possible. In the case of wafer #37, 0.5" off center, the MSE values were 11 and 76 for the low and high "depolarization" measurements respectively. The substrate dielectric function was measured on a blank $LaAlO_3$ wafer. A "standard" $Ba_xSr_{1-x}TiO_3$ dielectric function was also measured and presented at the Spring 2000 MRS [5]. The mixtures are all calculated using the EMA (Bruggeman Effective Medium Approximation) method. The variables in the least squares fit are: film and surface overlayer thicknesses and void fractions in the film itself and in the overlayer. The λ range of the fits was over the entire 245-900 nm experimental wavelength range. The model includes the $LaAlO_3$ substrate, the ferroeletcirc film and a top roughness layer. The film is assumed to be made of good quality $Ba_xSr_{1-x}TiO_3$, which is simulated as a mixture of $Ba_xSr_{1-x}TiO_3$ similar to that made by NREL using PLD on MgO and voids [4]. The larger the void fraction, the lower is the refractive index of the present film as compared to the NREL film. Lower refractive index is associated with lower quality material when comparing films in the tables. The roughness layer is again a mixture, this time of the film material and variable void fraction. In some cases, a constant value of 18% voids for the overlayer was chosen, as it does fit most of the films, and makes the comparison among wafers more standard.

Results

The full result for wafer #37, 0.5" off center (as an example) was:MSE=11.29, Layer #1 thickness 3616.8 Å, Layer #1 composition 5.05 % void by volume, Layer #2 (overlayer) thickness 106.4 Å, Layer #2 (overlayer) composition 16.8 % void by volume. The quality of the fits obtained after the least squares minimization can be seen in Fig. 3.

Fig. 3. Comparison of the experimental and the model calculated ψ and Δ vs. the wavelength λ, for the low polarization spot. (wafer # 37, 0.5" off center)

For comparison, the high "depolarization" spot in the same general area gave the following results: MSE=76.46, Layer #1 thickness 3422 Å, Layer #1 composition -2.42 % void by volume, Layer #2 (overlayer) thickness 138.1 Å, Layer #2 (overlayer) composition 18.3 % void by volume. The result above shows that the sample parameters are quite different from the low "depolarization" spot. The quality of the fits obtained after the least squares minimization in this case can be seen in Fig. 4, and it shows a much poorer fit than in Fig. 3.
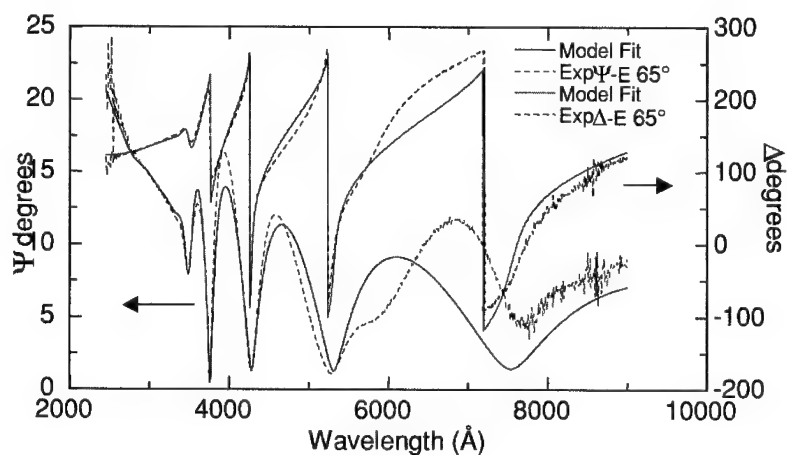
Fig. 4. Comparison of the experimental and the model calculated ψ and Δ vs. the wavelength λ, for the high polarization spot. (wafer # 37, 0.5" off center)

115

Another important consideration for any least squares fit is the resulting parameter correlations. The correlations, which were rather high among all 4 parameters in these measurements, mean that any value obtained for a single parameter out of the 4 parameters is not as reliable as needed for accurate comparisons. This correlation problem was in addition to the fact that different "depolarization" factors were measured on different wafers. These comparisons among wafers required very accurate values for each parameter, with accuracy much higher than the differences among the wafers. It was found that a one-parameter description of the films, although not as good mathematically as a full 4 parameters model, was a reasonably good description of the film for wafer comparison purposes. This one parameter model assumes that the film is a uniform NREL BSTO quality material, and the thickness is the only variable. This thickness is called the "equivalent" thickness and is conceptually connected with the total amount of $Ba_xSr_{1-x}TiO_3$ material in the film having the same high density as the NREL material.

The "equivalent" thickness values obtained in these simplified fits are similar (to within ~2%) to the values calculated using the film thickness multiplied by density and added to the same product for the overlayer. Here density means (1-void fraction) and is really the density normalized to the NREL $Ba_xSr_{1-x}TiO_3$ density. The quality of the fits as measured by the MSE is much poorer than for the 4 parameter fits, as the actual films do have an overlayer and have a lower density than the NREL films.

An example of a result for wafer #37, 0.5" off center, low depolarization spot: MSE=63.69, "Equivalent" film thickness 3573 Å. Result for wafer #37, 0.5" off center, high depolarization spot: MSE=104.1,"Equivalent" film thickness 3586.5 Å. This result shows the small sensitivity of the one-parameter model to the "depolarization" problem (figure 5). Numerical results for all samples are shown in figure 6.
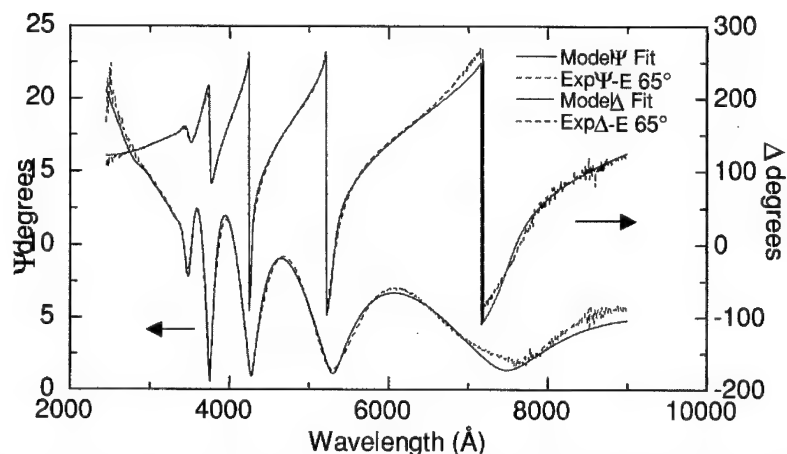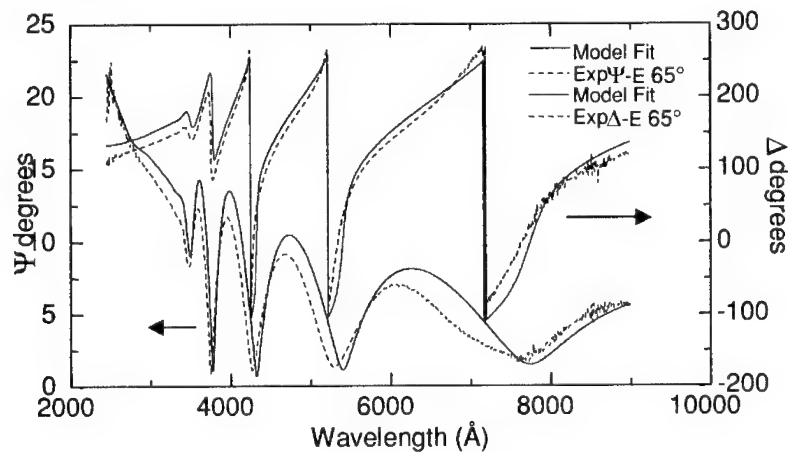

Fig. 5. Comparison of the experimental and the model calculated ψ and Δ vs. the wavelength λ, low polarization spot, one parameter model. (wafer # 37, 0.5 " off center)
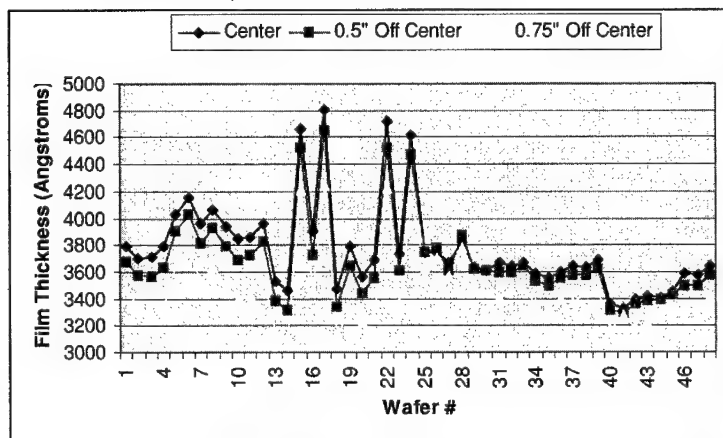
Fig 6. Summary of the film thickness variation within and across the 48 wafers.

The mean and (standard deviation) for the film thickness at the center, 0.5" and 0.75" off center are 3767 Å (340 Å), 3677 Å (313 Å), and 3469 Å (273 Å), respectively. Results have the following general features, as derived mostly from the "equivalent" thickness results:

1. The variation in film thickness among wafers is much larger in the group of wafers #1-24 vs. the group of wafers #25-48.
2. In the wafers group #1-24, the film thickness drops by about 150Å from the center to the 0.5" off-center point, and another ~200Å to the 0.75" off-center location. This is way above the requirement of ±4% around the thickness at the center. In the wafers group #25-48, there is only a negligible drop between the center and 0.5" off center and around 100Å to the 0.75" location.
3. The film thickness for the wafer group #1-24 is in the range 4000±800Å, with 8 wafers having the center location outside the required range of 3600-4400Å (4 are too thin and 4 are too thick). In the wafer group #25-48 the thickness range is 3550±350Å with 11 samples having the center location thickness lower than the required range of 3600-4400Å. These 11 wafers are all in the last group of wafers #34-48.
4. An estimate of the error in the refractive index as measured by the void fraction is in the range 1-2%. Using this error estimate, there is only a negligible difference in the quality of the film when we move from the center toward the periphery.

HIGH RESOLUTION X-RAY DIFFRACTION

The crystalline quality of the film was evaluated using a Phillips PW3720 HRXRD in the double-axis mode. The measurements were made at five different locations, at points lying successively further from the center of the wafer: (0,0 mm); (5,5 mm); (10, 10 mm); (15, 15 mm); and (18, 18 mm). Data for the center (0,0 mm) and practical usable limit insofar as device placement is concerned (15, 15 mm) is shown in figures 7 and 8.
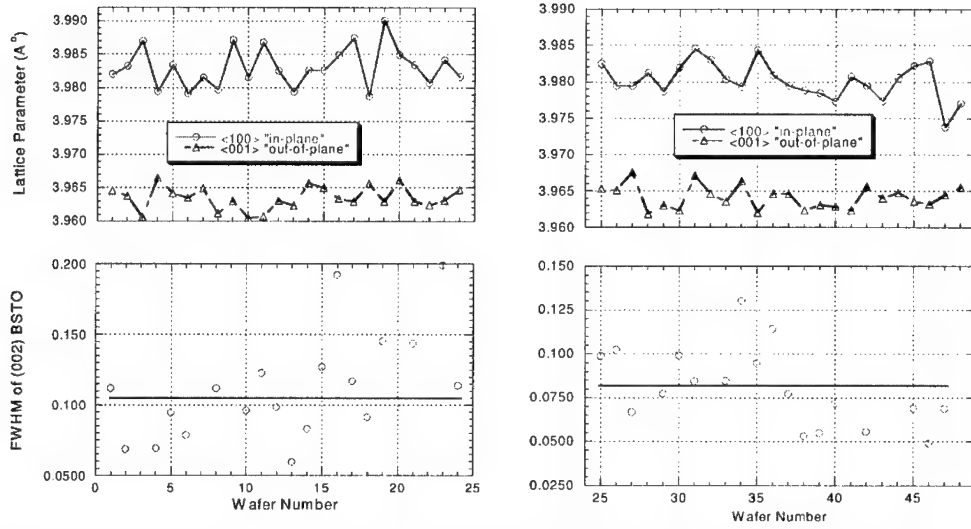
Fig 7. Lattice parameters and full width half maximum values for the 48 $Ba_{0.50}Sr_{0.50}TiO_3/LaAlO_3$ wafers at the center of each wafer (0,0 mm).
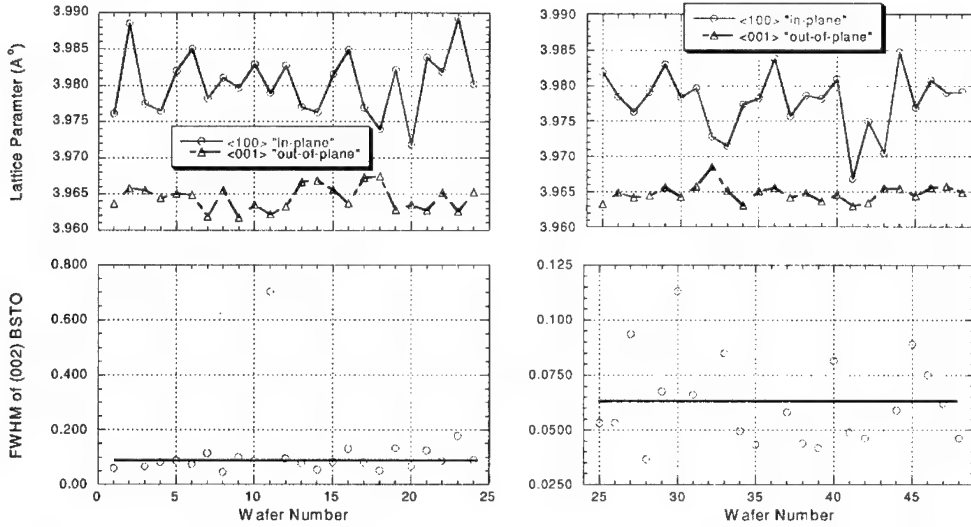
Fig 8. Lattice parameters and full width half maximum values for the 48 $Ba_{0.50}Sr_{0.50}TiO_3/LaAlO_3$ wafers near the perimeter of each wafer (15,15 mm).
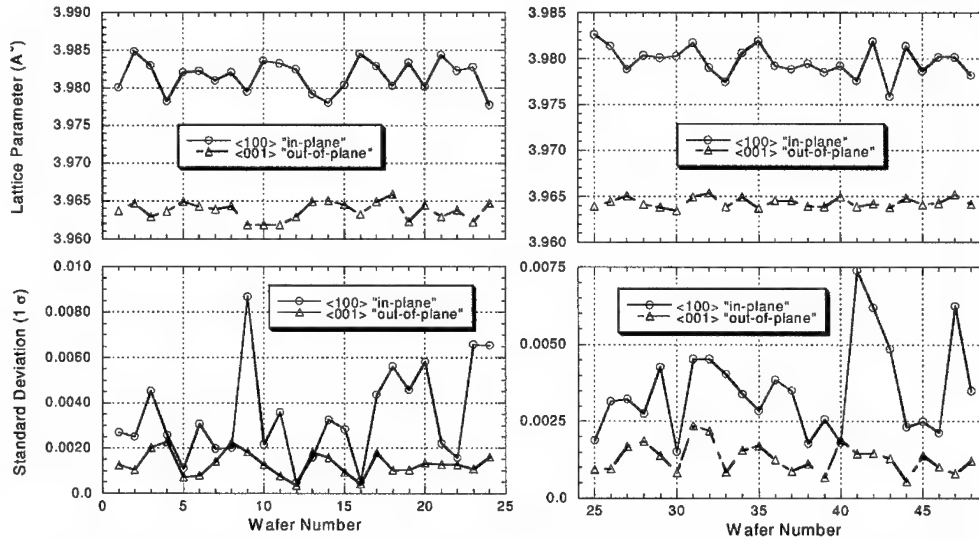
Fig. 9 Average of the lattice parameters and standard deviation across each wafer (all 5 spots). For wafers 1-24, the mean in-plane lattice parameter was 3.9816Å (σ=0.0021) and the mean out-of-plane lattice parameter was 3.9637 Å (σ=0.0012). For wafers 25-48 the mean in-plane lattice parameter was 3.9797Å (σ=0.0016) and the mean out-of-plane lattice parameter was 3.9643 Å (σ=0.0005).

Very good reproducibility was obtained both across the wafers and from wafer to wafer. Only wafer 11 was considerably poorer that the others based on the increase in FWHM. The film quality and reproducibility of the second set of wafers (25-48) was slightly better that the original set (1-24). The difference between in-plane and out-of-plane lattice parameters was approximately 0.015 Å. It would have been preferred to have the in-plane lattice parameters closer to 3.965 rather than 3.980 (so as to match the out-of-plane parameter).

MICROWAVE MEASUREMENTS

Several microwave test structures were patterned near the perimeter of each of the 48 wafers (approximately 0.75" from center) using standard lift-off techniques. The nominal metalization consisted of 250 Å Ti, 500 Å Au, 1.5 μm Ag, a 2500 Å Au cap. The test structures included λ/2 and λ ≈42 Ohm gap coupled microstrip resonators and a single coupled microstrip phase shifter element. The resonator coupling gap, that serves to isolate the resonator and facilitate extraction of unloaded Q, was 12.5 μm wide. The phase shifter section consisted of coupled microstrip lines that were 425 μm long separated by a 12 μm gap. Each device incorporated a coplanar virtual ground structure to allow on-wafer testing with 250 μm pitch ground-signal-ground probes. This technique has been described elsewhere [5]. The probes were calibrated to the device input/output ports. S11 and S21 were measured for the resonators and phase shifters, respectively, using a HP 8510C automatic network analyzer. The effective permittivity was determinedd from the λ/2 and λ resonator measurements using well-known techniques [6,7] and peak (0 dc field) permittivity of the

119

$Ba_{0.50}Sr_{0.50}TiO_3$ layer was deduced a quasi-TEM model [8]. The unloaded Q (Q_o) was determined from the $\lambda/2$ resonator. The resonant frequencies of the $\lambda/2$ and λ resonators were typically ≈ 17.5 and 18.5 GHz, respectively. The insertion phase shift was measured at 19 GHz by applying 0 and 200 V to the device. This step was conducted in vacuum (≈ 100 mTorr) to help prevent any breakdown problems across the coupled lines. Figure 10 summarizes the phase shift and Q_o for all available wafers.
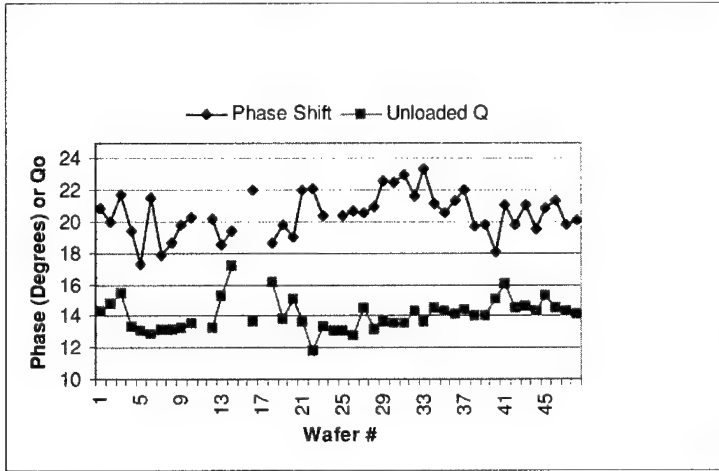
Fig 10. Insertion phase shift at 19.0 GHz for a single 425 micron long coupled line between 0 and 200 V and unbiased, unloaded Q (Q_o) near 17.5 GHz for a 42 Ohm microstrip resonator.

Wafers 15 and 17 were sacrificed earlier for device optimization purposes and were not included in this part of the study. The λ resonator on device 11 had a lithographic error but the $\lambda/2$ device yielded a Q_o near 16. The probe structure on phase shifter 24 shorted during testing. There were no other problems. The mean Q_o was 14.1 with a standard deviation of 1.0. The mean insertion phase shift was 20.5° with a standard deviation of 1.4°. The insertion loss near the mid-band of the phase shift structure (about 15 GHz), which included the effects of the probe transitions and 0.6 cm of microstrip, typically changed from 2.2 dB to 1.6 dB with a bias of 0 V and 200 V, respectively.

The estimated peak dielectric constant of the $Ba_{0.50}Sr_{0.50}TiO_3$ layer for each wafer is shown in figure 11. The mean peak dielectric constant was 2129 with a standard deviation of 149.
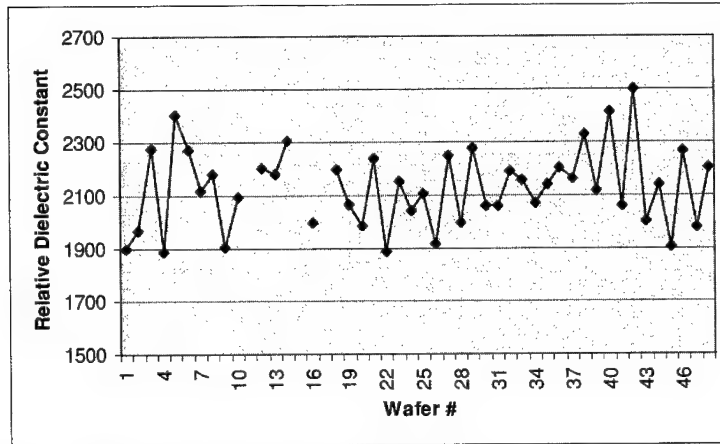
Fig 11. Peak (0 field) dielectric constant of the $Ba_{0.50}Sr_{0.50}TiO_3$ layer extracted from the $\lambda/2$ and λ microstrip resonators.

CONCLUSIONS

In order for any phased array antenna to be realized with ferroelectric materials, or any device technology for that matter, the phase shifters must be reproducible in terms of insertion loss and insertion phase shift. For example, a random 2 dB insertion loss variation may be tolerable (i.e. adequate beam profile maintained) but can degrade the power in the main beam by about 33 %. Similarly, a random phase error of $\pi/16$ may be negligible but a $\pi/8$ random phase error may degrade the beam by about 22%.

Very good reproducibility was obtained both across the 48 wafers and from wafer to wafer in terms of crystal quality. For wafers 1-24, the mean in-plane lattice parameter was 3.9816Å (σ=0.0021) and the mean out-of-plane lattice parameter was 3.9637 Å (σ=0.0012). For wafers 25-48 the mean in-plane lattice parameter was 3.9797Å (σ=0.0016) and the mean out-of-plane lattice parameter was 3.9643 Å (σ=0.0005). The FWHM of the (002) peak was generally better than 0.1° and significantly better than this for the second batch of 24 wafers.

Based on the ellipsometric analysis, The mean and (standard deviation) for the film thickness at the center, 0.5" and 0.75" off center are 3767 Å (340 Å), 3677 Å (313 Å), and 3469 Å (273 Å), respectively. There is a direct effect of the thickness measurements on peak permittivity calculations. The sensitivity of the calculation to measurement uncertainty is nearly linear. For example, a film thickness measurement uncertainty of 10% translates into about a 9% change in peak dielectric constant for the $Ba_{0.50}Sr_{0.50}TiO_3$ layer. We believe that the uncertainty is much smaller than this. Notice that several wafers had significant excursions in thickness from the mean value but their corresponding peak dielectric constant was consistent with the average value.

Despite some variations in thickness and crystallinity, the microwave performance was very consistent. The mean Q_o was 14.1 with a standard deviation of 1.0. The mean insertion phase shift was 20.5° with a standard deviation of 1.4°. The insertion loss near the mid-band of the phase shift structure (about 15 GHz), which included the effects of the probe transitions and 0.6 cm of microstrip, typically changed from 2.2 dB to 1.6 dB with a bias of 0 V and 200 V, respectively. In

121

the actual ferroelectric reflectarray application, the phase shifter will consist of ≈ 6 coupled line sections like the one used here and be operated in a reflection mode. Thus the insertion phase envelope can be expected to be better than plus or minus $18°$ or $\pi/10$ based on our statistical analysis. The loss variation quoted above represents an extreme case (0 to 200 V) and we expect the average loss variation to be within a plus or minus 1 dB envelope. The Q measurements suggest that the film quality, in terms of loss tangent, is very reproducible.

In summary, we believe that the two batches totaling 48 PLD $Ba_{0.50}Sr_{0.50}TiO_3/LaAlO_3$ wafers are suitable, from a microwave point of view, for fabrication into phase shifters and incorporation into a state-of-the-art phased array antenna. In the near future, the remaining 46 wafers will be patterned with approximately 30 phase shifters (or more) each. Then the phase shifters will be on-wafer sampled (about 10% tested) and inventoried for use in the ferroelectric reflectarray antenna.

REFERENCES

1. E. Brookner, Microwave Journal, May, 1997, pp. 288-293.
2. E. Brookner, Microwave Journal, June, 1997, pp. 84-92.
3. R. Romanofsky et al.,IEEE Tran. Microwave Theory Tech., 48, No. 12, pp. 2504-2510 (2000)
4. C. Mueller et al., MRS Spring Meeting, San Francisco, CA, April 24-28, (2000).
5. R. Romanofsky et al., Integrated Ferroelectrics, Vol. 39, pp. 1249-1260, (2001).
6. D. Kajfez and E.J. Hwan, IEEE Trans. Microwave Theory Tech., 32, No. 7, pp. 66-670, (1984).
7. T.C. Edwards, *Foundations for Microstrip Circuit Design*, John Wiley & Sons, 1981.
8. R. Romanofsky and A. Qureshi, IEEE Trans. Mag., 36, No. 5, pp. 3491-3494 (2000).

H4.3

Correlation of Microwave Dielectric Properties and Microstructure of Unpatterned Ferroelectric Thin Films

R. G. Geyer
National Institute of Standards, RF Technology Division, Boulder, CO 80303, U.S.A.,
303/497-5852 geyer@boulder.nist.gov

M.W. Cole, P.C. Joshi, E. Ngo, C. Hubbard, W. Nothwang, M. Bratcher, M. Ervin, M. Wood
U.S. Army Research Laboratory, Weapons and Materials Research Directorate
Aberdeen Proving Ground, MD 21005, U.S.A., 410/306-0747 mcole@arl.army.mil

ABSTRACT

The influence of low concentration (1 mol%) Mg doping on the structural, microstructural, surface morphological and dielectric properties of $Ba_{1-x}Sr_xTiO_3$ thin films has been measured and analyzed. The films were fabricated on MgO and Pt-Si substrates via the metalorganic solution deposition technique using carboxylate-alkoxide precursors and post deposition annealed at 800 °C (film/MgO substrates) and 750 °C (film/Pt-Si substrates). The structure, microstructure, surface morphology and film/substrate compositional quality were analyzed and correlated to the films dielectric and insulating properties. Dielectric properties of unpatterned films were measured at 10 GHz with a coupled/split dielectric resonator system and at 100 kHz using metal-insulator-metal capacitors. The Mg-doped BST films exhibited improved dielectric loss and insulating characteristics compared to the undoped $Ba_{0.6}Sr_{0.4}TiO_3$ thin films.   The improved dielectric properties, low leakage current, and good tunability of the low level Mg-doped BST thin films merit strong potential for utilization in microwave tunable devices.

INTRODUCTION

Thin films of $Ba_{1-x}Sr_xTiO_3$ (BST) have recently received considerable attention as promising candidates for applications in tunable electronically controllable microwave devices. For the realization of such tunable devices at microwave frequency it is important to develop a paraelectric thin film material with low microwave loss, high tunability, and good insulating properties. To date, thin film BST which simultaneously possesses both low loss at microwave frequency and a large tunability as required for many microwave applications has not been realized. It is well documented that small concentrations of acceptor dopants can dramatically modify the properties, i.e., lower dielectric loss, of ferroelectric materials such as BST [1-3]. Recently, we have investigated the effect of various acceptor dopants on the dielectric and insulating properties of BST thin films at frequencies between 10 kHz and 1 MHz and found a significant reduction of the loss tangent, enhanced film resistivity, and good dielectric tunability characteristics for Mg doped BST thin films [1,4]. In this paper we evaluate the process-structure-property relationships and report the microwave dielectric properties for pure and 1 mol% Mg doped BST thin films prepared via the metalorganic solution deposition technique.

EXPERIMENTAL

Undoped and 1 mol% Mg doped $Ba_{0.6}Sr_{0.4}TiO_3$ thin films were fabricated by the metalorganic solution deposition (MOSD) technique. Ba acetate, Sr acetate, and Ti isopropoxide were used as precursors to form BST. Acetic acid and 2-methoxyethanol were used as solvents and magnesium acetate was employed as the dopant precursor. The precursor films were spin coated onto Pt-coated silicon and (100) single crystal MgO substrates. Crystalline films were achieved via post-deposition annealing in an oxygen ambient at 750 °C and 800 °C, for the films deposited on the Pt-silicon and MgO substrates, respectively.

The films were characterized for dielectric, insulating, structural, compositional, and surface morphological properties. The dielectric properties were characterized utilizing both microwave and low frequency measurement techniques. The microwave dielectric properties of unpatterned undoped and Mg-doped BST thin films grown on MgO substrates were measured at 10 GHz with a coupled/split dielectric resonator system [5]. Figure 1 displays a schematic diagram of the split dielectric resonator system. This measurement technique is noncontacting and non-destructive. The measurement process is two-phase: First, the permittivity and dielectric loss of the MgO substrate is determined. Second, the permittivity and dielectric loss of the thin film is determined by the differences in resonant frequencies and Q-factors of the MgO substrate and the MgO substrate + thin film. The microwave measurement frequency is determined by the geometry and permittivity of high Q, temperature-stable dielectric resonators. In this method the electric field is tangential to the plane of the sample. Numerical methods are used to analyze these measured data. The measurement capabilities of this technique are currently from $1 - 30$ GHz and the uncertainty in permittivity is approximately twice the uncertainty in the thickness of the film. The low frequency (100 kHz) dielectric and insulating measurements were conducted on the undoped and Mg-doped BST thin films deposited on Pt-Si substrates in the metal-insulator-metal (MIM) capacitor configuration. The film capacitance (C_p) and dissipation factor (tan δ) were measured with an HP 4194A impedance/gain analyzer[a]. The insulating properties of the films were evaluated via I-V measurements using a HP 4140B semiconductor test system. The film crystallinity was assessed via glancing angle x-ray diffraction (GAXRD) using a Rigaku diffractometer with CuKa radiation at 40 kV. Cross-sectional film microstructure was examined using a Hitachi S4500 field emission scanning electron microscope (FESEM). The surface morphology of the films was assessed by a Digital Instrument's Dimension 3000 atomic force microscope (AFM) using tapping mode. The elemental distribution within and across the film-substrate interface was assessed using a Perkin-Elmer 660 scanning Auger microprobe.
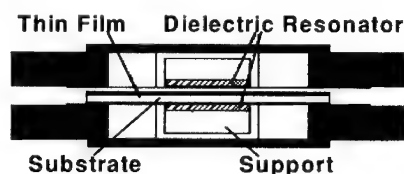

Figure 1. Schematic diagram of the split dielectric resonator system.

RESULTS AND DISCUSSION

The microwave dielectric measurements in this investigation were achieved in the unpatterned state, that is, without the use of any contact metallization. This measurement configuration has the advantage of eliminating the influence of conductor losses from the microwave dielectric loss measurement. However, without a contact metallization the tunability and leakage current measurements cannot be obtained. Thus, we have also characterized these thin films at low frequency (100 kHz) in the MIM configuration in order to acquire film tunability and leakage current/film resistivity values. The low frequency data is useful only as a composition-tunability trend indicator since the correletion between 100 kHz and 10 GHz data is not absolute [4]. The insulating (leakage current/film resistivity) thin film data is an electrical measure of the quality and reliability of a dielectric film, and the low frequency data is valid for this assessment. The room temperature thin film dielectric properties, measured at 10 GHz and 100 kHz, are summarized in Table I.   A comparison of the data tabulated in Table I clearly demonstrates that amounts as low as ~1 mol% of the Mg dopant have a noticeable influence on the dielectric and insulating properties of the BST thin films. The 1 mol% Mg-doped BST thin film possessed a lower dielectric loss than that of the undoped BST thin film at both low and microwave frequencies. The dielectric constant of the 1 mol% Mg-doped BST thin film was lower than that of the undoped BST at 100 kHz and 10 GHz.   The dielectric constant for both the undoped and 1 mol% Mg-doped thin films, at both frequencies, is reasonable for device impedance matching purposes, thereby allowing efficient power transfer in the device.   The electrical quality, that is, the insulating nature, of a dielectric film is determined by the value of leakage current which has been converted to resistivity in Table I. The Mg-doped BST thin film possessed an enhanced film resistivity (low leakage current) value with respect to that of the undoped BST thin film. Capacitance-voltage measurements, conducted on the MIM capacitors, were used to analyze the effect of Mg doping on the dielectric tunability of the BST thin films. The tunability, measured at 200 kV/cm was found to decrease with the addition of the Mg dopant. Considering the tradeoffs between tunability and the values of tan δ, dielectric constant and film resistivity, the 1 mol% Mg-doped BST film possessed better overall material properties with respect to that of undoped BST for tunable device applications. It is well documented that the variations in the dielectric properties of the BST based material system are strongly influenced by sample composition, crystallinity, grain size, stress, and the quality of the film-substrate interface. Therefore, in order to fully evaluate the properties discussed above the influence of the Mg dopant on the structural, microstructural, interfacial, and surface morphological properties must be evaluated and correlated with the films dielectric and insulating properties.

TABLE I. Dielectric and insulating properties of the undoped and 1 mol% Mg-doped BST thin films.

Sample	Frequency	ε_r (Zero bias)	tan δ (Zero bias)	Tunability (%) (200kV/cm)	ρ (Ω-cm (200kV/cm)
MgO subst.	10 GHz	9.71	2.88×10^{-5}	----	----
BST/MgO	10 GHz	406	2.50×10^{-2}	----	----
1 mol% Mg-BST/MgO	10 GHz	348	2.40×10^{-2}	----	----
BST/PtSi.	100 kHz	450	1.3×10^{-2}	28.1	0.40×10^{12}
1 mol% Mg-BST/PtSi	100 kHz	423	1.0×10^{-2}	23.0	0.55×10^{12}

The as-pyrolysed undoped and 1 mol% Mg-doped BST thin films were amorphous and post deposition annealing was required to impart crystallinity, increase the overall grain size of the film, and to remove film strain by filling oxygen vacancies. These factors are particularly important since the dielectric loss in ferroelectric thin films has been reported to be strongly influenced by stoichiometric deficiencies, which create vacancies, film strain, and the presence of a large grain boundary to grain ratio [4]. Therefore, in order to reduce the microwave dielectric loss the as-pyrolysed films on MgO substrates were post-deposition annealed for 1h in the temperature range of 600 to 800 °C in an oxygen atmosphere. Glancing angle x-ray diffraction (GAXRD) was utilized to assess film crystallinity and to determine whether or not the films possessed a single phase structure. Figure 2 displays the glancing angle x-ray diffraction patterns of the undoped and 1 mol% Mg doped BST films deposited on MgO substrates. The absence of diffraction peaks in the x-ray diffraction patterns for both film compositions annealed at 600 °C indicated that these films were amorphous in nature. Partially crystallized undoped and Mg-doped films were obtained at an annealing temperature of 650 °C with no evidence of secondary phase formation. As the annealing temperature was increased, the x-ray peak intensity increased and the full-width-half-maximum (FWHM) decreased indicating enhanced crystallinity and an increase in grain size with increasing annealing temperature up to 800 °C. The 800 °C annealed, undoped and doped, films were cubic, and possessed a non-textured polycrystalline structure with no evidence of secondary phases. Direct comparison of the GAXRD data for the undoped and doped films showed that the FWHM of the Mg doped film was larger than that of the undoped BST films at all annealing temperatures and indicating a smaller grain size for the Mg doped BST films with respect to that of the undoped films.
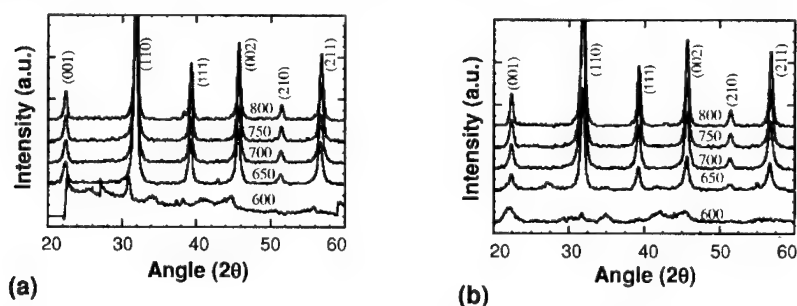
Figure 2. X-ray diffraction patterns of the (a) undoped and (b) 1 mol% Mg doped $Ba_{0.6}Sr_{0.4}TiO_3$ films deposited on MgO substrates annealed at temperatures from 600 to 800 °C for 60 min.

The surface morphology of the films was assessed via tapping mode AFM over a 1x1 μm^2 scan area. The AFM images of the films annealed at 800 °C are displayed in Fig. 3 and show that both the undoped and Mg-doped films exhibited a dense microstructure with no cracks or defects observed. The surface roughness as quantified by AFM, was found to increase with increasing annealing temperature resulting in an average surface roughness (R_{av}) of 2.25 nm at 800 °C for both film compositions. The parameter of film surface roughness is extremely important for device performance since the dielectric properties depend not only on a well-defined microstructure, but also on the quality the electrode (required for microwave devices)-film interface. It has been reported that surface roughness has a strong influence on the value of

leakage current or film resistivity [6], thus, the fact that the undoped and Mg doped MOSD films are extremely smooth is consistent with the excellent film resistivity values reported in Table I. The AFM results demonstrated that the Mg dopant had no appreciable affect on the films surface roughness; however, the AFM results did show a grain size difference between the annealed undoped and doped films. Figure 3c displays a plot of grain size as a function of annealing temperature for both the undoped and Mg doped films. The results support the GAXRD findings suggesting that even a small amount of Mg dopant added to BST depresses the grain size relative to that of undoped BST. This result was also observed for 5 mol% Mg doped films deposited on Pt-Si substrates [3]. The grain size for the fully crystallized films was 75 nm and 67 nm for the undoped and Mg doped films respectively.
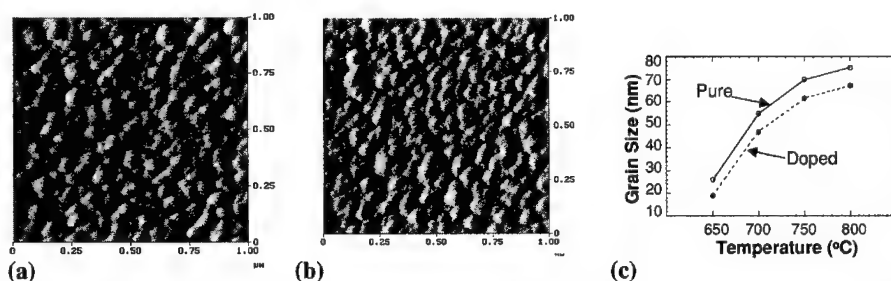
Figure 3. AFM micrographs of the (a) undoped BST and (b) 1 mol % Mg doped BST film surfaces postdeposition annealed at 800 °C. Grain size as a function of annealing temperature for the undoped and 1 mol% Mg doped BST thin films on MgO substrates is plotted in (c).

The films microstructure, in the direction perpendicular to the film surface was analyzed via cross-sectional FESEM. The cross-sectional FESEM micrographs of the 800 °C annealed films, not shown, demonstrated that both films possessed a dense well-crystallized microstructure with a uniform cross-sectional thickness of 165 nm. The films were polycrystalline and were composed of granular multigrains randomly distributed through out the film thickness. The FESEM micrographs show a distinct structural delineation between the film and the MgO substrate. No amorphous layer or voiding/defects was observed at the film-MgO interface. This defect free and structurally abrupt interface bodes well for the excellent mechanical integrity and good adhesion characteristics of the undoped and Mg doped BST film-MgO substrate.

The AES depth profiles of the undoped and 1 mol% Mg doped BST films revealed a sharp interface with no interdiffusion of constituent elements between the dielectric film and the MgO substrate. The depth profiles also revealed that each element component of the film possessed a uniform distribution from the film surface to the film-substrate interface. These data substantiate the fact that the undoped and Mg doped BST films on MgO substrates maintain chemical and thermal stability at processing temperatures up to 800 °C (annealing temperature). The fact that no impurities were observed in the AES elemental depth profile, without doubt, contributed to the films good dielectric and insulating properties.

Results of this investigation have demonstrated that Mg doping as low as 1 mol% had a notable influence on the films microstructure, dielectric, and insulating properties. The exact mechanism by which Mg altered the film properties is not fully understood. We suggest that the

Mg doping (composition alteration) is the parameter, which is responsible for the modification of the BST thin film material properties. Material doping has been reported to modify and control thin film dielectric and insulating properties by reducing the oxygen vacancy concentration [7, 8]. Acceptor type dopants can prevent the reduction of Ti^{4+} to Ti^{3+}, by neutralizing the donor action of the oxygen vacancies. Because the electrons resulting from the generation of oxygen vacancy can hop between different titanium ions and provide a mechanism for dielectric losses, the compensation for oxygen vacancy with the correct amount of acceptor dopant such as Mg^{2+}, should, in theory, help to lower the loss tangent. We further speculate that the Mg dopant served to enhance the insulation resistance (excellent film resistivity values listed in Table I) of the BST based film, by suppressing the concentration of oxygen vacancies, and growth of potential barrier at grain boundaries.

CONCLUSIONS

This investigation demonstrated that Mg doping as low as 1 mol% had a noteworthy influence on the material properties of BST thin films. The annealed undoped and 1 mol% Mg-doped BST films were single phase, possessed a dense defect free microstructure with a thermally stable film-substrate interface, and smooth continuous surface morphology. Improved dielectric and insulating properties were achieved for 1 mol% Mg-doped BST thin films with respect to that of pure BST films. The 10 GHz measured values of dielectric constant and dissipation factor of BST thin films doped with 1 mol% Mg were 348 and 0.024, respectively. The film resistivity was also enhanced as a result of the Mg doping. The compensation for oxygen vacancies via low amounts of Mg acceptor doping was suggested to be responsible for the enhanced material properties of the 1 mol% Mg doped BST thin film.

REFERENCES

1. P. C. Joshi, M. W. Cole, Appl. Phys. Lett. **77**, 289 (2000).
2. U. N. Weston, J. Am. Ceramic Soc. **52**, 253 (1969).
3. V. K. Varadan, D. K. Ghodgaonkar, V.V. Varadan, Microwave J. **30**, 116 (1992).
4. M. W. Cole, P. C. Joshi, M. H. Ervin, M. C. Wood, and R. L. Pfeffer, Thin Solid Films **374**, 34 (2000).
5. J. Krupka, R.G. Geyer, J. Baker-Jarvis, and J. Ceremuga, DMMA'96 Conf. Proc., 21 (1996)
6. M. S. Tsai and T. Y. Tseng, J. Am. Ceram. Soc. **82**, 351 (1999).
7. R. Moos and K.H. Hardtl, J. Appl. Phys. **80**, 393 (1996).
8. S. Shibagaki, A. Koga and J. Tanaka, J. Mater. Sci. **32**, 1449 (1997).

BST Bulk Materials
and Applications

Microfields Induced by Random Compensated Charge Pairs in Ferroelectric Materials

Frank J. Crowne, Steven C. Tidrow, Daniel M. Potrepka, and Arthur Tauber[1]
RF Electronics Division, Army Research Laboratory,
Adelphi, MD 20783-1197, U.S.A.
[1]GeoCenters Inc., Newton-Centre, MA

ABSTRACT

The dc and microwave responses of the $Ba_xSr_{1-x}(X,Y)_yTi_{1-y}O_3$ family of ferroelectric compounds with various substitutional additives X^{3+}, Y^{5+} are analyzed by combining the random-field technique with the mean-field (Landau-Devonshire) theory of ferroelectricity, along with a self-consistent computation of the dielectric constant of the host material in the presence of the impurity fields. The fields in the material are assumed to arise from charge compensation at the Ti^{4+} sites, leading to permanent dipoles made up of the resulting positive and negative ions separated by a few lattice constants. It is shown that whereas completely random placement of positive and negative ions generates a Holtsmark distribution of electric field, with infinite second moment and hence extremely large fluctuations in field strength, the association of ionized impurities into permanent dipoles leads to much lower fluctuations in field and a distribution with finite second moment, which makes a self-consistent dielectric constant meaningful.

INTRODUCTION

The usefulness of ferroelectric materials in the design of electronic devices arises from the ease with which their electrical characteristics, e.g., conductivity, dielectric constant, optical birefringence, etc., can be controllably modified so as to produce a desired functionality. A standard way of controllably modifying a material is to introduce foreign elements into a host material at concentrations that are too low to change its intrinsic chemical nature, but which modify its behavior at the macroscopic level. In ferroelectrics, these modifications are usually associated with the presence of built-in electric fields, which are generated by thermal ionization of the added impurity atoms. This type of processing is well known in the semiconductor industry, where materials are routinely "doped" to make them conductive and otherwise electrically active.

However, because semiconductors already contain large amounts of free, i.e., mobile, charge, it is normally assumed that there are no macroscopic fields inside them. Because doping such materials with impurities creates ionized donor and acceptor centers in addition to the free charge, it would seem that long-range fields should appear. However, the free charge can move to screen out any such fields [1] over distances that are larger than the Debye length in the bulk:

$$l_D = \sqrt{\frac{\varepsilon kT}{ne^2}} = 120\sqrt{\frac{\varepsilon}{n}} \quad \text{cm at room temperature,} \tag{1}$$

where n is the carrier density, ε the dielectric constant. For $n \approx 10^{12}$ cm^{-3}, which is a lower limit on how low the free charge can be in most semiconductors, this gives $l_D \approx 1.2$ μm, i.e., very small. Over these distances the fields can only create small potential fluctuations, which modulate the bottom of the material conduction band to produce so-called "bandtails", as shown long ago by Evan Kane [2] and Halperin and Lax [3]. In contrast, insulating materials can have vanishingly small amounts of free charge in their interiors, and hence can sustain long-range fields. Although these fields will vary randomly in magnitude and direction, they can superimpose and become quite large. In this paper we develop a statistical method to calculate the behavior of fields associated with charged impurities in ferroelectrics, and use it to discuss the effect these fields have on the host material's dielectric response.

FIELD PROBABILITY DISTRIBUTIONS

The appropriate description of random electric fields in an insulator is statistical, since the added charge centers are located randomly throughout the material bulk. This means that at any given point in the material we can assume that there is a probability distribution for the field, i.e., that the field is a random variable. The usefulness of this picture depends on what observable we plan to calculate. If the observables of interest involve volume averages, these can be evaluated conveniently by invoking the ergodic hypothesis, i.e., we can replace the volume average by an ensemble average. To proceed beyond this point the probability distribution of the quantity being averaged is required.

We begin by calculating the probability distribution for electric fields generated by one species of added impurity. If the impurity centers are uniformly distributed, then the probability $p_1(\vec{x})$ that there is an impurity at position $\vec{x}$ is simply $1/V$, where V is the host volume. To find the field distribution we use a method pioneered by Markov [4], discussed first in the astronomy literature by Holtsmark [5] and then in the astrophysics literature by Chandrasekhar [6], and finally in solid state by P. W. Anderson [7] to discuss electron localization in disordered media and by Stoneham [8] to discuss optical line shapes. First, we note that if the impurity positions $\vec{x}_1, \vec{x}_2, \vec{x}_3, ...$ are random vector variables with probability distributions $p_1(\vec{x}_1), p_2(\vec{x}_2), p_3(\vec{x}_3), ...$, and $\vec{f} = \vec{f}(\vec{x}|\vec{x}_1, \vec{x}_2, \vec{x}_3, ...)$ is some vector function of these variables and the position $\vec{x}$ of a point in the solid, then $\vec{f}$ is a random variable with a probability density given by the expression

$$P(\vec{f}(\vec{x}) = \vec{f}_0) = \left\langle \delta(\vec{f}_0 - \vec{f}(\vec{x}|\vec{x}_1, \vec{x}_2, \vec{x}_3, ...)) \right\rangle = \int \prod_{n=1}^{N} p_n(\vec{x}_n) d\vec{x}_n \delta(\vec{f}_0 - \vec{f}(\vec{x}|\vec{x}_1, \vec{x}_2, \vec{x}_3, ...)) \quad (2)$$

In our specific case, $\vec{f}$ will be the field due to the random charges.
Using the exponential representation of the δ-function

$$\delta(\vec{x}) = \int_{-\infty}^{\infty} e^{i\vec{q} \cdot \vec{x}} \frac{d^3 q}{(2\pi)^3} \quad (3)$$

we can write the following expression for the density P associated with the overall probability that the electric field $\vec{E}_I$ due to the charged impurities has a value $\vec{E}$ at the point $\vec{x}$:

$$P(\vec{E}_I(\vec{x}) = \vec{E}) = V^{-2N} \int \prod_n d\vec{x}_n \int_{-\infty}^{\infty} \exp[i\vec{q} \cdot \{\vec{E} - \vec{E}_I(\vec{x}|\vec{x}_1, \vec{x}_2, \vec{x}_3, ...)\}] \frac{d^3 q}{(2\pi)^3} \qquad (4)$$

Uncorrelated Positive and Negative Monopoles

Assume now that we put an equal number N of positive and negative charges ("donors" and "acceptors" in semiconductor language) into the material, so that it is electrically neutral (charge-compensated). Let these charges be at locations $\vec{x}_{D1}, \vec{x}_{D2}, \vec{x}_{D3}, ... \vec{x}_{A1}, \vec{x}_{A2}, \vec{x}_{A3}, ...$, with probability densities $p_{Dj}(\vec{x}_{Dj}), p_{Aj}(\vec{x}_{Aj})$ that are uniform and uncorrelated as asserted above, i.e., $p_{Dj}(\vec{x}_{Dj}) = p_{Aj}(\vec{x}_{Aj}) = \frac{1}{V}$.

Then the function $\vec{E}_I(\vec{x}|\vec{x}_1, \vec{x}_2, \vec{x}_3, ...)$ has the form

$$\vec{E}_I(\vec{x}|\vec{x}_{D1}, \vec{x}_{D2}, ..., \vec{x}_{A1}, \vec{x}_{A2}, ...) = \nabla \sum_{j=1}^{N} \frac{e}{|\vec{x} - \vec{x}_{Dj}|} - \frac{e}{|\vec{x} - \vec{x}_{Aj}|}$$

$$= \sum_{j=1}^{N} \vec{E}(\vec{x} - \vec{x}_{Dj}) - \vec{E}(\vec{x} - \vec{x}_{Aj}) \qquad (5)$$

where $\vec{E}(\vec{x}) = e \dfrac{\vec{x}}{\varepsilon |\vec{x}|^3}$ is the electric field of a point charge and ε is the relative permittivity of the host material. Then Eq. (1) can be rewritten as follows:

$$P(\vec{E}_I(\vec{x}) = \vec{E}) = \int_{-\infty}^{\infty} \exp[i\vec{q} \cdot \vec{E}] \frac{d^3 q}{(2\pi)^3} \left(V^{-1} \int \exp[-i\vec{q} \cdot \vec{E}(\vec{x})] d\vec{x}\right)^N \left(V^{-1} \int \exp[i\vec{q} \cdot \vec{E}(\vec{y})] d\vec{y}\right)^N \qquad (6)$$

If the densities of donors and acceptors are $n_D = n_A \equiv n$, we can write $V = n/N$. Using this notation, we have that

$$\left(V^{-1} \int \exp[-i\vec{q} \cdot \vec{E}(\vec{x})] d\vec{x}\right)^N = \left(1 - V^{-1} \int \{1 - \exp[-i\vec{q} \cdot \vec{E}(\vec{x})]\} d\vec{x}\right)^N \qquad (7)$$

This lets us write [9]

$$P(\vec{E}_I(\vec{x}) = \vec{E}) = \int_{-\infty}^{\infty} \exp[i\vec{q} \cdot \vec{E}] \exp[-2n \operatorname{Re} F(\vec{q})] \frac{d^3 q}{(2\pi)^3} \qquad (8)$$

Now, the integral

$$\operatorname{Re} F(\vec{q}) = \int \{1 - \cos[\vec{q} \cdot \vec{E}(\vec{x})]\} d\vec{x} \qquad (9)$$

reduces the function P to Holtsmark's distribution (see Ref. [5]) with a total density of carriers $2n$. Some manipulation gives

$$\operatorname{Re} F(\vec{q}) = \frac{4}{15}(2\pi)^{3/2} e^{3/2} |q|^{3/2} \tag{10}$$

which implies a distribution of the form

$$P(\vec{E}_I(\vec{x}) = \vec{E}) = \int_{-\infty}^{\infty} \exp[i\vec{q} \cdot \vec{E} - \sigma|\vec{q}|^{3/2}]\frac{d^3q}{(2\pi)^3} \tag{11}$$

where $\sigma = \frac{8}{15}(2\pi)^{3/2} ne^{3/2} = 8.400 ne^{3/2}$ is a scale factor with dimensions $[\text{field}]^{3/2}$.

This reduces to the 1D integral of Holtsmark

$$P(\vec{E}_I(\vec{x}) = \vec{E}) = \frac{1}{2\pi^2 |\vec{E}|^3} \int_{0}^{\infty} \exp[-\sigma x^{3/2}/|\vec{E}|^{3/2}] x \sin x \, dx \tag{12}$$

which cannot be reduced further.

If the host material has a lattice constant a, we can write $n = ca^{-3}$, where c is the impurity concentration (dimensionless). Then $\sigma = 8.400c \left(\frac{e}{\varepsilon a^2}\right)^{3/2}$ introduces a scaling electric field $E_{sc} = \frac{e}{\varepsilon a^2}$ into the problem, in terms of which $\sigma = 8.400cE_{sc}^{3/2}$. Taking a = 4 Å and $\varepsilon = 1000$, which are typical values for ferroelectrics, we find that this field is about 110 V/μm, i.e., close to breakdown of the material.

Fully dipole-correlated charge distributions

Suppose now that every donor is spatially paired with an acceptor, i.e., is physically separated from it by only a few lattice constants. The resulting pairs of charges can then be treated as unit sources of random electric field, i. e., dipoles. At low carrier concentrations (so that the dipoles are far apart) we can treat the fields of these dipoles as we did the fields above. Now, however, the field $\vec{E}(\vec{x}) = e^2 \frac{\vec{x}}{\varepsilon|\vec{x}|^3}$ is replaced by the field of a dipole, i.e., a field of the form

$$\vec{E}(\vec{x}) = \wp \frac{3\vec{x}(\vec{x} \cdot \hat{n}) - x^2 \hat{n}}{\varepsilon|\vec{x}|^5} \tag{13}$$

where $\vec{n}$ gives the direction of the dipole and $\wp$ its strength. For a cubic crystal the dipole direction can vary in 6 cubic directions for nearest neighbors and 8 for next nearest neighbors. Let us ignore the discreteness of the possible orientations and suppose that $\wp$ is a constant vector that can point in any direction, i.e., the Heisenberg problem. Then we can replace the sum by an angular average:

$$V^{-1}\int \exp[-i\vec{q}\cdot\vec{E}(\vec{x})]d\vec{x} \rightarrow V^{-1}\frac{1}{4\pi}\int d\hat{n}\int \exp[-i\vec{q}\cdot\vec{E}(\vec{x})]d\vec{x}$$

$$=V^{-1}\int d\vec{x}\,\frac{1}{4\pi}\int \exp\left[-i\frac{\wp}{|\vec{x}|^3}\vec{q}\cdot\vec{J}(\vec{x})\right]d\hat{n} \equiv \int <S>\,d\vec{x} \tag{14}$$

where

$$\vec{J} = 3\hat{n}(\hat{n}\cdot\hat{q}) - \hat{q}. \tag{15}$$

Considerable manipulation eventually gives the result

$$P(\vec{E}_I(\vec{x}) = \vec{E}) = \int_{-\infty}^{\infty} \exp[i\vec{q}\cdot\vec{E} - n\gamma|\vec{q}|]\frac{d^3q}{(2\pi)^3} \tag{16}$$

where $\gamma = \dfrac{\pi^2\wp}{3}\left(1+\dfrac{\sinh^{-1}\sqrt{3}}{2\sqrt{3}}\right) \approx 5.89\wp$. Unlike the Holtsmark distribution, this

expression can be evaluated in closed form, leading eventually to the result

$$P(\vec{E}_I(\vec{x}) = \vec{E}) = \frac{\gamma n}{\pi^2}\frac{1}{\left(E^2 + \gamma^2 n^2\right)^2} \tag{17}$$

which appears in the work of Ma [10]. Again, a scaling field enters into the problem: if we take the dipole moment to equal ea, where a is the lattice constant, this field is once more $E_{sc} = \dfrac{e}{\varepsilon a^2}$, where now we write $\gamma n = 5.89cE_{sc}$.
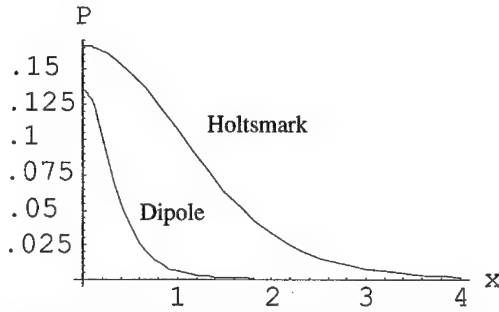

Figure 1. Holtsmark and dipole distributions. The dipole curve is scaled by a factor of 1/100.

Figure 1 shows a numerical plot of this function, together with the Holtsmark distribution, for the same lattice constant and scaling field. Note that both these functions are centered around zero, since they are vector distributions and there is no preferred direction in the crystal. For convenience purposes the functions plotted are actually

$2\pi^2\sigma^2 P_H(x)$ and $2\pi^2\sigma^2 P_D(x)$, where $x = \dfrac{E}{\sigma^{2/3}}$, since the Holtsmark function

$2\pi^2\sigma^2 P_H(x)$ is a universal function in this coordinate. In contrast, the dipole function

$2\pi^2\sigma^2 P_D(x)$ takes the form $\dfrac{2\Gamma}{\left(x^2 + \Gamma^2\right)^2}$, where Γ is a function only of the

concentration: $\Gamma = 1.43\, c^{1/3}$. The dipole plot shown is for $c = .05$, on a scale reduced by a factor of 100. Note that the Holtsmark distribution is much broader than the dipole distribution, with a longer tail. This difference is a manifestation of the long range of the Coulomb interaction, and in fact causes the Holtsmark distribution to have no second moment – i.e., the fluctuations are so large that their mean square deviation from the average field is infinite! In contrast, the dipole distribution has finite fluctuations, although it, too, is somewhat badly behaved, having no moments *higher* than the second.

THERMODYNAMIC VARIABLES

Let us characterize the ferroelectric by using the Landau-Devonshire theory [11]. In this picture, the properties of the ferroelectric near the Curie temperature are determined by its free energy, which is of the form

$$F = -\vec{E} \cdot \vec{D} + \frac{1}{2} a(T) D^2 + \frac{1}{4} b D^4 + \frac{1}{6} c D^6 \tag{18}$$

where D is the displacement, E denotes an external electric field, and a, b, and c are material parameters. We will assume here that (1) the material undergoes a second-order phase transition at T_C, which requires that $c = 0$, $b > 0$, and (2) that only a depends on temperature, specifically that $a(T) = \alpha(T - T_C)$, where T_C is the Curie temperature. Then the relation between the displacement $\vec{D}$ and the electric field $\vec{E}$ is found by minimizing the free energy with respect to the *vector $\vec{D}$* :

$$\frac{dF}{dD_i} = -E_i + \left[a(T) + bD^2\right]D_i = 0 \tag{19}$$

Normally we would just solve this equation for $\vec{D}$, but here the field $\vec{E}$ is a random variable so that a different approach is needed. If we assume that the crystal is isotropic, then the vectors $\vec{D}$ and $\vec{E}$ are always parallel and $\vec{D} = D\hat{n}$ where $\hat{n}$ is the direction of the field $\vec{E}$. Then

$$\vec{D} = \frac{1}{a + bD^2} \vec{E} \Rightarrow D = \frac{1}{a + bD^2} \left|\vec{E}\right| \equiv \frac{1}{a + bD^2} E \tag{20}$$

where E is the magnitude of $\vec{E}$. This implies that

$$E^2 = \left(a + bD^2\right)^2 D^2 \qquad (21)$$

In the presence of an applied field $\vec{E}_a$, the average displacement is given by

$$< D_i > = \int D_i(\vec{E}) P(\vec{E} - \vec{E}_a) d^3 E = \frac{E_f}{\pi} \int D_i(\vec{E}) \frac{d^3 E}{\left(E_f^2 + |\vec{E} - \vec{E}_a|^2\right)^2} \qquad (22)$$

where $E_f = \gamma n = 5.89 \left(\frac{e}{\varepsilon a^2}\right) c$ is the "width" of the field fluctuation distribution. Note

that the distribution is now centered around the deterministic external field $\vec{E}_a$.

Dielectric constant

Let us introduce the variable $x \equiv D^2$. Then $E^2 = x(a + bx)^2$ and $D = \frac{1}{a + bx} E$.

If the z – axis points along the applied field and we write $d^3 E = 2\pi E^2 dE d\xi$, where $\xi = \cos\theta$ depends on the angle between the integration field and the applied field, the integral becomes

$$< D > = < \hat{n}_a \cdot \vec{D} > = \frac{E_f}{\pi^2} \int_0^\infty \frac{E}{a + bx} 2\pi E^2 dE \int_{-1}^1 \frac{\xi d\xi}{\left(E_f^2 + E_a^2 + E^2 - 2EE_a\xi\right)^2}$$

$$= \frac{2E_f}{\pi} \int_0^\infty \frac{E^3 dE}{a + bx} \int_{-1}^1 \frac{\xi d\xi}{\left(E_f^2 + E_a^2 + E^2 - 2EE_a\xi\right)^2} \qquad (23)$$

For small external fields we can expand the angular integrand in a power series. Then the angular integrations are trivial, and we end up with

$$< D > = \frac{2E_f}{\pi} \int_0^\infty \frac{E^3 dE}{a + bx} \left\{ \frac{8E}{3\left(E_f^2 + E^2\right)^3} E_a + \frac{8E\left(-5E_f^2 + 3E^2\right)}{5\left(E_f^2 + E^2\right)^5} E_a^3 + \cdots \right\} \qquad (24)$$

$$= \varepsilon E_a + \beta E_a^3 + \cdots$$

where ε and β are the dielectric constant and tunability of the material. Near the Curie

point we can set $a = 0$, which simplifies the relation between E and x to $E = bx^{3/2}$. This in turn simplifies the integrals, and we find that

$$\varepsilon = \frac{14}{27}E_f^{-2/3}b^{-1/3} \qquad \beta = -\frac{14}{729}E_f^{-8/3}b^{-1/3} \qquad (25)$$

Self-consistency

In the spirit of mean-field theory we now specify that the dielectric constant used to determine the field fluctuation width E_f be the same as the one we calculate from the macroscopic theory, i.e., $E_f = 5.89\left(\dfrac{e}{\varepsilon a^2}\right)c$. At the Curie temperature, however, we know from the previous section that $\varepsilon = \dfrac{14}{27\left(E_f^2 b\right)^{1/3}}$, from which we obtain

$\left(\dfrac{E_f}{b}\right)^{1/3} = \dfrac{11.36 ec}{a^2}$. Solving this for E_f gives $E_f = 1466\left(\dfrac{ec}{a^2}\right)^3 b$. Then

$\varepsilon(T_C) = 5.89\left(\dfrac{ec}{a^2}\right)\dfrac{1}{E_f} = .004\left(\dfrac{ec}{a^2}\right)^{-2}\dfrac{1}{b}$, i.e., the peak in ε is $\propto c^{-2}$. Since the

fluctuation width is affected by the external field E_a, calculating the tunability requires some care. If $\varepsilon = \varepsilon_0\left(E_f\right) + \beta\left(E_f\right)E_a^2$, we apply self-consistency in the following form:

$$\varepsilon\left(E_f\right)E_f = 5.89\left(\dfrac{ec}{a^2}\right) \equiv C_0 \Rightarrow \varepsilon\left(E_f\right) = \dfrac{C_0}{E_f} \qquad (26)$$

Writing the width as $E_f = E_{f0} + \lambda E_a^2$ and equating powers of E_a^2 gives a zero-order equation

$$\varepsilon_0\left(E_{f0}\right) = \dfrac{C_0}{E_{f0}} \qquad (27)$$

and a first-order equation

$$\lambda = -\dfrac{\beta\left(E_{f0}\right)E_{f0}^2}{C_0 + \varepsilon_0{'}\left(E_{f0}\right)E_{f0}^2} \qquad (28)$$

If $\varepsilon = \varepsilon_0\left(E_f\right) + \tilde{\beta}\left(E_f\right)E_a^2$, then

$$\tilde{\beta}\left(E_{f0}\right) = -\lambda\dfrac{C_0}{E_{f0}^2} = 3\beta\left(E_{f0}\right) = -\dfrac{14}{243}E_f^{-8/3}b^{-1/3} \qquad (29)$$

At low concentrations we find that the tunability is $\propto c^{-8}$, i.e., a very strong function of c.

138

Numerical Results

In order to deal with finite temperatures we must allow a to be nonzero, which complicates the analysis. Making the integration variable change $E^2 = x(a+bx)^2$ and $D = \dfrac{1}{a+bx}E$ leads to the following expression for the average displacement:

$$< D > = < \hat{n}_a \cdot \vec{D} > = \frac{2E_f}{\pi} \int_0^\infty x^{3/2}(a+bx)^3(a+3bx)dx$$

$$\cdot \int_{-1}^1 \frac{\xi d\xi}{\left(E_f^2 + E_a^2 + x(a+bx)^2 - 2E_a x^{1/2}[a+bx]\xi\right)^2} \qquad (30a)$$

The angular integral can be carried out easily, but it leads to an awkward expression. Again it is clear that $< D >$ vanishes as $E_a \to 0$. It is possible to modify the theory slightly to obtain the behavior of the material below the Curie temperature as well, from the integral

$$< D > = \frac{2E_f}{\pi} \int_{|a|/b}^\infty x^{3/2}(-|a|+bx)^3(-|a|+3bx)dx$$

$$\int_{-1}^1 \frac{\xi d\xi}{\left(E_f^2 + E_a^2 + x(-|a|+bx)^2 - 2E_a x^{1/2}[-|a|+bx]\xi\right)^2} \qquad (30b)$$
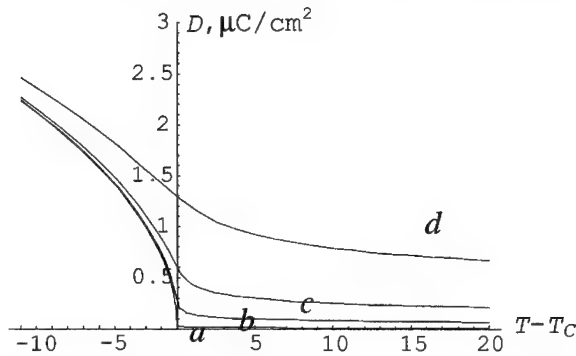

Figure 2. Spontaneous displacement versus temperature for BaSrTiO$_3$ with +3 and +5 ions added. Impurity concentrations: (a) 0.0001, (b) 0.001, (c) 0.01, and (d) 0.1.

Numerical evaluation of $< D >$ leads to the curves shown in Fig. 2. We find the low-field dielectric constant by linearizing in E_a, which yields:

$$\varepsilon = \frac{8E_f}{3\pi} \int_0^\infty \frac{x^{3/2}(a+bx)^3(a+3bx)dx}{\left(E_f^2 + x(a+bx)^2\right)^3}, \qquad T > T_C \qquad (31a)$$

$$= \frac{8E_f}{3\pi} \int_{|a|/b}^\infty \frac{x^{3/2}(-|a|+bx)^3(-|a|+3bx)dx}{\left(E_f^2 + x(-|a|+bx)^2\right)^3}, \qquad T < T_C \qquad (31b)$$
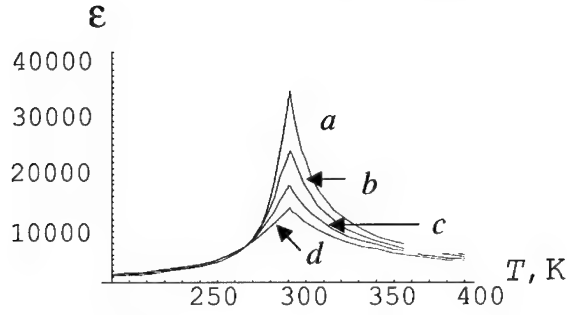

Figure 3. Dielectric constants vs. temperature for dipole-doped BaSrTiO$_3$. Concentrations: (a) 0.005 , (b) 0.006 , (c) .007 , (d) .008.

Self-consistency was imposed numerically on these functions to obtain the curves shown in Fig. 3. The results are within an order of magnitude of what we typically observed in experiments. However, these theoretical curves do not predict the experimentally observed shift in the Curie temperature with concentration [12].

CONCLUSIONS

In light of the crudeness of this theory, it is unlikely that it will be very predictive when applied to real $(Ba_xSr_{1-x})(X,Y)TiO_3$ systems, for a number of reasons: the actual phase transitions in these materials are first order, they are ceramics, etc. Including these phenomena will require at a minimum the use of a version of the Landau-Devonshire theory with $c \neq 0$, making the analysis more complex.
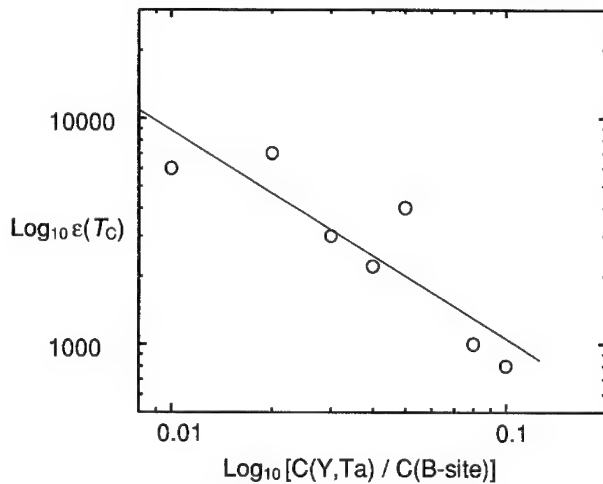

Figure 4. Peak dielectric constant vs. concentration. A least-squares fit gives

$$\text{Log}_{10}\,\varepsilon(T_C) = 2.1 - .92\,\text{Log}(\frac{c_{Y,Ta}}{c_{B-site}}).$$

As an example of the disagreement between theory and experiment, Fig. 4 shows the concentration dependence of the dielectric constant peak for members of the material set $(Ba_xSr_{1-x})(Y,Ta)_yTi_{1-y}O_3$. In contrast to the slope of -2 predicted by theory, a slope close to -1 is observed [13]. It is worth noting that all these materials had different grain sizes, and that the Curie temperature was different for every data point shown. This suggests that the correct dependence will only be derived when the theory can predict concentration-induced changes in T_C as well. We hope to explore this issue in a future publication.

REFERENCES

1. L. D. Landau and I. M. Lifshits, *Electrodynamics of Continuous Media* (Pergamon Press, London, 1960), §13.
2. E. Kane, *Phys. Rev.* **131**, 79 (1963).
3. B. I. Halperin and M. Lax, *Phys. Rev.* **148**, 722 (1966).
4. A. A. Markov, *Wahrscheinlichkeitsrechnung* (Leipzig, 1912), §16 and §33.
5. J. Holtsmark, *Ann. der Physik* **58**, 577 (1919).
6. S. Chandrasekhar, *Rev. Mod. Phys.* **15**, 1 (1943).
7. P. W. Anderson, *Phys. Rev.* **109**, 1492 (1958).
8. A. M. Stoneham, *Rev. Mod. Phys.* **41**, 82 (1969).
9. B. E. Vugmeister and M. D. Glinchuk, *Rev. Mod. Phys.* **62**, 993 (1990).
10. S. K. Ma, *Phys. Rev.* B **22**, 4484 (1980).
11. A. F. Devonshire, "Theory of Ferroelectrics," *Adv. in Phys.* **3**, 85 (1954).
12. D. Potrepka et al., session H, talk 5.5 of this conference.
13. D. M. Potrepka, S. C. Tidrow, and A. Tauber, *Mat. Res. Soc. Symp. Proc.* Vol. 656E, p. DD5.9.1 (2001); D. M. Potrepka, S. C. Tidrow, and A. Tauber, to be published in *Integrated Ferroelectrics*, Vol. 42 (April 2002).

Application of Ferroelectrics in Low-Cost Microwave Phased-Array Antennas

J. B. L. Rao[1], D. P. Patel[1], P. K. Park[2], T. K. Dougherty[3], J. A. Zelik[3], D. S. Prior[3], A. Moffat[4], and L. C. Sengupta[5]
[1]Naval Research Laboratory, Radar Division, Washington, DC, U.S.A.
[2]Raytheon Missile Systems, Tucson, AZ, U.S.A.
[3]Raytheon Electronic Systems, El Segundo, CA, U.S.A.
[4]SFA, Inc., Largo, MD, U.S.A.
[5]Paratek Microwave, Inc., Columbia, MD, U.S.A.

ABSTRACT

A novel, low-cost, phased-array antenna that uniquely incorporates bulk phase shifting using voltage-tunable dielectric (VTD) material is presented. The array does not contain an individual phase shifter at each radiating element. This paper presents the antenna concept and describes how it can be used as a low-cost phased array. The VTDs that are used in this antenna are described. The measured antenna patterns of a prototype phased array demonstrating electronic beam scanning at 10 GHz are also presented.

INTRODUCTION

A phased-array antenna can rapidly scan its beam without mechanical movement. Each radiating element of a phased array is usually connected to a phase shifter or a transmit/receive (T/R) module, which determines the phase of the signal at each element to form a beam at the desired angle. The most commonly used phase shifters are the ferrite and diode varieties. The phase shifters or T/R modules with their control circuitry along with the array feed network account for the major hardware cost in a phased-array antenna. A typical array may have several thousand elements and that many phase shifters or T/R modules; hence, it is very expensive. Therefore, reducing the cost and complexity of the phase shifters or T/R modules and their control circuitry is an important consideration in the design of phased arrays.

The concept of the novel antenna described in this paper has been published elsewhere [1]. We call it the ferroelectric lens phased-array antenna. It uniquely incorporates bulk phase shifting using voltage-tunable dielectrics (VTDs); the array does not contain an individual phase shifter at each element. The number of phase shifters are reduced from ($n \times m$) to ($n + m$), where n is the number of columns and m is the number of rows in a phased array. The number of phase shifter drivers and phase shifter controls is also reduced by the same factor using row-column phase control. This can potentially lead to low-cost phased-array antennas.

An ideal application for the ferroelectric lens is a semiactive tactical missile seeker [2]. Rapid beam switching can advance missile seeker capability including forward looking guidance-integrated fusing and tracking in shorter range.

In this paper, we review the ferroelectric lens concept. We describe the bulk VTD ceramics that we used. We present experimental results of a small column of the lens at X band (8-12.5

GHz). Radiation patterns of a prototype phased array demonstrating electronic beam scanning at 10 GHz are also presented.

DESCRIPTION OF THE FERROELECTRIC LENS

The main feature of the antennas that use VTD is the change of dielectric constant (ε_r) with an applied dc bias voltage. A lens type antenna is discussed in this paper. Figure 1 shows a dielectric lens made-up of dielectric slabs sandwiched between conducting plates. Dielectric slabs are VTDs whose dielectric constant can be changed by applying and varying the dc electric field (dc voltage sources V_1, V_2...V_n are used for this purpose, as shown in Fig. 1). If a plane wave is incident on one side of the lens with RF electric field E normal to the conducting plates, the beam coming out on the other side of the lens can be scanned in the E-plane if a linear phase gradient is introduced along the E-plane direction by adjusting the voltages V_1, V_2...V_n. The corresponding dielectric constants are shown as ε_{r1}, ε_{r2}...ε_{rn}, in Fig. 1.
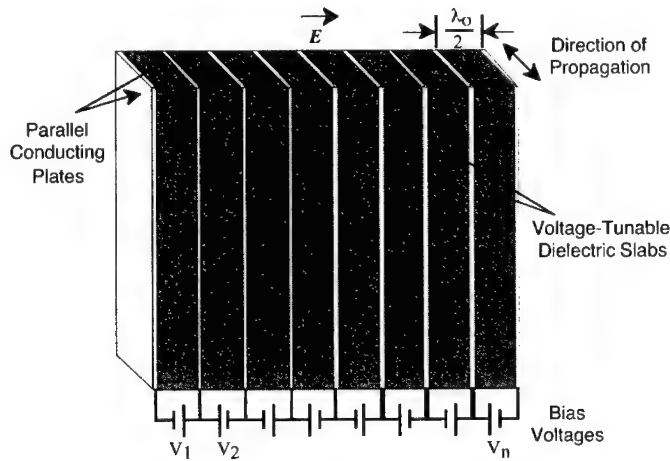

Figure 1. Basic configuration of the ferroelectric lens.

Figure 1 is used to illustrate the principle of operation of a ferroelectric lens. However, it has some limitations. To reduce the lens complexity and weight, the number of dc bias voltages and the number of conducting plates need to be minimized. This can be achieved by selecting the separation between the conducting plates to be slightly less than $\lambda_o/(1+ \sin \phi_s)$, where λ_o is the free space wavelength, and ϕ_s is the maximum scan angle; this separation is the maximum allowed to avoid grating lobes. Normally, the space between the conducting plates would be less than $\lambda_o/2$ to assure that only the dominant transverse electromagnetic (TEM) mode propagates. However, in a ferroelectric lens, this space is filled with a high dielectric constant VTD, and so the space

between the plates is much larger than $\lambda/2$, where λ is the wavelength in the VTD. This means that higher-order modes may propagate. To avoid problems with higher-order modes that may be excited, the spacing between the conducting plates should be reduced to less than $\lambda/2$. In addition, there should be some type of impedance matching arrangement to match the lens surface to free space.

Figure 2 shows a practical lens configuration. This configuration has several advantages over the basic configuration of Fig. 1. Each column of the lens is a parallel-plate waveguide, as shown in Fig. 2 (b). The separation between the parallel-plates at the input and output of the waveguide is $\lambda_o/2$. This separation is reduced using a step of height h. The center section of the column is filled with VTD material, which is bisected with a center bias plate such that the thickness of each VTD piece is less than $\lambda/2$; this eliminates higher-order mode propagation. The center bias plate halves the thickness across which the dc bias voltage is applied thus halving the maximum bias voltage requirement. The use of the center bias plate also allows the parallel plates to be at ground potential. This makes the handling of the lens safer. Quarter-wave dielectric transformers are used for impedance matching the input and output (empty) waveguide sections to the center (VTD-loaded) waveguide section. The dielectric constants of these transformers are between that of air ($\varepsilon_r=1$) and of the VTD ($\varepsilon_r\sim81$).
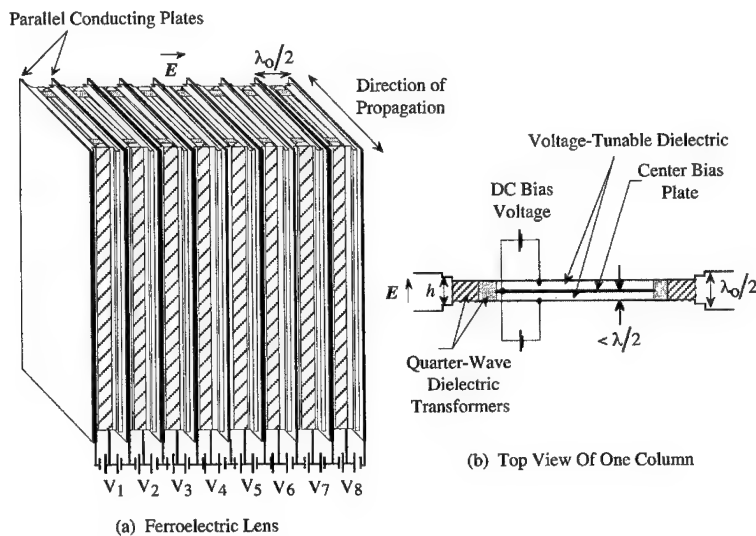

Figure 2. A practical configuration of the ferroelectric lens.

For electronic beam scanning, the VTD must provide 360° differential phase shift. The length of the VTD needed (in the direction of propagation) to obtain 360° differential phase shift is [1]

$$l = \frac{\lambda_o}{\sqrt{\varepsilon_{rmax}} - \sqrt{\varepsilon_{rmin}}} = \frac{\lambda_o}{\sqrt{\varepsilon_{rmax}}\left[1 - \sqrt{1 - \text{tunability}}\right]} \tag{1}$$

where ε_{rmax} is the dielectric constant when no bias voltage is applied, and ε_{rmin} is the dielectric constant when maximum dc bias is applied. The dielectric constant of a VTD decreases as the bias voltage increases. Tunability is the fractional change in the dielectric constant; it is defined as

$$\text{Tunability} = \frac{\varepsilon_{rmax} - \varepsilon_{rmin}}{\varepsilon_{rmax}}. \tag{2}$$

Also, it can be shown [1] that in order to obtain 360° phase shift, the dielectric loss through a low-loss VTD is

$$\alpha\,(dB) = \frac{27.3 \ \tan \delta}{1 - \sqrt{1 - \text{tunability}}} \tag{3}$$

where $\tan \delta$ is the loss tangent of the VTD.

In general, VTDs with larger ε_r (we will use ε_r to denote the dielectric constant with no bias voltage applied) offer higher tunability; both larger ε_r and higher tunability are desired to reduce the lens size. However, the lens impedance matching and fabrication tolerances are easier with smaller ε_r. Therefore, a compromise is a VTD with $\varepsilon_r = 81$ and tunability of 24% at a bias field of 8 V/μm. From Eq. (1), we can show that the length of VTD needed to obtain 360° differential phase shift is less than λ_o (e.g. 3 cm at 10 GHz). From Eq. (3), it can be shown that for a VTD that has 24% tunability, $\tan \delta$ must be 0.0047 to limit the loss due to the VTD to 1 dB, which is our goal. At 10 GHz, $\tan \delta$ of the VTD that we used is 0.007.

PHASED-ARRAY CONFIGURATIONS USING FERROELECTRIC LENS FOR 2-D SCANNING

A single ferroelectric lens provides one-dimensional (1-D) electronic beam scanning. Two-dimensional (2-D) beam scanning can be achieved by cascading two ferroelectric lenses or using one ferroelectric lens in a hybrid configuration with a phased array that can scan the beam in one plane [1].

Figure 3 shows the cascading of two spatially orthogonal ferroelectric lenses. The first lens provides an elevation scan of a vertically polarized wave. A passive 90° polarization rotator then rotates the RF electric field to become horizontally polarized. The second lens then provides the azimuth scanning of the horizontally polarized wave. In Fig. 3, a non-scanning planar array is shown as the illuminator (or feed) for the dual lenses. A space feed can also be used with the dual lens configuration, as shown in Fig. 4. In this configuration, in addition to scanning the beam, row-column phase controls can also be used to correct the spherical phase errors due to the point

space feed. However, this phase correction is not exact, but it is satisfactory for many applications.
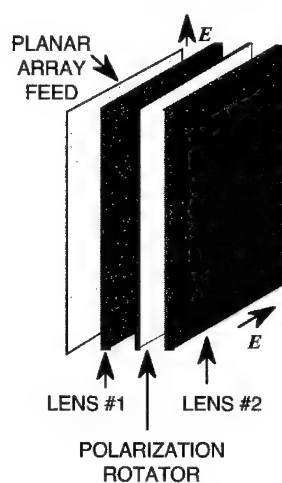

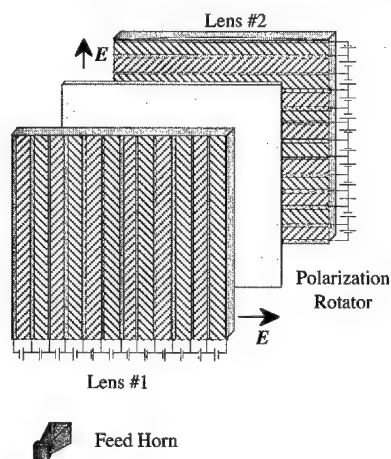**Figure 3**. Dual lens configuration with a planar array feed.

Figure 4. Dual lens configuration with a space feed.

Another method of achieving 2-D beam scanning uses a hybrid technique in which a planar array with phase shifters scans the beam in one plane and the ferroelectric lens scans the beam in

the other plane. For example, as shown in Fig. 5, a slotted waveguide array with phase shifters provides electronic beam scanning in the azimuth plane. Electronic beam scanning in the elevation plane is obtained by placing a ferroelectric lens in front of the slotted waveguide array.
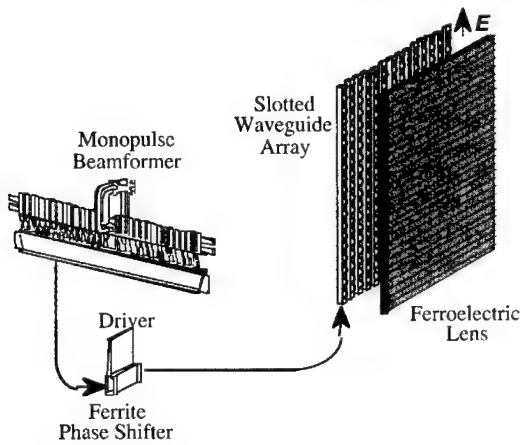

Figure 5. Hybrid phased array configuration for 2-D scanning.

VOLTAGE-TUNABLE DIELECTRICS

VTDs that we used are bulk composite ceramics of tunable ferroelectrics in the paraelectric phase and non-tunable materials [1,3]. In addition to providing bulk phase shift, VTDs offer reciprocal phase shift; i.e., the transmission coefficient through devices that use these materials is the same for different directions of propagation. Ferroelectrics are inherently broadband. That is, they do not have a low frequency limit like ferrites. Until the development of these bulk composites, the large ε_r and tan δ of ferroelectric materials excluded them from being used at microwave frequencies. VTDs can be manufactured in bulk, thick film and thin film forms. Only bulk ceramics are suitable for the ferroelectric lens because of the physical size and power handling requirements.

There are many known ferroelectrics. The ferroelectric in the VTD that we used was Barium Strontium Titanate, (BST), specifically $Ba_{0.55}Sr_{0.45}TiO_3$. BST is the most widely used ferroelectric at microwave frequencies. We are interested in applications at X band. Experiments were conducted at X band with a VTD whose ε_r and tan δ were 81 and 0.007, respectively at 10 GHz. Tunability was a respectable 24% at a bias of 8 V/μm. Curie temperature, T_c, was -75°C, which means that the BST is in the paraelectric phase at room temperature. T_c is controlled not only by the Ba:Sr ratio, but also by the amount of the non-tunable material that is added. Using Eq. (3), the loss due to the VTD for obtaining 360° differential phase shift was calculated to be 1.5 dB at 10 GHz.

EXPERIMENTAL RESULTS

Lens columns have been designed, built and tested at C band (4-8 GHz) and X band. Figure 6 shows the experimental setup with one column of the lens. A Network Analyzer is connected to a rectangular waveguide through a coax-to-waveguide transition. The width of the waveguide is flared to create an *H*-Plane horn, which feeds the parallel plate column. The network analyzer measures the s-parameters of the column as a function of frequency and dc bias voltage.
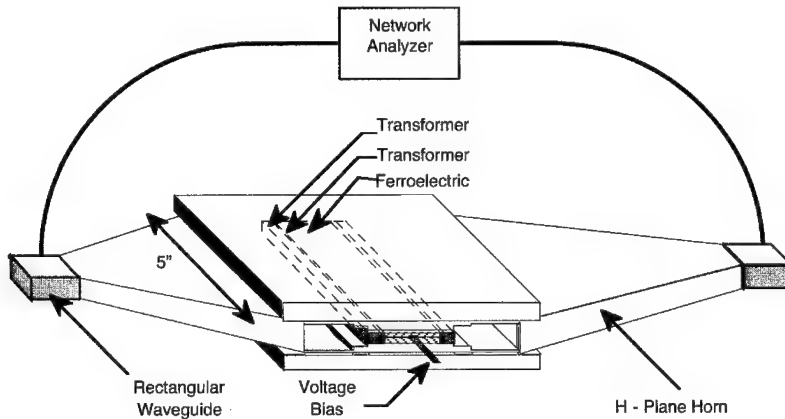

Figure 6. Experimental setup for one column.

At X band, the largest VTDs that we have used were 2.54 cm long (in the direction of propagation), 0.13 cm high and 12.7 cm wide [1]. Figure 7 shows the measured voltage transmission and reflection coefficients of a small lens column at X band when the dc bias is zero. This column included VTD whose ε_r and tan δ are 81 and 0.007, respectively, at 10 GHz. The transmission coefficient is inversely proportional to frequency. This is due to two reasons. First, tan δ increases with frequency; second, the electrical length (in terms of wavelengths) of the VTD in the direction of propagation increases with frequency since the physical length is kept constant (2.54 cm). The wideband impedance matching design that we have developed provides very low reflection coefficient over the broad frequency range of 8-12 GHz. The measured voltage reflection coefficient is less than 0.22, which corresponds to a voltage standing wave ratio (VSWR) of less than 1.6. The reflection coefficient does not increase as dc bias is applied to decrease the VTD's ε_r [1]. Figure 8 plots the measured differential phase shift at several frequencies as a function of the dc bias. As expected, the phase shift is fairly linear with frequency and dc bias. We have obtained more than 360° differential phase shift at 12 GHz at a dc bias of 8 V/μm. Using the measured data shown in Fig. 7, the loss due to the VTD can be calculated. This loss is plotted in Fig. 9 as a function of frequency. The loss is about 1.8 dB at 10

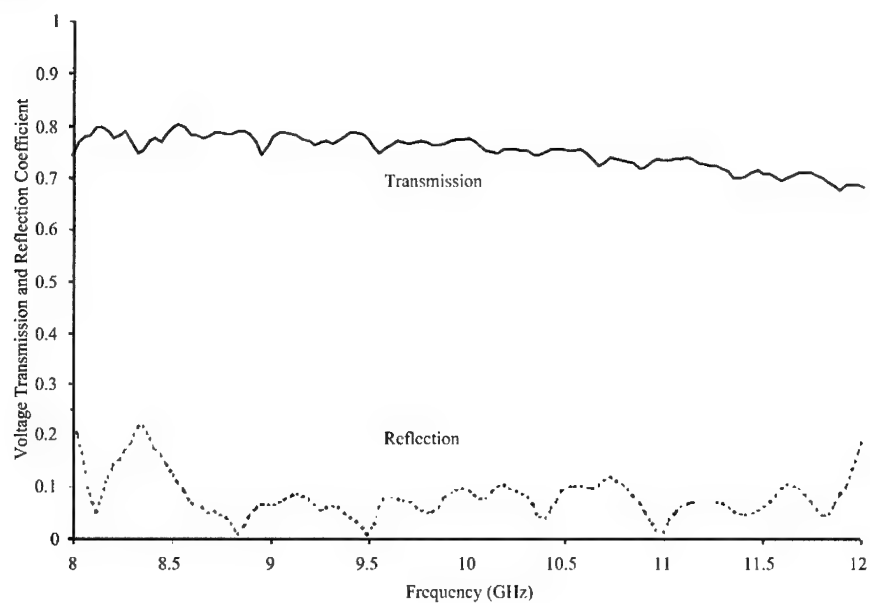GHz, and it is proportional to frequency. The measured loss agreed well with theoretical prediction.

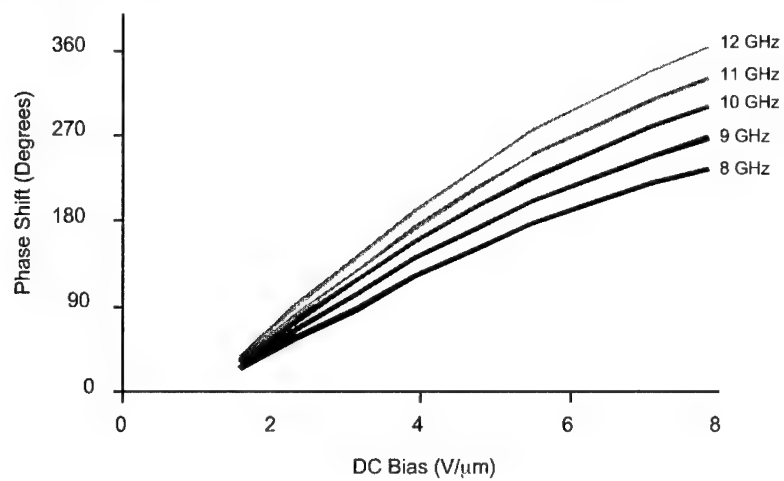**Figure 7**. Measured voltage transmission and reflection coefficient of a lens column.

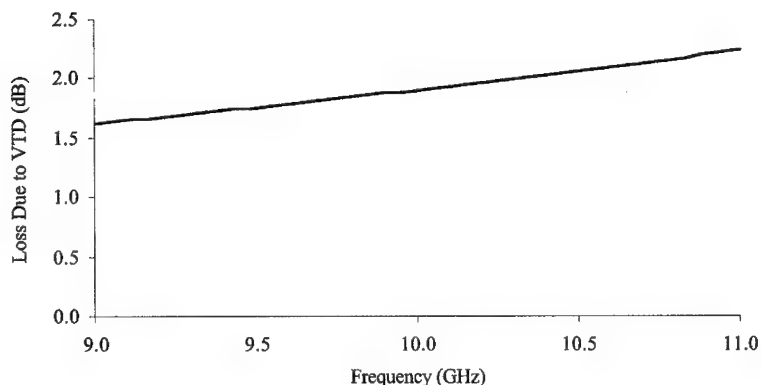**Figure 8**. Measured differential phase shift at X band.

Figure 9. Measured loss due to the VTD at X band.

A two-column interferometer and a 3-column lens have been built and demonstrated at the Naval Research Laboratory. The radiation patterns of these phased arrays were measured. Electronic beam scanning was demonstrated at X band. There was no indication of any material inhomogeneity in the patterns.

For the tactical missile seeker application, a 12-column lens was built and demonstrated at Raytheon [4]. The pattern was measured as dc bias was applied to each column to scan the phased-array antenna pattern. Fig. 10 shows the prototype antenna in an antenna test chamber. In Fig. 11 four of the measured patterns are plotted for 10 GHz frequency. Electronic beam scanning was again demonstrated; the beam clearly scanned to 60°.

PLANS

A ferroelectric lens phased-array antenna has been demonstrated at X band. There is strong interest to operate missile seekers at higher frequencies, especially Ka band (27-40 GHz). At these frequencies, wide frequency bandwidths and narrow antenna beamwidths can be achieved. Presently, we are developing two different ferroelectric lens phased arrays at Ka band. One architecture is based on the designs described in this paper, which were conceived at NRL. Another architecture which is under investigation at Raytheon may provide 2-D scanning with one lens. Compared to the NRL architecture, the design and manufacturing of this architecture would be complicated but the loss might be less. The results of these investigations will be published at a later time.
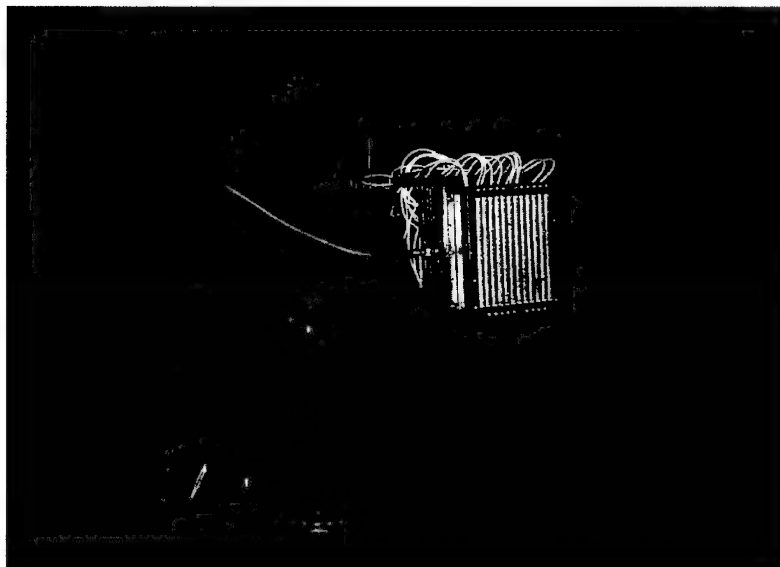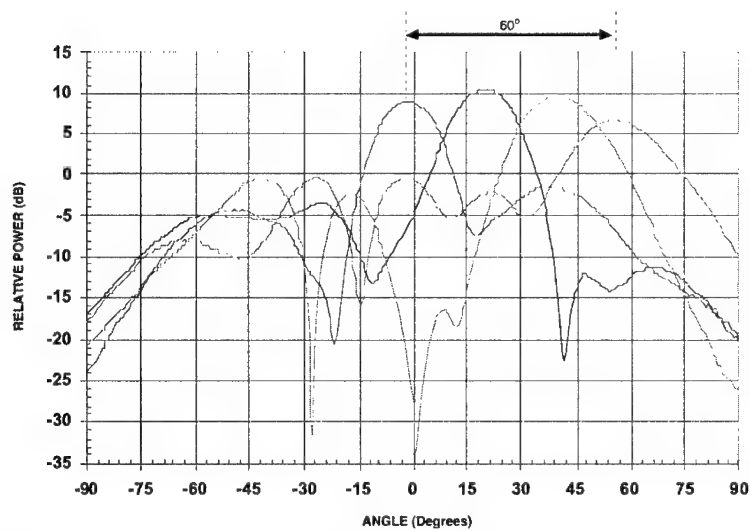
Figure 10. Prototype ferroelectric lens.

Figure 11. Measured radiation patterns of the prototype ferroelectric lens at 10 GHz for four different scan angles.

SUMMARY

The work done so far in developing the ferroelectric lens, a low-cost, phased-array antenna, was reviewed. The VTD ceramics that we used provide 360° differential phase shift with about 2 dB loss at 10 GHz. Electronic beam scanning has been demonstrated in a prototype ferroelectric lens at 10 GHz. Work is continuing in reducing the loss in the dielectrics.

ACKNOWLEDGMENTS

REFERENCES

1. J. B. L. Rao, D. P. Patel, and V. Krichevsky, "Voltage Controlled Ferroelectric Lens Phased Arrays," IEEE Trans. Antennas Propag., vol. 47, pp. 458-468, March 1999.
2. P. K. Park, S. H. Kim, J. Gandolfi, R. T. Tadaki, T. K. Dougherty, D. Patel, J. Rao, L. Sengupta, S. Wolf, and D. Treger, "Low Cost Planar Lens ESA," in Digest 2000 IEEE Antennas and Propag. Soc. Int. Symp., 2000, pp. 974-977.
3. L.C. Sengupta, E. Ngo, J. Synowczynski, and S. Sengupta, "Optical and Electrical Studies of Novel Ferroelectric Composites for Use in Phased Array Antennas," in Proc. 10th Int. Symp. Applications Ferroelectrics (*ISAF '96*). B. M. Kulwicki, A. Amin, and A. Safari, Ed. 1996, pp. 845-849.
4. J. B. L. Rao, D. P. Patel, P. K. Park, T. K. Dougherty, J. A. Zelik, A. Moffat, and L. C. Sengupta, "Application of Ferroelectrics in Microwave Phased-Array Antennas," in Program Summary and Extended Abstracts of the 10th US-Japan Seminar on Dielectrics and Piezoelectric Ceramics, 2001, pp. 95-98.

H5.3

An S-Band Reflection-Type Phase Shifter - A Design Example Using Ferroelectrics

Dongsu Kim[1], Yoonsu Choi[1], Mark G. Allen[1], J. Stevenson Kenney[1], David W. Stollberg[2], and David Kiesling[2]
[1]School of Electrical and Computer Engineering,
Georgia Institute of Technology, Atlanta, GA 30332, U.S.A.
[2]MicroCoating Technologies, Inc. Chamblee, GA 30341, U.S.A.

ABSTRACT

One of the challenges faced in using ferroelectrics in high frequency devices is how to effectively use the material in a circuit design. A compact reflection-type phase shifter fabricated on sapphire substrates coated with ferroelectric barium strontium titanate (BST) thin-films has been built which shows the promise of using BST thin films in the design of tunable microwave devices. The phase shifter, fabricated as one monolithic assembly, consists of a 3dB coupler, meandered line inductors and tunable interdigital capacitors. A continuously variable phase shift range of more than 100° using the branch-line coupler was obtained at a center frequency of 2.95 GHz, and more than 90° phase shift over 200 MHz bandwidth with a bias voltage range from 0 V to 175 V. The phase shifter using the Lange coupler has over 700 MHz bandwidth centered at 2.2 GHz with a phase shift of more than 90° and an insertion loss less than 2 dB and return loss of greater than 14 dB, over a bias voltage range from 0 V to 160 V. The loss of the BST phase shifter presented in this work is on the order of other commercially available RF front-end components, such as bandpass filters and RF switches. This holds promise for the practical realization of smart antenna systems in cellular handsets and wireless LAN cards.

INTRODUCTION

With the recent increase in market demand for mobile communications devices, there has been added pressure to minimize the size of microwave components, such as filters, couplers and phase shifters. It has been known that the high dielectric constant and electric field dependence of ferroelectric materials, such as strontium titanate ($SrTiO_3$) and barium strontium titanate ($Ba_xSr_{1-x}TiO_3$), allow for miniature tunable microwave components [1]-[6]. In addition, ferroelectric-based phase shifters have several advantages over *pin* diode and ferrite phase shifters: monolithic integration, fast speed of tuning and much lower control-line power dissipation [5]. The phase shifter presented in this paper is a fully integrated monolithic device. All components are fabricated directly on the BST coated substrate. The design was targeted for S-Band operation to demonstrate the ability of this technology to achieve good low frequency phase shifter performance in a small volume.

Coplanar waveguide (CPW) structures are used to confine electric fields near the substrate surface, keeping a large percentage of the electric field in the BST, hence maintaining a high effective dielectric constant and a large tunability. A thick copper (Cu) metallization process, adopted from MEMS techniques, is used to minimize conductor losses in the distributed elements [7]. Air bridge crossovers are also used to connect ground planes and suppress spurious modes. Two identical LC networks are connected to a coupler to achieve the phase shift. The integrated approach described herein allows better performance than a discrete approach in that phase shifter networks fabricated on one substrate are well matched, thus improving return loss.

SUBSTRATE FABRICATION

Barium strontium titanate (BST) thin films were prepared by MicroCoating Technologies (MCT) using their patented, open-atmosphere combustion chemical vapor deposition (CCVD) process [8]. Since the investigations will be carried out at room temperature, a composition of $Ba_{0.6}Sr_{0.4}TiO_3$ was used so that the material would be operating in the paraelectric phase where a large change in ε_r with respect to bias voltage would occur. The barium to strontium ratio gives an expected Curie temperature of $-10°C$. For this investigation, a single crystal aluminum oxide substrate was selected resulting in BST with a <111> orientation. A variety of material analytical techniques were used to determine the physical properties of the film samples. X-ray diffraction (XRD) was performed on all samples, θ-2θ scans, see Figure 1, to determine the crystal structure of the deposited films. Film surface morphology was examined using optical profilometry, Figure 2 (a), and scanning electron microscopy, Figure 2 (b). These analyses showed a smooth, dense-appearing uniform film. The thicknesses of $Ba_{0.6}Sr_{0.4}TiO_3$ and sapphire were 0.45 μm and 430 μm, respectively. A bulk BST dielectric constant of $\varepsilon_r = 800$ was found to give the best fit to measured data of CPW line using electromagnetic field simulation using the Microwave Office^{TM}.
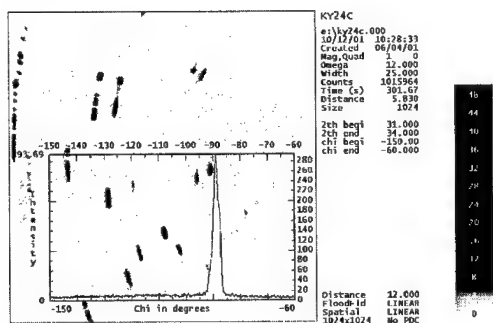

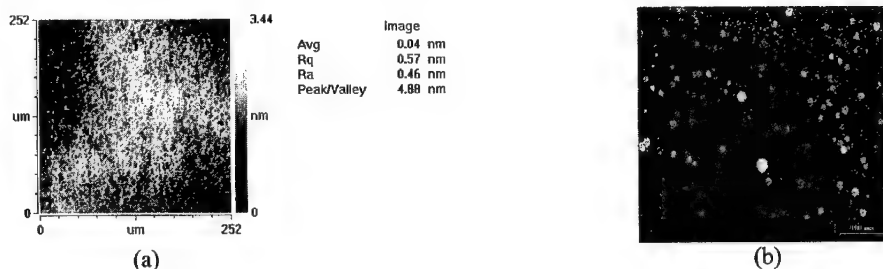**Figure 1.** Representative XRD analysis θ-2θ scan.

(a)

(b)

Figure 2. Film surface. (a) Representative optical profilometry map and (b) Representative scanning electron microscope micrograph.
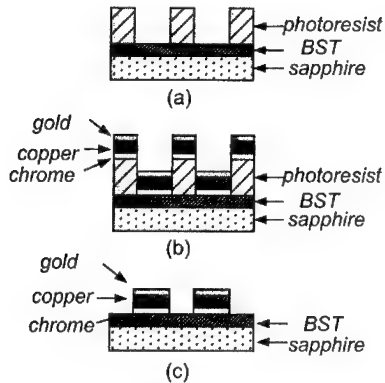
Figure 3. Metallization processing of the BST/sapphire substrate.

The metallization processing of the substrate is shown in Firgure 3. 200 Å of chrome deposited as an adhesion layer after patterning a thick photoresist layer. On top of the chrome, 2.7 μm of copper was deposited to form the main conductor layer with a cap of 0.3 μm of gold as an oxidation barrier for the copper. A lift-off process was then used to create the metal pattern on the substrate.

CIRCUIT DESIGN AND EXPERIMENTAL RESULTS

The schematic of the reflection-type phase shifter is shown in Figure 4. Because 90° phase shift increments may be switched in using quadrature hybrids, 90° is the minimum range of phase shift needed from a variable phase shifter. A 3-dB branch-line coupler was designed using meandered lines instead of straight lines in order to reduce total size of the phase shifter [9]. The 3-dB coupler is combined with two identical LC networks and bias network. The photomicrographs of the phase shifter using the branch-line coupler and the Lange coupler are shown in Figure 5.
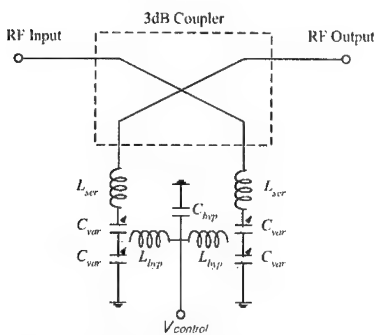

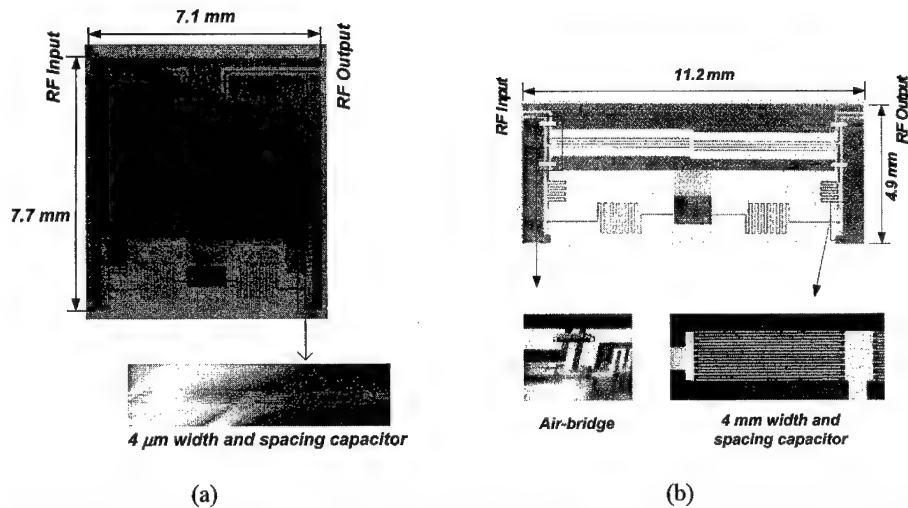**Figure 4.** Schematic of the reflection-type phase shifter.

(a)   (b)

Figure 5. Photomicrograph of the reflection-type phase shifter, air-bridge, and 4 μm interdigital capacitor using (a) the branch-line coupler (b) the Lange coupler.
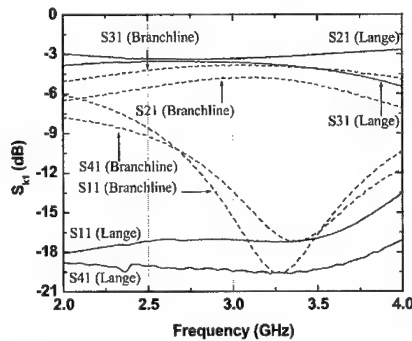

Figure 6. Measured results of the branch-line coupler and the Lange coupler.

S-parameters of the branch-line coupler, the Lange coupler and the phase shifter were measured using HP8753C network analyzer and Cascade Microtech ground-signal-ground microwave probes. S-parameters of the couplers as a function of frequency are shown in Figure 6. Magnitudes of signals at direct and coupled ports of the branch-line coupler at 3 GHz are 4.7 and 3.8 dB, respectively. The return loss and isolation are greater than 13 dB between 2.96 and 3.73 GHz. The Lange coupler has 3.5 ± 0.5dB in the range of 2-3.4 GHz or 52% for 1-dB amplitude balance. In addition, the isolation is greater than 18 dB, and voltage standing wave ratio (VSWR) is less than 1.4 in the same frequency range. Therefore, the Lange coupler has an advantage over the branch-line coupler because of larger bandwidth. The insertion and return loss of the reflection-type phase shifter are shown in Figure 7. The most equal insertion loss of the phase shifter using the branch-line coupler for all bias levels occurs at 2.95 GHz and is between 4.0 and

4.2 dB over the bias range. The insertion loss is less than 5 dB between 2.83 GHz and 3.03 GHz, with a variation of no more than 2 dB. The return loss is greater than 12.5 dB at 2.95 GHz, and greater than 10 dB over a range 200 MHz as shown in Figure 7(a). Except for the narrow band resonance associated with the Lange coupler isolation response at 2.35 GHz, the maximum insertion loss is 2 dB between 1.6 GHz and 3.7 GHz with all bias states in Figure 7(b). Also, the return loss is greater than 14 dB in the range of 1.85-3.8 GHz.
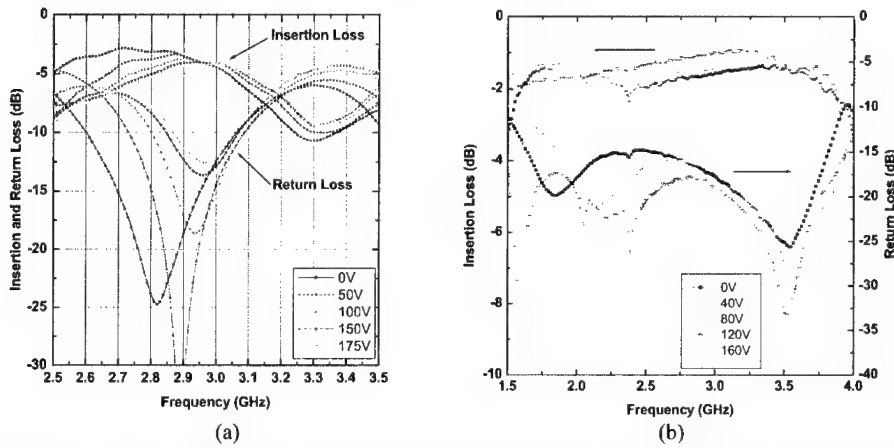

Figure 7. Insertion loss and return loss versus frequency (a) using the branch-line coupler (b) using the Lange coupler.
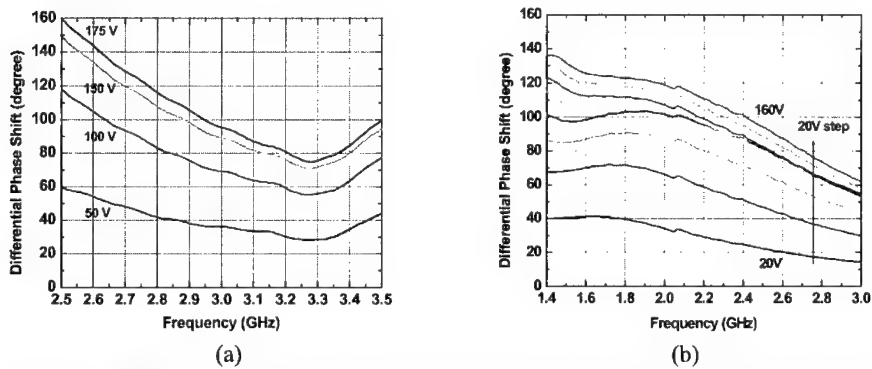

Figure 8. Differential phase shift with respect to phase at 0V using (a) the branch-line coupler (b) the Lange coupler.

Figure 8 shows the relative phase shift with respect to the phase at 0V. About 110° phase shift was achieved at 2.85 GHz over a 0V to 175 V range and more than 90° was achieved over ± 100 MHz about 2.95 GHz using the branch-line coupler as shown in Figure 8(a). Also, more than 136° phase shift is achieved at 1.42 GHz and more than 90° between 1.85 and 2.56 GHz with a

bias voltage of 160 V using the Lange coupler. The BST reflection-type phase shifter has maximum 89°/dB at 1.87 GHz and greater than 44°/dB in the range of 1.52-2.56 GHz with a bias voltage of 160 V.

CONCLUSION

A monolithic reflection-type phase shifters using the branch-line coupler and the Lange coupler on $Ba_{0.6}Sr_{0.4}TiO_3$/sapphire were designed, fabricated and tested. Experimental results showed more than 90° phase shift was achieved at 2.95 GHz over ± 100 MHz range using the branch-line coupler. Also, the phase shifter using the Lange coupler has a phase shift range of more than 90° with an insertion loss of less than 2 dB and a return loss of greater than 14 dB in the frequency range of 1.85-2.56 GHz over a bias voltage range from 0 V to 160 V. The maximum 89°/dB was achieved at 1.87 GHz with a bias voltage of 160 V.

ACKNOWLEDGEMENT

REFERENCES

1. G. Subramanyam, F.A. Miranda, R.R. Romanofsky, F.W. Van Keuls, C.L. Canedy, S. Aggarwal, T. Venkatesan, and R. Ramesh, "A Ferroelectric Tunable Microstrip Lange Coupler For K-Band Applications", *Microwave Symposium Digest, 2000 IEEE MTT-S International*, Vol. 3, pp.1363-1366, 2000.
2. E.G. Erker, A. S. Nagra, Y. Liu, P. Periaswamy, T. R. Taylor, J. Speck, and R. A. York, "Monolithic Ka-Band Phase Shifter Using Voltage Tunable BaSrTiO3 Parallel Plate Capacitors", *IEEE Microwave Guided Wave Lett.*, Vol. 10, No. 1,pp. 10-12, Jan. 2000.
3. A.Kozyrev, A.Ivanov, V.Keis, M.Khazov, V.Osadchy, T.Samoilova, O.Soldatenkov, A.Pavlov, G.Koepf, C.Mueller, D.Galt, and T.Rivkin, "Ferroelectric Films: Nonlinear Properties and Applications in Microwave Devices", *Microwave Symposium Digest, 1998 IEEE MTT-S International*, Vol. 2, pp. 985-988, 1998.
4. F. De Flaviis, N.G. Alexopoulos, O.M. Stafsudd, "Planar Microwave Integrated Phase-Shifter Design with High Purity Ferroelectric Material", *IEEE Trans. Microwave Theory Tech.*, Vol. 45, No. 6, pp. 963-969, June 1997.
5. A. Kozyrev, V. Osadchy, A. Pavlov, and L. Sengupta, "Application of Ferroelectrics in Phase Shifter Design", *Microwave Symposium Digest, 2000 IEEE MTT-S International*, Vol. 3, pp.1355-1358, 2000.
6. D. Kim, Y. Choi, M. G. Allen, J. S. Kenney, and D. Kiesling, "A Wide Bandwidth Monolithic BST Reflection-Type Phase Shifter Using A Coplanar Waveguide Lange Coupler", to appear in *the 2002 IEEE MTT-S Int. Microwave Symp. Dig.*, Seattle, WA, June, 2002
7. F. Cros, and M.G. Allen, "High Aspect Ratio Structures Achieved by Sacrificial Conformal Coating", *Proc. 1998 Solid State Sensors and Actuators Conf.*, Hilton Head, SC.
8. Microcoating Technologies, Inc. Chamblee, GA, http://www.microcoating.com
9. A.A. Omar, S. Meszarps and M.G. Stubbs, " Design of A Ku-Band Coplanar Waveguide 90° Branchline Coupler", *IEEE AP-S Digest*, Vol. 3, pp. 2216-2219, 1994

The Dependence of Dielectric Properties on Composition Variation in

$Ba_{0.6}Sr_{0.4}(YTa)_yTi_{1-2y}O_3$

Daniel Potrepka, Steven Tidrow, Arthur Tauber, Kevin Kirchner, Matthew Ervin, Krishna Deb, Bernard Rod, and Frank Crowne
Sensors & Electron Devices Directorate, U.S. Army Research Laboratory,
Adelphi, MD 20783-1197, U.S.A.

ABSTRACT

$Ba_{0.6}Sr_{0.4}(YTa)_yTi_{1-2y}O_3$ has been shown to have properties which are promising for tunable applications requiring low dielectric constant [1]. $Ba_{0.6}Sr_{0.4}(YTa)_yTi_{1-2y}O_3$ with $y \leq 0.10$ has been synthesized and well-characterized using x-ray diffraction, EDAX, and Raman Spectroscopy. The dependence of the dielectric properties on concentration, y, of Y and Ta are discussed along with implications for improved performance in device applications.

INTRODUCTION

It has been shown that binary charge-balanced substitutions of 3+ and 5+ ions into the B site (for Ti^{4+}) in $Ba_{1-x}Sr_xTiO_3$ (BST) lead to changes in the characteristics of the ferroelectric (FE) transition, Curie Temperature (T_c), and tunability of the dielectric constant that do not occur for non-charge-compensated doping of BST or for 4+ substitutions into the Ti^{4+} site [1,2]. The binary charge-balanced substitution of 3+ and 5+ ions for Ti lead to greater applicability of the FE technology due to broader temperature ranges of operation which include the U. S. Military Specification temperature range (mil spec). Such behavior is consistent with device requirements as discussed in References [3,4] where tunability is of major importance but losses are of less importance. For certain choices of charge-balanced substitution of 3+ and 5+ ions, T_c shifts dramatically by as much as $-60\ ^oC$ or more accompanied by a significant broadening of the FE transition. The behavior of the tunability in such cases is similar to that of the dielectric constant, reflecting the broadening and shifting of the difference between the dielectric constant at zero electric field and the dielectric constant tuned by the application of a DC electric field. This paper focuses on research investigations which seek to characterize, in more detail, the compositional dependence of the dielectric properties due to simultaneous variation of the Y and Ta content in the Ti site. Results of effects of sintering temperature (T_s) on selected charge-balanced substitutions, y, are presented and discussed. The character of the synthesized material has been studied using x-ray diffraction, Raman spectroscopy, density, and SEM measurements. Electrical properties were obtained through studies of the temperature dependence of the capacitance. The lattice constant, grain size, dielectric constant, tunability, and an electric-field– and temperature–dependent figure of merit (FOM) were studied to determine the effects of the Y and Ta concentration variation and changes in T_s.

EXPERIMENTAL DETAILS

Compositions of $Ba_{0.6}Sr_{0.4}(YTa)_yTi_{1-2y}O_3$ with $y \leq 0.10$ were prepared by mixing $BaCO_3$, $SrCO_3$, Y_2O_3, Ta_2O_5, and TiO_2 in stoichiometric proportions. The samples were then ground and pressed into pellets which were calcined at $1100\ ^oC$ for 8 hours. Next the samples were reground

and pressed at 50 kpsi, then sintered between 1450 °C and 1600 °C. There were particular samples with $y = 0.03$ and 0.05, which were separated into two parts of equal mass prior to sintering. One portion of each composition was then sintered at a temperature of $T_s = 1550$ °C and the other was sintered at 1600 °C. After sintering, a portion of each synthesized sample was cut away and ground and polished. Volume densities were obtained on a microbalance, θ-2θ x-ray diffraction scans and diffraction ring graphs were obtained using Cu Kα1 radiation, and Raman spectroscopy was performed. For each sample, contacts were then deposited to form a parallel plate capacitor, and capacitance was measured at a sampling frequency of 1 MHz with applied DC electric fields in the range $0 \leq E \leq 1$ V/μm and the temperature varied over –75 °C $\leq$ $T \leq 100$ °C using an environmental chamber. Selected samples were fractured and the grain structure was studied using SEM. Nominal grain sizes were estimated for samples with different y.

RESULTS

The ratio of the volume density to the theoretical value (in percent) was found to drop from ~ 95 % for $y = 0$ to ~ 60 % for $y \geq 0.03$. Theoretical densities were estimated using the lattice constants obtained by x-ray diffraction measurements. For samples with $y = 0.03$ and 0.05 that were sintered at 1450 – 1600 °C, T_s was found to have a modest effect on density, with the density increasing up to 10% with increases over this temperature range. The x-ray diffraction scans show that the samples are single phase and cubic up to $y = 0.08$. At $y = 0.10$ a peak due to second phase appears at d = 3.06502 Å and splitting is observed in the major peaks that are significantly above the noise levels indicating deviation from the cubic structure. For $y = 0.05$, spots associated with the beginnings of grain size enhancement or grain growth ordering in the samples were more enhanced in the x-ray diffraction rings for samples sintered at 1600 °C than at 1550 °C. Spots indicative of grain growth were seen in the rings for the $y = 0.03$ sample sintered at 1550 °C. In addition, for $T_s = 1600$ °C compared to $T_s = 1450$ °C, the lattice constant is smaller by a significant amount (0.005 Å) for $y = 0.03$, but by an insignificant amount (≤ 0.003 Å) for $y = 0.05$. This may be an indication of ordering [5]. There was no evidence of superlattice peaks in the x-ray diffraction scans. Further evidence of the nature of the lattice was obtained from the Raman studies. For $y \leq 0.05$, the 306 cm^{-1} position associated with the E(TO$_2$) Raman line in BaTiO$_3$ was monitored. The absence of an E(TO$_2$) peak was observed on a linear scale. This is consistent with the expected behavior for Ba$_{1-x}$Sr$_x$TiO$_3$, $x \geq 0.32$ [6]. However, on a log scale, there appears a shallow bump at ~ 306 cm^{-1} for each sample in the range $0.01 \leq y \leq$ 0.05 (Figure 1) which may be evidence of the onset, with YTa concentration, of the noncubic phase observed in the θ-2θ diffraction scan for the $y = 0.10$ phase.

Nominal grain sizes estimated from the SEM studies of samples are shown in Figure 2 for T_s and y values. The grain size drops by an order of magnitude from ~ 30 μm for $y = 0$ (BST) to ~ 1 μm for $y = 0.01$. Grain-like features are observed for $0.04 \leq y \leq 0.10$ at low T_s (1450 °C – 1500 °C) but do not appear to be well-defined. In all samples with $y > 0$, the porosity of the samples due to Ostwald ripening [7] can be observed and volume densities are ~ 65 % compared to ~ 93 % for $y = 0$. For $y = 0.03$ and 0.05, at the more elevated T_s values of 1550 °C and 1600 °C, distinct cubic grain features are clearly seen in the cleaved sections and at the walls of the porous regions. For an increase in T_s from 1550 °C to 1600 °C, the grain size is estimated to double, from 1 μm to 2 μm for both the $y = 0.03$ and the $y = 0.05$ samples.

The dielectric constant (real relative permittivity, ε) plotted versus temperature (Figure 3) is consistent with similar plots for the general case of simultaneous substitution of 3+ and 5+
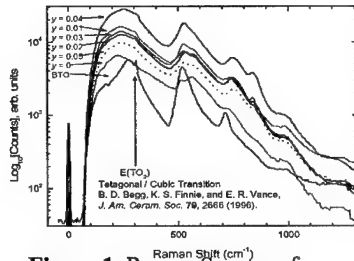
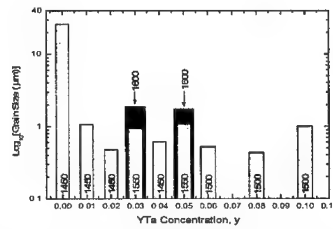**Figure 1.** Raman Spectra of $Ba_{0.6}Sr_{0.4}(YTa)_yTi_{1-2y}O_3$

Figure 2. Grain Size vs YTa content, y. Numbers denote sinter temperature, $T_s(^oC)$.

ions for Ti as reported in References [1,2]. In that work, T_c shifted to lower temperature, the FE transition broadened and the magnitude of ε was markedly reduced for small concentrations ($y = 0.03$) for many such ion pairs. In comparison, substitutions of 4+ ions for Ti do not shift the T_c of BST very much but can broaden the FE transition and reduce ε [2,8]. The behavior of T_c with concentration of Y and Ta is plotted in Figure 4 (in analogy to similar plots for BST [8]) and that of the peak value of the dielectric constant $\varepsilon(T_c)$, in Figure 5. For Figure 5, the values of $\varepsilon(T_c)$ for $y = 0.08$ and 0.10 are obtained by a graphical extrapolation of Fig. 4 and of $\varepsilon(T)$ below the minimum measurement temperature, $-75\ ^oC$, of the environmental chamber. For the device applications that these studies are relevant to, temperature-insensitive materials over the mil spec range are desired so that the device can operate without the added burden of refrigeration or heating and to eliminate sensitivity to sudden temperature spikes or fluctuations. The material must also be highly-tunable [4]. Therefore, a figure of merit (FOM) was developed for the perovskites studied which is given by the expression,

$$FOM = \frac{\left(\Delta\varepsilon / \Delta E\right)}{\left(\Delta\varepsilon / \Delta T\right)}\bigg|_T \tag{1}$$

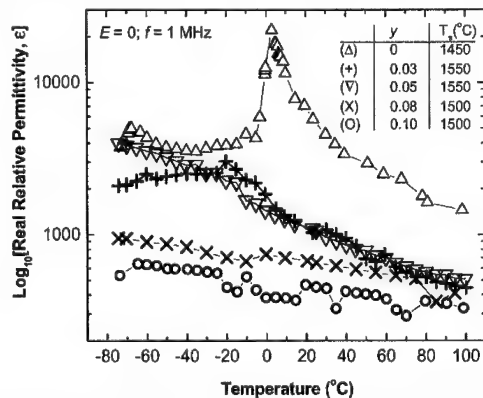Figure 6 shows the tunability plots for $y \leq 0.10$ and their respective values of the FOM evaluated

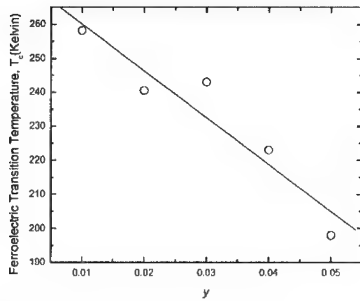**Figure 3.** Dielectric constant vs temperature for $y \leq 0.10$, $T_s \leq 1550\ ^oC$.

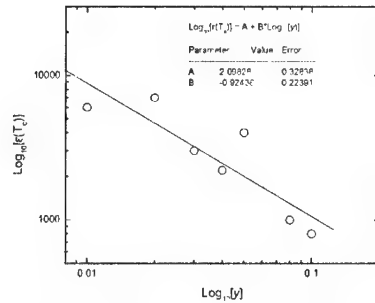**Figure 4.** Ferroelectric Transition Temperature, T_c, vs YTa content, y.

Figure 5. Dielectric constant at the critical temperature, $\varepsilon(T_c)$, vs YTa content, y.

at the maximum dielectric constant measured. This FOM is largest at the intermediate concentration of $y = 0.05$. More importantly, the FE transition and tunability broaden as y increases, and the FOM approaches a constant value over a larger portion of the mil spec range.

Figure 7 shows ε plotted versus temperature for $y = 0.03$ and 0.05 and $T_s = 1550$ °C and 1600 °C. Figure 8 shows the corresponding tunability plots and their FOM values. Recall that, in Figure 2, increased concentrations, y, of Y and Ta reduce the grain size for low T_s (≤ 1550 °C), but this can be reversed somewhat with increase in T_s with very little measured change in density. Spots, which are an indication of grain growth, begin to occur in the area detector images obtained from x-ray diffraction at 1550 °C and 1600 °C. Also for increase in T_s from 1550 °C to 1600 °C, grain size increases and grains become more faceted, as observed in the SEM micrographs, plus the FE transition is sharpened. Since grain size increases were observed for both decreased y and increased T_s, one may thus wish to see if grain size changes are the sole cause of the changes in the ferroelectric nature of the BST as Y and Ta are added while maintaining charge balance. However, when grain size is increased due to increase in T_s, not all the electrical characteristics are reversed relative to those due to decrease in y. T_c shifts to a lower temperature with both increased y and increased T_s. So the changes in the grain size that occur for changes in y due to increased but charge-balanced additions of Y and Ta to BST do not appear to be the sole cause of changes in the nature of the ferroelectric transition away from that of BST as y increases. A study of the dielectric constant and tunability for the $y = 0.03$ sample in
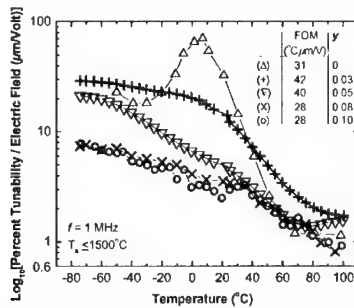

Figure 6. Percent tunability / Electric Field and figure of merit for $y \leq 0.10$.
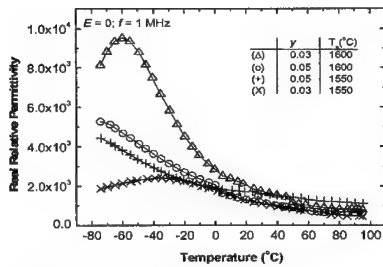
Figure 7. Dielectric constant vs temperature for $T_s = 1550\ ^{\circ}C$, $1600\ ^{\circ}C$.
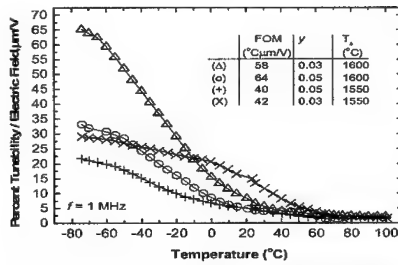

Figure 8. Percent tunability / E-Field and figure of merit (FOM), inset.

Figures 7 and 8 further shows that $\varepsilon(T)$ at the higher $T_s = 1600\ ^{\circ}C$, relative to that at the lower $T_s = 1550\ ^{\circ}C$, is sharper and higher in magnitude at or near the perceived T_c as though returning to a state more like that of BST, except shifted to a lower T_c. The $y = 0.05$ sample appears to have the same trend, although T_c is below the range of measurement. The FOM although lower by about 30 % for the $T_s = 1550\ ^{\circ}C$ samples applies over a broader temperature range than the FOM for $T_s = 1600\ ^{\circ}C$. Room-temperature losses at 1 kHz for the various y and T_s are given in Table I. It of note that for the samples with $T_s = 1600\ ^{\circ}C$, even though the measurements are made well above T_c, in the paraelectric (PE) regime, the losses are larger, by a factor of ten, than those for samples sintered at $1550\ ^{\circ}C$. This implies a resistance of FE domains to respond to external fields in the samples sintered at $T_s = 1600\ ^{\circ}C$ compared to those sintered at $1500\ ^{\circ}C$.

The shift in the T_c as a result of the introduction of $Y^{3+}Ta^{5+}$ pairs in the B site of BST (which does not occur for 4+ ion substitutions) suggests an array of dipole pairs distributed throughout the PE/FE domains in which the FE long range order is modified in such a way that T_c is shifted to a lower temperature compared to the unsubstituted BST. This modification occurs in coincidence with a reduction of grain size that correlates with the broadening of the FE transition. The sharpening of the FE transition, observed for $y = 0.03$ when T_s is increased from $1550\ ^{\circ}C$ to $1600\ ^{\circ}C$, also correlates with increase in grain size. The fact that T_c shifts to a lower temperature and losses increase at room temperature (well above T_c), at $y = 0.03$ for T_s increased from $1550\ ^{\circ}C$ to $1600\ ^{\circ}C$, suggests a difference in the nature of the relationship between the $Y^{3+}Ta^{5+}$ pairs and the FE/PE environments in these two samples. More studies are needed. Theoretical studies of how T_c is affected by the competition between short range dipole forces and the long range order of ferroelectricity in a dense frozen dipolar system have been carried

Table I
Dissipation Factor, D, and Quality Factor, Q, at 1 kHz

y	$T_s(^{\circ}C)$	D	Q
0	1450	0.005	200
0.02	1450	0.008	125
0.03	1450	0.002	500
0.04	1450	0.003	333
0.05	1500	0.005	200
0.06	1500	0.003	333
0.08	1500	0.005	200
0.10	1500	0.002	500
0.03	1550	0.003	333
0.05	1550	0.003	333
0.03	1600	0.03	33
0.05	1600	0.02	50

out by Klapp and Patey [9]. A number of other papers discuss dipolar effects in ferroelectrics (see for example References [10-13]) and the shift in $\epsilon(T_c)$ of Fig. 5 is modeled in [13], but there is no theoretical discussion of small percentages of 3+ and 5+ ions in charge-balanced substitution for the majority 4+ ions (which in our case is Ti^{4+}) in the B site of perovskites, which predict the observed T_c shifts.

CONCLUSIONS

Tunability, characterized by FOM, is the key parameter in frequency-agile device studies at ARL [4]. A study has been made to better understand the effects of concentration, y, and sinter temperature, T_s, on tunability in charge-balanced, 3+ and 5+ substitutions for Ti in BST. For $T_s \leq 1550\ ^\circ C$, increases in y cause T_c to decrease and the FE transition to broaden, leading to a reduction and less variation in dielectric constant, improvement in FOM over the mil spec range as $\epsilon(T)$ and tunability broaden, and decrease in grain size. An increase in T_s, from $1550\ ^\circ C$ to $1600\ ^\circ C$, also causes T_c to decrease. However, the FE transition sharpens, $\epsilon(T_c)$ increases, tunability increases near T_c (but FOM decreases away from T_c), grain size increases, and Q is reduced. For device applications, the improved FOM over the mil spec range, due to charge-balanced substitutions with $T_s \leq 1550\ ^\circ C$, small grain size, and broad FE transition, is preferred.

ACKNOWLEDGEMENTS

REFERENCES

1. D. M. Potrepka, S. C. Tidrow, and A. Tauber, *Mat. Res. Soc. Symp. Proc.* **656E** , DD5.9.1 (2001).
2. D. M. Potrepka, S. C. Tidrow, and A. Tauber, to be published in *Integrated Ferroelectrics* **42**, 97 (2002).
3. S. C. Tidrow *et al.*, *Integrated Ferroelectrics* **28**, 151 (2000).
4. F. J. Crowne and S. C. Tidrow in *Materials Issues for Tunable RF and Microwave Devices III, Proceedings of 2002 MRS Spring Meeting,* paper number H6.5, San Francisco, CA (2002).
5. P. Woodward, R.-D. Hoffmann, and A.W. Sleight, *J. Mater. Res.* **9**, 2118 (1994).
6. P. S. Dobal *et al.*, *Journal of Raman Spectroscopy* **32**, 147 (2001); B. D. Begg, K. S. Finnie, and E. R. Vance, *J. Am. Ceram. Soc.* **79**, 2666 (1996).
7. D. Kolar, *Proceedings of the International Conference on the Chemistry of Electronic Ceramic Materials*, edited by Peter K. Davies and Robert S. Roth, (NIST, 1990), p.3.
8. F. S. Galasso, *Perovskites and High T_c Superconductors*, Gordon and Breach (1990), p. 108.
9. S. H. L. Klapp and G. N. Patey, *J. Chem. Phys.* **115**, 4718 (2001).
10. B. E. Vugmeister and M. D. Glinchuk, *Rev. Mod. Phys.* **62**, 993 (1990).
11. S. M. Emelyanov *et al.*, *Phase Transitions* **A45**, 251 (1993).
12. B. Dkhil *et al.*, *Phys. Rev. B* **65**, 024104/1 (2002).
13. F. J. Crowne *et al.* in *Materials Issues for Tunable RF and Microwave Devices III, Proceedings of 2002 MRS Spring Meeting,* paper number H5.1, San Francisco, CA (2002).

New Materials and
Applications

H6.2

Dielectric and Room Temperature Tunable Properties of Mg-doped Ba $_{0.96}$ Ca $_{0.04}$ Ti $_{0.84}$Zr $_{0.16}$ O$_3$ Thin Films on Pt/MgO

T.S. Kalkur, Woo-Chul Yi, Elliott Philofsky* and Lee Kammerdiner*
Microelectronics Research Laboratories, Department of Electrical and Computer Engineering, University of Colorado at Colorado Springs, Colorado Springs, CO 80933-7150.
*Applied Ceramics Research Company, Colorado Springs, CO 80919.

ABSTRACT

Mg- doped Ba$_{0.96}$ Ca$_{0.04}$ Ti$_{0.84}$ Zr$_{0.16}$ O$_3$ (BCTZ) thin films were fabricated on Pt/MgO substrate by metallorganic decomposition method. The structure of the films were analyzed by x-ray diffraction. The electrical measurements were performed on metal-ferroelectric-metal capacitors with platinum as the top and bottom electrode. The dielectric properties were improved after the capacitors were post annealed at 700 °C in oxygen atmosphere for 30 min. A high dielectric constant of 504 and a dissipation factor of less than 4% was obtained at 1 MHz. The Pt/BCTZ/Pt/MgO capacitors exhibited high tunability of 55% at an applied field of 55 kV/cm.

INTRODUCTION

Thin films of barium strontium titanates Ba$_{1-x}$Sr$_x$TiO$_3$ have become very attractive as dielectrics for storage capacitors for high density dynamic random access memories(DRAM), decoupling capacitors and electric field tunable elements for high frequency microwave circuits[1-5]. Barium Titanium Zirconate Ba(Ti,Zr)O$_3$, which is a solid solution of barium titanate BaTiO$_3$ and barium zirconate BaZrO$_3$ shows a lot of analogies to BaSrTiO$_3$ solution[6]. Ba$_{1-x}$Ca$_x$Ti$_{1-y}$Zr$_y$O$_3$ (BCTZ) bulk ceramics used as dielectrics for chip capacitors, when prepared in oxidizing atmophere exhibit a broad dielectric constant-temperature (ε-T) curve near the critical temperature T$_c$, where peak values of ε = 18000 with nickel electrodes have been reported[7]. Since the dielectric constant of BCTZ is significantly higher than that of bulk BST, it was suggested to explore the possibility of using BCTZ thin film as a replacement for BST. The fabrication of doped and undoped BCTZ films on Pt/Ti/SiO$_2$/Si substrates by metalorganic decomposition (MOD) method and its dielectric properties have been reported by our group recently [8]. The tunability of high dielectric constant materials is an important factor for the fabrication of jitter free high frequency voltage controlled oscillators, matching networks and phase delay elements. So far most of the tunability investigations are confined to BST and strontium titanate thin films. In this paper, we are reporting on the results of electrical characteristics and tunability of magnesium(Mg) doped BCTZ films on Pt/MgO substrates.

SAMPLE PREPARATION

Platinum film of thickness 200 nm was deposited on (100) MgO substrate by DC sputtering. The MOD BCTZ film was deposited by spin on techniques. The details of the preparation of MOD BCTZ is described in our earlier publication [8]. After baking the films at 150 °C for 2 mins and 250 °C for 4 mins the films were annealed at a temperature of 600-900 °C for one hour in flowing oxygen ambient. The thickness of the MgO film deposited was about 180 nm and it was determined using an isoscope. The microstructure of the thin films was characterized by x-ray diffraction.

A top platinum electrode was also deposited by DC sputtering. The capacitor structures of diameter in the range 50 microns to 160 microns were defined by standard photolithography. The top electrode patterned structures were etched by ion milling After the removal of photoresist by plasma ashing, some of the samples were post annealed in oxygen environment for half an hour . Figure 1 shows the cross-sectional structure of the device fabricated. The capacitance – voltage (C-V) characteristics of the metal-ferroelectric-metal structures were determined by Hewlett-Packard HP 4275A multi-frequency LCR meter. The leakage current in the samples were obtained by Hewlett-Packard HP 4145A semiconductor parameter analyzer.
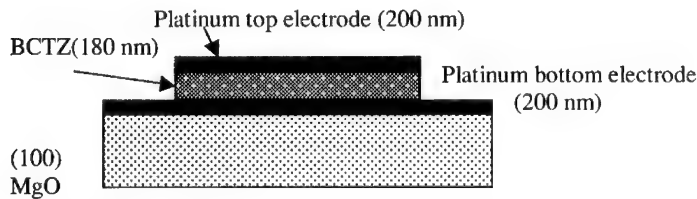

Figure 1. Structure of the fabricated sample.

RESULTS AND DISCUSSION

Figure 2 shows the x-ray diffraction(XRD) spectrum of platinum film on MgO which confirms the formation of (111)Pt film on MgO. In addition, JCPDS based analysis show peaks corresponding to Pt_3O_4 and (100) MgO. Figure 3 shows the XRD pattern of the Mg-doped BCTZ films annealed in the temperature range of 600- 900 °C for one hour in an oxygen environment on the Pt/MgO substrate. The XRD pattern is similar to the XRD pattern of BCTZ films on $Pt/Ti/SiO_2/Si$ substrate which we reported in our previous publication confirming the formation of perovskite phase[9,10]. With increasing annealing temperature from 600 °C to 900 °C the XRD peaks became sharper indicating better crystallinity and an increase in grain size . The grain size for films annealed at 900 °C was less than 100 nm in diameter as determined by Scherrer formula shown below:

$$t = C\lambda/B\cos\theta$$

where C is a factor (typically 0.9 to 1.0), B is the full width at half maximum, θ is the Bragg angle and λ is the x-ray wavelength.
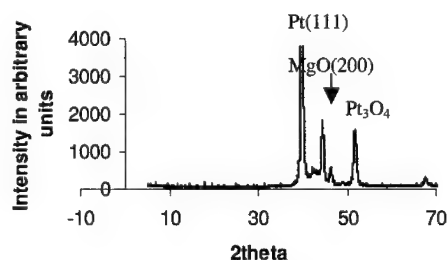

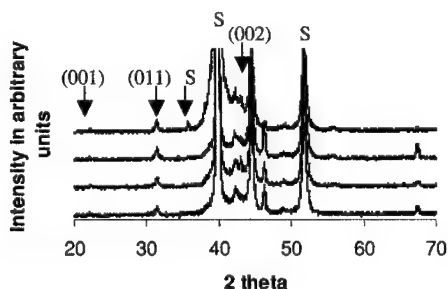Figure 2. XRD patterns of Platinum film deposited on MgO.

Figure 3. XRD patterns of BCTZ on Pt/MgO annealed at temperatures 600-900°C for one hour. (S: Substrate)

Figure 4 shows the capacitance versus voltage (C-V) characteristics of the Mg doped BCTZ thin film capacitors on MgO measured at a temperature of 300 K and at 1 MHz with an ac signal of 100 mV. The zero bias dielectric constant increased from 105 to 420 for annealing temperatures from 600 °C to 900 °C . The C-V measurements performed on Pt/BCTZ/Pt/Ti/SiO$_2$/Si showed dielectric constant of 350 at 900 °C annealing temperature. The increase in dielectric constant on MgO substrate may be due to better cystallanity, less interface stress and reduced inter-diffusion between the substrate and the film[11].   In the case of sputtered Pt/Ti on SiO$_2$/Si substrates, it was found that temperature cycling the films from room temperature to 800 °C in oxygen resulted in increase in tensile stress by 1200 MPa [12,13]. Although such temperature cycling

details are not available for Pt films on (100) MgO, the lattice mismatch between MgO and Pt is about 7.4% at room temperature.
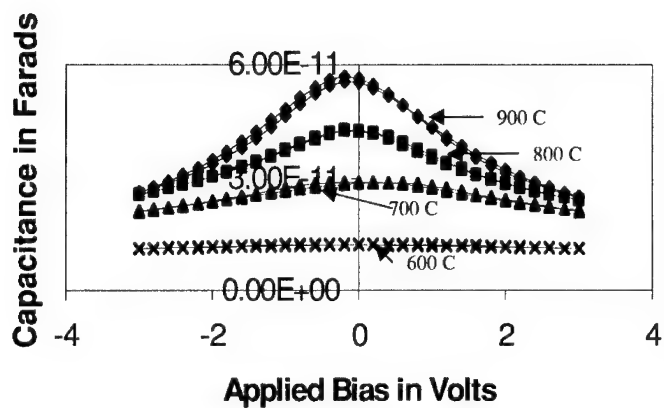

Figure 4. Capacitance vs voltage characteristics of BCTZ film on Pt/MgO annealed in the temperature range of 600-900 °C.
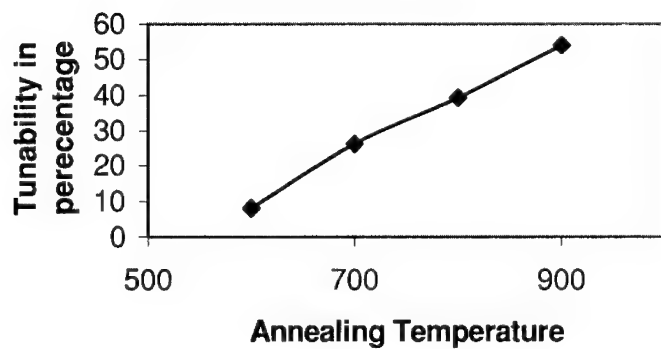

Figure 5. Variation of tunability with annealing temperature for BCTZ films on Pt/MgO.

The BCTZ films annealed at a temperature of 900 $^{\circ}$C were post annealed at a temperature of 700 $^{\circ}$C in oxygen environment for half an hour. The zero bias dielectric constant(ε) was found to increase from 420 to 504 due to post annealing in oxygen environment and this increase is about 20%. The dissipation factor tanδ for these films were found to be less than 0.04 at a measurement frequency of 1 MHz. The increase in dielectric constant is similar to one reported for Pt/Mg doped BCTZ /Pt/Ti/SiO$_2$/Si structure post annealed in oxygen environment [14,15]. The increase in dielectric constant due to post annealing in oxygen was attributed to removal of defects which were created during the deposition and patterning of top electrode. The patterning of top electrodes involves standard photolithographic technique using negative resist, ion milling, and plasma ashing. The dielectric constant, ε for the Mg-doped BCTZ film on Pt/MgO is significantly higher than those reported for BCTZ on Pt/Ti/SiO$_2$/Si, BaTi $_{0.88}$ Zr$_{0.12}$ O$_3$ and Ba $_{0.5}$ Sr $_{0.5}$TiO$_3$ thin films [8,16-18].

The tunability of the capacitance was measured in terms of the parameter $\Delta C/C_o$ where ΔC is the change in capacitance relative to the zero bias capacitance,C_o. The capacitance was measured at 1 MHz frequency with an ac small signal voltage of 100 mV. Figure 5 shows the dependence of tunability for an applied electric field of 55 kV/cm with the annealing temperature. With increase in annealing temperature from 600 $^{\circ}$C to 900 $^{\circ}$C, the tunability was found to increase from 8% to 55%. The tunability for BCTZ for an applied field of 55 kV/cm is significantly higher than that reported for Mg doped Ba$_{0.6}$Sr$_{0.4}$TiO$_3$ film[3]. Therefore, BCTZ is a better alternative for tunable capacitor applications.
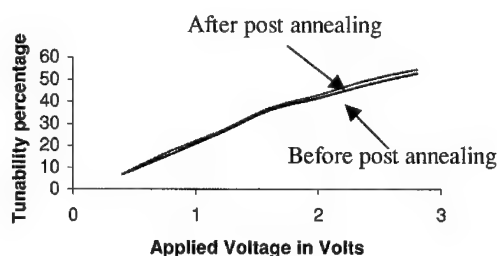

Figure 6. Variation of tunability with applied DC bias voltage.

Figure 6 shows the variation of tunability with bias voltage for sample annealed at a temperature of 900 $^{\circ}$C for one hour. The tunability increases linearly with increase of applied voltage from zero volts to 1.6 volts. Further increase in applied voltage resulted in reduced increase in tunability. Figure 6 also shows that the post annealing of samples

in oxygen environment at 700 °C did not show any significant increase in tunabilty with applied voltage.

CONCLUSION

Mg-doped BCTZ thin film was fabricated on a Pt/MgO substrate by metallorganic decomposition method. The electrical characterization of BCTZ film on Pt/MgO shows about 20% higher dielectric constant than films on Pt/Ti/SiO₂/Si substrates. The BCTZ capacitors annealed at 900 °C shows excellent tunability (about 55%) for an applied field of 55 kV/cm. Therefore, BCTZ might be a promising high dielectric constant material for the fabrication of tunable devices.

REFERENCES

1. A. I. Kingon, S. K. Streifer, C. Basceri, and S. R. Sommerfelt, Mat. Res. Bull.,21, 18 (1995).
2. K. R. Caroll, J. M. Pond, D. B. Christey, J. S. Horwitz and R. E. Leuchner, Appl. Phys. Lett., 62, 1845 (1993).
3. P. C. Joshi and M. W. Cole, Appl. Phys. Lett., 77, 289 (2000).
4. C.L. Chen, H.H. Feng, Z. Zhang, A. Brazdeikis, Z.J. Huang, W.K. Chu, C.W. Chu, F.A. Miranda, F.W. Van Keuls and R.R. Romanofsky, Appl Phys. Lett, 75, 412 (1999).
5. J. Im, O. Auciello, P.K. Baumann, and S.K. Striffer, Appl. Phys. Lett., 76, 625 (2000).
6. S. Hoffman and R.M. Waser, Integr. Ferroelectrics, 17, 141(1997).
7. P. Hansen, D. Henning and H. Schreinemacher, J. Am. Cearm. Soc. 81, 1369 (1998).
8. W .-C. Yi, T.S. Kalkur, E. Philofsky, and L. Kammerdiner, Appl. Phys. Lett., 78, 3517 (2001).
9. Powder Diffraction File (International Center for Diffraction Data, Swarthmore, PA, 1995) JCPDS card 36-19.
10. R. Thomas, D.C. Dube, M.N. Kamalasanan, and S. Chandra, Thin Solid Films, 346, 212 (1999).
11. P. Padmini, T.R. Taylor, M.J. Lefevre, A.S. Nagra, R.A. York and J.S. Speck, Appl. Phys. Lett, 75, 3186 (1999).
12. C. Ang, Z. Yu, and L.E. Cross, Appl. Phys. Lett, 62, 228 (2000).
13. G. Schindler, W. Hartner, V. Joshi, N. Solayappn, G. Derbenwick and C. Nazure, Integrated Ferroelectrics, 17, 421 (1997).
14. J. Narayan, P. Tiwari, K. Jagannadham and O.W. Holland, Appl. Phys.lett., 64, 2093 (1994).
15. Y. Shimakawa and Y. Kubo, Appl. Phys. Lett., 77,2590 (2000).
16. T.B.Wu, C.M. Wu, and M.L. Chen, Thin Solid Films, 334, 77 (1998).
17. H.J. Shy and T.B. Wu, Jpn. J. Appl. Phys. Part 1 37, 4049 (1998).
18. D.Wu, A. Li, H. Ling, X.Yin, C. Ge, M. Wang and N. Ming, Appl. Surf. Sci., 165, 309 (2000).

Studies of thin film ferroelectrics with charge-compensated substitutions in BST

Daniel Potrepka[1], Steven Tidrow[1], Arthur Tauber[1], Kevin Kirchner[1], and Bernard Rod[1], James Horwitz[2], Wontae Chang[2], Nissim Navi[3,4], and Daniel Bubb[2,5]
[1]Sensors & Electron Devices Directorate, U.S. Army Research Laboratory,
Adelphi, MD 20783-1197, U.S.A.
[2]Naval Research Lab, Washington, DC 20375, U.S.A.
[3]School of Engineering and Applied Science, George Washington University,
Washington, DC 20052, U.S.A.
[4]Permanent Address- Nuclear Research Center- Negev
Beer Sheva 9001, Israel
[5]Permanent Address- Department of Physics, Seton Hall University,
South Orange, NJ 07079, U.S.A.

ABSTRACT

Thin films were prepared from bulk targets by pulsed-laser deposition techniques. The targets were composed of $Ba_{0.6}Sr_{0.4}TiO_3$ with charge-compensated substitutions for Ti^{4+}. Results of the dielectric characterization measurements will be discussed and compared to the results of similar measurements in bulk materials with the same composition.

INTRODUCTION

Temperature dependence of thin film dielectric constants for $Ba_{0.6}Sr_{0.4}TiO_3$ (BST) and similar materials are of interest for frequency-agile applications due to the low voltages required to change capacitance and potential for adjustments to impedance for the purpose of matching properties to circuits in microwave devices. The temperature-dependent dielectric constants are typically broadened relative to those for the bulk samples [1]. This paper describes studies of thin films of $Ba_{0.6}Sr_{0.4}(YTa)_yTi_{1-2y}O_3$ which build on the successes of reduction in sensitivity to temperature variation for both dielectric constant and tunability in the bulk material $Ba_{0.6}Sr_{0.4}(YTa)_yTi_{1-2y}O_3$ compared to BST [1]. Using $Ba_{0.6}Sr_{0.4}(YTa)_yTi_{1-2y}O_3$ films deposited by pulsed-laser deposition and characterized by x-ray diffraction analysis, capacitance measurements, and estimated dielectric constants, the potential of these thin-film materials for device applications is studied.

EXPERIMENTAL DETAILS

Targets of $Ba_{0.6}Sr_{0.4}(YTa)_yTi_{1-2y}O_3$, $0 < y \leq 0.04$ and a comparison sample of $Ba_{0.6}Sr_{0.4}(AlTa)_{0.03}Ti_{0.94}O_3$ were synthesized as described in [1] and references therein. Using a KrF laser, the samples were pulsed-laser deposited onto MgO(100) substrates that were heated to 700 °C or 750 °C in 350 mTorr O_2. Subsequently, the samples were cooled to room temperature in ~ 700 mTorr O_2 atmosphere. For selected samples, a pre-deposition calibration was made using a shadow mask. Then thickness was measured using a Tencor P-10 profilometer which was used, along with the number of laser shots, to calibrate the deposition rate. In this way, the average thickness of deposited films was determined to be 0.5 μm. The θ-2θ x-ray diffraction spectrum for Cu Kα1 radiation was obtained for selected samples. Using the log plot of the results the 200 and 400 peaks for the MgO(100) substrate were identified. Due to the limited

number of (h00) lines for the films, it was not possible to determine the lattice constant with great accuracy. However, peaks consistent with (100), (200), and (400) BST were identified, and the lattice constants were nominally the same as bulk BST. Using electron beam evaporation, interdigitated capacitor structures (IDC) were deposited onto the films. The structures had fingers of 150 μm width, 200 μm length, and 5 μm gap. The capacitance was then measured at 1 MHz in the temperature range -75 °C $\leq$ T $\leq$ 60 °C using an applied dc bias of V $\leq$ 30 V.

DISCUSSION

The exact method for obtaining the dielectric constant involves the use of conformal mapping techniques as discussed in [2] and references therein. For the IDC structure used in this work, we assume that the electric field is nearly uniform and mostly confined to the gap area between the fingers of the IDC. The expression relating the capacitance to the dielectric constant can then be reduced to

$$C = \frac{\varepsilon_0 \varepsilon \cdot A}{d},$$
(1)

where A is the area given by the film thickness multiplied by the length, L (see Fig. 1), and the d = b (see Fig. 1) is the gap between fingers.

The dielectric constant of BST with charge-balanced substitutions, $y \leq 0.04$, of YTa is shown in Fig. 2. These are found to be significantly lower relative to the bulk values for similar y [3]. The dielectric constant of the $y = 0.01$ thin film ($T_c \sim$ -20 °C) shows broadening similar to that typically observed for BST depositions on LaAlO₃ or MgO substrates [4] and was found to be comparable to that of the $y = 0.03$ bulk sample. For $y = 0.02 - 0.04$, the dielectric constant is quite low and extremely broadened so that, in the temperature range of measurement, no ferroelectric T_c was observed. The similarity in magnitude of the dielectric constant curves for
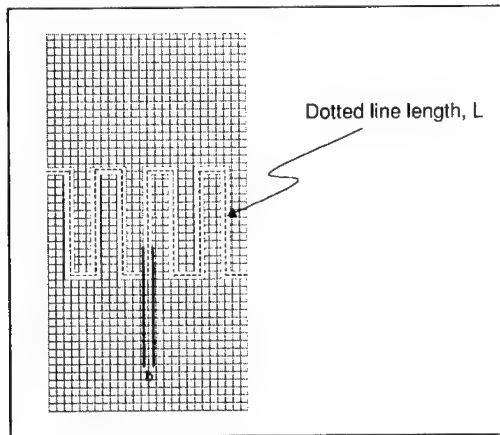

Figure 1. Dimensions of the interdigitated capacitor (IDC) structure that are used to estimate the dielectric constant.
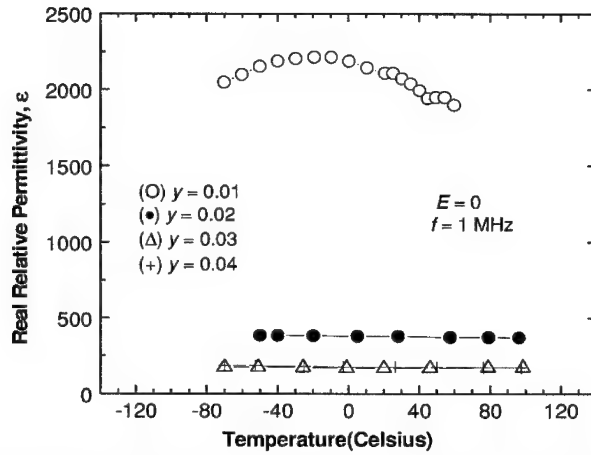
Figure 2. Dielectric Constant vs Temperature for $Ba_{0.6}Sr_{0.4}(YTa)_yTi_{1-2y}O_3$, for $0 < y \leq 0.04$.

the $y = 0.03$ and 0.04 films implies that, near these concentrations, a lower limit is achieved in the dielectric constant of ~ 200. Tunability measurements were also attempted, but capacitance changes were only obtained for the $y = 0.01$ sample (Fig. 3). The tunability of the $y = 0.01$ sample at 6 V/μm over the temperature range $-75\ ^oC \leq T \leq 60\ ^oC$ was ~ 20 % - 32 % at 6 V/μm (applied voltage of 30 V and gap of 5 μm) which gives a range of the electric-field normalized
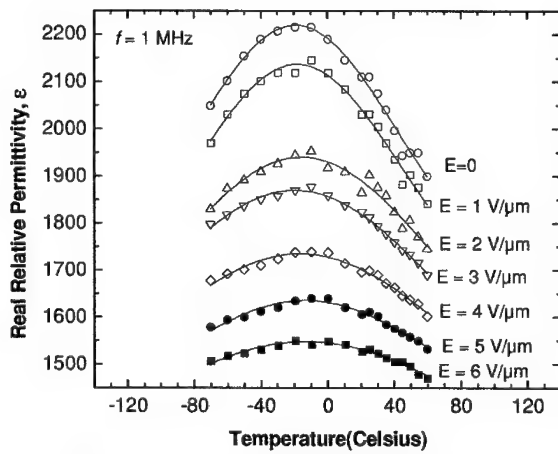
Figure 3. Variation of dielectric constant in $Ba_{0.6}Sr_{0.4}(YTa)_{0.01}Ti_{0.98}O_3$ for $0 \leq E \leq 6$ V/μm.

value of 3.3 - 5.3 %–μm/V. The figure of merit is estimated to be ~ 31 °C–μm/V, comparable to the values reported for bulk $Ba_{0.6}Sr_{0.4}(YTa)_yTi_{1-2y}O_3$ samples with $0 \leq y \leq 0.10$ sintered at 1450 °C $\leq$ T $\leq$ 1550 °C discussed in Reference [3]. A similarly deposited $Ba_{0.6}Sr_{0.4}(AlTa)_{0.03}Ti_{0.94}O_3$ sample with T_c ~ -60 °C had a peak dielectric constant, tunability range, and figure of merit of 975, 1.3 - 4.5 μm/V and 22.6 °C-μm/V, respectively.

CONCLUSIONS

$Ba_{0.6}Sr_{0.4}(YTa)_yTi_{1-2y}O_3$ films with $0 < y \leq 0.04$ have been successfully deposited on MgO(100) by the pulsed-laser deposition technique. The reduction in dielectric constant with increase in y mimics that of similar bulk samples, except it reaches an apparent minimum of ~ 200 for $y = 0.03$ and 0.04. Only the $y = 0.01$ film has a measurable capacitance change due to applied bias $V \leq 30$ V. The figure of merit is comparable to those obtained for bulk samples of $Ba_{0.6}Sr_{0.4}(YTa)_yTi_{1-2y}O_3$ with $0 \leq y \leq 0.10$ sintered at temperatures in the range 1450 °C $\leq$ T $\leq$ 1550 °C.

ACKNOWLEDGEMENTS

REFERENCES

1. D. M. Potrepka, S. C. Tidrow, and A. Tauber, to be published in *Integrated Ferroelectrics* **42**, 97 (2002).
2. H.-D. Wu, *et al.*, IEEE Trans. Appl. Supercond. **4**, 156 (1994).
3. D. M. Potrepka, S. C. Tidrow, A. Tauber, K. W. Kirchner, M. H. Ervin, K. K. Deb, B. J. Rod, and F. J. Crowne in *Materials Issues for Tunable RF and Microwave Devices III, Proceedings of 2002 MRS Spring Meeting*, paper number H5.5, San Francisco, CA (2002).
4. H.-D. Wu and F. S. Barnes, *Integrated Ferroelectrics* **22**, 291 (1998).

Evidence for Antiferroelectric Behavior in $KNbO_3$/$KTaO_3$ Superlattices

J. Sigman[1], H. M. Christen[2], P. H. Fleming[2], L. A. Boatner[2], and D. P. Norton[1]
[1]Department of Materials Science and Engineering, University of Florida, P.O. Box 116400, Rhines Hall, Gainesville, FL 32611.
[2]Solid State Division, Oak Ridge National Laboratory, P.O. Box 2008, Oak Ridge, TN 37831.

ABSTRACT

The dielectric response in artificially layered 1x1 $KTaO_3$/$KNbO_3$ perovskite superlattice structures is reported. While $KTaO_3$ and $KNbO_3$ are ferroelectric or paraelectric, respectively, superlattices appear antiferroelectric based on an increase in dielectric constant with applied dc bias. This "positive tunability" in dielectric response occurs at the same temperature region where a structural phase transition is observed. This dielectric behavior is inconsistent with the nonlinear response for either paraelectric or ferroelectric materials. However, an increase in the dielectric constant with applied electric field is consistent with antiferroelectric behavior. The antiferroelectric ordering correlates with cation modulation imposed by the superlattice.

INTRODUCTION

The dielectric properties of insulating materials are determined by the polarization behavior. Random alignment of dipoles yields a paraelectric response; parallel or anti-parallel ordering results in ferroelectric or antiferroelectric behavior, respectively. Controlling the nature of dipole polarization is key to tailoring material performance. The manipulation of dielectric properties can be achieved via doping or control of microstructure. In thin films, the formation of artificially layered structures offers opportunities to probe and manipulate dielectric material properties.

In this paper, we report on the dielectric properties of $K(Nb_xTa_{1-x})O_3$ based superlattice structures. Among the dielectric materials, the mixed-oxide compound $K(Nb_xTa_{1-x})O_3$ (or KTN) is a near-ideal material for both understanding and manipulating the dielectric properties of perovskites.[1-3] KTN is similar to $(Sr,Ba)TiO_3$ in that, as the composition is altered, the solid solution exhibits a continuous transition from a paraelectric to a ferroelectric material. Pure $KTaO_3$ is cubic ($a_{300 K}$ = 3.9885 Å) and paraelectric at all temperatures. Decreasing the temperature results in a softening of the TO_1 transverse optic, zone-center phonon branch. The soft mode is stabilized by zero-point quantum fluctuations, however, so that $KTaO_3$ does not undergo a ferroelectric transition but remains cubic and paraelectric down to 0 K. Hence $KTaO_3$ exhibits so-called "incipient ferroelectric" or "quantum ferroelectric" behavior.[4,5] Pure $KNbO_3$, in contrast, exhibits a first-order ferroelectric phase transition accompanied by a change from the cubic to the tetragonal structure at 701 K (a_p = 4.02 Å along $[100]_p$ and $[010]_p$ directions, and c_p = 3.97 Å along the $[001]_p$). Upon further cooling, the structure changes to orthorhombic at 498 K, with lattice parameters a = 5.696 Å, b = 5.7213 Å, and c = 3.9739 Å. For the ferroelectric state, the polarization direction is along the [010] (b axis). As a solid solution, the KTN Curie temperature varies continuously according to the formula T_c = 676x + 32 (for x > 4.7 %). For x > 0.35, the solid solution exhibits a first-order ferroelectric phase transition similar to $KNbO_3$. Due to its low dielectric loss, high saturation polarization, large

electro-optic effects, and low driving voltage for modulation, $KTa_{1-x}Nb_xO_3$ is an attractive material for applications involving holographic data storage, parametric oscillators, pyroelectric detectors, and second harmonic generators.[6-9]

Recent developments in oxide film growth provide the opportunity to understand, control, and manipulate the growth of epitaxial oxide films and multilayers in the KTN system at the atomic scale.[10,11] Specifically, the properties of symmetric $KNbO_3/KTaO_3$ superlattices grown by pulsed laser deposition on $KTaO_3$ (001) have been studied.[12-14] Excellent film flatness and crystallinity are evidenced in these films, and the interfaces are found to be compositionally sharp on an atomic scale. Unlike $(Sr,Ba)TiO_3$, the $K(Nb,Ta)O_3$ system displays very little change in the average d-spacing in moving across the alloy composition. This significantly minimizes the effects of strain in superlattices, and permits the synthesis of commensurate structures with low defect density. Previous work has shown that while relatively thick $KNbO_3$ films are characterized by an orthorhombic structure, $KTaO_3/KNbO_3$ superlattices can be uniformly strained in-plane without misfit dislocations, imposing an in-plane $KNbO_3$ lattice spacing that is identical to that of the $KTaO_3$ substrate. Temperature-dependent x-ray diffraction measurements indicate a tetragonal-to-tetragonal phase transition for superlattices,[15-17] with the structural phase transition temperature, T_c, dependent on the $KNbO_3$ layer thickness. As the superlattice period decreases, a reduction of T_c is observed. For symmetric superlattices with periodicities of 50 Å or less, the structural phase transition temperature is identical to that of the $K(Ta_{0.5}Nb_{0.5})O_3$ random alloy film.

EXPERIMENTAL DETAILS

We have investigated of the temperature-dependent dielectric response of $KTaO_3/KNbO_3$ superlattices, focusing on 1-unit-cell x 1-unit-cell (1x1) superlattice structures. The dielectric properties were measured using inter-digitated capacitors, with specific attention given to the dielectric behavior near the structural phase transition as observed in the x-ray diffraction results reported earlier.[12-14] The dielectric response of (1x1) $KTaO_3/KNbO_3$ superlattices and $K(Ta_{0.5}Nb_{0.5})O_3$ alloy films were studied at frequencies of 100 kHz and 1 MHz by measuring the capacitance of inter-digitated Au/Cr electrodes deposited on the film surface. The epitaxial structures were deposited by pulsed-laser deposition as previously described.[13] The electrode finger separation and width for the inter-digitated electrodes were 10 μm. Each capacitor structure consisted of 26 fingers. The capacitance was measured as a function of temperature from 25 to 300 °C in air. This temperature range encompasses the structural transition temperature (~200°C) for the (1x1) $KTaO_3/KNbO_3$ superlattices and $K(Ta_{0.5}Nb_{0.5})O_3$ alloy films as observed in previous x-ray diffraction data. In addition to zero-bias measurements, the dc voltage tunability was measured over this temperature range by measuring the capacitance with applied dc bias voltages ranging from 5 to –5 V.

DISCUSSION

The temperature-dependent capacitance for a (1x1) $KTaO_3/KNbO_3$ superlattice structure, measured at 100 kHz, is shown in Fig. 1. A weak, but discernable, local maximum in capacitance is observed at ~ 200°C, which corresponds with the structural transition. However, the capacitance behavior with applied bias reveals a more complex behavior. The temperature-dependent capacitance taken with applied dc bias voltages of 0 and 4.7 V is illustrated in Fig. 1.

For temperatures less than approximately 140°C, the capacitance is nearly temperature independent with no discernable bias voltage dependence for dc voltages less than 5 V. This is consistent with a film that is either ferroelectric or paraelectric, given that the electric field strength is only 2 kV/cm. From the phase diagram for K(Ta,Nb)O$_3$ and the x-ray diffraction results reported earlier, we anticipate that the film is ferroelectric in this temperature regime. However, as the sample temperature is increased above 140°C, the capacitance shows an anomalous increase with applied dc voltage. This "positive tunability" in the superlattices with applied bias is clearly seen in the

Figure 1 Capacitance for inter-digitated capacitor on 1x1 KTaO$_3$/KNbO$_3$ superlattice at 0 and 4.7 V dc bias. Also shown is the expected behavior for a ferroelectric (FE)-paraelectric (PE) system based on qualitative prediction only.

capacitance versus dc bias voltage plots at fixed temperatures, shown in Fig. 2. This is inconsistent with either ferroelectric or paraelectric behavior. The application of a dc electric field results in a decrease in dielectric constant for ferroelectric or paraelectric materials.

For measurements performed at 100 kHz, a maximum in the positive dc bias tunability is observed at approximately 175°C. 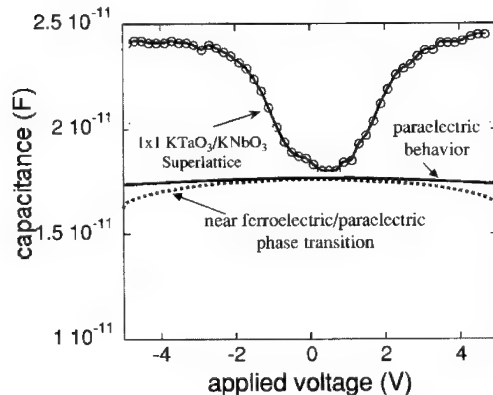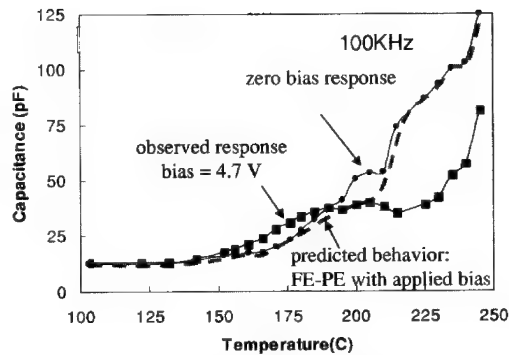As the temperature is increased to ~200°C, a crossover is observed where the tunability becomes negative, indicative of conventional ferroelectric and paraelectric behavior. Note that this crossover temperature for tunability is in the temperature range where the structural phase transition is observed from the temperature-dependent x-ray diffraction data as is illustrated in Fig. 3.[13,14] At approximately 200°C, a "conventional" paraelectric tunability greater than 50% with an applied voltage of 4.7 V is observed.

Figure 2 Capacitance versus voltage for superlattice at 170 °C. Also shown is the qualitatively predicted paraelectric behavior.

The temperature-dependent capacitance was also measured at 1 MHz for the same 1x1 KTaO$_3$/KNbO$_3$ superlattice sample. Again, a large positive tunability is observed. For $\nu = 1$ MHz, the positive tunability is pronounced only at the temperature corresponding to the structural phase

transition. While the zero-bias capacitance curve shows no identifiable structure suggesting a phase transition, the biased curves clearly show evidence for a transition at ~195 °C.

Similar measurements of the temperature-dependent capacitance with applied dc bias voltage were performed on $K(Ta_{0.5}Nb_{0.5})O_3$ alloy films and are shown in Fig. 4. The alloy film does not exhibit this anomalous tunability behavior. Changes in the slope of the temperature-dependent capacitance are observed at 190°C, corresponding to the

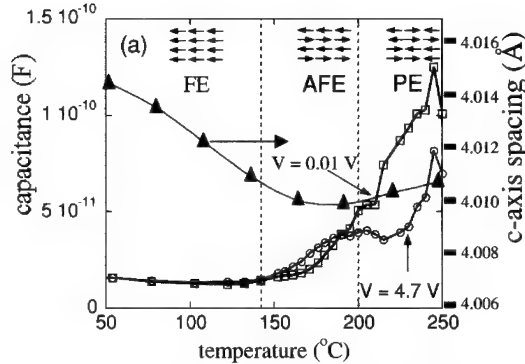**Figure 3.** Structural transition (inflection in c-axis lattice spacing) and dielectric anomaly as function of temperature.

structural phase transition. Since the average film composition is the same in both the alloy and superlattice film, the discrepancy in the tunability behavior must be associated with the artificial ordering.

An increase in the dielectric constant (observed via capacitance measurements) with applied dc electric field is inconsistent with the expected behavior for either a paraelectric or ferroelectric material.[15]   However, the observed behavior for the 1x1 $KTaO_3/KNbO_3$ superlattices is remarkably similar to that for antiferroelectric perovskites.[16-19]   An increase in dielectric constant with applied field is a signature behavior indicating antiferroelectric ordering.   An antiferroelectric is characterized by an antiparallel ordered array of local dipoles.   It can be viewed as two interpenetrating sublattices of equal and opposite polarization with no net spontaneous polarization.   In many cases, the antiferroelectric ordering of dipoles can be transformed to ferroelectric ordering via the application of an electric field.   This is the origin of the increase in dielectric constant with applied dc voltage. The difference in free energy between ferroelectric and antiferroelectric phases can be quite small.   An additional signature of antiferroelectric behavior is a hysteresis in the dielectric constant versus field behavior as voltage is swept between positive and negative polarity. Hysteresis is observed in traces of the capacitance vs. voltage for the 1x1 $KTaO_3/KNbO_3$ superlattice.

Based on the tunability behavior, a reasonable description of the superlattice dielectric properties is as follows. Below approximately 140°C, relative insensitivity of the dielectric in the 1x1 superlattice is consistent with a ferroelectric phase. This assumption is based on the typical phase development of antiferroelectrics, where ferroelectricity is observed at temperatures below the antiferroelectric regime. This is also consistent with the bulk behavior of $K(Ta,Nb)O_3$ alloys. As the temperature is raised above ~140°C, an antiferroelectric phase is observed. For temperatures greater than 200°C, the superlattice becomes paraelectric.

It is interesting to consider the origin of antiferroelectric behavior in superlattice structures whose constituent compounds are ferroelectric or paraelectric. For several complex perovskite materials (e.g., $Pb_2B'B''O_6$) in which multiple B-site cations order into a superstructure,

antiferroelectric behavior is observed.[20,21] In fact, for many of these compounds, the antiferroelectric phase correlates directly with the B-site superstructure. Cation substitution that randomizes B-site ordering also suppresses antiferroelectric behavior. This is true even for solid solutions in which the two end members are antiferroelectric, as seen in $Pb(Yb_{1/2}Ta_{1/2})O_3$-$Pb(Lu_{1/2}Nb_{1/2})O_3$.[22] With the $KTaO_3/KNbO_3$ superlattices, B-site cation modulation is artificially imposed. The resulting change in free energy apparently favors antiferroelectric dipole alignment. Understanding the nature of the

Figure 4. Capacitance vs. temperature for an alloy $K(Ta_{0.5}Nb_{0.5})O_3$ film

interaction that leads to anti-parallel dipole orientation will require theoretical calculations of the dipole configuration free energy. The characterization of additional symmetric and asymmetric superlattice structures will also be useful in understanding these results.
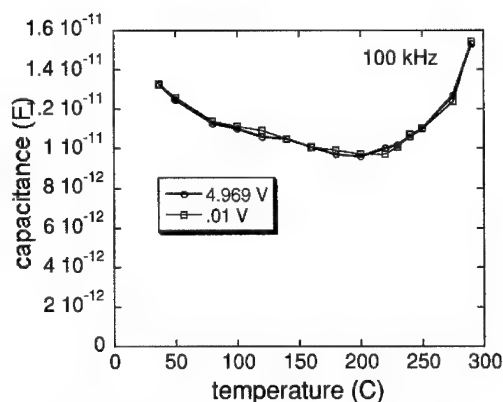
ACKNOWLEDGEMENTS

REFERENCES

1. D. G. Bozinis and J. P. Hurrell, *Phys. Rev. B* **13**, 3109 (1976);
2. Y. Fujii and T. Sakudo, *J. Phys. Soc. Jpn.* **41**, 888 (1976);
3. J. Toulouse, X. M. Wang, L. A. Knass, and L. A. Boatner, *Phys. Rev. B* **43**, 8297 (1991).
4. U. T. Höchli, H. E. Weibel, and L. A. Boatner, *Phys. Rev. Lett.* **39**, (18) 1158–1161 (1977).
5. U. T. Höchli and L. A. Boatner, *Phys. Rev. B* **20**, (1) 266–275 (1979).
6. F. S. Galasso, "Perovskites and High T_c Superconductors," (Gordon and Breach, New York, 1990).
7. D. Rytz, M. B. Klein, B. Bobbs, M. Matloubian, and H. Fetterman, *Jpn. J. Appl. Phys.* **24** Suppl. 24-2, 1010 (1985)
8. A. C. Carter, J. S. Horvitz, D. B. Chrisey, J. M. Pond, S. W. Kirchoefer, and W. Chang, *Integrated Ferroelectrics* **17**, 273 (1997)
9. H. Khemakhem, J. Ravez, and A. Daoud, *Phys. Stat, Sol. (a)* **161**, 557 (1997).
10. S. Yilmaz, T. Venkatesan, and R. Gerhard-Multhaupt, *Appl. Phys. Lett.* **58**, 2479 (1991);

11. F. E. Fernandez, M. Pumarol, P. Marrero, E. Rodriguez, and H. A. Mourad, *Mat. Res. Soc. Symp. Proc.* **493**, 365 (1998).
12. H.-M. Christen, L. A. Boatner, J. D. Budai, M. F. Chisholm, L. A. Gea, P. J. Marrero, and D. P. Norton, *Appl. Phys. Lett.* **68**, 1488 (1996).
13. H.-M. Christen, E.D. Specht, D.P. Norton, M.F. Chisholm, and L.A. Boatner, *Appl. Phys. Lett.* **72**, 2535 (1998)
14. E.D. Specht, H.-M. Christen, D.P. Norton, and L.A. Boatner, *Phys. Rev. Lett.* **80**, 4317 (1998).
15. W. Chang, J. S. Horwitz, W.-J. Kim, J. M. Pond, S. W. Kirchoefer, C. M. Gilmore, S. B. Qadri, and D. B. Chrisey, *MRS Symp. Proc.* **541**, (Materials Research Society, Warrendale, 1999), p. 693-698.
16. G. A. Smolenskii, V. A. Bokov, V. A. Isupov, N. N. Krainik, R. E. Pasynkov, and A. I. Sokolov, "Ferroelectrics and Related Materials," (Gordon and Breach, London, 1984), pp. 607-659
17. B. Xu, L. E. Cross, and J. J. Bernstein, *Thin Solid Films* **377-378**, 712 (2000).
18. S. Chattopadhyay, P. Ayyub, V. R. Palkar, M. S. Multani, S. P. Pai, S. C. Purandare, and R. Pinto, *J. Appl. Phys.* **83**, 7808 (1998)
19. S. S. N. Bharadwaja and S. B. Krupanidhi, *J. Appl. Phys.* **86**, 5862 (1999).
20. J. R. Kwon and W. K. Choo, *J. Phys.: Condens. Matter* **3**, 2147 (1991)
21. A. A. Bokov, I. P. Raevskii, and V. G. Smotrakov, *Sov. Phys. Solid State* **25**, 1168 (1983).
22. Y. Park and K. Cho, *J. Am. Ceram. Soc.* **83**, 135 (2000).

The Ferroelectric Slab Waveguide: a Geometry for Microwave Components that Incorporate Ferroelectric Materials

Frank J. Crowne and Steven C. Tidrow
RF Electronics Division, Army Research Laboratory,
Adelphi, MD 20783-1197, U.S.A.

ABSTRACT

A slab geometry, in which ferroelectric is inserted between two "cladding" layers with a microstrip electrode placed on top, is proposed as a way to integrate the properties of ferroelectric materials into microwave components. This structure distributes the propagating microwave fields between the ferroelectric and the cladding, so that the microwave dielectric constant is a weighted average of the dielectric constants of the two materials. It is shown that this geometry drastically reduces dissipation due to dielectric losses in the ferroelectric. In addition, by applying a dc bias to the microstrip line, the dielectric constant of the ferroelectric layer can be varied and with it the microwave properties of the structure.

INTRODUCTION

Due to its lack of moving parts and potential for conformal installation on vehicles, missiles and aircraft, the electrically scannable (E-scan) antenna is an important weapon in the arsenal of the Army's Future Combat Systems [1]. Most approaches to designing such antennas involve some type of phased array, in which beam steering is implemented by phase shifters. It has long been known that ferroelectric materials can be used to make such components, since they can provide voltage-controlled phase shifts by virtue of their nonlinear dielectric response.

Our recent in-house efforts on E-scan antennas at the Army Research Laboratory has centered on a true-time-delay approach to generating the antenna phase shifts, in which a tapped delay line, usually some sort of microwave transmission line, is used to phase the antenna signals by sampling a nondispersive propagating wave at equal intervals along its path. If the delay line is uniform, it is easy to show that an array phased in this way has a far-field pattern whose main lobe points at an angle θ_{MB} given by

$$\theta_{MB} = \sin^{-1}\left(\frac{D\sqrt{\varepsilon}}{d}\right) \tag{1}$$

where D is the spacing between taps, d is the distance between array radiators, and ε is the dielectric constant of the delay line. If ε is frequency independent, the angle θ_{MB} is also, so that broadband signals can be transmitted without causing the beam to move. In addition, if the transmission line is a microstrip line on a ferroelectric substrate, the field dependence of ε makes it possible to steer the beam electrically with a single dc voltage between the strip and the ground plane.

However, this scheme turns out to be difficult to implement. In order to suppress coupling between array radiators, the spacing d between them is usually $\lambda/2$, where λ is
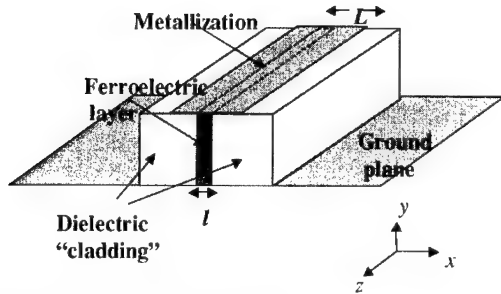
Figure 1. Ferroelectric slab structure.

the free-space wavelength of the carrier signal (typically a few centimeters down to a millimeter for our applications). Because dielectric constants are extremely high in ferroelectrics (1000 to 4000), satisfying Eq. (1) with an ε of 1000 requires values of $D < \dfrac{d}{30}$, which puts the delay line taps quite close together. This causes arcing and cross talk, and makes the line difficult to manufacture.

THEORY

Our approach to this problem is to replace the ferroelectric substrate with a guiding structure consisting of a thin slice of ferroelectric sandwiched between two "cladding" layers of low-ε material. We have found that there is a frequency range within which a delay line based on this structure, which we call a *ferroelectric slab waveguide*, looks like a microstrip transmission line with an "effective" dielectric constant much lower than that of the ferroelectric. This ferroelectric-slab (FS) structure is shown in Fig. 1. By analogy with microstrip [2], let us assume that the region of the slab where the wave fields exist is bounded laterally at $x = \pm L/2$, by magnetic walls. Then for waves propagating along z with propagation constant $q(\omega)$, the structure has a set of TE modes whose electric field $E_y(x)$ is perpendicular to the ground plane and the microstrip metal. This field satisfies the wave equation:

$$\left(\partial_x^2 + \varepsilon(x)\frac{\omega^2}{c^2} - q^2 \right) E_y(x) = 0$$

where $\varepsilon(x) = \varepsilon_1$ for $x \in [l/2, L/2]$ and ε_2 for $x \in [0, l/2]$. In contrast to ordinary microstrip, these FS modes are nonuniform in x due to the nonuniformity of $\varepsilon(x)$:

$$E_y(x) = A\cos K_2 x, \qquad\qquad x \in [0, l/2]$$
$$= A\left(\frac{\cosh K_2 l/2}{\cosh K_1 \Lambda/2} \right)\cosh K_1(L/2 - x), \qquad x \in [l/2, L/2] \qquad (2)$$

186

where $K_1^2 = q(\omega)^2 - \varepsilon_1 \dfrac{\omega^2}{c^2}$ and $K_2^2 = \varepsilon_2 \dfrac{\omega^2}{c^2} - q(\omega)^2$. Note that the field is oscillatory inside the ferroelectric and exponentially decaying outside in the cladding, like the field of an optical fiber mode [3]. Matching the field and its derivative at the boundary (which ensures continuity of the longitudinal magnetic field H_z), gives the relation

$$K_1 \tanh K_1 \Lambda / 2 = K_2 \tan K_2 l / 2 \tag{2a}$$

where $\Lambda = L - l$. Combining this with the equation

$$K_2^2 + K_1^2 = (\varepsilon_2 - \varepsilon_1) \frac{\omega^2}{c^2} \tag{2b}$$

and solving (2a) and (2b) numerically for K_1 and K_2 as a function of frequency, we

obtain the propagation constant from $q(\omega)^2 = \varepsilon_1 \dfrac{\omega^2}{c^2} + K_1^2$.

Figure 2 shows the fundamental-mode electric field distribution of an FS with $L = $ .3 cm, $l = .005$ cm, $\varepsilon_2 = 1000$, and $\varepsilon_1 = 3.6$, at two frequencies: $f = 3$ GHz and $f = 50$ GHz. At the lower frequency, the electric field is almost uniform across the structure, like the fundamental mode of an ordinary microstrip line. At $f = 50$ GHz the confinement is apparent. The width of the ferroelectric is too small to see on this scale.

At low frequencies the mode problem can be solved analytically. Let us write $K_1 = \Xi \sin \phi$, $K_2 = \Xi \cos \phi$, where $\Xi^2 = (\varepsilon_2 - \varepsilon_1) \dfrac{\omega^2}{c^2}$. Then (2a) becomes

$$\sin \phi \cdot \tanh\left[(\Xi \Lambda / 2) \sin \phi\right] = \cos \phi \cdot \tan\left[(\Xi l / 2) \cos \phi\right] \tag{3}$$
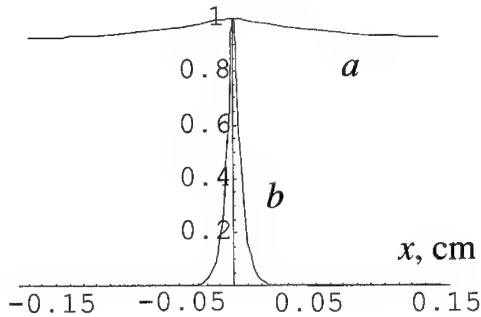

Figure 2. Fundamental modes of an FS at $f = 3$ GHz (a) and 50 GHz (b). Structural parameters: $L = .3$ cm, $l = .005$ cm, $\varepsilon_2 = 1000$, and $\varepsilon_1 = 3.6$ [$A = 1$ in Eq. (2)].

For small Ξ (low frequencies), the tangents in (3) can be replaced by their arguments:

$$(\Xi\Lambda/2)\sin^2\phi = (\Xi l/2)\cos^2\phi. \qquad (4)$$

Solving (4) gives $\cos\phi = \sqrt{\dfrac{\Lambda}{\Lambda+l}}$, $\sin\phi = \sqrt{\dfrac{l}{\Lambda+l}}$, and hence $K_1 = \dfrac{\omega}{c}\sqrt{\dfrac{l}{\Lambda+l}(\varepsilon_2 - \varepsilon_1)}$,

$K_2 = \dfrac{\omega}{c}\sqrt{\dfrac{\Lambda}{\Lambda+l}(\varepsilon_2 - \varepsilon_1)}$, from which we obtain $q = \sqrt{\varepsilon_1\dfrac{\omega^2}{c^2} + K_1^2} = \dfrac{\omega}{c}\sqrt{\dfrac{\varepsilon_2 l + \varepsilon_1(L-l)}{L}}$.

In this limit the FS mode looks like the fundamental mode of an ordinary microstrip line on a substrate with dielectric constant equal to the weighted average of the dielectric constants of the two FS layers, i.e.,

$$\varepsilon_{eff} = \varepsilon_2\frac{l}{L} + \varepsilon_1(1-\frac{l}{L}), \qquad (5)$$

which is derivable from a simple parallel capacitor model. Note that the electric field is uniform in this same limit, like that of microstrip.

As the frequency increases, the dispersion increases along with the confinement. Figure 3(a) shows the full dispersion relation for the structure described in Fig. 2. It is clear that there is a turnover point around 7 GHz where dispersionless propagation ends. This point is a critical design number for high-frequency devices, and must be identified for each structure. The perturbation analysis reveals that lack of dispersion depends on smallness of the quantity Ξ defined above. Clearly there are two ways to make Ξ small: either by operating at low frequencies or making the two dielectric materials have almost the same dielectric constant. The former method precludes high-frequency operation, while the latter is of no practical use because there are no perovskite ferroelectrics with small ε_2. However, a third limit in which the line is dispersionless is when l is small but
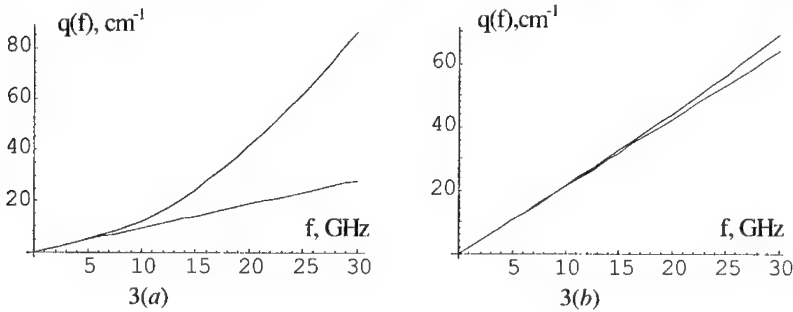

Figure 3. (a) Dispersion curve for FS with parameters listed in Fig. 2. Straight line: small-ω approximation ($\varepsilon_{eff} = 20$). (b) Dispersion curve for FS with parameters $L = .025$ cm, $l = .0025$ cm, $\varepsilon_2 = 1000$, and $\varepsilon_1 = 3.6$. Straight line: small-ω approximation ($\varepsilon_{eff} = 103$).

ε_2 is large. In this limit we have $K_1 \to 0$, which makes the electric field $E_y(x)$ independent of x, while at the same time $\varepsilon_{eff} \neq \varepsilon_2, \varepsilon_1$ as long as l and ε_2 are chosen so that the product $\varepsilon_2 \frac{l}{L}$ remains sizable. Although K_2 does not vanish in this limit, the volume occupied by ferroelectric becomes too small to affect the propagation. Figure 3(b) shows a more useful dispersion curve, with a drastically narrower microstrip electrode. The effective dielectric constant is now very large, and the dispersionless regime now extends to almost 30 GHz.

Another advantage of the FS structure is that it can greatly reduce losses intrinsic to the ferroelectric by putting most of the electric field of the wave in the cladding, where losses can be miniscule. A perturbation analysis of the propagation [4] for a line with lossy ferroelectric gives the following expression for the complex propagation constant:

$$\tilde{q}_s \approx q(\omega) + j \frac{\omega^2}{2q(\omega)c^2} \int \varepsilon_I(x) E_y^2(x) dx$$

where $E_y(x)$ is the lossless mode shape given by Eq. (2) and $\varepsilon_I(x)$ is the imaginary part of $\varepsilon(x)$, which is nonzero only in the ferroelectric. This equation can be used to derive the loss tangent, and shows clearly how a small volume of ferroelectric leads to low losses.

Figure 4 shows the line losses for the structure defined in Fig. 2, for two values of ferroelectric loss tangent: a "fair" value (a) and a "good" value (b). Despite the fact that these numbers are terrible compared to ordinary dielectrics, the losses over a line a few centimeters long are extremely low. Note that these loss reductions were achieved with no sacrifice of "tuning," i.e., the rate of change of ε with bias.
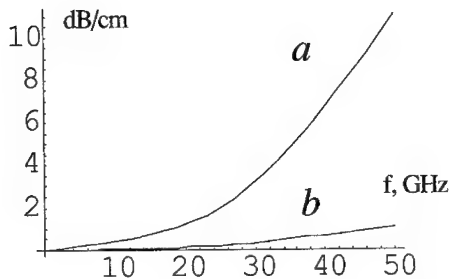

Figure 4. Line losses for an FS with structural parameters $L = .3$ cm, $l = .005$ cm, $\varepsilon_2 = 1000$, and $\varepsilon_1 = 3.6$, and ferroelectric loss tangents .03 (a) and .003 (b).
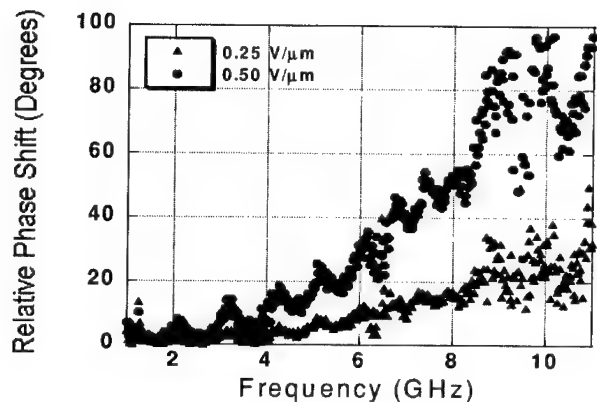
Figure 5. Phase shifts for untapped delay line.

EXPERIMENT

Figure 5 shows preliminary experimental results for an untapped structure about 5 cm long. The S- parameter S_{21}, which corresponds to the transmission of a passive line, was measured in an HP network analyzer, and its phase was extracted. The peaks in the data correspond to resonances due to imperfect impedance matching at the end of the line. Reflections also suppress the phase shift, which should have been around 400 degrees for this structure. The remarkably small fields needed to change this linear trend attest to the promising nature of our approach. The percent change in ε here was 10%.

CONCLUSION

In conclusion, we believe that these microwave structures address and solve many of the problems that limit the use of ferroelectrics in microwave devices. We have begun to address some of the hard issues relating to impedance matching and aperture coupling of these lines to other microwave devices, e.g., patch antennas, and will report on our progress in a future publication.

REFERENCES

1. S. Weiss, E. Adler, R. Dahlstrom, E. Viveiros, S. Tidrow, and F. J. Crowne, "A Low-Profile Architecture Implementation of an Electrically Scanned Antenna", *GOMAC2002*, Mar. 11-14, Monterey, CA, talk 13.2.
2. K. C. Gupta, R. Garg, and I. J. Bahl, *Microstrip Lines and Slotlines* (Artech House, Dedham, Massachusetts, 1979).
3. H. C. Casey Jr. and M. B. Panish, *Heterostructure Lasers: Part A* (Academic Press, New York, 1978).
4. A. Yariv, *Quantum Electronics* (2nd ed.,Wiley and Sons, New York, 1975), ch. 19.

Microwave Phase Shifters Using Ferroelectric (Ba,Sr)TiO$_3$ Films

Won-Jeong Kim, Eun-Kyoung Kim, Seung-Eon Moon, Seok-Kil Han, Su-Jae Lee, and Kwang-Yong Kang
Basic Research Laboratory, Electronics and Telecommunications Research Institute,
Kajung-Dong 161, Taejon, 305-350, Korea

ABSTRACT

The ferroelectric (Ba$_{0.6}$Sr$_{0.4}$)TiO$_3$ (BST) films were prepared on (001) MgO single crystals by pulsed laser deposition. Coplanar waveguide (CPW) type phase shifters controlled by external dc bias field were fabricated on BST films using a 2 μm thick metal layer to reduce metal loss. Microwave properties of the CPW phase shifter were measured using a HP 8510C vector network analyzer from 0.1 – 20 GHz. The fabricated CPW phase shifters (8 mm long) exhibited differential phase angle of 100 ° at 10 GHz with a dc bias field of less than 80 kV/cm between center and ground conductors. Furthermore, a stable differential phase angle (102 ± 3.5 °) was observed from another CPW while changing the power of incident microwave from –10 to +30 dBm. Gap size dependent dielectric constant of the BST film was observed and a simple correction method was suggested in the paper. These results demonstrate the possible application of ferroelectric tunable devices on a high power tunable wireless telecommunication.

INTRODUCTION

Ferroelectric thin films with electric field dependent dielectric constant are being used to develop a new class of tunable microwave devices.[1-7] An important tunable microwave device using ferroelectric film is a wideband phase shifter which is the most important component of the phased array antenna. A simple co-planar waveguide (CPW) type phase shifter has advantages over other type phase shifters; easy fabrication with one-mask, easy to measure the microwave characteristics, and easy to extract film parameters.

In this paper, we report the microwave characteristics of the CPW fabricated on (Ba$_{0.6}$Sr$_{0.4}$)TiO$_3$ (BST) in terms of differential phase shift, and dielectric constant of BST. The fabricated CPW phase shifters exhibited a large differential phase angle with a dc bias field of less than 80 kV/cm between center and ground conductors. Furthermore, a stable differential phase angle was observed from another CPW while changing the power of incident microwave from –10 to +30 dBm.

At the end of this paper, we will discuss dielectric properties of the BST film in terms of the gap size of the device, which exhibits that the dielectric constant of the BST extracted by the conformal mapping increases with decreasing gap size. We introduced a simple empirical method to correct dielectric constant of a thin layer of high-k material.

FILM GROWTH AND DEVICE FABRICATION

Single phase BST films were deposited using a well-known pulsed laser deposition (PLD) method onto (001) MgO single crystal. A focused Kr:F excimer pulsed laser was used to ablate BST target. MgO substrates were heated at 750 °C and the deposition chamber was kept in the oxygen pressure of 170 mTorr. The thickness of the BST films were controlled by changing the deposition time, and confirmed from a cross-sectional view of the film by scanning electron
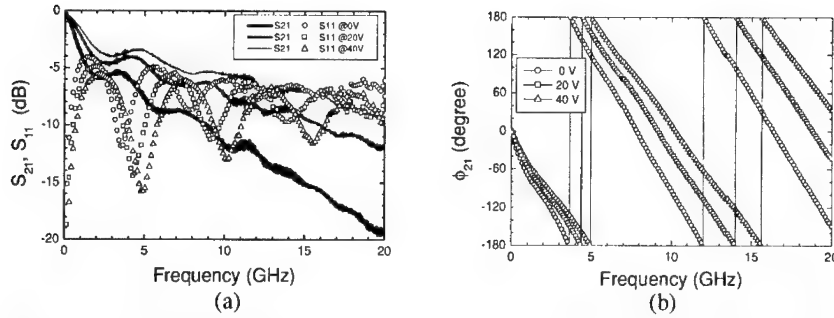
Figure 1. Frequency dependant measured microwave properties of CPW with changing bias voltage; (a) magnitudes of S_{11} and S_{21}, and (b) phase of S_{21}.

microscopy. The structure of the films were routinely investigated by x-ray diffraction, and found be epitaxial film growths. A thick Au/Cr layer (2 μm) was deposited by sputtering method. Devices were fabricated on BST films through a conventional photo-lithography with a dry etching technique. Microwave properties of the CPW's were measured at 0.1 - 20 GHz range by a HP 8510C network analyzer. Dielectric constants of the films were extracted using a modified conformal-mapping method from measured S-parameters and dimensions of devices.

A TYPICAL CPW PHASE SHIFTER

Figure 1 shows a typical frequency dependent microwave property of the CPW with external bias voltages (0 - 40 V). Note that the maximum dc bias voltage was limited to 40 V to protect the network analyzer. The dimension of the corresponding CPW is 25 μm (width), 5 μm (gap), and 8 mm (length), and the thickness of the BST film is 3000 Å. From fig. 1. (a), the measured insertion loss S_{21} decreases with increasing frequency, and improving with bias voltage, which is a typical trend of CPW type. Decreasing electrical length of device with increasing bias voltage is evident from the frequency dependant phases of S_{21} shown in fig. 3 (b). The measured phase shift angle between 0 and 40 V ranges $100 - 177$ ° at $10 - 20$ GHz, respectively. These values are significant since large differential phase shifts are achieved with such a low bias voltage of 40 V. Since differential phase shift angle with 40 V is not saturated yet (fig. 3 (b)), it will increase further with a higher dc bias voltage and expected to reach at least 180 ° at 10 GHz with 100 V. Maximum of return loss (S_{11}) ranges from -4 ~ -7 dB, which
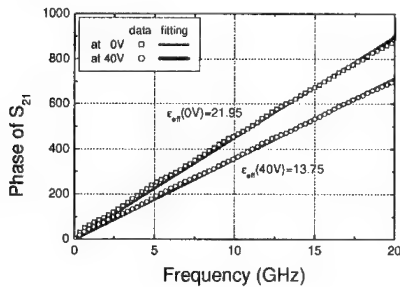
Figure 2. Total phase of S_{21} and linear fitting to extract effective dielectric constant of CPW.

192

suggests that the impedance of the device is not matched to the probe impedance of 50 Ω. However, S_{11} can be suppressed further using a matched design by controlling the dimension of the device. The measured insertion loss at 10 GHz ranges from -12 to -5.5 dB with 0 and 40 V, respectively, which mostly caused by a poor impedance matching, an electrode loss, and an unexpectedly lossy BST film (0.12 (at 0V) > tan δ > 0.03 (at 40V)).

Dielectric constant of the ferroelectric BST film is calculated from the total phase of S_{21}, which is equivalent with the electrical length. The electrical length of the device can be expressed as following,

$$\phi_{21} = 2f_o \sqrt{\varepsilon_{eff}\mu_{eff}} \times l \times 180/c , \quad \text{---------- (1)}$$

where f_o is the operating frequency, ε_{eff} and μ_{eff} are the effective dielectric constant and magnetic permearbility of the device, respectively, l is the length of CPW, and c is the light velocity in the air. Figure 2 shows that the measured total phase ϕ_{21} of the CPW agrees well with those of fitted using eq. (1) when $\mu_{eff} = 1$. Minor deviations at low and high frequency ends are observed in the graph, which may attributed to the frequency dependent non-linear response of ferroelectrics. To extract the dielectric constant of ferroelectric film, a modified conformal mapping technique has been used.[8,9] Dielectric constant of substrate, film, and air have the following relation,

$$\varepsilon_{eff} = k_{sub}\varepsilon_{sub} + k_{film}\varepsilon_{film} + k_{air}\varepsilon_{air}, \quad \text{--------(2)}$$

where k's are corresponding to the filling factors for the substrate, film and air. The calculated film dielectric constant decreases from 510 at 0 V to 250 at 40 V. This is corresponding to 50 % of dielectric constant change with 80 kV/cm of a dc bias field, which is comparable with those of the reported BST films.[1-7]

Another CPW with 10 μm gap has been exposed to high power microwaves upto +28.3 dBm (~1 Watt) to test device reliability under high microwave powers.[10] The input microwave power were swept from $-$ 10 to 28.3 dBm, which have been accomplished with appropriate sets of microwave power amplifiers and/or attenuators with power dividers to monitor the input and
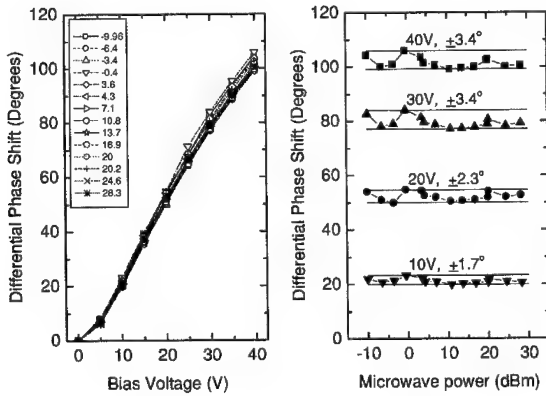

Figure 3. (a) Bias voltage dependent differential phase shift with varying microwave power from -10 to 28.3 dBm, and (b) stable differential phase angle with microwave power sweep.

output power of the device. Figure 3 exhibits stable differential phase shifts with less than 4% of deviations while changing microwave powers. Note that relatively large deviation can be attributed to minor fluctuations caused by changed microwave accessories on the path to change microwave power. A stable phase shift of 102 ± 3.5 ° were achieved with bias voltage of 40 V, while changing input microwave power from –10 to +28.3 dBm. This result clearly demonstrates that the high power stability of the ferroelectric devices.

GAP DEPENDENT PROPERTIES OF PHASE SHIFTERS

It is difficult to extract a dielectric constant from a high dielectric thin layer. Though dielectric constants of BST films have been calculated using (modified) conformal mapping method, the validity of the model with extreme boundary conditions need further verifications with experimental results.

To investigate the dielectric constant of the films, microwave properties have been measured from devices with different gap sizes (20, 15, 10, 7, and 5 μm), while the width of the center conductor was kept in 20 μm and the length of the device was fixed at 3 mm. Thickness of the BST film used in this experiment is 630 nm measured by SEM. Figure 4 shows frequency dependent total phases of two CPW's with gap size of 5 and 20 μm. The effective dielectric constants of CPW's were extracted by using the eq. 1. Then, the dielectric constant of the BST film was calculated from the effective dielectric constant based on the conformal mapping method (eq.2), and the resulting dielectric constant of the film without bias field are shown in figure 5.

From the figure 5, one can find an interesting tendency that the calculated dielectric constant decreases with increasing gap size. The dimensions of the devices were investigated using SEM, and found to be 1 μm larger width and narrower gap than the original design. Though lower dielectric constants with measured device dimensions were extracted, dielectric constants still decrease with increasing gap size as shown in Fig. 5. This suggests that the conformal mapping and/or the nature of the ferroelectrics are not understood completely. Since we are dealing with high dielectric constant materials, the conformal mapping developed for low dielectric constant materials may cause some degree of deviation when the condition is extreme, such as high-k,
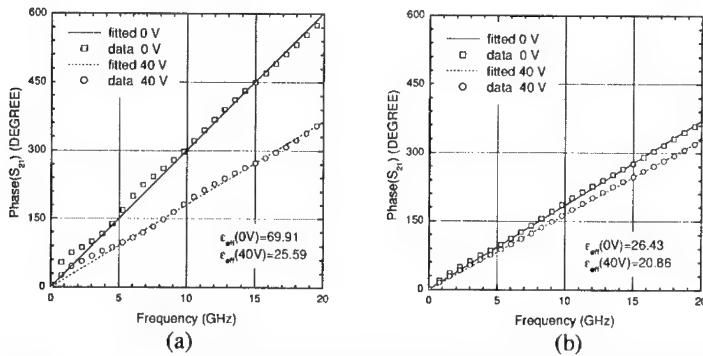

Figure 4. Total S_{21} phase of the CPW's with 3 mm in length, 20 μm in width, and (a) 5 μm and (b) 20 μm of gap sizes.
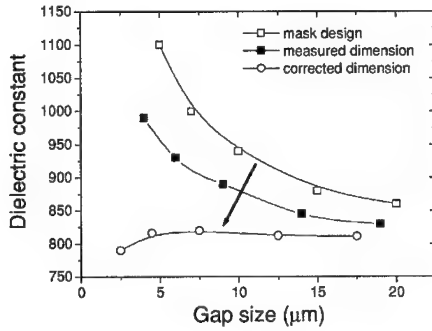
Figure 5. Gap dependent dielectric constant of the high dielectric BST film without bias fields.

thin-layer, and narrow gap, and etc. The other possible origin of deviation may come from the anisotropic dielectric constant of ferroelectric films hinted from the orientation dependent dielectric constants of tetragonal and distorted cubic ferroelectrics.[1, 11-13] This should investigated further to get clear picture in a future.

Assuming that the dielectric constant of the film without dc bias field is unique and independent from the gap dimension, and the modified conformal mapping is valid, a simple correction procedure has been developed to find a unique dielectric constant of the film without a complicate scheme.

An empirical method suggested in here is introducing a virtual device dimension: increased center width and decreased gap size from the measured ones to calculate dielectric constants using the same modified conformal mapping. Dielectric constants calculated with the virtual device dimensions (2.5 μm wider width and 2.5 μm narrower gap than those of design) are shown in Figure 5. Corrected dielectric constants are 810 with a small deviation (less than 2%), which is match well with EM simulation value of 750. More detailed discussion including EM simulation results will be published in elsewhere.

SUMMARY

CPW type phase shifters have been fabricated on BST/MgO using a 2 μm thick metal layer. Microwave properties of the CPW's presented in here have been summarized in Table 1. The fabricated CPW phase shifter (25um (width), 5um (gap), and 8mm (length)) exhibited differential phase angle of 100 – 177 ° at 10 - 20 GHz with a dc bias field of 80 kV/cm between Table 1. Summary of microwave properties from the CPW devices reported in this paper.

	Dimension (g, w, l)	Film thickness	$\Delta\phi_{21}$ (10,20GHz)	ε_{BST} (0, 40V)	S_{21} (0, 40V) @10 GHz	S_{11} (0, 40V) @10 GHz
CPW I	5μm, 25μm, 8mm	3000Å	100, 177	510, 250	-12, -5.5	-6, -12
CPW II	10μm,10μm, 10mm	3200Å	102, 191	---	-13, -8	-18, -19
CPW III	5μm, 20μm, 3mm	6300Å	119, 223	790, 245	-10, -3	-3, -10
CPW IV	20μm,20μm, 3mm	6300Å	23, 40	811, 590	-2.8, -1.4	-11, -18

center and ground conductors. Furthermore, a stable differential phase angle (102 ± 3.5 °) has been observed although the power of incident microwave was swept from –10 to +30 dBm. Gap size dependent dielectric constant of the BST film was observed, and a simple correction method was suggested by adjusting width and gap of devices. The corrected dielectric constant of the BST film was found to be 810 ± 5.

In this paper we clearly demonstrated that possible application of ferroelectric tunable devices on a high power wireless telecommunication.

ACKNOWLEDGEMENT

REFERENCES

1 W. J. Kim, W. Chang, S. B. Qadri, J. M. Pond, S. W. Kirchoefer, D. B. Chrisey, and J. S. Horwitz, Appl. Phys. Lett. **76**, 1185 (2000)

2 F. W. Van Keuls, C. H. Mueller, F. A. Miranda, R. R. Romanofsky, C. L. Canedy, S. Aggarwal, T. Venkatesan, R. Ramesh, J. S. Horwitz, W. Chang, and W. J. Kim, IEEE MTT-S **2**, 737 (1999)

3 C. M. Carlson, T. V. Rivkin, P. A. Parilla, J. D. Perkins, D. S. Ginley A. B. Kozyrev, V. N. Oshadchy, and A. S. Pavlov, Appl. Phys. Lett., **76**, 1920 (2000)

4 C. L. Canedy, S. Aggarwal, H. Li, T. Venkatesan, R. Ramesh F. W. Van Keuls, R. R. Romanofsky, and F. A. Miranda, Appl. Phys. Lett., **77**, 1523 (2000)

5 J. Im, O. Auciello, P. K. Baumann, S. K. Streiffer, D. Y. Kaufman, and A. R. Krauss, Appl. Phys. Lett., **76**, 625 (2000)

6 E. G. Erker, A. S. Nagra, Y. Liu, P. Periaswamy, T. R. Taylor, J. Speck, and R. A. York, IEEE Micro. And Guided Wave Lett., **10**, 10 (2000)

7 B. H. Park, E J. Peterson, Q. X. Jia, J. Lee, X. Zeng, W. Si, and X. X. Xi, Appl. Phys. Lett., **78**, 533 (2001)

8 S. S. Gevorgian, T. Martinsson, P. I. J. Linner, and E. L. Kollberg, IEEE Trans. Microwave Theory Tech., **44**, 896 (1996)

9 E. Carlsson, and S. Geovorgian, IEEE Trans. Microwave Theory Tech., **47**, 1544 (1999).

10 E. K. Kim, S. E. Moon, S. J. Lee, S. K. Han, K. Y. Kang, and W. J. Kim, Ferrolectrics (Accepted)

11 W. J. Kim, W. Chang, S. B. Qadri, J. M. Pond, S. W. Kirchoefer, J. S. Horwitz, and D.B. Chrisey, Appl. Phys. A, **70**, 313 (2000)

12 Y. G. Wang, M. E. Reeves, W. J. Kim, J. S. Horwitz, and F. S. Rachford, Appl. Phys. Lett., **78**, 8372 (2001)

13 S. K. Streiffer, C. Basceri, C. B. Parker, S. E. Lash and A. I. Kingon, J. of Appl. Phys., **86**, 4565 (1999)

Influence of the Laser Repetition Rate on Crystalline Structure, Composition, and Magnetic Properties of Laser Deposited $Y_3Fe_5O_{12}/Gd_3Ga_5O_{12}(111)$ Films

S. Kahl, V. P. Denysenkov, S. I. Khartsev, S. Kranzusch[1], and A. M. Grishin
Condensed Matter Physics, Royal Institute of Technology, S-16440 Stockholm, Sweden;
[1]Laserlabor Göttingen e.V., D-37077 Göttingen, Germany

ABSTRACT

$Y_3Fe_5O_{12}$ (YIG) films have been deposited onto single crystal $Gd_3Ga_5O_{12}$ (GGG) substrates by pulsed laser deposition. For a given set of experimental parameters, the oxygen background pressure and substrate temperature were optimized to achieve the narrowest ferromagnetic resonance (FMR) lines. The repetition rate was then varied from 10 to 50 Hz. There is a clear transition from films with low saturation magnetization $4\pi M_S \approx 300$ Gs, high coercive fields $H_C > 20$ Oe, and broad FMR lines $\Delta H > 100$ Oe to films with $4\pi M_S > 1400$ Gs, $H_C < 10$ Oe, and $\Delta H \leq 10$ Oe. This crossover occurs when the laser repetition rate is changed from 20 to 30 Hz. No significant differences could be detected in any of the other investigated properties: crystalline structure, cation concentration ratio, and surface roughness do not depend on the repetition rate. Annealing experiments show that the films deposited at 10 and 20 Hz repetition rate are oxygen deficient. We loaded the film deposited at 20 Hz with oxygen, so that it reached the bulk value for $4\pi M_S$. The coercive field, however, remained large.

INTRODUCTION

$Y_3Fe_5O_{12}$ (YIG) films prepared by liquid phase epitaxy have attracted strong attention during the past decades. These films of the garnet structure have been grown with high perfection onto garnet single crystal $Gd_3Ga_5O_{12}$ (GGG) substrates, which have nearly zero lattice mismatch with the film. With sometimes sophisticated substitutions, garnet films have been proposed for two important applications in the past, as bubble memory films and for magnetostatic wave devices [1,2]. In the past two decades, interest in their magneto-optical properties has grown [3–6].

In this paper, we investigate the magnetic, structural and compositional properties of laser deposited YIG films on GGG(111) substrates. Our investigations add information to prior publications about laser deposited YIG films [7,8] on GGG substrates. We focus onto the interesting and technically important role of the laser repetition rate.

EXPERIMENTAL PROCEDURE

YIG films were grown onto GGG(111) single crystal substrates by the technique of pulsed laser deposition at 248 nm wavelength. Directly after preparation, the films were annealed in the deposition chamber at 700 mbar of oxygen pressure for 20 min. The target was ground before every new deposition.

The films were structurally characterized by three circle x-ray diffractometry (XRD). Film thicknesses were determined by profilometry over film edges and ranged between 400

and 600 nm. A qualitative picture of the film morphologies was obtained in an optical microscope. Film roughnesses were obtained in an atomic force microscope (AFM).

Rutherford Backscattering (RBS) allowed us to determine cation concentration ratios of the films and the target. We used He^4 ions at 1510 keV. The obtained backscattering spectra were fitted by the SIMNRA 4.0 simulation programme [9].

Magnetic moments and coercive fields were measured with a vibrating sample magnetometer. A broadband ferromagnetic resonance (FMR) spectrometer using a network analyzer as both source and receiver of the microwave radiation was used to determine position and width of the ferromagnetic resonance lines.

Further annealing was done in a separate oven under oxygen gas flow of 1000 cm^3/min at atmospheric pressure for 90 min at temperatures up to 950 °C.

RESULTS AND DISCUSSION

Keeping the laser energy fixed to 2.5 J/cm^2, the substrate-to-target distance to 4.5 cm, the laser repetition rate to 40 Hz, and the deposition time to 30 min (corresponding to 72000 pulses), we optimized the substrate temperature to 650 °C and the oxygen pressure to 0.034 mbar in order to achieve the narrowest FMR line of 6 Oe. According to our experience, the narrowest FMR line occurs under some specific angle, which is different for every film.

We found the best parameters of deposition at temperatures much lower than reported in Ref. [8], where the smallest FMR linewidth and the lowest coercive fields were found for substrate temperatures above 800 °C. In that investigation, however, the deposition rate (film thickness divided by total time of deposition) was twice as high as the one we used. We therefore concluded that the deposition rate plays a major role for the growth of laser deposited YIG films.

All films grew epitaxially, examples of a wide angle $\theta - 2\theta$ and a ϕ scan are shown in Figure 1. The (222) and (666) reflections are forbidden in the garnet structure and could stem from edges of the substrate or inhomogeneities of the film.
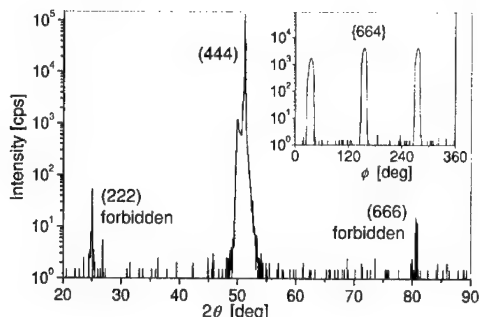
Figure 1. XRD patterns of a $Y_3Fe_5O_{12}/Gd_3Ga_5O_{12}(111)$ film deposited at the laser repetition rate of 30 Hz. The main graph shows a wide angle $\theta - 2\theta$ scan. The inset shows a ϕ scan of the {664} oblique lattice planes.

It is impossible to see the main part of the film reflections in $\theta - 2\theta$ scans due to the extremely small lattice mismatch between YIG and GGG. This is demonstrated for films made with deposition rates from 10 to 50 Hz in figure 2. At deposition rates above 20 Hz, there are low intensity platforms to the left of the Bragg peaks. However, these platforms only have 1% of the peak height and do not show any peak structures.

Figure 3 shows the RBS spectrum of the film deposited at 30 Hz repetition rate. The edges in the spectrum correspond to the four heavy elements in the film and substrate. The oxygen edge is not resolved clearly. From carefully fitting the heights behind the Fe and Y edges, we determined the concentration ratio of Fe and Y irons (see inset of figure 3 for the fit). The cation concentration ratios in the other films and in the target were determined the same way. This analysis revealed slight Y deficiencies both in target and films (see table 1 for films, in the target $c_Y/c_{Fe} = 0.5$). The transfer from target to substrate was nearly stoichiometric for all films.

In transmitting light in the optical microscope, some differences between the films could be observed. The films deposited at the repetition rates of 30, 40, and 50 Hz look very similar: they show plain surfaces, with occasional voids. The film deposited at 20 Hz shows more and larger voids (around 10 μm in diameter), which possess irregular shapes. The film deposited at 10 Hz has even more voids, but they are smaller and circular. All films possess a large number of small dark spots, which are probably pits resulting from the small error in stoichiometry.

Film rms roughnesses averaged over areas of 20 μm^2 to 30 μm^2 are essentially the same and less than half the lattice parameter for all five films, see table 1.

The saturation magnetization is much higher for the three films deposited at the higher
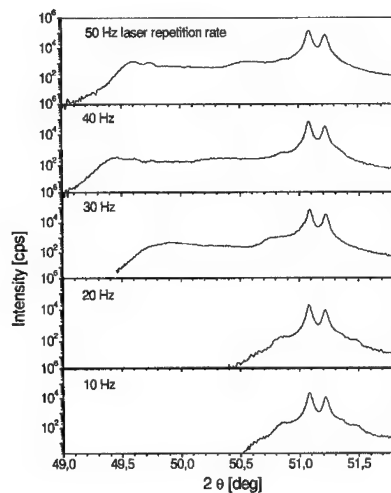
Figure 2. (444) reflections from $Y_3Fe_5O_{12}/Gd_3Ga_5O_{12}(111)$ films deposited at identical conditions, except for the laser repetition rate, which is indicated for all spectra.

Table 1. Summary of the film properties at different repetition rates

	error	10 Hz	20 Hz	30 Hz	40 Hz	50 Hz
XRD: plateau left of (444)		no	no	yes	yes	yes
concentration c_Y/c_{Fe}	±0.01	0.49	0.50	0.56	0.47	0.52
rms roughness [nm]	±0.05	0.47	0.37	0.47	0.45	0.35
coercive field H_C [Oe]	±0.2	45	20	0.4	9	1.3
sat. magn. $4\pi M_S$ [Gs]	15%	310	250	1950	1590	1450
dark/light brownish color		dark	dark	light	light	light

repetition rates (table 1). Look at figure 4 to compare hysteresis loops (as prepared) of the films deposited at 20 and 30 Hz. The main error in determining the saturation magnetization comes from measuring sample volumes and can reach as much as 15%.

Figure 5 depicts the changes in coercive field and saturation magnetization as a function of the repetition rate. The coercive field H_C for 40 Hz is larger than for 30 and 50 Hz, which could be due to the better cation concentration ratio of the films deposited at 30 and 50 Hz.

The films also differ in color: The two films deposited at 10 and 20 Hz look dark brownish whereas the other three films look light brownish.

Considering the results described above, it seems likely that the differences in magnetic hysteresis loops are caused by differences in the oxygen contents of the samples. This hypothesis was tested by simultaneously annealing a 'bad' sample (deposited at 20 Hz repetition rate) and a 'good' sample (deposited at 30 Hz) for 90 min in 1 atm of oxygen at the temperatures of 500 °C, 650 °C, 800 °C, and 950 °C. Magnetic hysteresis loops were measured for both samples after every annealing step. The hysteresis loops of the good sample did not show any changes, but the saturation magnetization of the bad sample increased significantly and reached the same value as in the good sample (within the 15% error margin). The coercive field of the bad sample increased through annealing at 650 °C and then decreased
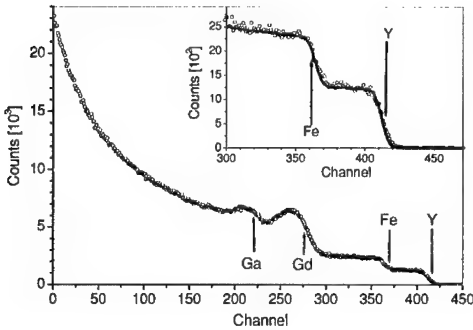
Figure 3. RBS spectrum of a $Y_3Fe_5O_{12}/Gd_3Ga_5O_{12}(111)$ film deposited at the repetition rate of 30 Hz. The inset shows the fit of the film edges.

200
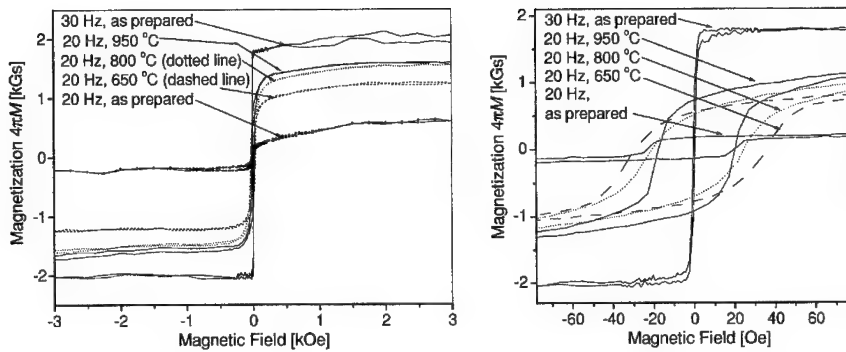
Figure 4. Magnetic hysteresis loops of two laser deposited $Y_3Fe_5O_{12}/Gd_3Ga_5O_{12}(111)$ films recorded with the magnetic field parallel to the film plane. The films were deposited at the deposition rates indicated in the figure. After preparation they were subjected to postannealing in oxygen atmosphere for 90 min at the temperatures given in the left figure. The right figure shows the region of low magnetic fields in magnification.

again to approximately its original value. See figure 4 for hysteresis loops recorded with the magnetic field parallel to the film plane. The color of the bad film became lighter with every annealing step until both films looked the same after annealing at 800 °C.

The magnetic superexchange coupling in YIG is mediated by oxygen ions. Oxygen deficiency is therefore expected to result in reduced saturation magnetization. By increasing the oxygen content in the bad sample through annealing in oxygen atmosphere, the saturation magnetization was increased significantly.

In order to maintain charge neutrality at oxygen deficiency, a fraction of the metallic cations will change their valence states. Mixed valence states allow for charge transitions
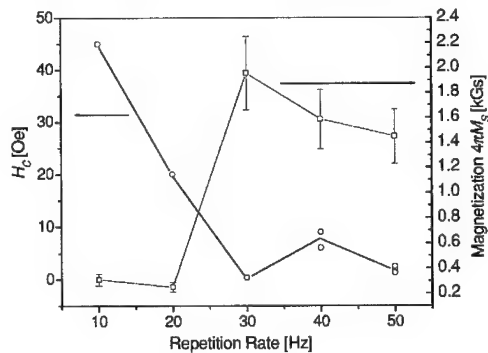
Figure 5. Coercive fields and saturation magnetizations for $Y_3Fe_5O_{12}/Gd_3Ga_5O_{12}(111)$ films deposited at different deposition rates.

and increase the optical absorption in the sample. The bad sample was therefore of a dark color directly after preparation, but its optical absorption was reduced through the annealing experiments.

One question remains, and this is *why* the two bad films possess oxygen deficiencies and the three good films do not. Most plausible is that oxygen left the growing film during the deposition process. There could be a change from films with microstructures permitting fast diffusion of oxygen to films with slower channels of oxygen diffusion as the repetition rate is increased from 20 to 30 Hz. Such a change in growth mode can occur abruptly when deposition parameters are changed over certain threshold values. The fact that the bad films possess larger coercive fields (even after annealing) supports the supposition that they are different from the good films with respect to microstructure.

CONCLUSIONS

The laser repetition rate is a very important parameter for the pulsed laser deposition of thin epitaxial YIG films. The search for films with narrowest FMR lines leads to different sets of experimental parameters, if the search is done for different fixed deposition rates. In our investigations, by changing the deposition rate and keeping all other parameters fixed, we observed a sharp transition in magnetic properties when the repetition rate was changed from 20 to 30 Hz. The reason is that films with low deposition rates are oxygen deficient.

One of our best films showed the following parameters: rms surface roughness is smaller than $1/3$ of the lattice constant, saturation magnetization $4\pi M_S \approx 1950$ Gs is about the same as in crystalline bulk samples, the magnetic coercive field H_C is below 1 Oe, and the smallest FMR linewidth is $\Delta H \leq 10$ Oe. These values confirm that pulsed laser deposition is an interesting alternative to prepare high quality epitaxial YIG films.

REFERENCES

1. A. H. Eschenfelder, *Magnetic Bubble Technology.* (Springer-Verlag, 1980).

2. G. Rodrigue, *Proc. IEEE*, **76**, 121 (1988).

3. P. Hansen, K. Witter, and W. Tolksdorf, J. Appl. Phys. **55**, 1052 (1984).

4. G. F. Dionne and G. A. Allen, J. Appl. Phys. **73**, 6127 (1993).

5. J. Wei, H. Hu, and H. He, Phys. Stat. Sol. (a) **168**, 501 (1998).

6. J. Fujita, M. Levy, R. M. Osgood, Jr., L. Wilkens, and H. Dötsch, Appl. Phys. Lett. **76**, 2158 (2000).

7. N. B. Ibrahim, C. Edwards, and S. B. Palmer, J. Magn. Magn. Mater. **220**, 183 (2000).

8. P. C. Dorsey, S. E. Bushnell, R. G. Seed, and C. Vittoria, J. Appl. Phys. **74**, 1242 (1993).

9. M. Mayer, http://ibaserver.physics.isu.edu/sigmabase/programs/simnra44.html.

Rapid Gel Cast Prototyping of Complex Paraelectric (Ba,Sr)TiO$_3$/MgO Composites

Jennifer Synowczynski, Samuel Hirsch, and Bonnie Gersten
Weapons and Materials Research Directorate, Army Research Laboratory
Aberdeen Proving Grounds, MD 21005-5069

ABSTRACT

A rapid prototyping process for manufacturing complex three-dimensional RF structures in ceramic systems was developed. The process combines fundamentals from lost wax investment casting and ceramic gelcasting. The first step is to directly deposit a mold made of a low melting point wax using a high precision inkjet rapid prototyper. Then, a gelcasting slurry containing polymeric precursors, a high solids loading of ceramic powders and a free radical initiator is cast into the mold and polymerized to lock in the structure. Finally, the mold is melted and the remaining green part is sintered. Aqueous gelcasting slurries were developed for MgCO$_3$, (Ba,Sr)TiO$_3$, and a composite of (Ba,Sr)TiO$_3$ and MgO. The maximum solids loading attained for each of the powders was 22 V%, 50 V%, and 25 V% respectively. The 50V% gelcast part had a more uniform microstructure, higher sintered density, less open porosity and smaller grain size than parts produced through dry pressing. The microstructural improvements resulted in a high dielectric permittivity.

INTRODUCTION

Recent efforts to reduce the weight, cost, and size of microwave devices such as electronic scanning antennas and voltage tunable filters have created the need for low-loss, voltage-tunable paraelectric materials. The critical materials parameters for RF device designs are (1) low dielectric constant for impedance matching (ε_R ~100) (2) low dielectric loss tangent (3) high tunability (i.e. % change in dielectric constant with voltage) and (4) small temperature coefficient of permittivity. To meet these requirements, investigators at ARL [1,2] composite paraelectric (Ba,Sr)TiO$_3$ (BST) with the low-loss, temperature-stable dielectric MgO. The resulting voltage-tunable materials have dielectric constants in the range from 800 to 100 and loss tangents as low as 0.008 at 10GHz with a voltage tunability of 7% at 2 volts/micron. New processing challenges arise for more complicated three-dimensional structures such as photonic bandgap devices [3]. In this investigation, we seek to develop a rapid prototyping method based on ceramic gelcasting and lost wax investment casting for manufacturing complex 3D structures from BST / MgO composites.

There are four major steps in lost wax investment casting: (1) create a sacrificial mold (2) cast a concentrated ceramic slurry into the mold (3) cure the slurry and (4) remove the mold. The ceramic slurry must have no destructive chemical interactions with the wax mold, a cure temperature below the mold softening point, and minimal drying shrinkage. Ideally, it would also produce a homogeneous microstructure and have a high green strength at low binder concentration. Of the available casting methods (slip casting, injection molding, physical gelation, etc [4, 5], chemical gelation (a.k.a gelcasting [6]) comes closest to meeting these requirements. Gelcasting forms a permanently bonded polymeric network with high green strength that locks the ceramic particles in place. This network also locks in an open pore structure making it easier to remove the solvent. Since the solids loading is high (>50V%), there is little drying shrinkage during solvent removal. Gelcasting can be used to make large (>6kg) or

small parts with submillimeter features and few defects. These advantages make it the ideal choice for a lost wax investment casting process.
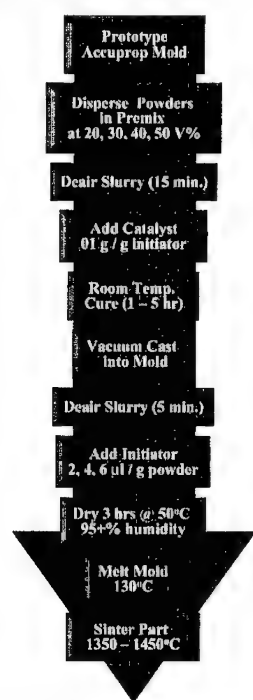
EXPERIMENTAL DETAILS

Figure 1. Process Flow Diagram

Figure 1 contains the process flow diagram and experimental conditions for the lost wax investment casting / ceramic gelcasting procedure. The accuprop molds were prototyped on our high precision Sanders Rapid Toolmaker in 0.05mm thick layers. All powders in the study were characterized to determine their surface area and particle size using BET (Micromeretics ASAP 2010) and dynamic laser scattering (Horiba LA-910). The dispersants listed in Table 1 were screened for their effect on the rheological properties (Brookfield Model LDTDV-I viscometer, small sample adapter, $20^{\circ}C$) of slurries containing a 20 V% loading of BST / MgO powders. The rheological properties of 35 V% BST slurries with DAR concentrations between 0 and 2 wt% were also measured. To determine the optimal initiator concentration, we conducted spectroscopic investigations (950 Raman Spectrometer, Nicolet Inst., WI) of the cure kinetics of the MAM-MBAM polymerization reaction. The polymeric distribution within the green bodies and the resulting sintered grain size distribution were monitored via Scanning Electron Microscopy (JEOL 840A, Japan). The Archimedes method was used to determine the open porosity and sintered density. Finally, low frequency dielectric properties were established through parallel plate capacitance measurements (HP4194 LCR) using Ag electrodes with a guard ring configuration.

Table I. Chemicals Investigated

Powder (Supplier)
BST - $Ba_{0.55}Sr_{0.45}TiO_3$ (see ref. 1)
BST / MgO – 40 wt% $Ba_{0.55}Sr_{0.45}TiO_3$ / 60 wt% MgO (see ref. 1)
$MgCO_3$ (Alfa Aesar, MA) + 3 wt% oxalic acid (Fisher Scientific, NY)
MgO (Alfa Aesar, MA)
Surfactant (Supplier) – 1wt% based on powder
DAR – Darvan 821A (RT Vanderbilt, CT)
PAA - Polyacrylic acid (Acros Organics, NJ)
HPC - Hydroxypropyl cellulose (m.w. 100,000 Alfa Aesar, MD)
DAXAD 32 - Ammonium polymethacrylate (WR Grace, KY)
DAXAD 34 - Polymethacrylic acid (Hampshire Chemical, MA),
EDTA - Ethylenediaminetetraacetic acid (Aldrich, WI)
SH - Sodium hexametaphosphate (Mallinckrodt, KY)
Aerosol 22 (Cytec, NJ)

Monomer and Crosslinker (Supplier)
MAM - methylacrylamide (98%, Aldrich, WI)
MBAM - methylene bisacrylamide (Aldrich, WI)
PEGDMA - poly(ethylene glycol) dimethacrylate (Aldrich, WI)
Premix (monomer:crosslinker, wt% in water)
MAM:MBAM (5:1, 12%)
MAM:PEGDMA (1:1, 15%)
Defoamer - 0.01 g/g powder (Supplier)
SURF - Surfnyol (Air Products and Chemicals, PA)
Catalyst - 0.01 g/g initiator (Supplier)
TEMED - tetramethylethylene diamene (Avocado Chemical, LS)
Free Radical Initiator - 2, 4, 6 μl / g powder (Supplier)
APS - ammonium persulfate (Aldrich, WI)

DISCUSSION

The surface area and median particle size were 1.639 ± 0.0175 m^2/g and 5.3μm for Ba $_{0.55}$Sr$_{0.45}$TiO$_3$ and 30.912 ± 0.1632 m^2/g and 5.2 μm for MgCO$_3$. The 40 wt% Ba $_{0.55}$Sr$_{0.45}$TiO$_3$/ 60wt% MgO powder had a bimodal distribution with a surface area of 4.751 ± 0.636 m^2/g and median particle sizes of 0.3μm and 1.2μm. Of the dispersants evaluated DAR, PAA, and SH yielded the least viscous slips (cf. Table II). Since SH contains inorganic contaminants that may adversely affect the dielectric properties, PAA and DAR were chosen for further optimization.

Table II. Effect of dispersants on room temperature viscosity

Dispersant ID	Viscosity (cp)
DAR	230
PAA	213
SH	264
EDTA	712
DAXAD 32	864
Aerosol 22	963
DAXAD 34	1124
HPC	5512

As shown in Figure 1a, the viscosity curve had a minimum at 0.085 wt% PAA, whereas DAR yielded fluid slips for all concentrations less than 1.75 wt%. The maximum castable BaSrTiO$_3$ loading was 35 V% for 0.125 wt% PAA [7] and 50V% for 1 wt% DAR. Slips made with 1 wt% DAR showed shear thinning behavior (cf. figure 1B). The degree of shear thinning and the viscosity increased as the solids loading increased. At loading > 40V%, the slips also exhibited slight thixotropic hysteresis. The change in viscoelastic properties at higher solids loading may be due to the short interparticle distance forming a particle network. This network breaks down at high shear rates (i.e. shear thinning) into individual flocs that flow past each other. As it breaks down the constrained solvent is freed, thereby reducing the effective volume fraction of the flocs and leading to thixotropic behavior.
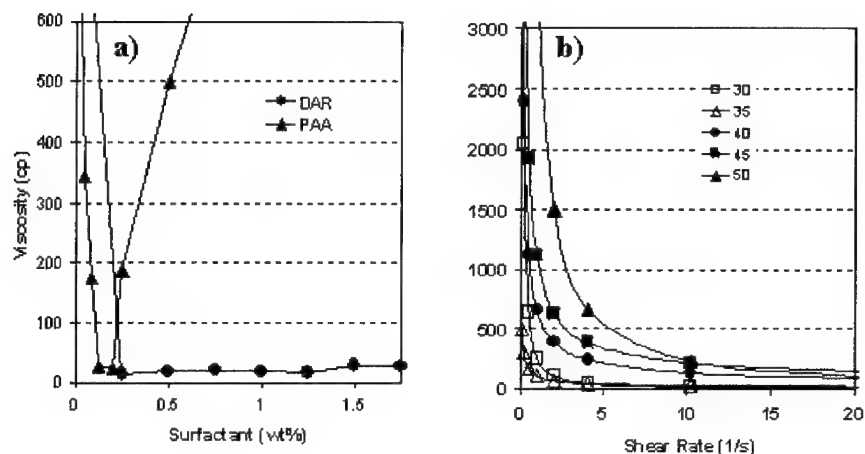
Figure 1. Viscosity vs. a) wt% surfactant b) shear rate (30, 35, 40, 45, 50 V%) with 1% DAR.

The MAM-MBAM curing kinetics were determined through the disappearance of the C=C bond at 1640 cm^{-1} and the emergence of the C-C at 1200 cm^{-1} (cf. Figure 2a). Results indicate that initiator concentrations less than 4 µl/g provided sufficient time to deair and cast the slurries. However, the kinetics change when BST is added to the gel. This change cannot be directly monitored using Raman spectroscopy because BST produces a strong fluorescence peak over a broad frequency range. This may be prevented in the future by changing the frequency of the laser.
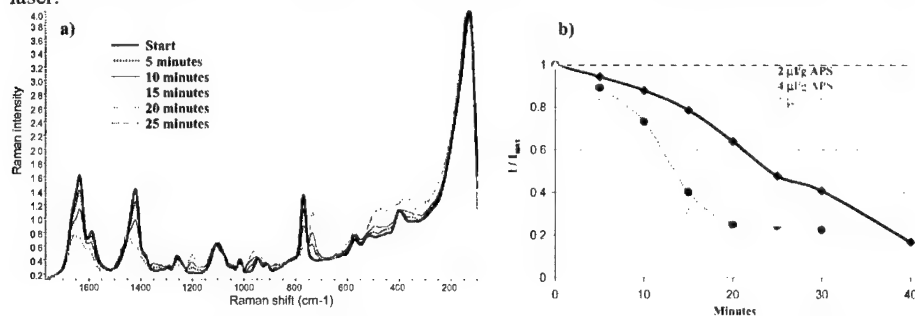
Figure 2. a) Cure Kinetics at 6µl/g initiator concentration b) 1640 band intensity vs. time.

Slurries containing 2µl/g initiator and 50V% BaSrTiO$_3$ were successfully cast and sintered (cf. Figure 4a). Parts cast under the same conditions but using the composite BST / MgO powders did not fully cure at room temperature after 24 hours. They lacked sufficient green strength to survive the dewaxing procedure. SEM analysis of the green bodies (cf. Figure 3a) revealed that the polymer network consisted of short chains that may have prematurely polymerized due to the interaction of dissolved Mg with the functional group of the monomer. To prevent this interaction, the solubility of Mg in water was reduced by switching to MgCO$_3$

and coating the particles with oxalic acid to produce a thin surface layer of magnesium oxalate (cf. Figure 3b).
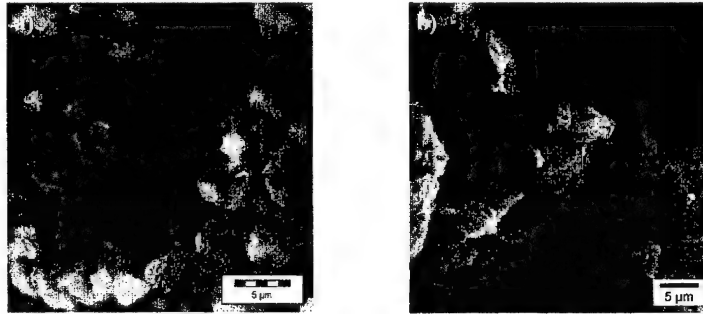
Figure 3. Green body interior a) 40wt% Ba $_{0.55}$Sr$_{0.45}$TiO$_3$/ 60wt% MgO b) coated MgCO$_3$.

Table III lists the microstructural analysis and dielectric properties for the sintered composites. For BST, the green and sintered densities did not change significantly as the solids loading increased from 30 to 45 V%. However, at 50 V% they exceeded the properties attained through dry pressing. The grain size was consistently lower for gelcast samples than the dry pressed. The combination of higher density and smaller grain size lead to improvements in the permittivity and dielectric loss tangent. For the composite gelcasts, the sintered density increased as the solids loading increased. The solids loading attained was not high enough for the density to equal that obtained during dry pressing. This degraded the electrical performance. However, the BST and MgO grains were more uniformly distributed in the gelcast samples (cf. Figure 4b,c). The segregation in the dry pressed samples is most likely due to agglomeration and differential settling within the die set caused by differences in the density and particle size of the powders. Since gelcasting is a colloidal process, the powders are uniformly dispersed immediately prior to producing the green body.

Table III. Microstructural and Dielectric Properties.

MgO (wt%)	Solids (V%)	Green ρ (g/cc)	Sinter ρ (g/cc)	% Open Porosity	Grain Area (μm^2)	ε_R (1MHz)	Tanδ (1MHz)
0	Pressed	2.53	5.05	3.1	74 ± 34	2597	0.0010
0	25	2.21	4.89	6.5	44 ± 23	2065	0.0013
0	30	2.37	5.20	4.6	150 ± 136	2360	0.0010
0	35	2.51	5.20	6.2	52 ± 38	2360	0.0009
0	40	2.44	5.17	1.9	49 ± 33	2331	0.0014
0	45	2.44	5.16	0.6	50 ± 22	2150	0.0010
0	50	2.66	5.40	2.6	56 ± 28	2651	0.0006
60	Pressed	2.23	4.30	3.1		81	0.0002
60	15	1.24	2.84			45	0.0010
60	20	1.51	3.23	3.2		68	0.0002
60	25	1.34	3.80	1.9		74	0.0004

Figure 4. Microstructure of 40wt% Ba $_{0.45}$Sr$_{0.55}$TiO$_3$/ 60wt% MgO a) dry pressed b) gelcast.

CONCLUSION

Three-dimensional paraelectric parts were cast using a combination of lost wax investment casting and ceramic gelcasting. The most fluid slips were prepared using darvan 821A at concentrations less than 1.75 wt% based on powder. These slurries were shear thinning and slightly thixotropic at high solid loading. The maximum loading attained was 50V%, 22V%, and 25V% for Ba $_{0.55}$Sr$_{0.45}$TiO$_3$, MgCO$_3$, and 40wt% Ba $_{0.45}$Sr$_{0.55}$TiO$_3$/ 60wt% MgO respectively. The BaSrTiO$_3$ gelcast samples had a smaller grain size, more uniform microstructure and higher sintered density than the dry pressed. This resulted in improvements in the low frequency permittivity and dielectric loss tangent over the conventionally processed Ba $_{0.55}$Sr$_{0.45}$TiO$_3$. It was not possible to achieve the same solids loading for aqueous MgO slurries due to their unique surface chemistry. Lower loadings resulted in low-density parts with poor dielectric properties. By coating the particle surface with magnesium oxalate, the interaction between the dissolved Mg and the functional group of the monomer was eliminated. In the future, the solids loading may be improved by either switching to a non-aqueous gelcasting system or coating the MgO surface to change the surface chemistry.

ACKNOWLEDGEMENTS

REFERENCES

1. J. Synowczynski, B. Gersten, Army Science Conference, December (2000).
2. J. Synowczynski, L. Sengupta and L. Chiu, Integrated Ferroelectrics **22**[1-4] 861-872 (1998).
3. V. Berger, Optical Materials **11** 131-142 (1999).
4. W. Sigmund, J. Am. Ceram. Soc. **83**[7] 1557-74 (2000).
5. J. Lewis, J. Am. Ceram. Soc. **83**[10] 2341-59 (2000).
6. O. Omatete, M. Janney and S. Nunn, J. Euro. Ceram. Soc. **17**[2-3], 407-413 (1997).
7. J. Synowczynski, S. Hirsch, B. Gersten, Electroactive Polymers and Rapid Prototyping, MRS Fall Proceedings **698** in press (2001)

AUTHOR INDEX

SUBJECT INDEX